# Orthomagmatic Fluids and Saline Melts in Iron Oxide-Apatite and Porphyry-Copper Systems

by

Wyatt M. Bain

A Thesis submitted in partial fulfillment of the requirements for the degree of

Doctor of Philosophy

Department of Earth and Atmospheric Sciences

University of Alberta

**Abstract**

The physical and chemical properties of aqueous fluids and melts, and how these evolve through time and space, are key controlling factors that govern the formation of mineral deposits. For some metal-rich system types such as iron oxide-apatite deposits (IOA), the sources and chemical compositions of mineralizing fluids are still unknown and genetic models for these systems are therefore largely speculative. For other, well-studied system types such as porphyry deposits, the sources and compositions of mineralizing fluid are unambiguous, but questions remain as to how these fluids evolve between their sources and the site of ore formation.

In this thesis, I describe the results and implications of detailed studies aimed at determining the sources, properties and evolution of mineralizing fluids in three IOA systems and one small, but exemplary porphyry system. The overarching objective of these works are to document the physical and chemical properties of the ore-forming fluids, and to clarify the geologic factors that govern these properties. The main tool employed throughout this thesis is analysis of fluid and melt inclusions by a combination of detailed petrography and chemical microanalysis. A number of major themes emerge: For each of the studied systems (IOA and porphyry), I present evidence for a central role of immiscible fluids and melts, and show that particular aspects of the geologic setting of each deposit gave rise to critical features of the ore-forming fluids and melts.

Regarding the IOA deposits (Buena Vista, Nevada; Iron Springs, Utah; and El Laco, Chile), I report that the inclusion record reveals ubiquitous polycrystalline melt inclusions with compositions ranging from carbonate rich (Buena Vista) through carbonate-sulfate (Iron Springs) to sulfate rich (El Laco). These polycrystalline inclusions represent aliquots of previously unknown, Fe-rich, carbonate-sulfate melts, which appear to be a common, fundamental feature of IOA ore formation. I interpret that these melts were generated by anatexis and assimilation of

chemical sediments (limestones and/or evaporites). In each case, the inclusion record shows that these melts exsolved an aqueous fluid (brine and/or vapor), which explains the widespread hydrothermal alteration associated with each deposit. I argue that these previously unrecognized carbonate-sulfate melts represent a key factor in IOA ore formation and explain the overlapping magmatic and hydrothermal features of these deposits.

Regarding the porphyry deposit (Saginaw Hill, Arizona), I report evidence of cyclic fluid exsolution and degassing of a metal-rich brine from a highly-evolved melt at the magmatic-hydrothermal transition. The main intrusive phase at Saginaw Hill displays well-developed unidirectional solidification textures (USTs) that host abundant assemblages of coeval silicate melt and aqueous brine inclusions, indicative of direct exsolution of highly saline brines from the silicate melt. High-resolution, time-resolved data from petrographically well-constrained assemblages of fluid and melt inclusions reveal that the Saginaw Hill system underwent hundreds of repeated pulses of gradual fluid buildup, punctuated by rapid bursts of fluid release. These latter bursts are recorded by quartz with elevated and highly variable trace element contents indicative of rapid (disequilibrium) growth, which contains assemblages of coexisting brine and vapor inclusions indicative of decompression and boiling. This cyclic process of brine exsolution, accumulation, and pressurization followed by rapid decompression, boiling and venting occurred repeatedly, and each pulse led to the formation of an individual UST band. This process took place only after the melt had fractionated extensively- to a muscovite-saturated, near-eutectic composition in an intermediate to felsic silicate system. The highly-fractionated character of the melt provides the best explanation for exsolution of highly-saline, Cu-rich fluids.

While the circulation of aqueous brines is a factor in both porphyry-Cu and Iron oxide-apatite systems, this thesis demonstrates that other factors are likely prerequisites for the

formation of mineralization in each. In the case of IOA systems carbonate-sulfate melts are required for iron transport and precipitation while aqueous brines are likely more central in the formation of Na-Ca alteration. In porphyry systems aqueous fluids (i.e. brines) are responsible for metal transport but the interplay of aqueous fluid accumulation and release and melt fractionation are main controls on the volume, salinity, and metal enrichment of mineralizing fluids. Thus, this thesis illuminates key processes in the deep levels of both systems which act as direct controls on the mineralization in both.

**Preface**

This thesis is the original work of Wyatt M. Bain.

Chapter 2 of this thesis has been accepted for publication as: Bain, W.M., Steele-MacInnis, M., Li, K., Li, L., Mazdab, F.K., and Marsh, E.E. (2020) A fundamental role of carbonate-sulfate melts in formation of iron oxide-apatite deposits. Nature Geoscience, in press. I was responsible for the collection and interpretation of the data, and preparation of the manuscript. Matthew Steele-MacInnis guided the initial concept of this work, collaborated in the interpretation and analysis of the data, and contributed to preparation of the manuscript. Kan Li and Long Li aided in collection, interpretation, and presentation of the stable-isotope data. Frank Mazdab aided in the interpretation of the data. Erin E Marsh aided in the collection and interpretation of the data.

I was responsible for collection and interpretation of data and preparation of manuscripts for Chapters 3 and 4 of this thesis. These latter two chapters are currently in preparation for submission to academic journals. Co-authors of chapter 3 will include Matthew Steele-MacInnis, Fernando Tornos, John M. Hanchar and Emily C. Creaser. Matthew Steele-MacInnis guided the initial concept of this work, collaborated on interpretation and analysis of the data, and contributed to preparation of the manuscript. Fernando Tornos and John Hanchar were responsible for field work and sample collection and assisted with interpretation of the data. Emily Creaser aided in collection of the data and preparation of the manuscript. Co-authors of chapter 4 will include Pilar Lecumberri-Sanchez, Erin E. Marsh, and Matthew Steele-MacInnis. Pilar Lecumberri-Sanchez contributed to data processing and interpretation and preparing manuscript. Erin Marsh aided in data collection. Matthew Steele-MacInnis guided the initial concept of this work, collaborated on interpretation and analysis of the data, and preparation of the manuscript.

Chapters 1 and 5 are my own work, written for this thesis.

To

Peggy and Don

MaryJane and Dale

and

Lisa and Mike


Your truth is marching on…

**Acknowledgments**

 This thesis was made possible by the guidance and support of many individuals over the course of my graduate work, and indeed my life. I acknowledge some of those people here. While the following paragraphs are not exhaustive, I am grateful and deeply humbled by the contributions of all of my colleagues, family, and friends. I wouldn't be writing this now without them.

 Firstly, I would like to thank my advisor, Matthew Steele-MacInnis. I am very lucky to have been recruited as his first PhD student and to have his depth of knowledge to guide my doctoral work. With his support and infinite patience, I have had the opportunity to make genuine discoveries, be a part of impactful research, and study fascinating rocks in faraway places. I do not think any true geologist could ask for more. To work with him was truly an honor and a privilege and I am forever grateful for all of the things he helped cultivate in my life.

 Much of this work could not have been done without the help of numerous colleagues and associates throughout the many facilities I worked at during my graduate studies. Thanks to Erin Walton, Mike Xai, and Emmanuel Soignard for their help with Raman analysis at MacEwan University, the National Institute of Nano Technology, and Arizona State University, respectively. Thank you to Nathan Gerein for his assistance with the EVO SEM at University of Alberta (by far my favorite analytical instrument). Thank you to Andy Dufrane and Erin Marsh for all their help with collecting LA-ICPMS data at the Canadian Center for Isotopic Microanalysis and the USGS. Thank you to Andrew Locock for his expert assistance with collecting and preparing EPMA data. A big thank you to Igro Jakab for his help in the DIF lab, and to Mark Labbe for his help with sample preparation. A special thank you to Jean Cline and Simon Jowitt at UNLV for their help in collecting microthermometric data, especially prior to our establishment of the fluid inclusion lab at the University of Alberta. Also, thank you to Drew Barkoff for his recommendation of the Iron Springs district in Utah for my study of IOA systems and for his help in conducting field work. Similarly, I would like to thank Miao Wang for his help with data interpretation and analysis. Finally, an enormous thank you to Frank Mazdab for his help with the EPMA at University of Arizona and all of the other support and guidance he has given along the way.

# Table of Contents

**List of Figures**

**List of Tables**

# Chapter 1: Introduction

**1.1** Overview

The very existence of concentrated, metal-rich mineral deposits in the upper crust begs the fundamental question of what processes drive the formation of features which contrast so dramatically with the bulk Earth (McDonough and Sun, 1995) and bulk continental crust (Rudnick and Gao, 2003). In order to better understand these processes, research must focus on the nature of mineralizing *fluids*, as it is in a fluid medium that metals can be selectively partitioned from the bulk rock, mobilized and transported to a suitable geologic sink, and concentrated by precipitation of distinct mineral phases to ultimately form a deposit (Heinrich and Candela, 2014). In many cases, mineralizing fluids are aqueous solutions with significant concentrations of ligands, which greatly increase the solubility of particular elements (Yardley, 2005). This is the case, for example, in porphyry systems in which base and precious metals are transported in hydrothermal aqueous solutions enriched in ligands such as $Cl^-$ and $HS^-$ (Sillitoe, 2010). Similarly, orthomagmatic fluids (i.e. melts) can be highly enriched in incompatible lithophile elements (e.g. REEs, W, Nb, Zr, P) as a result of selective melting, igneous fractionation, and the propensity for certain elements to partition preferentially into silicate, sulfide, or carbonate liquids (Heinrich and Candela, 2014; Mungall, 2014). Selective enrichment of particular elements in specific fluid types and geologic settings is therefore a major factor governing mass transport and the formation of mineral deposits in the upper crust .

The following chapters examine the source and evolution of mineralizing fluids that contributed to the formation of iron-oxide apatite (IOA) deposits in the Southwestern United States (Buena Vista, Nevada, and Iron-Springs, Utah; Chapter 2) and Chile (El Laco; Chapter 3), and in a small, shallowly emplaced Cu-Ag-Au mineralized porphyry-type magmatic-hydrothermal system in southern Arizona, USA (Saginaw Hill; Chapter 4). Each of these systems contains exceptionally well-preserved features that offer insights into the physical and chemical conditions of ore-forming fluids at their initial source. In the case of IOA systems, I attempt to address the outstanding question about the fundamental genetic mechanisms for these systems and offer a novel model for their formation. Likewise, I also address the nature of fluids generated at the magmatic-hydrothermal transition in a Cu-Ag-Au mineralized system during the

buildup and release of fluids exsolved from the causative silicate melt. The following sections of this introductory chapter describe some of the general background and motivation for these works, and outline the specific aims of the subsequent three chapters (2, 3 and 4). Chapter 5 concludes with a synthesis of the major implications derived from these studies.

**1.2 Mineralizing fluid in iron-oxide apatite (IOA) systems**

Kiruna-type iron-oxide apatite deposits are characterized by massive magnetite-apatite-actinolite ore bodies enveloped by voluminous Na-Ca and Na-K alteration. These deposits exhibit textures and geochemical characteristics that variably suggest both orthomagmatic and hydrothermal genetic mechanisms (Nyström and Henríquez, 1994; Barton and Johnson, 1996; Li et al., 2015; Hofstra et al., 2016; Tornos et al., 2017; Simon et al., 2018). The source and nature of mineralizing fluids in these systems is uncertain and has been the subject of a wide-ranging and intense contemporary debate. This has led to the development of a wide array of disparate and contradictory genetic models, which include orthomagmatic, magmatic-hydrothermal, and amagmatic hydrothermal endmembers (Westhues et al., 2017; Velasco et al., 2016; Ovalle et al., 2018; Jonsson et al., 2013; Barton and Johnson, 1996). These models differ markedly in terms of the fluids involved in ore formation, with orthomagmatic models favoring the emplacement of Fe-P-rich magmas, whereas hydrothermal models invoke the circulation of aqueous fluids of magmatic, metamorphic, or basinal origin (Barton , 2014). Several factors underpin this current debate. First, while experiments have successfully produced Fe-P-rich magmas in a laboratory setting (Hou et al., 2018; Veksler et al., 2009; Philpotts, 1982), the temperatures required to form and stabilize Fe-P-rich magmas are in excess of what is inferred for IOA formation (>1400°C) and the compositions reported for these melts are commonly distinctive from the compositions of IOA ore determined by bulk rock analysis. Thus, it is still unclear whether such magmas can occur in Earth's upper continental crust (Lindsley and Epler, 2017). This is puzzling, as many IOA system exhibit features that appear unmistakably orthomagmatic in origin (Chen et al., 2010; Lyons , 1988). This is particularly true in places like El Laco, Chile, where magnetite ore bodies occur as vesiculated flow structures connected to feeder dikes which emanate from a central volcanic edifice (Velasco et al., 2016, Tornos et al., 2017). Second, other systems contain contrasting textures indicative of a hydrothermal origin, such as stratigraphically controlled replacement zones surrounded by voluminous Na-Ca alteration, as well as skarn-like features in

which magnetite has apparently replaced well-preserved sedimentary features (Li et al., 2015). However, the solubility of $Fe^{3+}$ in aqueous solution is quite low compared to $Fe^{2+}$, meaning that iron would have to be transported as $Fe^{2+}$ and precipitated via a redox trap. In the case of IOA ore hosted in sedimentary strata, this could be accomplished by chemical interaction with evaporites at the site of IOA ore formation (Li et al., 2015), but this would not explain how magnetite is transported and precipitated in dominantly igneous host rocks. Lastly, it is unclear where the iron itself comes from initially, as many systems display geochemical signatures consistent with magmatic, magmatic-hydrothermal, and basinal reservoirs (Knipping et al., 2019; Gleeson and Smith, 2009; Dare et al., 2015). In recent years, various flavors of hybrid orthomagmatic-hydrothermal models have attempted to reconcile these observations (Simon et al., 2018), but still no consensus has been found.

In **chapters 2 and 3**, I report on results derived from field observations and laboratory examination and analysis of inclusions hosted in primary minerals from three IOA localities. **Chapter 2** describes the results of my studies of the Buena Vista and Iron Springs IOA systems in the southwestern United States (Nevada and Utah, respectively). The mineralization in both systems is essentially identical in terms of mineral assemblage and textures, and consists of magnetite-apatite dikes flanked by massive replacement zones, abundant magnetite breccias, and an association with intermediate to mafic intrusions which cross-cut evaporite-bearing sedimentary sequences. In addition, the Buena Vista system contains large carbonate bodies which resemble dikes (referred to herein as carbonate dikes) that cross-cut the magnetite orebodies. Apatite, actinolite, and magnetite from IOA ore in both systems, as well as the carbonate dikes in Buena Vista, host abundant aqueous and polycrystalline inclusions, which are the main focus of this chapter. **Chapter 3** focuses on the classic IOA system at El Laco in northern Chile, and in particular reports on the results of examination and analyses of inclusions associated with pegmatitic diopside-magnetite-anhydrite "veins" (dikes) which cap a massive ore body present at depth beneath the volcanic system. These dikes are similar to the carbonate dikes in the Buena Vista systems in terms of their occurrence as a paragenetically late, course-grained, magnetite-bearing feature associated with IOA mineralization. These features are analogous to the carbonate dikes which crosscut the magnetite ore bodies at Buena Vista, and contain abundant polycrystalline inclusions hosted in diopside, albite, apatite, and magnetite.

**The primary research questions** I address in **chapters 2 and 3** are:

1.  What are the nature and source of the mineralizing fluids in these systems?
2.  What is the likely mechanism for Fe-transport and precipitation?
3.  Are the processes which transport and precipitate Fe in these systems unique, or are they applicable elsewhere?

Each of the studied systems contains well preserved, unambiguous assemblages of primary and secondary inclusions. In the case of Buena Vista and Iron Springs, inclusions are dominantly coeval polycrystalline and brine inclusions, while only polycrystalline inclusions were observed throughout most of the paragenesis at El Laco. In order to address the aforementioned research questions, I employed a combination of detailed petrography and compositional analysis of inclusions hosted in all three systems, as well as C-O isotopic analyses of carbonate from the Buena Vista ore bodies and surroundings. I evaluate and interpret the results in conjunction with the geologic framework of these systems based on field relationships. Through this work, I demonstrate that the mineralizing fluids in all three IOA ore bodies include iron-rich carbonate-sulfate melts, which range in composition from carbonate-dominated at Buena Vista, through approximately equal carbonate+sulfate at Iron Springs, to sulfate-dominated at El Laco. In all three cases, the origin of these rather exotic salt melts is best explained by anatexis and assimilation of chemical sediments (limestones ± sulfate evaporites). Hence, I propose a novel genetic model for these systems that reconciles the overlapping magmatic and hydrothermal features. Furthermore, I show that this model likely applies to other IOA systems more broadly.

## 1.3 Porphyry systems, the magmatic-hydrothermal transition, and unidirectional solidification textures (USTs).

The general genetic model for the formation of porphyry systems involves emplacement of a hydrous, calc-alkaline magma into a magmatic arc setting and the gradual degassing of the melt to produce a magmatic-hydrothermal ore-forming fluid (Cloos, 2001; Sillitoe, 2010). The formation of porphyry systems in general occurs between about 1.5 and 4 km depth, but less commonly occurs as deep as >9 km, such as at Butte, Montana, USA (Rusk et al., 2008), or as shallow as <1 km, such as at the Refugio district, Chile (Muntean and Einaudi, 2000). Circulation of the mineralizing fluids outward from the silicate melt is accommodated by both diffuse (grain boundary) and focused flow through large fracture networks formed via fluid over-

pressure and hydraulic fracturing (Burnham, 1997; Phillips, 1986). Thus, much of the mineralization in these systems is hosted in quartz veins enveloped by zones of hydrothermal alteration formed by fluid-rock reaction.

The nature and evolution of mineralizing fluids exsolved at the magmatic-hydrothermal transition in these systems is a key factor that controls the size and character of the associated mineralization. These fluids are involved in the extraction of metals from their igneous source and thus play a central role in forming sulfide mineralization at shallower depths. Some studies indicate that early exsolved phases are dominantly intermediate density, moderately saline fluids that undergo decompression and immiscibility to form low-density vapor and highly saline brine that are associated with many porphyry ore bodies (Muntean and Einaudi, 2001; Rusk et al., 2008; Stefanova et al., 2014). Others indicate that magmas may exsolve highly saline fluid directly (Mernagh and Mavrogenes, 2018, Kodêra et al. 2014). Many of these previous studies have focused on hydrothermal features such as veins and miarolitic cavities that likely trap fluids which have undergone physical and chemical modification after exsolution but prior to entrapment. While useful information about the nature of fluids deeper in the system can be derived from such inclusions hosted in veins and miarolitic cavities, they do not necessarily represent the properties of exsolved fluids at their source.

In **chapter 4**, I examine the evolution of mineralizing fluids at the magmatic-hydrothermal transition in a small (~0.3 km$^2$), composite quartz latite / quartz monzonite stock associated with a localized hydrothermal system that produced small quantities of Cu-Au-Ag mineralization (Frank, 1970). I characterize populations of well preserved, quartz-hosted fluid and melt inclusions trapped in unidirectional solidification textures (USTs). Unidirectional solidification textures in this system are characterized by parallel, alternating bands of euhedral, monomineralic quartz and fine-grained aplite. At Saginaw Hill, USTs occur in several meter-thick packages which extend laterally parallel to the margins of a massive quartz vein that cuts through the center of the system and hosts the bulk of the sulfide mineralization. Outward from the UST bands are abundant comb-textured quartz veins that decrease in abundance with greater distance from the central massive quartz vein (Frank, 1970). The distribution of these features is consistent with a system that underwent a progressive, inward sequence of crystallization that coincided with the gradual degassing of increasing amounts of Cu-rich fluid. Such a scenario is consistent with numerical models that predict a gradual increase in fluid volume, salinity, and Cu

content over time in crystallizing calc-alkaline magmas (Cline and Bodnar, 1991), as well as other models that predict an episodic, cyclic pattern of fluid buildup and release (Mercer and Reed, 2013, Lowenstern and Sinclair, 1994, Weis et al., 2012).

The primary research questions I investigate in **chapter 4** are:

1. What were the controls on degassing of metal-rich fluid in the Saginaw Hill system?
2. How did the composition of silicate melt at Saginaw Hill evolve during fluid exsolution and release?
3. What was the physical and chemical nature of hydrothermal, ore-forming fluids during fluid exsolution and prior to circulation outward to form veins?

In order to address these questions, I examined and analyzed the paragenesis and composition of fluid and melt inclusions in the several meter-thick packages of well preserved and exposed UST bands at Saginaw Hill. These features formed as the melt was actively degassing metal-rich fluids. I used the petrographic and compositional analyses of aqueous fluid inclusions and coeval silicate melt inclusions preserved in individual UST bands to characterize the interplay of physical and chemical factors—both in the melt and the exsolving brine—that led to the formation of UST bands and Cu-Ag-Au mineralization in this system. The results show that the exsolved aqueous fluids are invariably highly saline brines that evolved via a dynamic pressure fluctuations, which drove the cyclic formation of UST bands. The exsolution of such a highly saline brine in this system was in part driven by the highly-fractionated composition of the melt at Saginaw Hill during the period of UST formation

**1.4 References**

Barton, M.D., 2014, Iron Oxide(-Cu-Au-REE-P-Ag-Co) Systems, *In* Treatise on Geochemistry
2nd Edition, p. 515-541.

Barton, M.D., and Johnson, D.A., 1996, Evaporitic source model for igneous-related Fe oxide–
(REE–Cu–Au–U) mineralization, Geology, v. 24, p. 259–262.

Bodnar, R.J., Lecumberri-Sanchez, P., Moncada, D., and Steele-MacInnis, M., 2014, Fluid
inclusions in Hydrothermal Ore Deposits: Treatise on Geochemistry, Second Edition v.
13, p. 119-142.

Burnham, C.W., 1997, Magmas and hydrothermal fluids, in Barnes, H.L., ed., Geochemistry of
hydrothermal ore deposits (third edition): New York, John Wiley and Sons, p. 63–123.

Chen, H., Clark, A. H., and Kyser, T. K., 2010, The Marcona magnetite deposit, Ica, south-
central Peru: A product of hydrous, iron oxide-rich melts?: Economic Geology, v. 105, p.
1441-1456.

Cloos, M., 2001, Bubbling magma chambers, cupolas, and porphyry copper deposits:
International Geology Review, v. 43, p. 285–311.

Dare, S.A.S, Barnes, S., and Beaudoin, G., 2015, Did the massive magnetite "lava flows" of El
Laco (Chile) form by magmatic or hydrothermal processes? New constraints from
magnetite composition by LA-ICP-MS: Mineralium Deposita, v. 50, p. 607-617.

Frank, T.R., 1970, Geology and mineralization in the Saginaw Hill area, Pima County, Arizona:
PhD Dissertation, The University of Arizona, Tucson AZ USA, 151 pp.

Gleeson, S.A., and Smith, M.P., 2009, The sources and evolution of mineralizing fluids in iron
oxide–copper–gold systems, Norrbotten, Sweden: Constraints from Br/Cl ratios and
stable Cl isotopes of fluid inclusion leachates: Geochimica et Cosmochimica Acta, v. 73,
p. 5658-5672.

Heinrich, C.A., and Candela, P.A., 2014, Fluids and Ore Formation in the Earth's Crust: Treatise
on Geochemistry, Second Edition v. 13, p. 1-23.

Hofstra, A.H., *et al.* 2016, Mineral thermometry and fluid inclusion studies of the Pea Ridge iron
oxide-apatite-rare Earth element deposit, Mesoproterozoic St. Francois Mountains
terrane, Southeast Missouri, USA: Economic Geology, v. 111, p. 1985-2016

Hou, T. *et al.,* 2018 Immiscible hydrous Fe-Ca-P melt and the origin of iron oxide-apatite ore
deposits: Nature Communications, v. 9, p. 1-7.

Jonsson, E. et al., 2013 Magmatic origin of giant 'Kiruna-type' apatite-iron-oxide ores in central Sweden: Scientific Reports, v. 3, p. 1-8.

Knipping, J.L., Fiege, A., Simon, A.C., Oeser, M., Reich, M., and Bilenker. L.D., 2019, In-situ iron isotope analyses reveal igneous and magmatic-hydrothermal growth of magnetite at the Los Colorados Kiruna-type iron oxide-apatite deposit, Chile: American Mineralogist, v. 104, p. 471-484.

Koděra, P., Heinrich, C.A., Wälle, M., and Lexa, J., 2014, Magmatic salt melt and vapor: Extreme fluids forming porphyry gold deposits in shallow sub volcanic settings: Geology, v.42, p. 495-498.

Li, W., Audétat, A., and Zhang, J., 2015, The role of evaporites in the formation of magnetite–apatite deposits along the Middle and Lower Yangtze River, China: Evidence from LA-ICP-MS analysis of fluid inclusions: Ore Geology Reviews, v. 67, p. 264-278.

Lindsley, D., and Epler, N., 2017, Do Fe-Ti-oxide magmas exist? Probably not!: American Mineralogist, v. 102, p. 2157–2169.

Lowenstern, J.B., and Sinclair, W.D., 1996, Exsolved magmatic fluid and its role in the formation of comb-layered quartz at the Cretaceous Logtung W-Mo deposit, Yukon Territory, Canada: Transactions of the Royal Society of Edinburgh, Earth Sciences, v. 87, p. 291–303.

Lyons, J.I., 1988, Volcanogenic Iron Oxide Deposits, Cerro De Mercado and Vicinity, Durango, Mexico: Economic Geology, v.83, p. 1886-1906

McDonough, W.F., and Sun, S., 1994, The Composition of the Earth: Chemical Geology, v. 120, p. 223-253.

Mernagh, T.P., and Mavrogenes, J., 2019, Significance of high temperature fluids and melts in the Grasberg porphyry copper-gold deposit: Chemical Geology, v. 508, p. 210-224.

Mungall, J.E., 2014, Geochemistry of Magmatic Ore Deposits: Treatise on Geochemistry, Second Edition v. 13, p. 195-215.

Muntean, J.L., and Einaudi, M.T., 2001, Porphyry gold deposits of the Refugio district, Maricunga belt, Northern Chile: Economic Geology, v. 95, p. 1445-1472.

Nyström, J. O., and Henríquez, F., 1994, Magmatic features of iron ores of the Kiruna type in Chile and Sweden: ore textures and magnetite geochemistry: Economic Geology. v. 89, p. 820–839.

Ovalle, J.T. et al., 2018, Formation of massive iron deposits linked to explosive volcanic eruptions: Scientific Reports. v. 8. p. 1-11.

Phillips, W.J., 1986, Hydraulic fracturing and effects in the formation of mineral deposits: Transactions of the Institution of Mining and Metallurgy, Section B: Applied Earth Sciences, v. 95, p. p. B17–B24.

Philpotts, A.R., 1982., Compositions of immiscible liquids in volcanic rocks: Contributions to Mineral Petrology, 80, 201–218.

Rusk, B.G., Reed, M.H., and Dilles, J.H., 2008, Fluid inclusion evidence for magmatic-hydrothermal fluid evolution in the porphyry copper-molybdenum deposit at Butte, Montana: Economic Geology, v. 103, p. 307–334.

Sillitoe, R.H., 2010, Porphyry copper systems: Economic Geology, v. 105, p. 3–41.

Simon, A. et al., 2018, Kiruna-type iron oxide-apatite (IOA) and iron oxide copper-gold (IOCG) deposits form be a combination of igneous and magmatic-hydrothermal processes: evidence from the Chilean iron belt: Society of Economic Geologist special publications, v. 21, p. 89-114.

Stefanova, E., Driesner, T., Zajacz, Z., Heinrich, C.A., Petrov, P., and Vasilev, Z., 2014, Melt and Fluid Inclusions in Hydrothermal Veins: The Magmatic to Hydrothermal Evolution of the Elatsite Porphyry Cu-Au Deposit, Bulgaria: Economic Geology, v. 109, p. 1359-1381.

Tornos, F., Velasco, F., and Hanchar, J., 2016, Iron-rich melts, magmatic, magnetite, and superheated magmatic-hydrothermal systems, The El Laco deposit, Chile: Geology, v. 44, p. 427–430.

Tornos, F., Velasco, F., and Hanchar, J. M., 2017, The magmatic to magmatic hydrothermal evolution of the El Laco deposit (Chile) and its implications for the genesis of magnetite-apatite deposits: Economic Geology, v. 112, p. 1595–1628.

Veksler, I.V., 2009, Extreme iron enrichment and liquid immiscibility in mafic intrusions: Experimental evidence revisited: Lithos, v. 111, p. 72-82.

Velasco, F., Tornos, F., and Hanchar, J.M., 2016, Immiscible iron- and silica-rich melts and magnetite geochemistry at the El Laco volcano (northern Chile): Evidence for a magmatic origin for the magnetite deposits: Ore Geology Reviews, v. 79, p. 346-366.

Weis, P., Driesner, T., and Heinrich, C.A., 2012, Porphyry-Copper Ore Shells Form at Stable Pressure-Temperature Fronts Within Dynamic Fluid Plumes: Science, v. 338, p. 1613-1616.

Westhues, A., Hanchar, J.M., LeMessurier, M.J., and Whitehouse, M.J., 2017, Evidence for hydrothermal alteration and source regions the Kiruna iron oxide-apatite ore (northern Sweden) from zircon Hf and O isotopes: Geology. v. 45, p. 571-574.

Yardley, B.W.D, 2005, Metal Concentrations in Crustal Fluids and Their Relationship to Ore Formation: Bulletin of the Society of Economic Geologists, v. 100, p 613-632.

# Chapter 2: A fundamental role of carbonate-sulfate melts in formation of iron oxide-apatite deposits

## 2.1 Introduction

Kiruna-type iron oxide-apatite (IOA) deposits are enigmatic iron resources characterized by massive and disseminated magnetite-apatite ± actinolite ore bodies and Na-Ca- and K-rich alteration assemblages (Barton, 2014). Formation mechanisms of IOA mineralization are extremely contentious, with proposed genetic models spanning a diverse spectrum between amagmatic-hydrothermal replacement and orthomagmatic endmembers (Nyström and Henríquez, 1994; Barton and Johnson, 1996; Jonsson et al., 2013; Dare et al., 2015; Velasco et al., 2016; Tornos et al., 2016; Westhues et al., 2017; Tornos et al., 2017; Simon et al., 2018; Ovalle et al., 2018). In hydrothermal models, iron oxide ore bodies are thought to form via fluid-rock reactions involving aqueous fluids from magmatic degassing, metamorphic devolatilization, or sedimentary sources (Barton and Johnson, 1996 Oliver et al., 2004; Li et al., 2015; Hofstra et al., 2016). However, the factors that promote iron transport and trigger the deposition of $Fe^{3+}$-rich ores are unclear in the latter models. In orthomagmatic models, Fe-oxides are thought to form via direct emplacement, crystallization, and degassing of an iron-rich silicate magma, or in some cases from an immiscible Fe-P melt (Nyström and Henríquez, 1994; Veksler et al., 2007; Veksler, 2009; Chen et al., 2010; Hou et al., 2018). However, the existence and role of Fe-P melts are hotly debated, with some recent studies arguing for a central role of such liquids (Hou et al., 2018) and others arguing that they are unlikely to exist in upper crustal settings (Lindsley and Epler, 2017). Adding to the puzzle, many IOA deposits show geologic features that seem to indicate both hydrothermal (i.e. replacement zones, breccias, cruciform magnetite veins, and voluminous metasomatic alteration) and orthmagmatic processes (i.e. tabular magnetite+apatite dikes, columnar magnetite, and Fe-rich lava flows and tuffs). Hence, several recent studies have argued for a variety of hybrid, orthomagmatic-hydrothermal processes in the generation of IOA ores (Ovalle et al., 2015; Tornos et al., 2016; Tornos et al., 2017; Simon et al., 2018). Still, no consensus exists, and the nature and source(s) of ore-forming fluid(s) remain elusive.

Here, we characterize the properties of IOA ore-forming fluids by analysis of inclusions in apatite, actinolite and magnetite from two IOA deposits in the southwestern USA: Buena Vista (Churchill County, Nevada, Fig. 2.1), and Iron Springs (Iron County, Utah; Fig. 2.2). Buena Vista has been invoked as an example of a purely hydrothermal endmember IOA deposit, formed via the circulation of amagmatic brines (Barton and Johnson, 1996; Johnson, 2000; Johnson and Barton, 2000). This interpretation was based on widespread miarolitic scapolite-rich alteration, mass-balance calculations between ore and host rocks, and petrographic observations of high-salinity (halite-bearing) aqueous inclusions in apatite (Johnson and Barton, 2000). The Iron Springs deposits have been described as being of magmatic-hydrothermal origin (Bullock, 1970; Rowley and Barker, 1978; Whiting et al., 1992), on account of their skarn-like features, including massive replacement-style ore bodies occurring at the intrusive contact between monzonite and adjacent limestone. These two deposits are ideal localities to evaluate IOA ore-forming fluids, because both systems contain abundant and well-preserved geologic features including tabular magnetite-apatite bodies, unidirectional solidification textures, and euhedral magnetite and apatite (Figs. 2.3, 2.4), all of which were analyzed here.

## 2.2 Methods

### 2.2.1 Sample preparation

All samples analyzed in this study were collected as individual hand specimens and prepared into doubly polished sections with a thickness of 100-150 μm.

### 2.2.3 Petrography and microthermometry of fluid and melt inclusions

Fluid inclusion assemblages (FIAs) were characterized by detailed petrography and microthermometry. The optical petrographic methods used to identify and characterize the coeval assemblages of inclusions have been described in detail by Goldstein and Reynolds, (1993). The main additional considerations here relate to the discovery and characterization of polycrystalline inclusions. Polycrystalline inclusions (PIs) were initially identified by their occurrence as part of the same coeval assemblages as coexisting aqueous inclusions. The PIs

were differentiated from the aqueous inclusions by their appearance of being filled with crystalline solids, which were initially identified as mineral grains by the contrast in birefringence between grains (Fig. 2.5). Assemblages were categorized as primary or secondary based on criteria outlined by Goldstein and Reynolds (1993). Because magnetite is opaque to visible and infra-red light, petrography of inclusions in magnetite was done by reflected-light microscopy on polished surfaces, upon which breached inclusions could be observed and characterized. The latter obviously precludes analysis of the liquid phase within aqueous inclusions, but is suitable for analysis of polycrystalline inclusions as well as crystalline phases adhered to the walls of breached aqueous inclusions.

Low temperature microthermometry was conducted using a Linkam THMSG600 (-100-600 °C) stage calibrated using the triple point of $CO_2$ at -56.6 °C, the triple point of $H_2O$ at 0.0 °C, and the critical point of $H_2O$ at +374.1 °C. Estimated precision and accuracy of the temperature measurements is ±0.1 °C at subzero temperatures and ±0.5 °C at temperatures >100 °C. During low-temperature experiments, sample chips were first cooled to about -130 °C and subsequently heated. A rate of 1 °C/minute was used between -80-60 °C, 30-20 °C, and 0-+10 °C as phase transitions were observed between these intervals. Following low-temperature measurements, aqueous inclusions were heated at 5 °C/minute to a maximum temperature of 500 °C to measure salt-melting and homogenization temperatures.

High temperature (>500 °C) microthermometry was conducted using a Linkam TS1400XY stage calibrated using the critical point of $H_2O$, the α/β transition of quartz at 574 °C, and the melting point of NaCl at ~1 bar (801 °C). Estimated precision and accuracy of the temperature measurements at >500 °C is ±1 °C.

Both high- and low-temperature stages were mounted on a customized Olympus BX53M petrographic microscope at the Earth and Atmospheric Sciences department at the University of Alberta.


*2.2.4 Raman spectroscopy*


Raman spectroscopy of inclusions and decrepitate mounds was conducted at MacEwan University (Edmonton, AB) using a Bruker SENTERRA spectrometer and a 532 nm $Ar^+$ laser focused to a 1 μm spot through a 100x objective mounted on a petrographic microscope. All

spectra were acquired on unoriented grains using a laser power of 20 mW and two to three, 5-30 second exposures summed to the final reported spectra. Baseline subtraction and background reduction were applied using the Opus 6.1™ (by Bruker) and Fityk™ (third party) software packages. Spectra were interpreted using the RRUFF database (Lafuente et al., 2016). It should be noted that in many cases luminescence of apatite presented a major challenge during the analysis of most apatite-hosted materials. This was particularly problematic in the case of apatite samples from Buena Vista.

*2.2.5 Scanning Electron Microscope – Energy Dispersive Spectroscopy (SEM-EDS)*

Back scattered electron (BSE) images, and energy dispersive spectroscopy (EDS) mapping and point analysis were used to determine the compositions of decrepitate mounds, polycrystalline inclusions, and solid phases in aqueous inclusions exposed via sample polishing (either intentional exposure subsequent to identification of aqueous inclusions *in situ*, or accidental exposure of inclusions in well-defined assemblages during sample preparation). The scanning electron microscope (SEM) analyses were done at the Earth and Atmospheric Sciences department at the University of Alberta. The system consisted of a Zeiss EVO SEM with a LaB6 electron source and Bruker energy dispersive X-ray spectrometer (EDS) system with a silicon drift detector. The resolution was 123 eV and the window area was 10 mm$^2$. Analyses were carried out in variable pressure mode with an aperture of 100 μm, an acceleration voltage of 20-25 kV, a beam current of 225-275 pA, and a working distance of 7.0-8.5 mm. Element maps and EDS spectra were collected using collection times of 10-30 minutes and 1-2 minutes, respectively. None of the samples were carbon coated.

*2.2.6 Decrepitate Mounds*

To help ascertain the chemical compositions of aqueous inclusions, including the anion load, we used SEM-EDS mapping, point analysis, and Raman spectroscopy of evaporative solute mounds (i.e. decrepitate mounds) precipitated on the host apatite or on a glass substrate (Palmer and Williams-Jones, 1996; Kontak, 2004; Kenderes and Appold, 2017). Decrepitate mounds were prepared by first mapping the distribution of FIAs within sample chips and then heating the chips to 550 °C at a rate of 50 °C/minute. During initial experiments, wherein decrepitate

mounds were analyzed via EDS and Raman spectroscopy on the host apatite, we found that the compositional signal (apatite contains Ca as a major element, as well as Na, S, C and other analytes of interest as minor or trace elements) and luminescence from the host mineral commonly obscured the results to some degree. Therefore, in order to avoid any signal from the host, we conducted experiments to precipitate mounds on a glass substrate (Palmer and Williams-Jones, 1996; Kontak, 2004). To do so, the sample was placed between two clean glass slides prior to heating. The cleaned glass slides were first examined by optical microscopy to verify the cleanliness of the glass and to check for debris and were then analyzed with EDS to verify that the glass substrate showed no signal for S, C, Na, or Cl. Sample chips were then placed between the two glass slides, and the samples were heated to induce decrepitation. This process resulted in evaporation of the salt load of some inclusions onto the glass slides. After heating, the positions of individual decrepitated FIs relative to the upper and lower glass slides were recorded and the glass slides were carefully extracted and examined first by optical microscopy and subsequently by SEM, Raman, etc. This method successfully enabled characterization of the major cations and anions that made up the solute load in the decrepitated aqueous inclusions.

Raman and EDS analyses of decrepitate mounds on glass and apatite host were preformed following the same procedures outlined above. During point analysis with EDS, the Phi-rho-z matrix correction was used to compensate for x-ray interference from trace elements (i.e. C, Na, and Zn) in the glass substrate or host apatite (Kontak, 2004).

### 2.2.7 Carbon and oxygen isotopes

Carbon and oxygen isotopic analyses of calcite were carried out at the Stable Isotope Geochemistry Laboratory at University of Alberta using the traditional acid dissolution method (McCrea, 1950). Calcite samples were loaded into a glass tube with ~2 ml 100% $H_3PO_4$ being loaded into the side arm of the tube. After pumping to high vacuum, $H_3PO_4$ was poured out from the side arm to react with the calcite at 25 °C overnight. The generated $CO_2$ gas was then purified via low-temperature distillation and collected into a sampler, which was then sent to a Thermo Scientific Delta V Plus isotope-ratio mass spectrometer for isotope measurements at dual-inlet mode. Isotopic compositions were reported as $\delta$ notation relative to the VPDB standard for $\delta^{13}C$

and the VSMOW standard for $\delta^{18}O$. Analytical uncertainty ($2\sigma$) based on repeated analyses of reference material GBW 04417 and NBS-18 was <0.2 ‰ for both $\delta^{13}C$ and $\delta^{18}O$.

**2.3 The Buena Vista and Iron Springs deposits**

The Buena Vista deposit is hosted in the Humboldt mafic complex, where arc basalts and gabbros intruded Early to Middle Jurassic evaporite-bearing carbonate rocks of the Lovelock and Muttlebury Formations (Speed, 1976) during Middle Jurassic (170 Ma) back-arc extension (Johnson and Barton, 2000). Sodium-rich alteration (absent potassic alteration) is pervasive in this system (>900 km$^3$) and almost all of the iron mineralization is hosted by heavily scapolitized mafic volcanic and intrusive rocks which are overprinted by albite-dominated alteration (Johnson, 2000; Johnson and Barton, 2000). In the southern portion of Buena Vista, magnetite+apatite ore bodies occur largely as breccia cements (Fig. 2.3d) and massive replacement zones in the mafic host rocks. These magnetite-rich breccias and replacement zones are crosscut by tabular, dike-like features composed of coarsely crystalline calcite+apatite+titanite (i.e. carbonate+apatite+titanite) with subordinate magnetite+hematite, which we refer to as carbonate dikes (Fig. 2.3i). Farther north, replacement zones are focused around tabular, near-vertically oriented, magnetite-dominated bodies referred to as magnetite+apatite dikes (Fig. 2.3a-c, g, h). These dikes are composed of successive bands of comb-textured, subhedral-euhedral magnetite and euhedral apatite±actinolite with distinctive unidirectional solidification textures (Fig. 2.3 e-j).

The Iron Springs deposits occur around the periphery of three NE-SW trending, 22-21 Ma monzonitic plutons that intruded the Middle Jurassic Carmel Formation (Gregory and Moore, 1931), a sulfate and halite-rich sequence of siltstone, shale, limestone, evaporite (Rowley and Barker, 1978; Whiting et al., 1992). Much of the mineralization is hosted in the adjacent evaporite-bearing limestone strata of the Carmel Formation, and occurs as massive bodies of magnetite ± apatite which occur as tabular zones parallel to the sedimentary stratigraphy (Rowley and Barker, 1978; Whiting et al., 1992). Both the replacement zones and the monzonitic plutons are crosscut by magnetite+apatite dikes (Fig. 2.4a-c) identical to those at Buena Vista in terms of minerology and texture. Where crosscutting the monzonite intrusions, the magnetite+apatite dikes show well-developed unidirectional solidification textures defined by apatite which appear to nucleate along the dikes outer margin and grown inward perpendicular to the long axis of the dike (Fig. 2.4d-g),

columnar jointing, and vesiculated centerlines (outlined in red in Fig. 2.4d,e), all suggestive of an orthomagmatic origin.

*2.3.1 Sample locations: Buena Vista*

We collected samples from three localities in the area of the main Buena Vista mine; the southernmost focus of IOA mineralization in the complex (Fig. 2.1). Locality BV1 was dominated by massive magnetite-apatite ore and magnetite-apatite dikes (Fig. 2.3 a-c) hosted in highly scapolitized mafic host rock. Locality BV2 consisted of carbonate-apatite-titanite dikes which crosscut a breccia-hosted magnetite ore body (Fig. 2.3 d, i). These dikes were previously referred to as veins or vugs (Johnson and Barton, 2000) but are better classified as dikes based on the evidence presented in the following sections and are referred to as such in the following sections. Both sampling locations correspond to field-trip stops described by Johnson and Barton (2000). Magnetite-apatite ore samples from magnetite-cemented breccia (HUUS-04; Table 2.1) and magnetite-apatite dikes (HB-1, HB-2, and HUUS-04; Table 2.1; Fig. 2.3 e-h) were collected from outcrops near the main open cut in the Buena Vista mine area (39°58'25.65"N, 118°10'09.01"W; BV1 in Fig. 2.1). Magnetite-apatite dike samples consist of massive euhedral to subhedral magnetite crystals intergrown with subhedral to euhedral apatite (Fig. 2.3 j), all of which indicate growth in a fluid medium and are crosscut by later chlorite, calcite, and quartz. Representative carbonate-apatite dike samples (HB-3, HB-4, HB-5; Table 2.1) were collected from ~200 m east-northeast of the main open cut (39°58'28.04"N, 118°10'01.57"W; BV2 in Fig. 2.1). These latter rocks are composed primarily of blocky calcite and contain large (>15cm along the c-axis), euhedral apatite crystals as well as cm-sized, euhedral titanite grains, plus minor euhedral actinolite and anhedral potassium feldspar.

Locality BV3 is along the contact between limestone and a gabbro-diorite intrusion. All limestone samples reported in this study (distal and proximal) were collected within 1 km of this location (39°51'28.5"N, 118°12'42.5"W). Samples included powders of fresh limestone with primary sedimentary banding, and coarse recrystallized limestone at or near the gabbro-diorite contact.

In addition, several other IOA localities occur throughout the Humboldt Complex north of the main Buena Vista mine (Fig. 2.1). These localities are the site of several small open pits and

include the Ford Pit and the American Ore Mine. Both areas were investigated and photographed during field surveys. However, the sampling and microanalysis of IOA mineralization presented here focuses primarily on features observed in the main Buena Vista pit in the southern portion of the district.

Coordinates of the sampling locations BV1 and BV2, thin-section scans, and sample descriptions are provided in Table 2.1.

*2.3.2 Sample locations: Iron Springs*

Samples were collected from four localities in the Iron Springs district, Utah shown in Fig. 2.2. Sampling locations IS1 and IS2 comprise two open pits on the western end of the district and adjacent tailings piles (37°37'24.7116"N, 113°24'2.3976"W and  37°36'51.6816"N, 113°23'29.054"W, respectively). Samples from these locations consist of vein-hosted magnetite ore and magnetite+apatite dikes (Fig. 2.4 a-c) which crosscut magnetite replacement zones in limestone along the southwestern periphery of the Three Peak monzonite intrusion. All samples from these areas are composed of magnetite (~75-90%), euhedral-subhedral comb-textured apatite ± actinolite (Fig. 2.4 d-g), and minor calcite. Sampling locality IS3 was a prospect pit near the peak of Iron Mountain (37°38'19.3092"N, 113°22'6.5711"W) and comprised a single 3-5 m wide, near vertically oriented NE-SW trending magnetite-apatite dike and subordinate magnetite+apatite veinlets which crosscut Three Peaks Monzonite (Fig. 2.4 b,c). Adjacent to the magnetite+apatite dike, the Three Peak Monzonite is almost completely replaced by massive to euhedral magnetite and minor pyrite. Euhedral calcite, amphibole, and apatite commonly occur in vugs in the magnetite-apatite dike and altered host rock (Fig. 2.4 h). Samples from the magnetite+apatite dike are dominantly magnetite (~75-90%) with comb-textured apatite. Sampling location IS4 is located ~11 km northwest of Cedar City and comprises several tabular NE-SW trending, near vertically oriented magnetite-apatite dikes which crosscut the northern extension of the Three Peak pluton (37°44'15.8244"N, 113°10'54.7284"W; locally referred to as the "Corey fissure veins", Fig. 2.4 a). Sample descriptions are provided in Table 2.2. All samples reported in this study were prepared as doubly polished, 100-150 μm-thick sections.

**2.4 Fluid and melt inclusions**

At both Buena Vista and Iron Springs, apatite, actinolite, and magnetite in the ore bodies host fluid inclusion assemblages containing aqueous inclusions, as well as inclusions composed of polyphase crystalline material, hereafter referred to as polycrystalline inclusions (Figs. 2.6-2.8). Aqueous and polycrystalline inclusions occur throughout the paragenesis of both systems and form well-defined coeval assemblages within the same primary and secondary host phases.

Aqueous inclusions in both localities contain liquid, vapor, and a yellow translucent daughter mineral (halite) along with one to three additional opaque or translucent, birefringent crystals that adhere to and extend inward from the inclusion walls (Figs. 2.6b, 2.10b, 2.11b). Most aqueous inclusions reported in this study have a negative crystal shape and are 5-10 μm in diameter. Some aqueous inclusions showed petrographic evidence of migration or water loss (inclusions halos and trails, Fig. 2.8a, b), and such inclusions were not considered for microthermometry or further analyses. Polycrystalline inclusions in both systems always occur alongside the aqueous inclusions in coeval assemblages and are composed primarily of granular crystalline solids—most of which are translucent and birefringent, with one to two additional black or reddish opaque solids (Figs. 2.6c,f, 2.7, 2.8)—along with a small fraction (0-2 vol%) of aqueous liquid+vapor, which is commonly discernible by the motion of the vapor bubble within the liquid portion. Coeval polycrystalline and aqueous brine inclusions occur in both unambiguously primary and secondary assemblages (Figs. 2.7, 2.8). In addition, samples from Iron Springs contain rare vapor-rich inclusions in these same coeval assemblages. The coexistence of both aqueous and polycrystalline inclusions in coeval assemblages provides unequivocal evidence of simultaneous trapping. Detailed descriptions of inclusion assemblages from both localities are presented in the following sections.

*2.4.1 Inclusion petrography: Buena Vista*

Apatite and actinolite from all the locations sampled in this study host abundant coeval FIAs of polycrystalline and halite-bearing aqueous inclusions with one or more opaque or translucent crystals (Fig. 2.6, 2.7, 2.10). Magnetite in the same samples hosts FIAs containing polycrystalline inclusions as well as (likely aqueous) inclusions that became partially evacuated when breached by polishing. Polycrystalline inclusions are apparent in cross-polarized light due to the contrast between the birefringence of the host mineral and the mineral phases within the

inclusion (Fig. 2.5). These inclusions occur alongside aqueous inclusions in secondary FIAs and in clusters of primary inclusions in the cores of apatite crystals, which are crosscut by secondary FIAs (Fig. 2.7). Polycrystalline inclusions also occur in magnetite as linear arrays of secondary inclusions. Most polycrystalline inclusions range in size from 10-50 μm. Inclusions in apatite and magnetite have a round or negative-crystal shape. Inclusions in actinolite tend to have somewhat more irregular shapes. Solid (and liquid) phases in the polycrystalline inclusions occur in consistent volumetric proportions in apatite and actinolite and commonly include two faintly translucent white to tan-orange birefringent crystals or a yellow-brown translucent mass which occupies ~85-95 % of the inclusions volume, plus 1-2 red or black/opaque granules (1-10 μm). The volumetric proportions of solid phases in inclusions in magnetite were consistent with the inclusions in apatite and actinolite, based on reflected-light microscopy (i.e., in 2D cross section; Fig. 2.7, g, h). In apatite- and actinolite-hosted polycrystalline inclusions, a small amount of aqueous fluid is commonly present and is discernable by the motion of a vapor bubble at room temperature or, rarely, as a thin film around its margins which is accompanied by a halo of single-phase aqueous inclusions around its periphery (Fig. 2.8 a, b), indicating variable degrees of water loss in these latter inclusions (Audétat and Günther,1999). Many secondary, negative-crystal shaped polycrystalline inclusions also exhibit small (<5 μm) cracks which emanate from the corners of the inclusions (Fig. 2.8 c, d), indicating high internal pressures within polycrystalline inclusions and the expansion of these inclusions in response to a relaxation of the confining pressure of the host mineral with exhumation and sample preparation (Tait, 1992; Ferrero, 2012). These petrographic features indicating $H_2O$ loss and overpressure are typical of melt inclusions from various settings, and thus provided some initial evidence that the polycrystalline inclusions were indeed melt inclusions. Nevertheless, inclusions showing petrographic evidence of partial decrepitation or $H_2O$ loss were not used for further geochemical analysis or microthermometry.

### 2.4.2 Inclusion petrography: Iron Springs

Apatite from all locations sampled at Iron Springs (Fig. 2.2; Table 2.2) contains abundant coeval FIAs of polycrystalline and aqueous inclusions. In most samples, secondary assemblages of polycrystalline inclusions dominate, with lesser coeval aqueous brine and rare vapor inclusions. Secondary inclusions occur along healed fractures which crosscut primary apatite, have a negative

crystal shape, and range in size from 10-35 μm (Fig. 2.9). Primary assemblages of coeval polycrystalline and aqueous brine inclusions are common in cores and along the margins of primary apatite. Primary inclusions have an elongate negative-crystal shape, and are typically smaller in size (5-15 μm) than the secondary inclusions (Fig. 2.9 c,d). The aqueous inclusions typically contain liquid, vapor, a single halite crystal and rarely 1-2 additional translucent mineral grains along the outer margin of the inclusion (Fig. 2.11). Within an assemblage, aqueous inclusions have consistent phase ratios of liquid, vapor, and crystalline components and are rarely coeval with vapor-rich inclusions (Fig. 2.9 a,c). In the primary assemblages, halite-bearing aqueous inclusions are rare. Polycrystalline inclusions in apatite commonly contain 3-5 colorless, yellow, and/or red-brown translucent phases which occupy ~75-95% of the inclusion volume, plus 1-2 additional opaque phases. Translucent phases occur as euhedral crystals or aggregations of granular solids which fill most of the volume of the inclusions. Opaque phases occur as euhedral square crystals or as rounded granular masses. Polycrystalline inclusions also rarely contain 1-5% liquid or vapor (by volume) which is apparent as either a translucent film of shadow around the outer margin of the inclusion. Polycrystalline inclusions were also observed in magnetite and occur as linear arrays along healed fractures. Magnetite-hosted inclusions have negative crystal shape and phase ratios consistent with polycrystalline inclusions in translucent phases.

## 2.5 Results

### 2.5.1 Microthermometry of Polycrystalline Inclusions: Buena Vista

Microthermometric measurements are summarized in Table 2.3. During heating, polycrystalline inclusions showed signs of initial melting at ~200-290 °C, at which point the translucent and opaque areas of polycrystalline inclusions began to change in size and distribution. This commonly coincided with the formation of a dark "rind" along the edge of the inclusions, which we interpret as the formation of minute vapor bubbles at the onset of melting. Between 400 and 460 °C, the inclusions contained ~10-25 % liquid by volume, and the opaque areas had decreased in size by 10-25 %. With continued heating from 460-800 °C, the liquid portion of the inclusions grew progressively, while the opaque areas showed only a minor decrease in size. Generally, the polycrystalline inclusions contained >90 % liquid by volume between 850-875 °C (Fig. 2.12). However, complete melting did occur as low as 720 °C in some polycrystalline

inclusions that contained visible $H_2O$ prior to heating, or as high as 950 °C in polycrystalline inclusions that lacked obvious $H_2O$. Volumetrically minor opaque or translucent crystals (<5 vol%) along the inner wall of some inclusions persisted to >875 °C. The polycrystalline inclusions tended to decrepitate between 850 and 1000 °C, although some inclusions showed formation of small cracks and evidence of leakage at temperatures as low as 340-550 °C, indicating high internal pressures. Rapid cooling (~100°C/minute) from the maximum temperature via the manual removal of the sample from the heating element to open air resulted in a homogenous appearance of some inclusions. Some inclusions contained newly formed vapor bubbles after rapid cooling to room temperature (Fig. 2.13 a, b). The homogeneous appearance of these previously heated inclusions at room temperature, and the newly formed vapor bubbles generated during cooling to room temperature, were rapidly lost as the inclusions apparently recrystallized to a granular mass of solid grains over the course of minutes to hours (Fig. 2.13 c).

*2.5.2 Microthermometry of Polycrystalline Inclusions: Iron Springs*

Microthermometric measurements are summarized in Table 2.3. During heating, polycrystalline inclusions commonly showed the onset of melting at <270 °C, and as low as 70 °C in some inclusions. Between 350 and 500 °C, inclusions contained ~5-15% liquid and commonly nucleated (or, in the case of inclusions that had contained a visible vapor phase prior to heating, coalesced) a vapor bubble. Between ~500-700 °C, the opaque phases in most inclusions had commonly changed in shape and decreased in size by ~5-15%. Above 700 °C, the majority of the translucent phases abruptly melted, and the inclusions contained ~60 to >90 % liquid by volume between 785-845 °C. Inclusions containing >15 vol% opaque material commonly did not completely homogenize. In all inclusions, decrepitation was observed at temperatures >880 °C and occasionally as low as 600 °C. Rapid cooling (~100 °C/minute) from maximum temperature via the manual removal of the sample from the heating element to open air resulted in the formation of a granular solid interspersed with minute vapor bubbles, either immediately or within minutes of quenching (Fig. 2.14).

*2.5.3 Raman analyses of quenched polycrystalline inclusions*

We performed Raman analyses of heated/re-melted polycrystalline inclusions after cooling the sample to ambient temperature, following high-temperature experiments, to check for formation of glass or changes in the mineral assemblage. These Raman analyses after cooling to room temperature were identical to and indistinguishable from those collected prior to heating, suggesting that heated inclusions did not quench to glass, and were composed of fine crystalline material after the heating run (Fig. 2.15). This result was unsurprising, because (with very rare exceptions) the majority of carbonate and sulfate liquids are known to be non-glass-forming liquids due to the lack of polymerization in carbonate- and sulfate-dominated liquids (Jones et al., 2013).

*2.5.4 Microthermometry of Aqueous inclusions: Buena Vista*

Low-temperature microthermometric behavior of aqueous brine inclusions from Buena Vista is shown in and Fig. 2.16, and Table 2.4. Aqueous brine inclusions showed multiple phase changes between -80 and +100°C, consistent with complex, multi-component systems (Steele-MacInnis et al., 2016). Aqueous fluid in brine inclusions solidified to a brown, granular mass of solids during cooling to -130 °C. During incremental heating from -130 °C, the onset of melting occurred at -80 to -70 °C, although only a vanishingly small intergranular film of liquid was apparent from this temperature until approximately -30 °C. Immediately following the onset of melting, halite – which was present at room temperature prior to microthermometry – was no longer visible. With further heating, the granular solid changed slightly in texture and distribution until approximately -30 to -22 °C, at which point ~35 vol% of the inclusion appeared to rapidly melt, forming a visible liquid phase, in which the vapor bubble moved freely, and a translucent solid which occupied the remaining ~65 vol% of the inclusion (labeled SH in Fig. 2.13). From -24 to +7 °C, no change was observed in the translucent solid. At +7 to +12 °C, the translucent solid abruptly decomposed and the halite crystal – which was invisible from -80-+12°C – became clearly visible along the wall of the inclusion. These observations are consistent with the decompositions of carbonate- or sulfate-bearing salt hydrates (e.g. $Na_2CO_3$ $10H_2O$, $Na_2CO_3$ $7H_2O$) to liquid+halite at +7 to +12 °C in alkali-carbonate and -sulfate bearing aqueous chloride systems. With heating above 12 °C, the halite crystal grew in size until ~100 °C, indicating retrograde temperature dependence of halite solubility between 12 to 100 °C. At temperatures >100 °C, the halite crystal began to visibly decrease in size. The vapor bubble was

fully dissolved (Th) between 90 to 135 °C (115°C average), and halite melting (Tm) occurred at 280-330 °C (300°C average). Other crystalline phases in aqueous brine inclusions, when present, showed only partial dissolution up to the temperature of decrepitation. All aqueous inclusions decrepitated at >350 °C.

Homogenization by halite dissolution has been interpreted previously as either evidence of high-pressure trapping, or of accidentally trapping halite under halite-saturated conditions (Lecumberri-Sanchez et al., 2012). Our measurements show very consistent halite melting temperatures among inclusions within an FIA, which is strong evidence against accidental trapping of halite. As such, we interpret that these inclusions represent a homogeneous liquid at the time of trapping. Furthermore, the homogenization by halite dissolution does not necessarily imply high pressures of trapping, because (as described in more detail in the next section) our microanalytical data indicate that these inclusions contain high concentrations of carbonate ± sulfate salts. The effect of the carbonate and sulfate salts on the pressure-temperature-volume characteristics of aqueous brines has not yet been evaluated experimentally. We suggest that the high concentrations of these salts in the aqueous inclusions is the likely explanation for several of the anomalous features of the microthermometric observations, including the melting at +7 to +12 °C; the retrograde solubility of halite between +12 to 100 °C, and the homogenization by halite dissolution.

### 2.5.5 Microthermometry of Aqueous inclusions: Iron Springs

Low-temperature microthermometric behavior of aqueous brine inclusions from Iron Springs was remarkably similar to that of aqueous brine inclusions from Buena Vista and is shown in Fig. 2.17, and summarized in Table 2.4. Aqueous inclusions from Iron Springs solidified to a brown or translucent, granular mass of solids during cooling to -130 °C. During incremental heating from -130 °C, the onset of melting occurred at -80 to -70 °C, and was apparent by the formation of an intergranular film of liquid. Between -50 to -30 °C, the salt crystal in many inclusions was either no longer visible or appeared to react with the liquid phase and disappear. At approximately -28 to -19 °C, ~40-50 vol% of the inclusion appeared to rapidly melt, forming a visible liquid phase in which the vapor bubble moved freely, and a faintly translucent solid which occupied the remaining volume of the inclusion. From -19 to +3°C, no change was observed in the translucent solid. At +4 to +12 °C, the translucent solid abruptly

decomposed and the halite crystal became clearly visible along the wall of the inclusion, implying the decomposition of a carbonate- or sulfate-bearing salt hydrate to liquid+halite. With continued heating above 150 °C, many aqueous inclusions decrepitated – indicating high internal pressures. In a small number of inclusions, halite melting was observed between 220-230 °C, followed by complete homogenization via vapor disappearance between 240-270 °C. Given the consistent microthermometric behavior described here, we interpret that these inclusions represent a homogeneous liquid at the time of trapping. As with aqueous inclusions from Buena Vista, we suggest that high concentrations of carbonate and sulfate salts in the aqueous inclusions from Iron Springs is the likely explanation for the ubiquitous observation of melting between +4 and +12 °C.

*2.5.6 Analysis of decrepitate mounds*

Energy dispersive spectroscopy and Raman spectroscopy of decrepitate mounds on the surface of host apatite (Fig. 2.18) and glass substrate (Fig. 2.19) were used to analyze the solute content of aqueous inclusions. Analyzed mounds ranged in diameter from 10-50 µm and occurred as rounded or elongate microcrystalline masses. Element maps and spot analyses of decrepitate mounds on glass substrate showed dramatic contrasts between the mound and the glass substrate and indicated that the major solute constituents in the inclusion were: Na, Cl, Ca, C and S, plus lesser Mg (Fig. 2.19). Some mounds appeared mostly homogeneous (left hand column in Fig. 2.19) in composition, whereas others (right hand column in Fig. 2.19) showed discrete grains of distinct compositions. For example, the mound shown in the right-hand column in Fig. 2.19 contains several smaller grains composed primarily of Na and Cl (evidently, halite grains) plus one larger grain composed primarily of Ca and C (interpreted as a calcium carbonate phase). Areas of the mounds that are enriched in C, Ca and Mg are birefringent in transmitted, cross-polarized light. Raman analysis of C, Ca and Mg rich areas on glass and apatite-hosted mounds showed peaks at 282, 714, and 1088 cm$^{-1}$ which is a perfect match with Mg-calcite (Frezzotti et al., 2012) (Fig. 2.20).

*2.5.7 Analysis of solid phases in breached aqueous inclusions*

Energy dispersive spectroscopy and backscatter imaging was used to analyze the composition and distribution of solid phases in aqueous inclusions exposed during polishing. Fig. 2.21d and 2.22 shows BSE images and x-ray maps of solid phases in exposed, apatite-hosted aqueous inclusions. The solid phases are mostly microcrystalline masses along the walls of the inclusions, and/or 1-2 discrete crystals which are <3 µm in size and extend inward from the walls of the inclusion. Most inclusions show discrete areas rich in C, Fe, and Si, which are interpreted to represent carbonate, Fe-oxide/hydroxide, and quartz within the inclusion. Fluorine, Cl, Na and Mg are also detected in most inclusions. Aluminum and Ti were also detected in some inclusions. Note that Ca and S could not be discerned by EDS analyses of breached inclusions owing to x-ray interference from the apatite host, but were both detected by analyses of decrepitate mounds precipitated on a glass substrate (described above).

*2.5.8 Analysis of solid phases in polycrystalline inclusions*

Analysis of the polycrystalline inclusions by Raman and EDS showed that these inclusions are composed of carbonates, sulfates, silicates, and Fe-Ti oxides (Figs. 2.13, 2.18). The volumetric proportions of these phases are remarkably consistent within any given fluid inclusion assemblage. At Buena Vista, the principal phase assemblage is 60-65 % carbonate (Mg-calcite), 25-30 % quartz, and 5-10 % hematite+anatase by volume in each inclusion. At Iron Springs, principal phases are 55-60% sulfates (gypsum, anhydrite, and barite), 10-20% carbonates (trona, natrite), 10-20 Fe-oxides % (goethite and hematite), and 10-25% silicates (principally wollastonite; Fig. 2e, 2f). Magnetite-hosted inclusions in both systems also consistently contained sulfate, hematite, Ti-oxide, and a Ca+Mg-rich phase (Fig. 2.23), though exact phase ratios were difficult to constrain given the opacity of the magnetite host.

Energy dispersive spectroscopy and Raman analysis were also used to evaluate the phases present in magnetite-hosted polycrystalline inclusions exposed during polishing. X-ray maps of breached secondary polycrystalline inclusions in magnetite from Buena Vista and Iron Springs show discrete areas rich in Ca, Mg, Ti, Al, Si, and Sr (Fig. 2.23) which suggest the presence of anatase, an aluminosilicate mineral, and Mg-rich calcite. In addition, Raman analysis of breached inclusions from both localities consistently indicated the presence of hematite, Fe-bearing phosphates, and sulfates (Fig. 2.24).

*2.5.9 C and O isotopes*

The $\delta^{13}C$ and $\delta^{18}O$ values of limestone from the southern portion of Buena Vista (Fig. 2.1) are plotted alongside data of carbonate from magnetite ore in Fig. 2.25 and shown in Table 2.5. Limestone samples are split into two groups, proximal and distal, based on their spatial association with the gabbro-diorite intrusion. Distal limestone was collected about 1-2 km from the gabbro-diorite contact, showed no signs of recrystallization, and is assumed to have undergone minimal alteration by the gabbro-diorite intrusion. Proximal limestone was sampled along the contact with the gabbro-diorite intrusion and was highly recrystallized with no sign of original sedimentary features. Carbonate from the magnetite ore was collected from throughout the Buena Vista system and features samples from replacement zones, carbonate dikes, and magnetite+apatite dikes.

Carbon ($\delta^{13}C$) and oxygen ($\delta^{18}O$) isotopic compositions of calcite from magnetite ore bodies at Buena Vista ranged between -3.3‰ and -11.5‰ (-5.8‰ median) and 10.3‰ and 17.3‰ (11.6‰ median), respectively (Fig. 2.25). Most of these values are within the $\delta^{13}C$ (-1.7‰ to -8.9‰) and $\delta^{18}O$ (-3.6‰ to 17.9‰) ranges of limestone collected in the southern portion of the Buena vista system near an intrusive contact with gabbro-diorite, but consistently lower than the $\delta^{13}C$ (-2.4‰ to -3.6‰) and $\delta^{18}O$ (15‰ to 21‰) ranges of fresh limestone distal to the intrusion.

In order to interpret the isotopic data of the carbonate from these three sample types, we carried out Rayleigh distillation modeling of $\delta^{13}C$ and $\delta^{18}O$ data. The Rayleigh model can be expressed by the following two equations:

$$\delta^{13}C_f = (\delta^{13}C_0 + 1000) \cdot f^{\alpha_C - 1} - 1000 \tag{1}$$

$$\delta^{18}O_f = (\delta^{18}O_0 + 1000) \cdot f^{\alpha_O - 1} - 1000 \tag{2}$$

Here, $\delta^{13}C_f$ and $\delta^{18}O_f$ denote the final carbon and oxygen isotope compositions of the remaining carbonate after decarbonation; $\delta^{13}C_0$ and $\delta^{18}O_0$ denote the initial carbon and oxygen isotope compositions of the carbonate before decarbonation, which are assumed to be -2‰ and 22‰ respectively, based on the isotopic signature of the distal limestone; $\alpha_C$ and $\alpha_O$ denote the temperature-dependent carbon and oxygen isotope fractionations between $CO_2$ and calcite, which were calculated from Chacko et al. 1991; $f$ denotes the fraction of the remaining carbonate after decarbonation. At low temperature, the isotope fractionation factor is relatively large for oxygen and relatively small for carbon resulting in a dramatic shift in $\delta^{18}O$ values to lower

values and a relatively small change in $\delta^{13}C$ . At high temperatures, the O-isotopic fractionation factor shrinks faster than the corresponding C-isotopic fractionation factor, resulting a dramatic shift in $\delta^{13}C$ toward lower values, and hence a steep trend on a $\delta^{13}C$ vs $\delta^{18}O$ diagram (Fig. 2.25).

The distribution of $\delta^{13}C$ and $\delta^{18}O$ values for proximal carbonate are in good agreement with the trends defined by the Rayleigh distillation model, and indicate that the limestone along the gabbro-diorite contact experienced decarbonation (i.e. carbon isotope fractionation) over a temperature range from 230 ºC to > 1000 ºC.

Carbonate from the magnetite ore shows a large $\delta^{13}C$ range between -3.3‰ and -11.5‰ with a median value of -5.8‰. The large range and very negative $\delta^{13}C$ values in magnetite ore is consistent with high-temperature decarbonation. Furthermore, the heterogeneous $\delta^{13}C$ values of calcite in the ore bodies would be difficult to explain by precipitation from a hydrothermal source, which would be expected to produce a homogeneous isotopic value. Instead, these heterogeneous $\delta^{13}C$ values suggest that the calcite has preserved highly variable decarbonation effects, which has not been re-homogenized during the subsequent processes (e.g., carbonate migration, recrystallization). This suggests that the carbonate migration in the Buena Vista system was not achieved by pervasive flux of hydrothermal fluids, but is consistent with transport and deposition by aliquots of carbonate melt. In contrast, the $\delta^{18}O$ values of the carbonate from the magnetite ore show relatively little variation, with most values between 10.3‰ and 13.9‰ (Fig. 2.25). This likely reflects interaction with a mantle derived fluid (i.e. gabbro-diorite melt), which would shift the data away from the high-temperature decarbonation trend towards slightly lower $\delta^{18}O$ values (Fig. 2.25).

## 2.6 Evidence for anatectic carbonate-sulfate melts

Based on petrographic characteristics, consistent phase assemblages and volumetric ratios, and consistent melting behavior during microthermometry, the polycrystalline inclusions at Buena Vista and Iron Springs were originally trapped as homogeneous *carbonate-sulfate-rich melts*. Such melts can exist at temperatures as low at 600°C (Durand et al., 2015; Floess et al., 2015) and are distinctive from aqueous fluids in terms of their carbonate-sulfate dominated compositions. While the melts in each system differ in terms of their sulfate content, the melts are strikingly similar in having compositions rich in carbonate and Fe-oxide and occurring in coeval assemblages with carbonate- and sulfate-bearing brines. These observations indicate that carbonate-sulfate melt and

aqueous brine coexisted immiscibly during ore formation in both systems. Furthermore, the ubiquitous presence and high abundance of Fe-oxides in polycrystalline inclusions (~5-10 wt% $Fe_2O_3$) indicates that the carbonate-sulfate melts were key media for iron transport and precipitation in both systems.

The core implication of these findings is that IOA deposition was *not* a purely hydrothermal process, and was rather driven by immiscible aqueous fluids and carbonate-sulfate melts. As such, the present results fundamentally undermine previously proposed amagmatic-hydrothermal genetic models for IOA systems (Barton and Johnson, 1996). The Buena Vista system has been cited as a type example of a hydrothermal IOA formed by amagmatic (basinal) fluids (Barton and Johnson, 1996), but such a model is incompatible with the ubiquitous occurrence of carbonate melt inclusions throughout its paragenesis. Rather, Buena Vista—as well as Iron Springs—is evidently a hybrid orthomagmatic-hydrothermal system, in which circulation of an Fe-rich, carbonate-sulfate melt played a central role.

We interpret that the carbonate-sulfate melts at both Buena Vista and Iron Springs were produced by anatexis of sulfate- and halite-bearing carbonate rocks in response to magma injection. The regional geology of both localities shows no indication of mantle-derived carbonatitic magmas, and the large $\delta^{13}C$ variations of carbonate from magnetite ore (-3.3‰ to -11.5‰) cannot be explained by either degassing or re-equilibration from the narrow $\delta^{13}C$ range of carbonatites (-7.7‰ to -3.1‰) (Jones et al., 2013; Eiler, 2001) (Fig. 2.25). Instead, intrusion of hot (>1000 ºC), gabbro-diorite or monzonite magma into carbonate- and sulfate-rich sedimentary strata induced assimilation and anatexis, generating flux-rich melts in both systems (Fig. 2.26). Early in the paragenesis, the carbonate-sulfate melts likely leached Fe from the silicate magma and volcanic country rocks (Johnson and Barton, 2000) and crystallized mostly magnetite and apatite in the early comb-textured dikes. Precipitation of iron oxides drove the ephemeral liquid residue to more carbonate- and sulfate-rich compositions. Later in the paragenesis, the ongoing generation of anatectic melt and accumulation of spent ore fluid gave rise to late-stage carbonate dikes. Meanwhile, aqueous brines formed via unmixing of the carbonate-sulfate liquid that circulated outward and produced pervasive Na-Ca metasomatic alteration (Fig. 2.26).

Experimental studies in the $CaO-H_2O-CO_2$ and $CaO-MgO-H_2O-CO_2$ systems show that calcite and dolomite commence melting at water-saturated conditions at temperatures as low as 600-650 °C (Wyllie and Tuttle, 1960; Lentz, 1999; Durand et al., 2015; Floess et al., 2015), and

even lower with the addition of fluxes (Lentz, 1999; Durand et al., 2015) such as chlorides and sulfates. These temperatures are well below the wet solidus of gabbro and monzonite, implying that normal temperatures of mafic to intermediate melts are sufficient to initiate melting of wet carbonate and sulfate- and halite-rich evaporite rocks. Evidence for crustal anatexis of evaporite-bearing carbonates has been documented in a variety of settings in which mafic to intermediate melts intrude carbonate strata (Floess et al., 2015; Wenzel et al., 2002; Fulignati et al., 2001; Rocco et al., 2012; Ganino et al., 2013; Gozzi et al., 2014). In all cases, low silica content (<60%) of the intruding magma (Carter and Dasgupta, 2016), and the presence of excess volatiles and chloride salts (Fulignati et al., 2001) contributed to depressing the carbonate eutectic, buffering the fugacity of $CO_2$, and promoting melting (Wyllie and Tuttle, 1960; Lentz, 1999). All of the latter are features consistent with Buena Vista, Iron Springs and other IOA localities worldwide (Table 2.6).

Carbon and oxygen isotopic compositions of carbonate from Buena Vista corroborate local interaction between limestone and magma during the formation of magnetite ore in this system. Compared with the narrow $\delta^{13}C$ and $\delta^{18}O$ ranges of fresh limestone distal to the ore body, the carbonates along the gabbro-diorite contact show significant decreases in $\delta^{13}C$ and $\delta^{18}O$ (Fig. 2.25). Assuming the $\delta^{13}C$ and $\delta^{18}O$ values of distal, fresh limestone in the Buena Vista system represents their initial isotopic signature, Rayleigh distillation modeling shows that carbonates along the intrusive contact record decarbonation at temperatures from >1000 ºC to 230 ºC (Fig. 2.25). Carbonates in the magnetite ore bodies have $\delta^{13}C$ values mostly similar to those of the proximal carbonate but extend to even more negative values. This suggests that the carbonate in the ore bodies originated from the proximal carbonates, with some undergoing a higher degree of high-temperature decarbonation. The $\delta^{18}O$ values of carbonate in magnetite ore bodies (10.3‰ to 17.3‰) show much less variability than the proximal carbonate (Fig. 2.25). This can be explained by isotopic re-equilibration with voluminous gabbro-diorite melt, which buffered the isotopic signature of the carbonate melt. Furthermore, the heterogeneity of $\delta^{13}C$ of calcite in the magnetite ore bodies is strong evidence for transport in a melt rather than a hydrothermal fluid. This is because melts can be sequestered within dikes and fluid conduits, giving rise to poor mixing at the deposit scale and locally distinct compositional domains, whereas hydrothermal fluids show more pervasive flux and thus produce a more homogeneous carbon-isotopic signature.

The occurrence of carbonate-sulfate melts and immiscible brine during IOA formation reconciles major outstanding questions underpinning genetic models for IOA systems, including:

1) What process(es) account for observations of both apparently orthomagmatic and hydrothermal features? And 2) How is iron mobilized and oxidized? Firstly, immiscibility between melt and brine explains the superposition of magmatic dikes (crystallized from the melt) and associated hydrothermal alteration (formed as the brine flowed outward). Secondly, carbonate melts are highly reactive, low-viscosity metasomatic agents which can infiltrate country rock, interact with silicate melt, and mobilize transition metals (Giuliani et al., 2012; Jones et al., 2013). Experiments and analyses of natural carbonatites show that ferric iron (as well as Ti and rare-earth elements) is highly soluble in carbonate melts (Hsu et al., 1987; Jones et al., 2013). Indeed, the melt inclusions analyzed here show high iron concentrations up to 10 wt% iron oxide, well in excess of what has been reported of hydrothermal fluids in a variety of settings (Yardley, 2005). Moreover, to form an IOA deposit, the iron must be highly oxidized, and this too is explained by the presence of oxidized carbon and sulfur species in the carbonate-sulfate melt. All of these factors render carbonate-sulfate melts an ideal medium for mobilizing, concentrating *and* oxidizing iron—and thus, ideal ore-forming fluids for IOA mineralization.

**2.7 Carbonate-sulfate melt: a key factor for IOA genesis**

Given the striking similarities between Buena Vista, Iron Springs and other well-known IOA deposits, it stands to reason that the IOA mineralization in these systems formed via similar processes. Table 2.6 lists ten districts that host iron oxide-apatite mineralization, in which geologic and geochemical observations are consistent with the anatexis of evaporate-bearing carbonate rock rich in sulfate and halite. All of these areas are strikingly similar to the Buena Vista and Iron Springs systems in terms of 1) morphology of the iron oxide-apatite ore bodies, which include breccia zones and tabular, vertically oriented magnetite-apatite dikes; 2) presence of widespread Na-[Ca] alteration; 3) occurrence of late-stage carbonate dikes which crosscut the Fe-oxide ore; and 4) crosscutting relationships between evaporite-bearing carbonate strata rich in halite and sulfate, and mafic to intermediate plutonic rocks. The references provided in Table 2.6 describe the geologic setting of each system, and also include other observational data that are consistent with the genetic model described in the present study, such as: isotopic data indicating magmatic temperatures of formation, but mixed magmatic and sedimentary geochemical signatures (Harmon et al., 1984; Baker et al., 2008; Li et al., 2015; Velasco et al., 2016; Tornos et al., 2017); trace element data from Fe-oxide mineralization and associated alteration that indicate mixed magmatic

and sedimentary sources; and unambiguous field observations of carbonate and evaporate assimilation by igneous rocks (e.g. sedimentary xenoliths: Matthew et al., 1996; Moore and Modabberi, 2003; Li et al., 2015) which are clearly associated with IOA mineralization (Table 2.6). Two well-known IOA localities where these features have been extensively documented are El Laco, Chile and the Luzong and Ningwu basins, China (Li et al., 2015; Velasco et al., 2016; Tornos et al., 2017). In both systems, primary fluid inclusions have been reported to be completely filled with granular solids, including anhydrite (Broman et al., 1999; Li et al., 2015) —thus, resembling the polycrystalline (melt) inclusions described in detail here. At El Laco, anhydrite+magnetite+diopside "veins" (which we would characterize as dikes) are also reported, and Sr and Nd isotopic data indicate that the magnetite ores have a mixed mantle and crustal signature (Tornos et al., 2017) suggesting a significant crustal component in this system. This, together with the fact that El Laco is underlain by phosphatic, evaporite-bearing, carbonate sediments (Tornos et al., 2016; Velasco et al., 2016; Tornos et al., 2017; Mungall et al., 2018), indicates ideal conditions for formation of anatectic carbonate-sulfate melt. Thus, an array of observations consistently suggests that carbonate-sulfate melts generated by crustal anatexis play a central, critical role in mobilizing, oxidizing, and precipitating iron in IOA systems. In addition, our genetic model reconciles the geochemistry of IOA genesis with the occurrence of magnetite-apatite ores in carbonatite pipes and phoscorites (Giebal et al., 2019) as well as in "antiskarn," Nolans-type rare-earth element deposits (Anenburg et al., 2018) and in anatectic silicocarbonatitic mineralization (Lentz et al., 1998). Thus, we suggest that carbonate-sulfate melts are a common feature linking iron oxide mineralization in a variety of geologic settings, and the key to IOA formation.

## 2.8 References

Anenburg, M., Burnham, A.D., and Mavrogenes, J.A., 2018, REE redistribution textures in altered fluorapatite: Symplectites veins, and phosphate-silicate-carbonate assemblages from the Nolans Bore P-REE-Th deposit, Northern Territory, Australia: Canadian Mineralogist, v. 56, p. 331-354.

Audétat, A., and Günther, D., 1999, Mobility and H2O loss from fluid inclusions in natural quartz crystals: Contributions to Mineral Petrology, v. 137, p. 1-14.

Baker, T. et al., 2008, Mixed messages in iron oxide–copper–gold systems of the Cloncurry district, Australia: insights from PIXE analysis of halogens and copper in fluid inclusions: Mineralium Deposita, v. 43, p. 599-608.

Baker, T. et al., 2008, Mixed messages in iron oxide–copper–gold systems of the Cloncurry district, Australia: insights from PIXE analysis of halogens and copper in fluid inclusions: Mineralium Deposita, v. 43, p.599-608.

Barton, M.D., 2014, Iron Oxide(-Cu-Au-REE-P-Ag-Co) Systems: *in* Treatise on Geochemistry 2nd Edition, p. 515-541.

Barton, M.D., and Johnson, D.A., 1996, Evaporitic source model for igneous-related Fe oxide–(REE–Cu–Au–U) mineralization: Geology. v. 24, p. 259–262.

Bertelli, M., and Baker, T., 2010, A fluid inclusion study of the Suicide Ridge Breccia Pipe, Cloncurry district, Australia: Implication for Breccia Genesis and IOCG mineralization: Precambrian Research, v. 179, p. 69-87.

Bonyadi, Z., Davidson, G.J., Mehrabi, B., Meffre, S., and Ghazban, F., 2011, Significance of apatite REE depletion and monazite inclusions in the brecciated Se–Chahun iron oxide–apatite deposit, Bafq district, Iran: Insights from paragenesis and geochemistry: Chemical Geology, v. 281. p. 253-269.

Broman, C., Nystr.m, J.O., Henriquez, F., and Elfman, M., 1999, Fluid inclusions in magnetite-apatite ore from a cooling magmatic system at El Laco, Chile: Journal of the Geologic Society of Sweden, v. 121, p. 253–267.

Broman, C., Nyström, J.O., Henriquez, F., and Elfman, M., 1999, Fluid inclusions in magnetite-apatite ore from a cooling magmatic system at El Laco, Chile: Journal of the Geological Society of Sweden, v. 121, p. 253–267.

Bullock, K.C., 1970, Iron deposits of Utah: Utah Geological and Mineralogical Survey Bulletin. v. 88, p. 101.

Calzia, J.P., Frisken, J.G., Jachens, R.C., McMahon, A.B., and Rumsey, C.M., 1988, Mineral resources of the Kingston Range Wilderness study area, San Bernardino County, California: USGS Bulletin, v. 1709-D.

Carter, L. B., and Dasgupta, R., 2016, Effect of melt composition on crustal carbonate assimilation: Implications for the transition from calcite consumption to skarnification

and associated $CO_2$ degassing: Geochemistry, Geophysics, Geosystems, v. 17, p. 3893–3916.

Chacko, T., Mayeda, T.K., Clayton, R.N., and Goldsmith, J.T., 1991, Oxygen and carbon isotope fractionations between $CO_2$ and calcite: Geochimica et Cosmochimica Acta, v. 55, p. 2867-2882.

Chai, F. et al., 2009, Geochronology of metarhyolites from the Kangbutiebao Formation in the Kelang basin, Altay Mountains, Xinjiang: Implications for the tectonic evolution and metallogeny: Gondwana Research, v. 16, p. 189-200.

Chai, F. et al., 2014, The Abagong apatite-rich magnetite deposit in the Chinese Altay Orogenic Belt: a Kiruna-type iron deposit: Ore Geology Reviews, v. 57, p. 482-497.

Chen, H. et al., 2010, Evolution of the giant Marcona-Mina Justa iron oxide-copper-gold district, south-central Peru: Economic Geology, v. 105, p. 155-185.

Chen, H., Clark, A. H., and Kyser, T. K., 2010, The Marcona magnetite deposit, Ica, south-central Peru: A product of hydrous, iron oxide-rich melts?: Economic Geology. v. 105, p. 1441-1456.

Chen, H., Clark, A.H., and Kyser, T.K., 2010, The Marcona magnetite deposit, Ica, south-central Peru: a product of hydrous, iron oxide-rich melts?: Economic Geology, v. 105, p. 1441-1456.

Chen, H., Kyser, T.K., and Clark, A.H., 2011, Contrasting fluids and reservoirs in the contiguous Marcona and Mina Justa iron oxide–Cu (–Ag–Au) deposits, south-central Perú: Mineralium Deposita, v. 46, p. 677-706.

Dare, S.A.S, Barnes, S., and Beaudoin, G., 2015, Did the massive magnetite "lava flows" of El Laco (Chile) form by magmatic or hydrothermal processes? New constraints from magnetite composition by LA-ICP-MS: Mineralium Deposita, v. 50, p. 607-617.

Durand, C., Baumgartner, L. P., and Marquer, D., 2015, Low melting temperature for calcite at 100 bars on the join CaCO3-H2O – some geological implications: Terra Nova. v. 27, p. 364-369.

Eiler, J.M., 2001, Oxygen isotope variations of basaltic lavas and upper mantle rocks: Reviews in Mineral Geochemistry, .v. 43, p. 319-364.

Ferrero, S., 2012, Microstructures of melt inclusions in anatectic metasedimentary rocks: Journal of Metamorphic Geology, v. 30, p. 303–322.

Floess, D., Baumgartner, L. P., and Vonlanthen, P., 2015, An observational and thermodynamic investigation of carbonate partial melting: Earth and Planetary Science Letters, v. 409, p. 147-156.

Frezzotti, M.L., Tecce, F., and Casagli, A., 2012, Raman spectroscopy for fluid inclusion analysis: Journal of Geochemical Exploration, v. 112, p. 1-20.

Frietsch R., Tuisku P., Martinsson O., and Perdahl J. A., 1997, Early Proterozoic Cu–(Au) and Fe ore deposits associated with regional Na–Cl metasomatism in northern Fennoscandia: Ore Geology Reviews, v. 12, p. 1–34.

Fulignati, P., Kamenetsky, V. S., Marianelli, P., Sbrana, A., and Mernagh, T. P., Melt inclusion record of immiscibility between silicate, hydrosaline, and carbonate melts: Applications to skarn genesis at Mount Vesuvius: Geology, v. 29, p. 1043-1046

Ganino, C., Arndt, N. T., Chauvel, C., Jean, A., and Athurion, C., 2013, Melting of carbonate wall rocks and formation of the heterogeneous aureole of the Panzhihua intrusion, China: Geoscience Frontiers, v. 4, p. 535-546.

Giebel, R.J., Marks, M.A.W., Gauert, C.D.K., and Markl, G. A., 2019, model for the formation of carbonatite-phoscorite assemblages based on the compositional variations of mica and apatite from the Palabora Carbonatite Complex, South Africa: Lithos v. 324-325, p. 89-104.

Giuliani, A. et al., 2012, Nature of alkali-carbonate fluids in the sub-continental lithospheric mantle: Geology, v. 40, p. 967-970.

Gleeson, S.A., and Smith, M.P., 2009, The sources and evolution of mineralising fluids in iron oxide–copper–gold systems, Norrbotten, Sweden: Constraints from Br/Cl ratios and stable Cl isotopes of fluid inclusion leachates: Geochimica et Cosmochimica Acta, v. 73, p. 5658-5672.

Goldstein, R. H., and Reynolds, T. J., 1993, Systematics of Fluid Inclusions in Diagenetic Minerals: SEPM Society for Sedimentary Geology.

Gozzi, F. et al., 2014, Primary magmatic calcite reveals origin from crustal carbonate: Lithos, v. 190, p. 191-203.

Gregory, H. E., and Moore, E. C., 1931, The Kaiparowits region, a geographic and geologic reconnaissance of parts of Utah and Arizona: U.S. Geol. Survey Prof. Paper v. 164, p. 161 p.

Harmon, R., et al., 1984, Regional O-, Sr-, and Pb-isotope relationships in late Cenozoic calc-alkaline lavas of the Andean Cordillera: Journal of the Geologic Society of London, v. 141, p. 803-822.

Hofstra, A.H. et al., 2016, Mineral thermometry and fluid inclusion studies of the Pea Ridge iron oxide-apatite-rare earth element deposit, Mesoproterozoic St. Francois Mountains terrane, Southeast Missouri, USA: Economic Geology. v. 111, p. 1985-2016.

Hou, T. et al., 2018, Immiscible hydrous Fe-Ca-P melt and the origin of iron oxide-apatite ore deposits: Nature Communications. v. 9, p. 1-7.

Hsu, H.S., DeVan, J.H., and Howell, M., 1987, Corrosion of iron in molten carbonates at 650 °C: Journal of the Electrochemical Society, v. 134, p. 3038-3043.

Hunt, J.A., Baker,T., and Thorkelson, D.J., 2007, A Review of iron oxide copper-gold deposits, with focus on the Wernecke breccias, Yukon, Canada, as an example of a non-magmatic end member and implications for IOCG genesis and classification: Exploration and Mining Geology, v. 16, p. 209-232.

Jami, M., Dunlop, A.C., and Cohen, D.R., 2007, Fluid inclusion and stable isotope study of the Esfordi apatite-magnetite deposit, Central Iran: Economic Geology, v. 102. p. 1111-1128.

Johnson, D. A., 2000, Studies of Iron-Oxide (Cu–REE–Au–Co–Ag–Ni–U) Mineralization and associated sodic alteration in the Great Basin: 277. PhD Dissertation, University of Arizona.

Johnson, D. A., and Barton, M. D. 2000, Time-space development of an external brine-dominated, igneous-driven hydrothermal system; Humboldt mafic complex, western Nevada: Society of Economic Geologists Guidebook Society of Economic Geologists Guidebook Series. v. 32, p. 127-144.

Jones, A. P., Genge, M., and Carmody, L., 2013, Carbonate melts and carbonatites: Reviews in Mineral geochemistry, v. 75, p. 289-322.

Jonsson, E. et al., 2013, Magmatic origin of giant 'Kiruna-type' apatite-iron-oxide ores in central Sweden: Scientific reports, v. 3, p. 1-8.

Kenderes, S.M., and Appold, M.S., 2017, Fluorine concentrations of ore fluids in the Illinois-Kentucky district: evidence from SEM-EDS analysis of fluid inclusion decrepitate: Geochimica et Cosmochimica Acta, v. 210, p. 132-151 (2017).

Kendrick, M.A. Honda, M., Gillen, D., Baker, T., and Phillips, D., 2008, New constraints on regional brecciation in the Wernecke Mountains, Canada, from He, Ne, Ar, Kr, Xe, Cl, Br and I in fluid inclusions: Chemical Geology, v. 255, p. 33-46.

Kontak, D., 2004, Analysis of evaporate mounds as a complement to fluid-inclusion thermometric data: case studies from granitic environments in Nova Scotia and Peru: Canadian Mineralogist, v. 42, p. 1315-1329,

Lafuente, B., Downs, R. T., Yang, H., and Stone, N., 2016, the power of databases: The RRUFF project: in Highlights in Mineralogical Crystallography. P. 1-29.

Lecumberri-Sanchez, P., Steele-MacInnis, M., and Bodnar, R.J., 2012, A numerical model to estimate trapping conditions of fluid inclusions that homogenize by halite disappearance: Geochimica et Cosmochimica Acta, v. 92, p. 14-22.

Lee, C.A. et al., 2007, Trace-element composition of Fe-rich residual liquids formed by fractional crystallization: Implications for the Hadean magma ocean: Geochimica et Cosmochimica Acta, v. 71, p. 3601-3615.

Lentz, D.R., 1998, Late-tectonic U-Th-Mo-REE skarn and carbonatitic vein-dyke systems in the southwestern Grenville Province: A pegmatite-related pneumatolytic model linked to marble melting: *in* Mineralized Intrusion-related Skarn Systems (Lentz, D.R., ed.): Mineralogical Association of Canada, Short Course v. 26, p. 519-657.

Lentz, D.R., 1999, Carbonatite genesis: A reexamination of the role of intrusion-related pneumatolytic skarn processes in limestone melting: Geology. v. 27, p. 335-338.

Li, R. et al., 2017, Ore fluid evolution in the giant Marcona Fe-(Cu) deposit, Perú: Evidence from in-situ sulfur isotope and trace element geochemistry of sulfides: Ore Geology Reviews, v. 86, p. 624-638.

Li, W., Audétat, A., and Zhang, J., 2015, The role of evaporites in the formation of magnetite–apatite deposits along the Middle and Lower Yangtze River, China: Evidence from LA-ICP-MS analysis of fluid inclusions: Ore Geology Review, v. 67, p. 264-278.

Lindsley, D., and Epler, N., 2017, Do Fe-Ti-oxide magmas exist? Probably not!: American Mineralogist. v. 102, p. 2157–2169.

Lyons, J.I., 1988, Volcanogenic iron oxide deposits, Cerro de Merecado and vicinity, Durango, Mexico: Economic Geology, v. 83, p. 1886-1906.

Martinsson O., 1997, Tectonic Setting and Metallogeny of the Kiruna Greenstones: PhD Thesis, Luleå University of Technology, v. 19.

Martinsson O., and Virkkunen R., 2004, Apatite iron ores in the Gällivare, Svappavaara, and Jukkasjaärvi areas: Society of Geologic Geologist, Guidebook Series v. 33, p. 167–172.

Matthews, S.J., Marquillas, R.A., Kemp, A.J., Grange, F.K., and Gardeweg, M.C., 1996, Active skarn formation beneath lascar volcano, northern Chile: A petrographic and geochemical study of xenoliths in eruption products: Journal of Metamorphic Geology, v. 14, p. 509-530.

Matthews, S.J., Marquillas, R.A., Kemp, A.J., Grange, F.K., and Gardeweg, M.C., 1996, Active skarn formation beneath lascar volcano, northern Chile: a petrographic and geochemical study of xenoliths in eruption products: Journal of Metamorphic Geology, v. 14, p. 509–530.

McCrea, J.M., 1950, On the isotopic chemistry of carbonates and paleotemperature scale: Journal of Chemical Physics, v. 18, p. 849-857.

Moore, F. and Modabberi, S., 2003, Origin of Choghart iron oxide deposit, Bafq mining district, central Iron: new isotopic and geochemical evidence: Journal of Science, v. 14. P. 259-269.

Moore, F., and Modabberi, S., 2003, Origin of Choghart iron oxide deposit, Bafq mining district, central Iron: New isotopic and geochemical evidence: Journal of Science, v. 14, p. 259-269.

Mungall, J.E., Long, K., Brenan, J.M., Smythe, D., and Nuslund, H.R., 2018, Immiscible shoshonitic and Fe-P-oxide melts preserved in unconsolidated tephra at El Laco volcano, Chile: Geology, v. 46, p. 255-258.

Mungall, J.E., Long, K., Brenan, J.M., Smythe, D., and Nuslund, H.R., 2018, Immiscible shoshonitic and Fe-P-oxide melts preserved in unconsolidated tephra at El Laco volcano, Chile: Geology. v. 46, p. 255-258.

Nyström, J.O., and Henríquez, F., 1994, Magmatic features of iron ores of the Kiruna type in Chile and Sweden: Ore textures and magnetite geochemistry: Economic Geology. v. 89, p. 820–839.

Oliver, N.H.S. et al., 2004, Modeling the role of sodic alteration in the genesis of iron oxide-copper-gold deposits, eastern Mount Isa Block, Australia: Economic Geology v. 99, p. 1145-1176.

Oliver, N.H.S. et al., 2004, Modeling the role of sodic alteration in the genesis of iron oxide-copper-gold deposits, eastern Mount Isa Block, Australia: Economic Geology, v. 99, p. 1145-1176.

Ovalle, J.T. et al., 2018, Formation of massive iron deposits linked to explosive volcanic eruptions: Scientific reports: v. 8, p. 1-11.

Palmer, D.A.S., and Williams-Jones, A.S., 1996, Genesis of the Carbonatite-hosted fluorite deposit at Amba Dogar, India: Evidence from fluid inclusions, stable isotopes, and whole rock-mineral geochemistry: Economic Geology, v. 91, p. 934-950.

Perring, C.S., Pollard, P.J., Dong, G., Nunn, A.J., and Blake, K.L., 2000, The Lightning Creek Sill complex, Cloncurry District, Northwest Queensland: a source of fluids for Fe Oxide Cu-Au mineralization and sodic-calcic alteration: Economic Geology, v. 95, p. 1067-1089.

Rocco, T., Freda, C., Gaeta, M., Mollo, S., and Dallai, L., 2012, Magma chambers emplaced in carbonate substrate: Petrogenesis of skarn and cumulate rocks and implications for CO2 degassing in volcanic areas: Journal of Petrology, v. 53, p. 2307-2332.

Rowley, P.D., and Barker, D.S., 1978, Geology of the Iron Springs mining district, Utah: Guidebook to Mineral Deposits of Southwestern Utah: Utah Geological Association Publication. v. 7, p. 1-7.

Rudnick, R.L. and Gao, S., 2014, Composition of the continental crust: *in* Treatise on Geochemistry 2nd Edition, v. 3, p. 1-64.

Sabet-Mobarhan-Tala, A., Alinia, F., Ghannadpour, S., and Hezarkhani, A., 2015, Geology, geochemistry, and some genetic discussion of the Chador-Malu iron oxide-apatite deposit, Bafq District, Central Iran: Arabian Journal of Geosciences v. 8, p. 8399-8418.

Shan, Q. et al., 2012, Zircon U–Pb ages and geochemistry of the potassic and sodicrhyolites of the Kangbutiebao Formation in the southern margin of Altay, Xinjiang: Acta Petrologica Sinica, v. 28, p. 2132–2144.

Simon, A. et al., 2018, Kiruna-type iron oxide-apatite (IOA) and iron oxide copper-gold (IOCG) deposits form be a combination of igneous and magmatic-hydrothermal processes: Evidence from the Chilean iron belt: SEG. Special publications, v. 21, p. 89-114.

Speed, R.C., 1976, Geologic map of the Humboldt lopolith and surrounding terrane, Nevada: Geologic society of America. Map and Chart Series MC-14.

Steele-MacInnis, M., Ridley, J., Lecumberri-Sanchez, P., Schlegel, T. U., and Heinrich, C. A., 2016, Application of low-temperature microthermometric data for interpreting multicomponent fluid inclusion compositions: Earth Science Reviews, v. 159, p. 14–35.

Tait, S., 1992, Selective preservation of melt inclusions in igneous phenocrysts: American Mineralogist, v. 77, p. 146-155.

Torab, F.M., 2008, Geochemistry and metallogeny of magnetite apatite deposits of the Bafq Mining District, Central Iran: Unpub Thesis.

Tornos, F., Velasco, F., and Hanchar, J., 2016, Iron-rich melts, magmatic, magnetite, and superheated magmatic-hydrothermal systems: The El Laco deposit, Chile: Geology, v. 44, p. 427–430.

Tornos, F., Velasco, F., and Hanchar, J.M. 2017, The magmatic-hydrothermal evolution of the El Laco deposit (Chile) and its implications for the genesis of magnetite-apatite deposits: Econominc Geology. v. 112, p. 1595-1628.

Tornos, F., Velasco, F., and Hanchar, J.M., 2016, Iron-rich melts, magmatic magnetite, and superheated hydrothermal systems: The El Laco deposit, Chile: Geology. v. 44, p. 427-430.

Veksler, I.V., 2007, et al. Liquid immiscibility and the evolution of basaltic magma: Journal of Petrology, v. 48, p. 2187-2210.

Veksler, I.V., 2009, Extreme iron enrichment and liquid immiscibility in mafic intrusions: Experimental evidence revisited: Lithos. v. 111, p. 72-82.

Velasco, F., Tornos, F., and Hanchar, J.M., 2016, Immiscible iron- and silica-rich melts and magnetite geochemistry at the El Laco volcano (northern Chile): Evidence for a magmatic origin for the magnetite deposits: Ore geology reviews. v. 79, p. 346-366.

Wen, G., Bi, S. and Li, J., 2017, Role of evaporitic sulfates in iron skarn mineralization: a fluid inclusion and sulfur isotope study from the Xishimen deposit, Handan-Xingtai district, North China Craton: Mineralium Deposita, v. 52, p. 495-514.

Wenzel, T., Baumgartner, L. P., Brügmann, G. E., Konnikov, E. G., and Kislov, E. V., 2002, Partial melting and assimilation of dolomitic xenoliths by mafic magma: The Ioko-Dovyren intrusion (North Baikal region, Russia): Journal of Petrology, v. 43, p. 2049-2074.

Westhues, A., Hanchar, J.M., LeMessurier, M.J., and Whitehouse, M.J., 2017, Evidence for hydrothermal alteration and source regions the Kiruna iron oxide-apatite ore (northern Sweden) from zircon Hf and O isotopes: Geology. v. 45, p. 571-574.

Whiting, D.L., Grover, J.D. Jr., and Benson, W.R., 1992, Geology and mine reclamation studies, iron mines near Cedar City, Utah: in Engineering and environmental geology of southwestern Utah: Utah Geological Association Publication, v. 21, p. 287-313.

Wyllie, P. J., and Tuttle, O. F., 1960, The system $CaO-CO_2-H2O$ and the origin of carbonatites: Journal of Petrology. v. 1, p. 1-46.

Yardley, B.W.D., 2005, Metal concentrations in crustal fluids and their relationship to ore formation: Economic Geology, v. 100, p. 613-632.

Yu, J., Che, L., and Wang, T., 2015, Alteration, oxygen isotope, and fluid inclusion study of the Meishan iron oxide–apatite deposit, SE China: Mineralium Deposita, v. 50, p. 847-869.

Yu, J., Lu, B., Wang, T., and Che, L., 2015, Cretaceous Cu–Au, pyrite, and Fe-oxide–apatite deposits in the Ningwu basin, Lower Yangtze Area, Eastern China: Journal of Asian Earth Sciences, v. 103, p. 150-168.

Yu, J.J., Chen, Y.C., Mao, J.W., Pirajno, F., and Duan, C., 2011, Review of geology, alteration and origin of iron oxide–apatite deposits in the Cretaceous Ningwu volcanic basin, Lower Yangtze River Valley, eastern China: implications for ore genesis and geodynamic setting: Ore Geology Reviews, v. 43, 1p. 70–181.

**Figure 2.1: Satellite image of the Humboldt district including the Buena Vista mine area (featured in inset) and the town of Lovelock.**
Inset map of Nevada in upper left shows the regional location. Inset map of the Buena Vista mine in the lower left shows two sampling locations referenced in the text and Table 2.1. The locations of the Ford Pit and American Ore Mine are denoted by yellow and red stars, respectively.
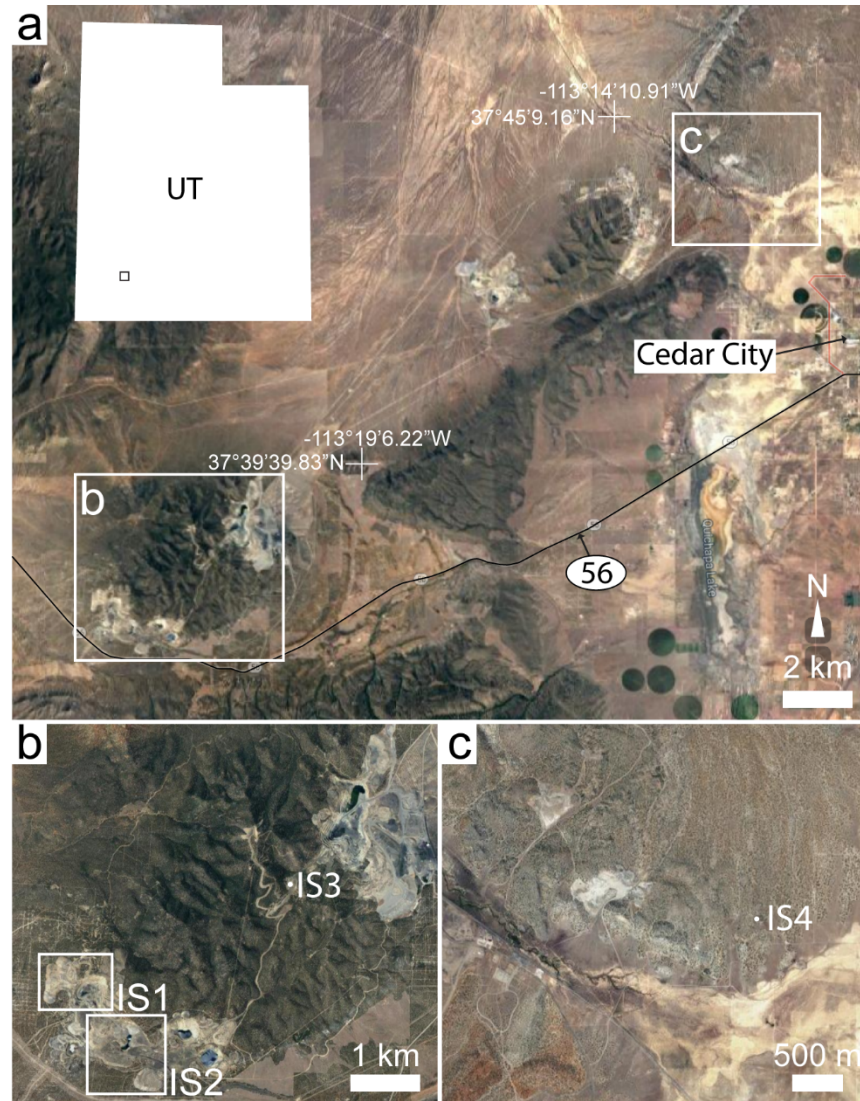
**Figure 2.2: Satellite image of the Iron Springs district, west-northwest of the town of Cedar City, Utah.**

a. satellite image showing the location of Iron Springs in Utah (inset map) and the locations of sampling areas. b. Satellite image showing sampling locations IS1-IS3 relative to the Iron Peak portion of the Three Peak pluton. c. Satellite image showing sampling locations IS4 ("fissure veins").
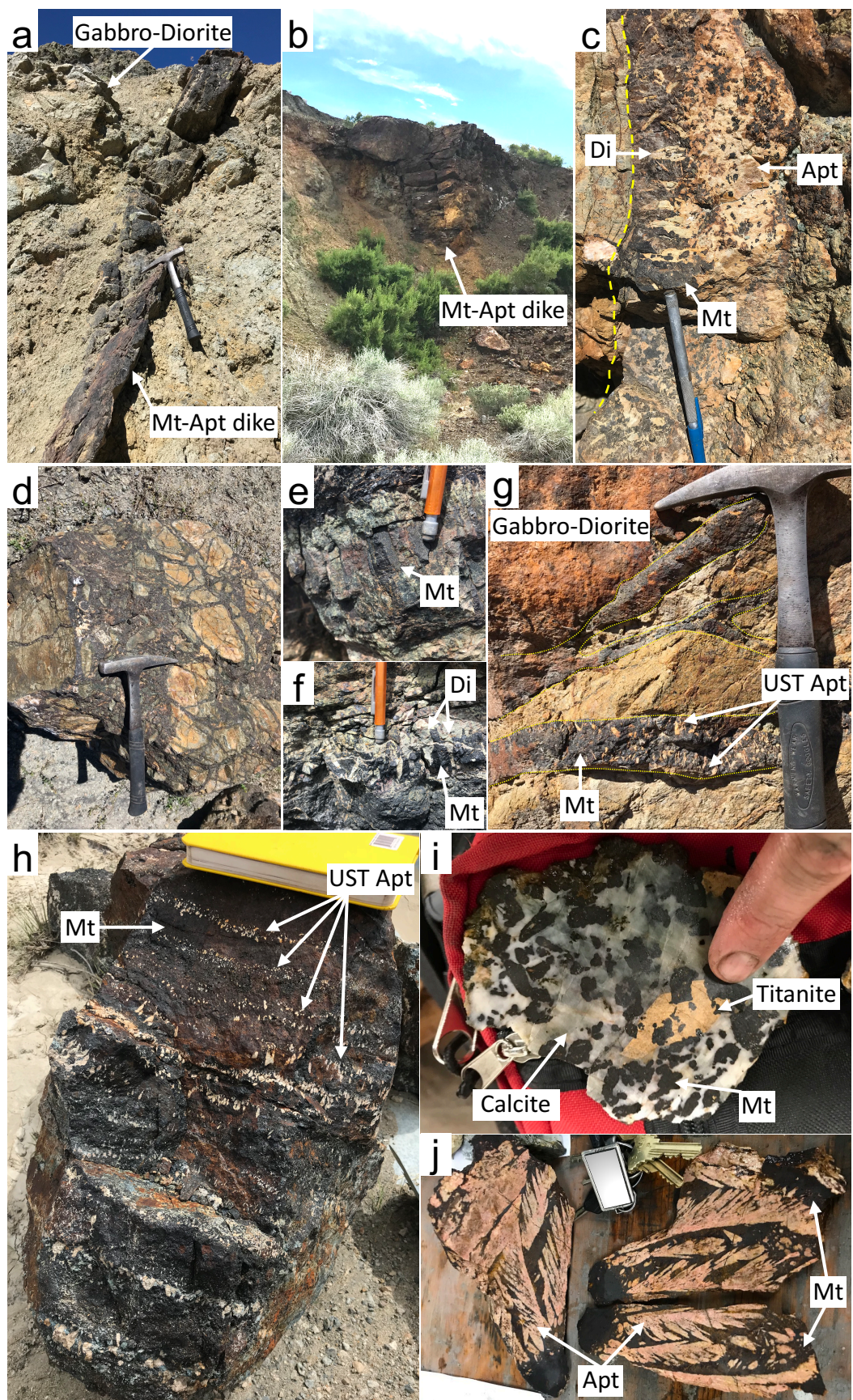
**Figure 2.3: Images of samples and outcrops from the Buena Vista system.**
a,b Magnetite-apatite (Mt-Apt) dikes from the Ford Pit (a) and American Ore Mine (b) cutting gabbro-diorite country rock. c. Magnetite-apatite dike from BV1 showing well developed unidirectional solidification textures (USTs) defined by euhedral diopside, magnetite, and apatite. Note the sharp contact with the host rock (denoted by a yellow dotted line). d. Magnetite-cemented breccia (BV2). e,f . Euhedral UST magnetite (Mt) and UST diopside (Di) from American Ore Mine. g,h. Comb-textured magnetite-apatite dikes (American Ore Mine). i. Cut sample of carbonate dike (BV2). j. Cut sample of magnetite ore with euhedral apatite showing epitaxial, skeletal growth textures (American Ore Mine).
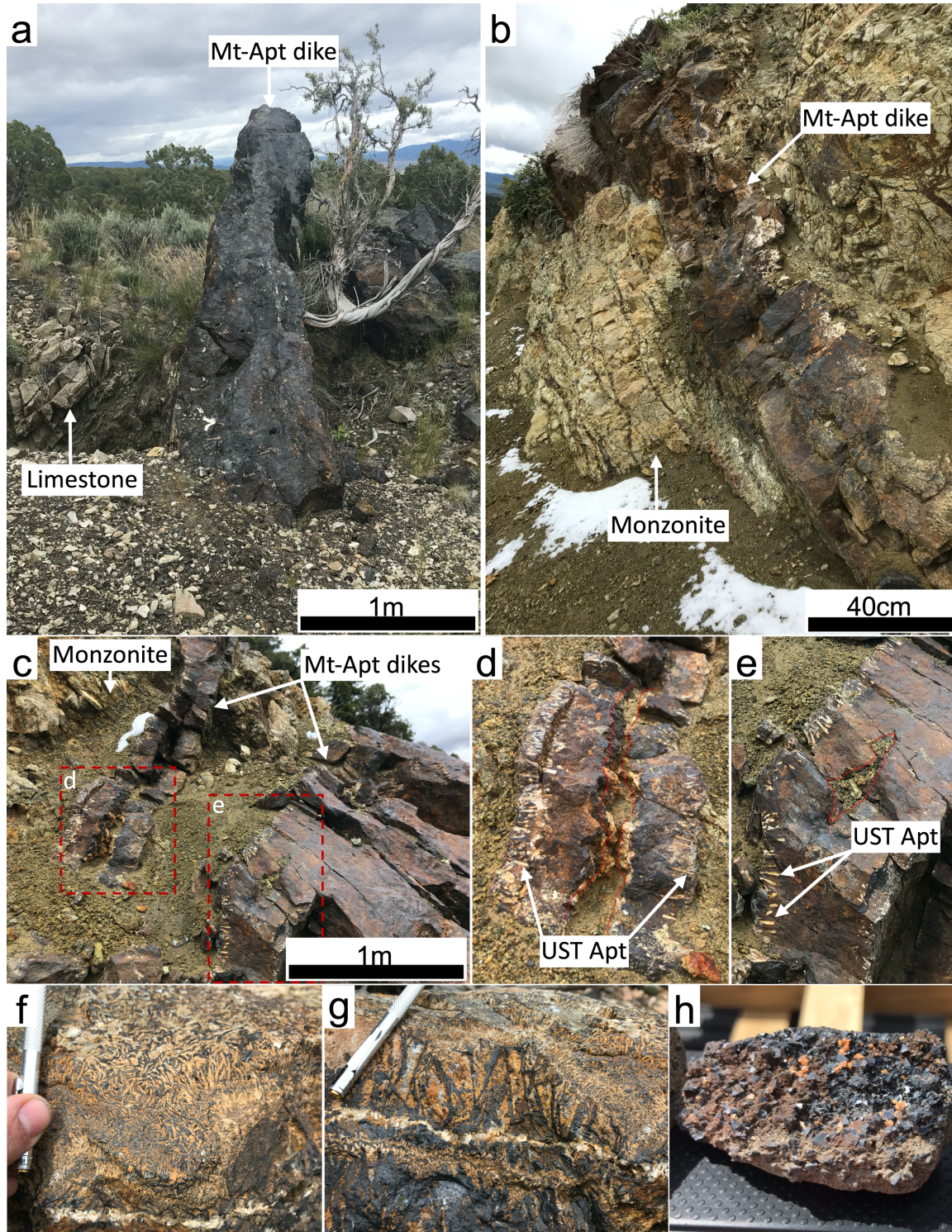
**Figure 2.4: Images of samples and outcrops from Iron Springs.**

a. Vertically oriented magnetite-apatite dike crosscutting limestone (IS4). b,c. Magnetite-apatite dikes crosscutting monzonite (IS3). Note the columnar jointing of the magnetite bodies and the sharp contact they share with the monzonite host rock. d,e. Close-up images of the magnetite-

apatite dikes shown in panel c. Note the euhedral comb textured/UST apatite along the margin of the dike and the large voids (vugs or vesicles) running along the centerlines of individual dikes (outlined in red). f,g. UST bands defined by intergrown diopside and euhedral magnetite (IS2). h. Open-space filling euhedral magnetite and calcite (IS3).
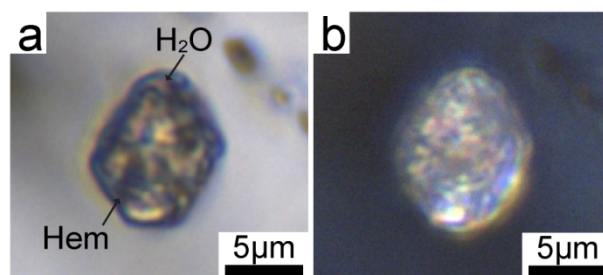
**Figure 2.5: Photomicrographs of a polycrystalline inclusion.**

a, b. A typical, negative-crystal-shaped polycrystalline inclusion in apatite, seen in plane (a) and cross-polarized (b) light. While the bulk of the inclusion is comprised of translucent, crystalline phases (mostly carbonate) apparent by their birefringence, $H_2O$, and hematite are both visible. This inclusion is representative of the polycrystalline inclusions targeted for microthermometric and geochemical analyses.
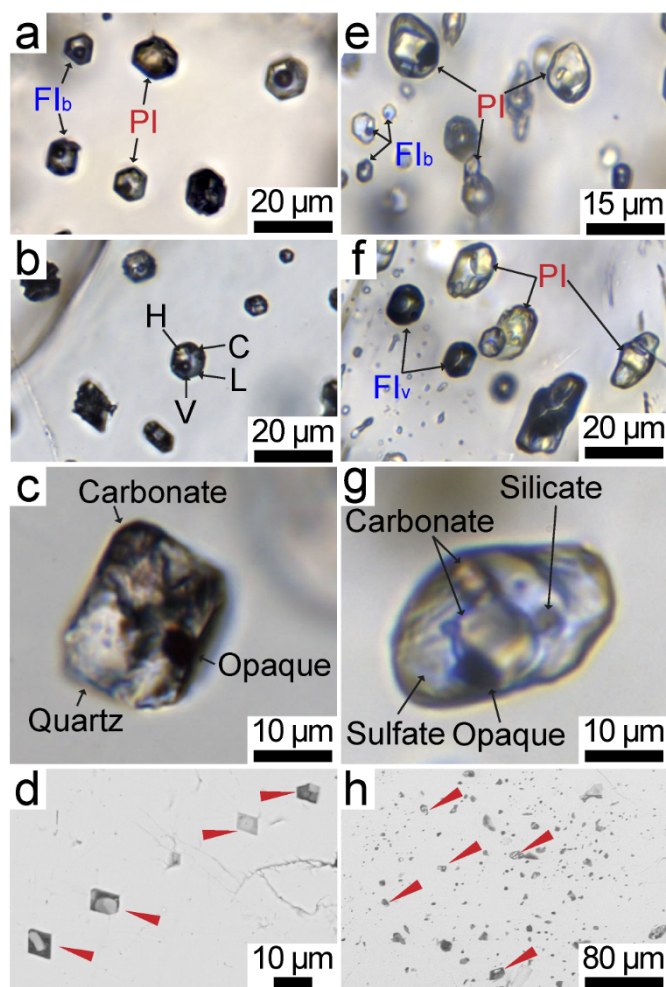
**Figure 2.6: Fluid and melt inclusions in apatite and actinolite from Buena Vista (a-d) and Iron Springs (e-h).**

a. Coexisting brine ($FI_b$) and polycrystalline (PI) inclusions in apatite (HB-5). b. Brine inclusions at 25 °C showing liquid (L), vapor (V), halite (H), and additional unidentified solids (C) (HB-5). c. Apatite-hosted, polycrystalline inclusion (HB-5). d. Back-scattered electron (BSE) image of magnetite-hosted polycrystalline inclusions (red arrows)(HUUS-04) e. Coexisting brine Inclusions ($FI_b$) and polycrystalline inclusions (PI) in apatite (UTMt-1-1-2). f. Coexisting vapor ($FI_v$) and polycrystalline (PI) inclusions in apatite (UTMt-1-1-2). g. Apatite-hosted, polycrystalline inclusion (UTMt-1-1-1). h. BSE image of magnetite-hosted polycrystalline inclusions (red arrows) (UTMt-1-1-1).
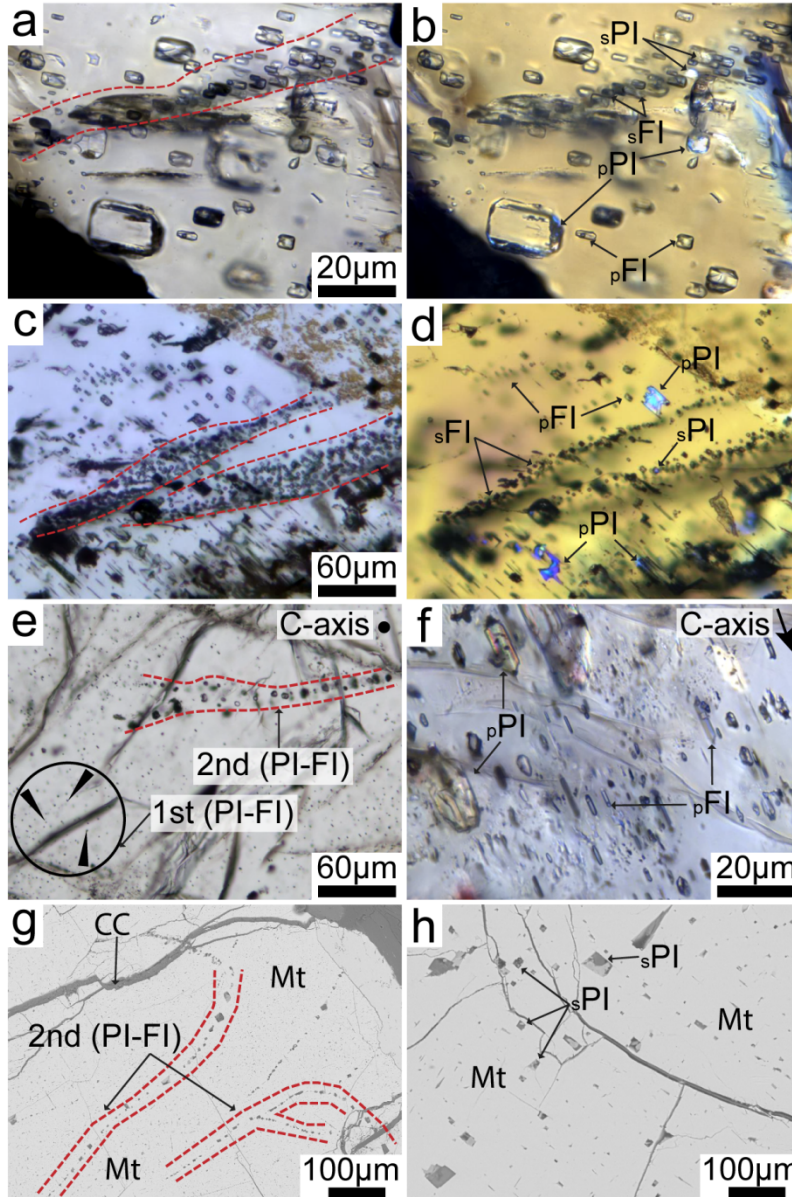
**Figure 2.7: Photomicrographs of primary and secondary assemblages of coexisting aqueous and polycrystalline inclusions.**

a Composite photomicrograph showing a secondary trail (outlined by red dotted line) of aqueous fluid inclusions (sFI) and polycrystalline inclusions (sPI) crosscutting an assemblage of primary fluid inclusions (pFI) and polycrystalline inclusions (pPI) hosted in apatite from the magnetite ore (HUUS-04). b. The same composite image shown in panel a, in cross-polarized light. Note the characteristic birefringence of the primary and secondary polycrystalline inclusions. c, d. Composite image of crosscutting primary and secondary assemblages of coexisting aqueous fluid inclusions and polycrystalline inclusions hosted in apatite from the magnetite ore in plane

polarized light (c) and cross-polarized light (d) (HUUS-04). e, f. Composite image of crosscutting primary (1$^{st}$ PI-FI) and secondary (2$^{nd}$ PI-FI) assemblages of coexisting aqueous fluid inclusions and polycrystalline inclusions hosted in apatite from the carbonate dikes. Note that primary inclusions in carbonate dikes (some examples circled in black and denoted by black arrows) have elongate shapes oriented parallel to the c-axis, thus appearing as small dots in samples cut perpendicular to the c-axis. Hence, primary inclusions in carbonate dikes are best visible in thin sections cut parallel to the c-axis of the host crystal (f) (HB-5). g.h Back-scattered electron images of secondary assemblages of polycrystalline inclusions in magnetite (HUUS-04).
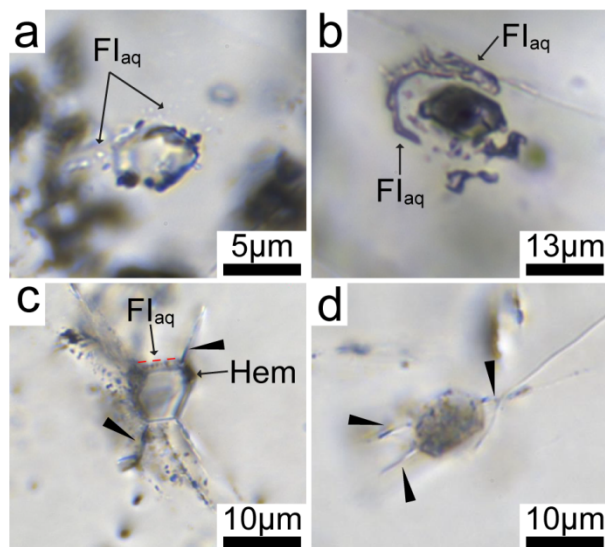
**Figure 2.8: Polycrystalline inclusions showing evidence of H₂O loss, partial decrepitation, and internal overpressure**.

a, b. Modified polycrystalline inclusions showing halos of aqueous in fluid inclusions ($FI_{aq}$) around their periphery. c, d. Polycrystalline inclusions showing microfractures that extend outward from the periphery of the inclusion, indicating high internal pressures. Note that such inclusions showing evidence of $H_2O$ loss or partial decrepitation were excluded from further microthermometric and geochemical analyses.
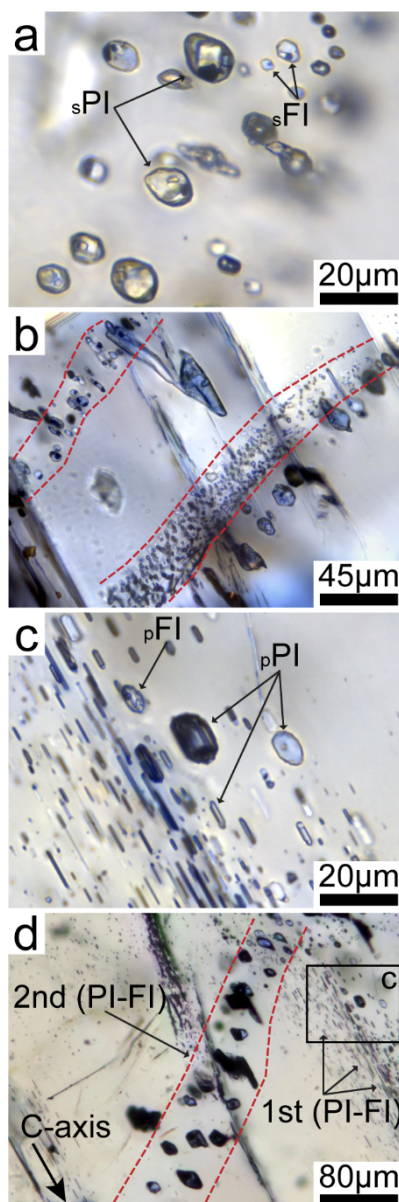
**Figure 2.9: Photomicrographs of primary and secondary assemblages of coexisting aqueous and polycrystalline inclusions from Iron Springs.**

a. Composite photomicrograph showing a secondary assemblage of coeval aqueous fluid inclusions (sFI) and polycrystalline inclusions (sPI). b. Coeval polycrystalline and aqueous inclusions aligned along a healed fracture in apatite (outlined by red dashed lines). c. Composite image of a primary assemblage of coexisting aqueous fluid inclusions (pFI) and polycrystalline inclusions (pPI) hosted in apatite. Note that one of the polycrystalline inclusions (center) contains a substantial portion of vapor. d. Composite image of crosscutting primary ($1^{st}$ PI-FI) and secondary ($2^{nd}$ PI-FI) assemblages of coexisting aqueous fluid inclusions and polycrystalline

inclusions hosted in apatite. Note that primary inclusions have an elongate shape that runs parallel to the c-axis. The area shown in panel c in denoted by the black square. All images shown are taken from sample UTMt-1-1-2.
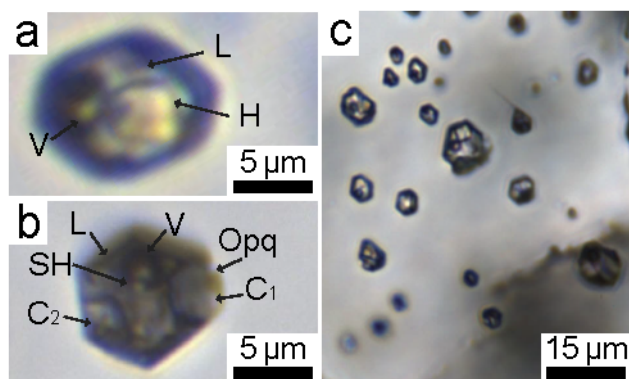
**Figure 2.10: Photomicrographs of aqueous inclusions from Buena Vista.**

a. Three-phase, negative crystal-shaped inclusion containing liquid (L), vapor (V) and halite (H). b. Negative crystal-shaped aqueous inclusion containing liquid, vapor, two translucent crystals ($C_1$ and $C_2$), salt hydrate/halite (SH), and an opaque (Opq, partially obscured by $C_1$). Notice that the salt hydrate/halite is encroaching on the lower edge of the vapor bubble. Both inclusions shown in a and b have identical halite melting and homogenization temperatures. c. Assemblage of negative crystal-shaped aqueous inclusions. All Images shown are from sample HB-5
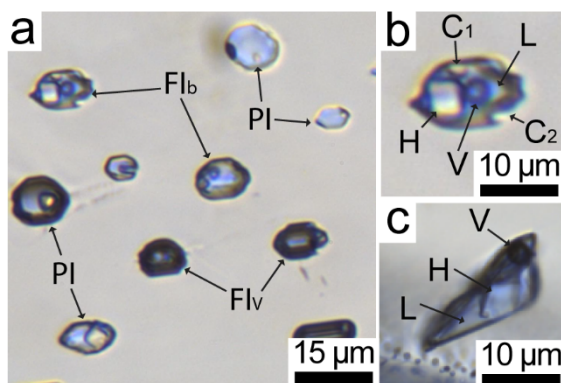
**Figure 2.11: Photomicrographs of aqueous inclusions from Iron Springs.**

a. Coexisting aqueous brine ($FI_b$), vapor ($FI_v$) and polycrystalline inclusions (PI) from Iron Springs. Note that one of the polycrystalline inclusions (left-center) contains a substantial vapor portion. b. Photomicrograph of an aqueous brine inclusion showing liquid (L), vapor (V), halite (H) and two additional unidentified translucent daughter crystals ($C_1$, $C_2$). c. Photomicrograph of an aqueous brine inclusions showing liquid, vapor, and halite. All images shown are form sample UTMt-1-1-2.
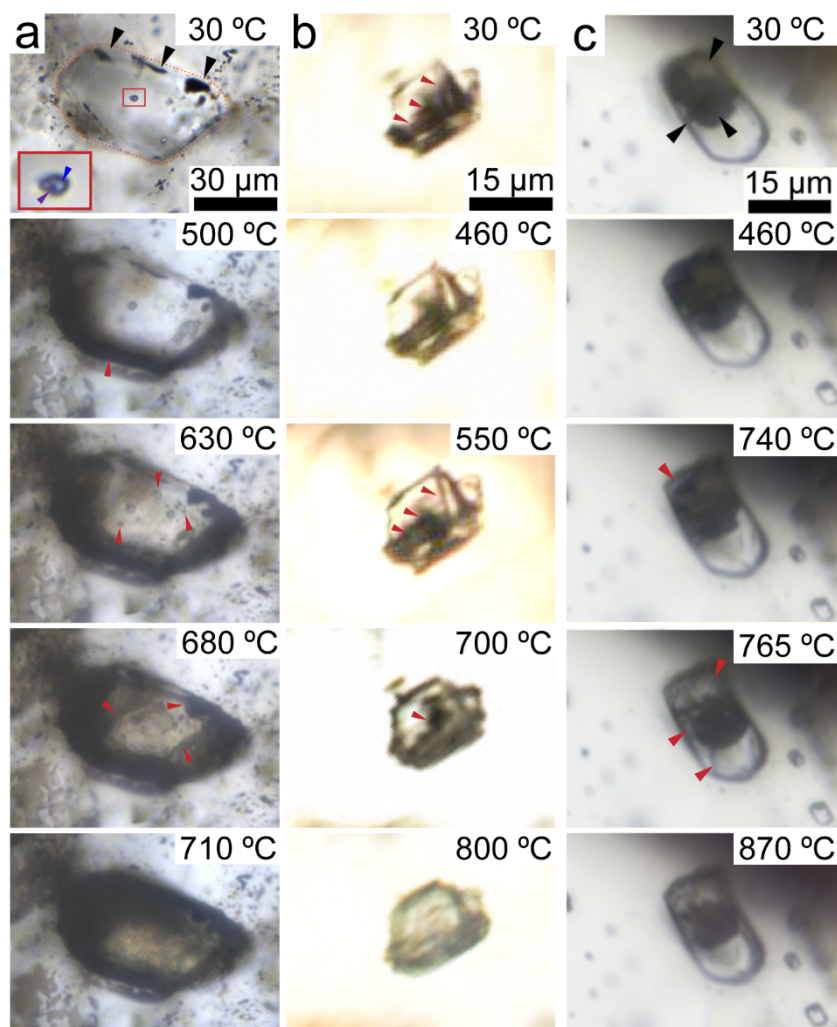
**Figure 2.12: Melting of polycrystalline inclusions.**

a.b. Polycrystalline inclusions in apatite from Buena Vista. Black arrows denote opaque phases which shrink during heating. A pocket of liquid $H_2O$ is outlined in white and shown in the inset image with blue and purple arrows denoting the liquid and vapor phases, respectively. Orange arrows denote features (melt pockets and grain boundaries) which show melting behavior. c. Polycrystalline inclusion in apatite from Iron Springs. Orange arrows denote areas that show distinct melting behavior.
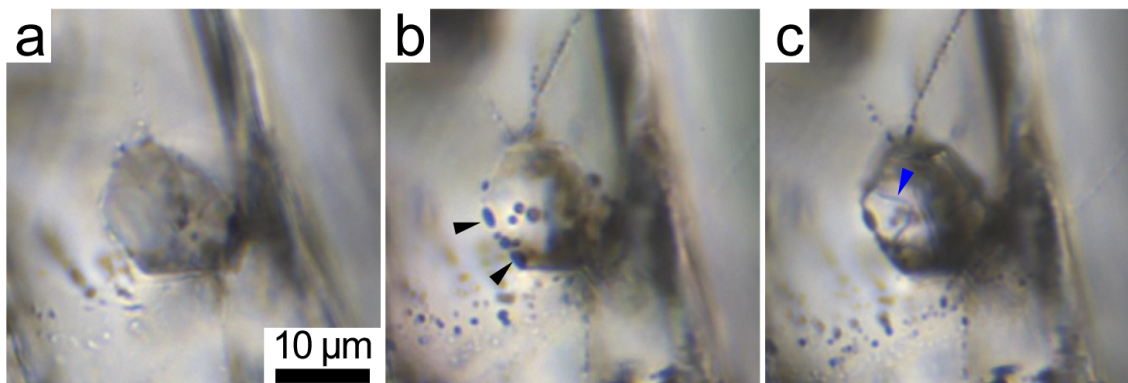
**Figure 2.13: Photomicrographs showing changes in polycrystalline inclusions from Buena Vista after quenching from high temperature.**

a. Polycrystalline inclusion prior to heating. b. The same inclusion as in panel a, immediately after heating to 850 °C and removal from the heating element. Notice that the inclusion contains several dark, round features in the center and along its margin after cooling to room temperature; these are vapor bubbles formed at high temperature (black arrows). Also notice that the inclusion has begun to partially decrepitate during the heating experiment, evinced by the trails of sub-micron fluid inclusions emanating from the upper corners of the inclusion. c. The same inclusion, 40 minutes after quenching. Notice that the vapor bubbles along the edges have shrunk, and the inclusion now has a more crystalline appearance (blue arrow).
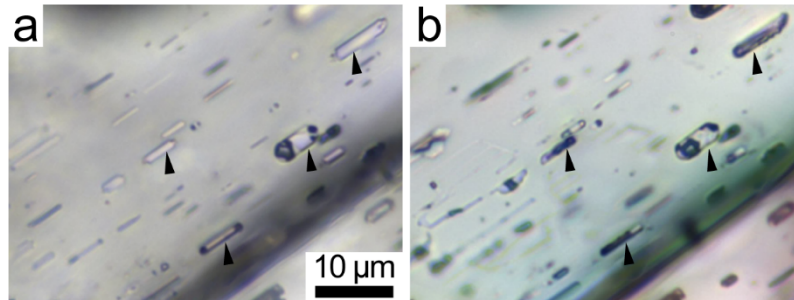
**Figure 2.14: Photomicrographs showing changes in polycrystalline inclusions from Iron Springs after quenching from high temperature.**

a. Array of primary polycrystalline inclusions prior to heating. b. The same inclusions as in panel a, immediately after heating to 900 °C and removal from the heating element. Notice the dark, crystalline appearance of the inclusions and the distortion of the vapor bubble in the large inclusion on the right-hand side after quenching.
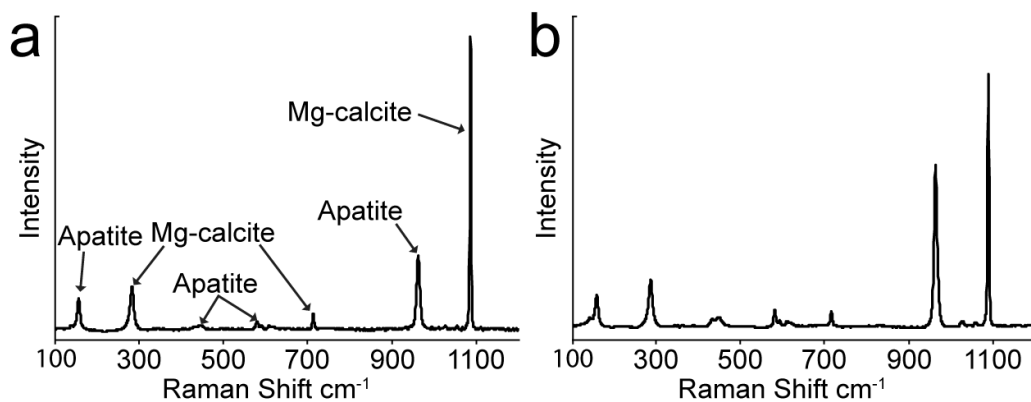
**Figure 2.15: Raman spectrum of a polycrystalline inclusion from Buena Vista, before heating (a) and immediately after heating to 875°C and rapid cooling to room temperature (b).**
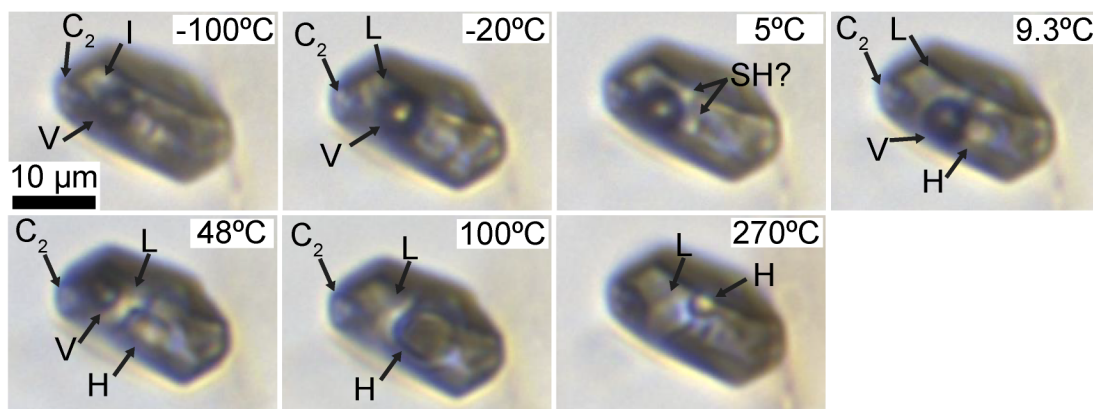
**Figure 2.16: Temperature series showing phase transitions in an aqueous inclusion from Buena Vista between -100°C and 270°C.**

Note the abrupt change in the position of the vapor bubble and disappearance of hydrate between +5°C and +9.3°C and the growth of the halite crystal between +9.3°C to 100°C.
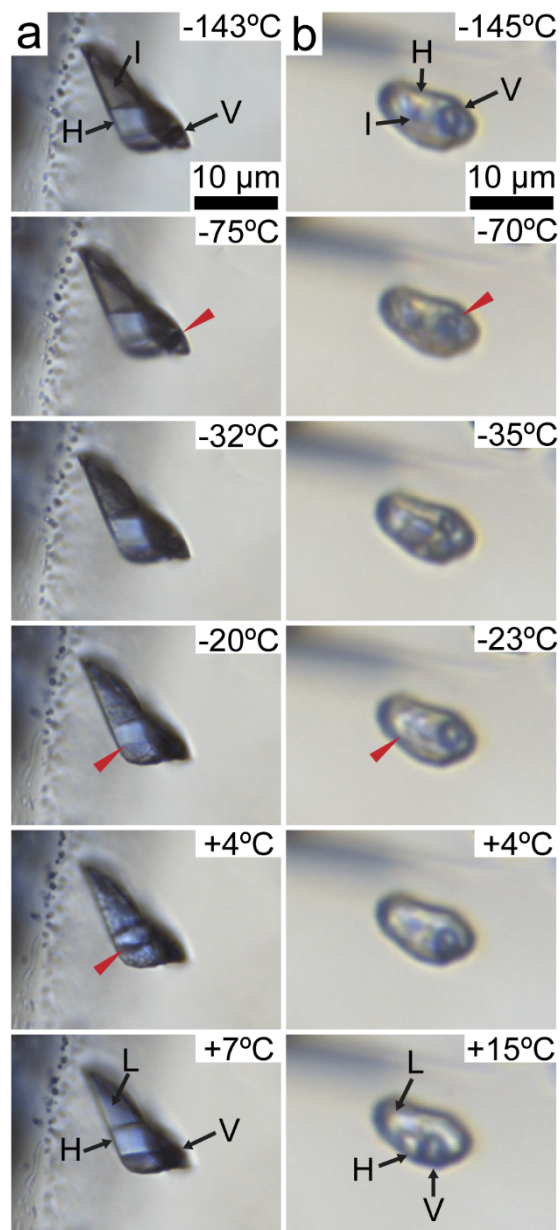
**Figure 2.17: Temperature series showing phase transitions in aqueous inclusions from Iron Springs between -150°C and +20°C.**

a. First melting is apparent from the deformation of the vapor bubble (V) at -75 °C (denoted by the red arrow). At temperatures above -20 °C, ice (I) appears to melt and the halite crystal (H) shrinks (denoted by red arrows). At +4 °C, the halite crystal is partially consumed by the salt hydrate (granular mass), and at +6 °C the salt hydrate abruptly decomposes and the salt crystal returns to its original size. b. First melting is apparent from the deformation of the vapor bubble at -70°C (denoted by the red arrow). At temperatures above -23°C, ice appears to melt and the

halite crystal disappears (denoted by red arrows). At +4 °C, salt hydrate occurs as a granular mass alongside the vapor phase, and at +14°C the salt hydrate abruptly decomposes and the salt crystal reappears.
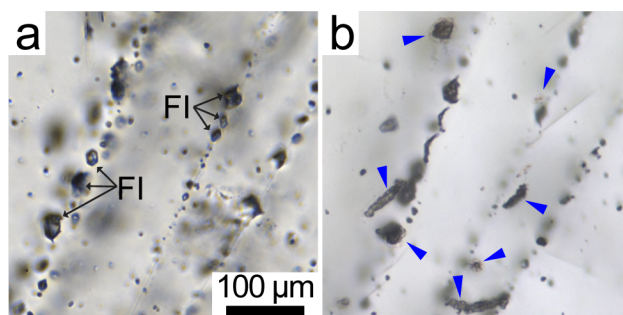
**Figure 2.18: Photomicrographs of aqueous inclusions (FI) in transmitted light (a) and corresponding mounds (blue arrows) in reflected light (b).**
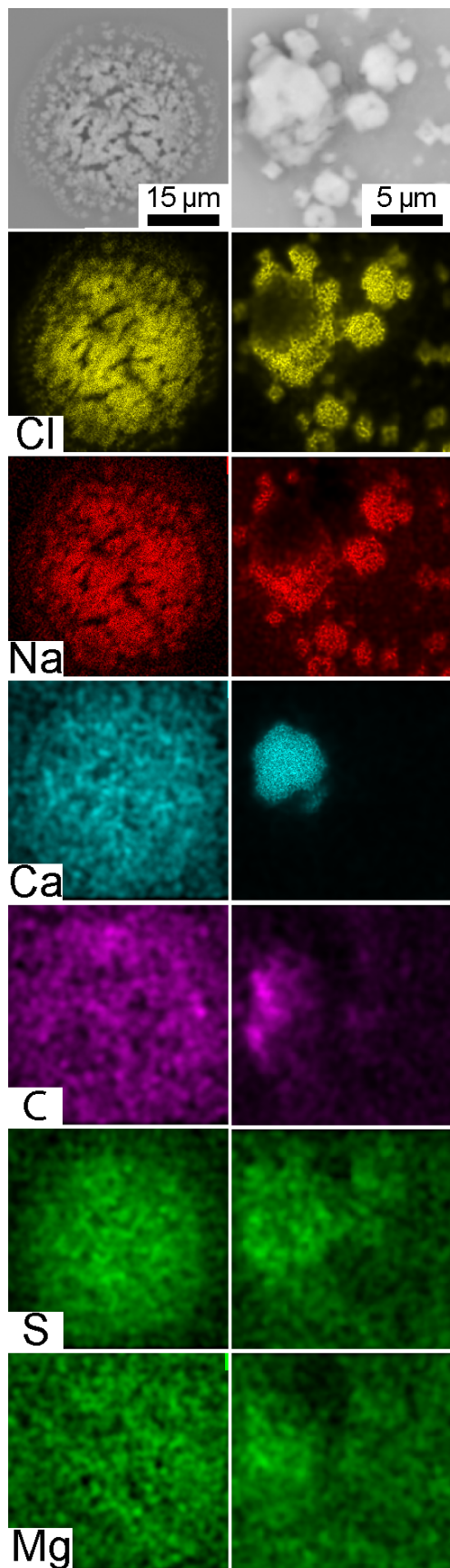
**Figure 2.19: Back-scatter electron images of decrepitate mounds precipitated on a glass substrate (top row) and corresponding x-ray maps of the same areas shown in the BSE images.**

Note the heterogeneous distribution of Ca and C. Mounds shown here are derived from sample HB-5
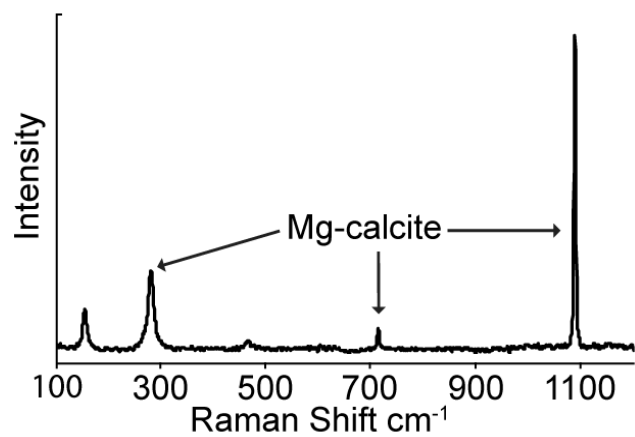
**Figure 2.20: Raman spectra from a birefringent, Ca-C-Mg-rich portion of a decrepitate mound precipitated on a glass substrate.**
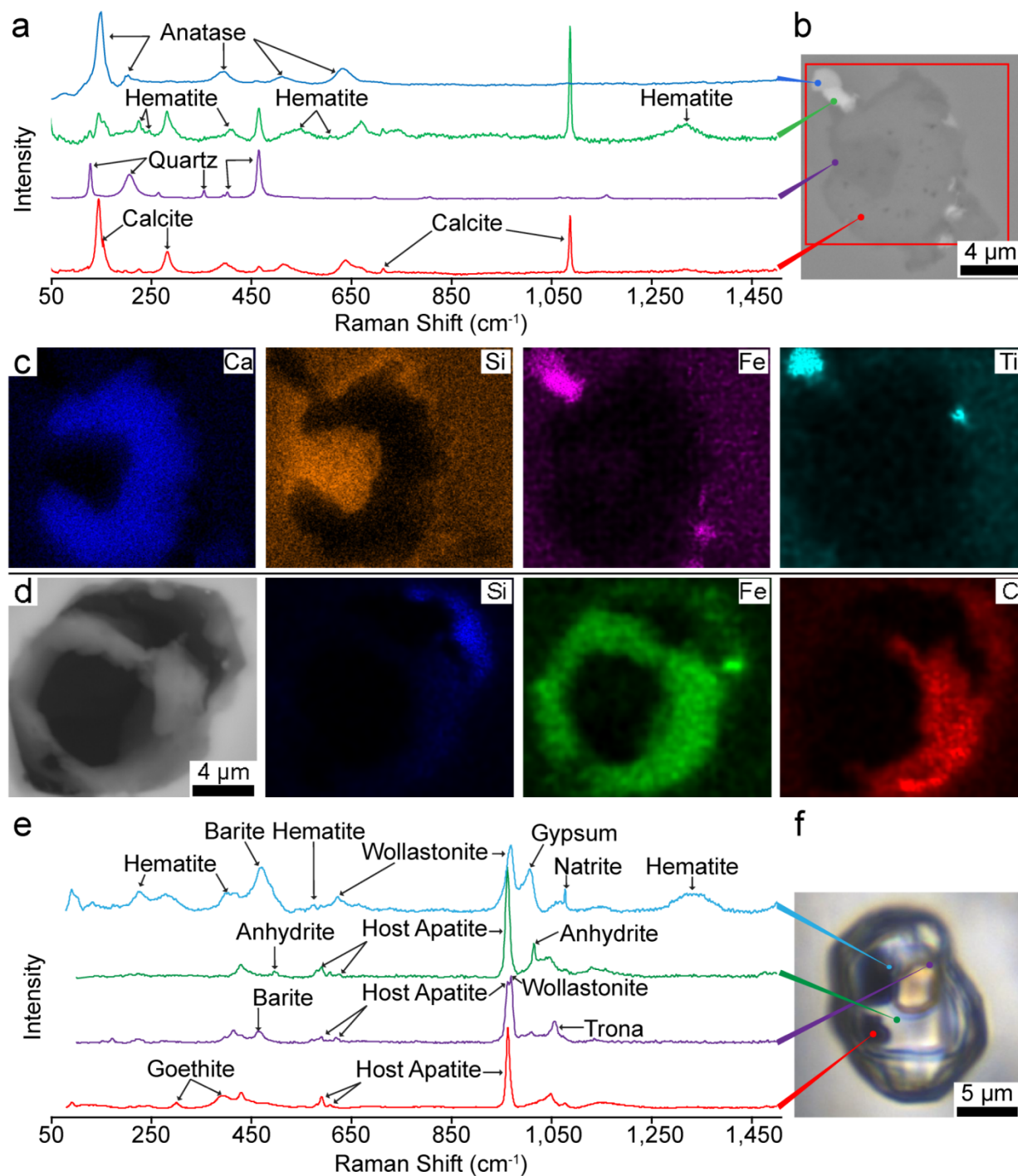
**Figure 2.21: Phases within polycrystalline (melt) inclusions from Buena Vista.**

a. Raman spectra of phases in an actinolite-hosted polycrystalline inclusion (shown in b). b. Back-scattered electron (BSE) image of polycrystalline inclusion exposed at the surface of a host crystal. c. EDS element maps of the inclusion shown in b. d. BSE image (far left) and EDS

element maps of solid phases present in a breached aqueous inclusion. e. Raman spectra of phases in an apatite-hosted polycrystalline inclusion (shown in transmitted light in f).
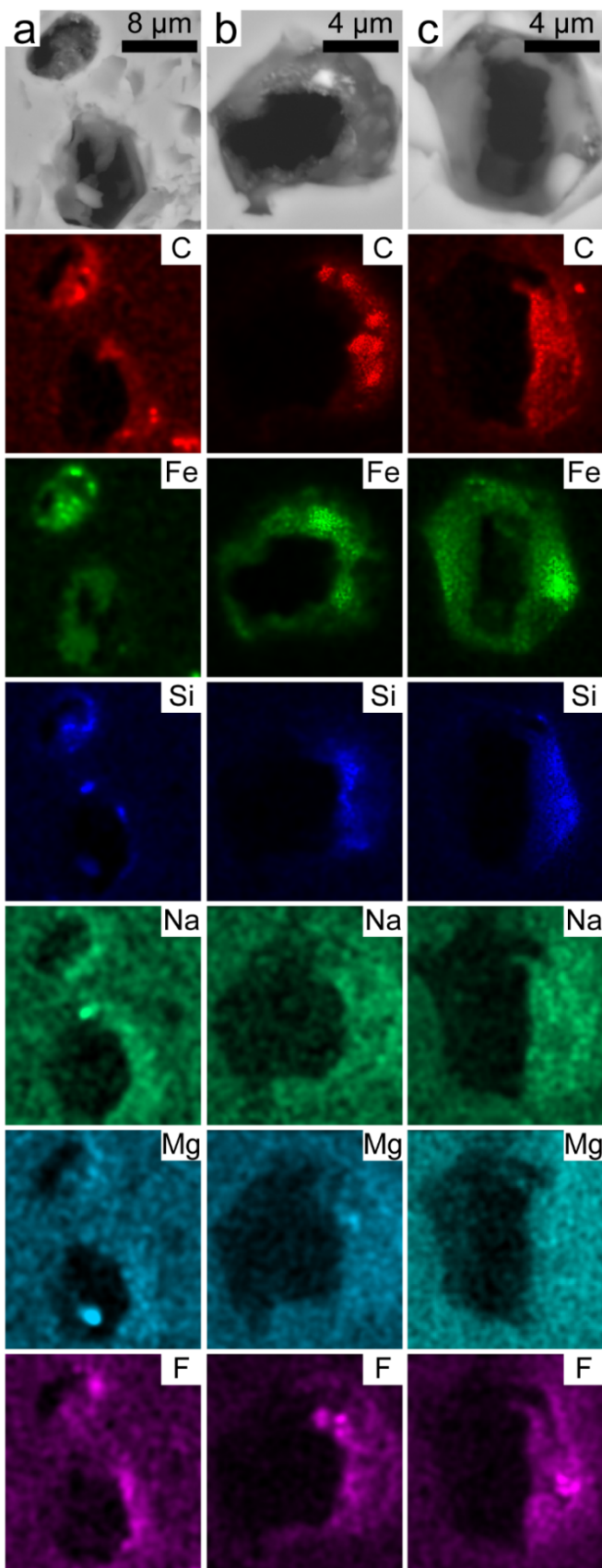
**Figure 2.22: Back-scatter electron images of solid phases in exposed aqueous inclusions (top row) and corresponding x-ray maps of the same areas shown in the BSE images**

The centers of the inclusions were filled with aqueous liquid prior to polishing and are empty space (black areas) in the images. Inclusions shown are from sample HB-5.
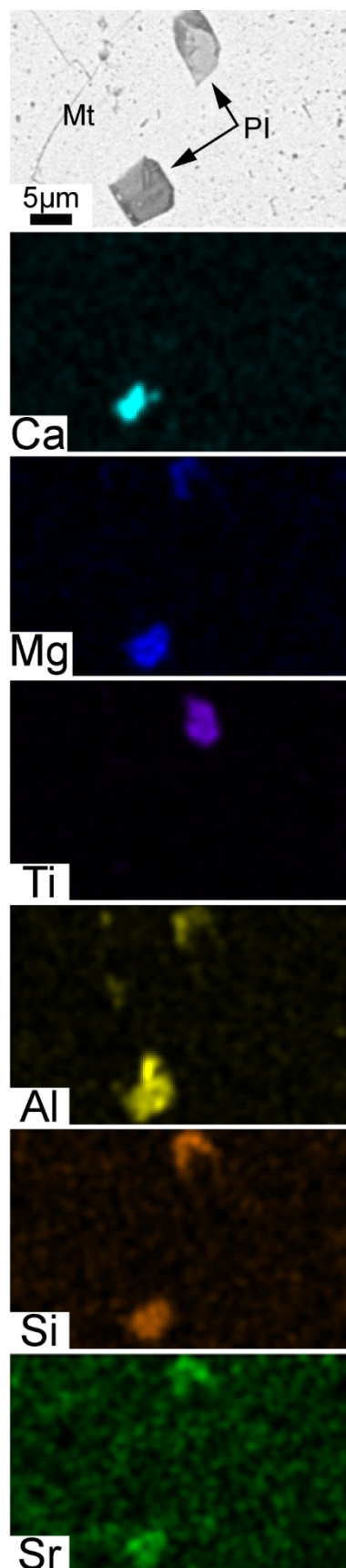
**Figure 2.23: Solid phases in magnetite-hosted polycrystalline inclusions.**

Back-scatter electron image (Top) of solid phases in polycrystalline inclusions (PI) in magnetite (Mt) and corresponding x-ray maps of the same area showing the distribution of elements in the crystalline phases. Inclusions shown are hosted in magnetite from sample HUUS-04.
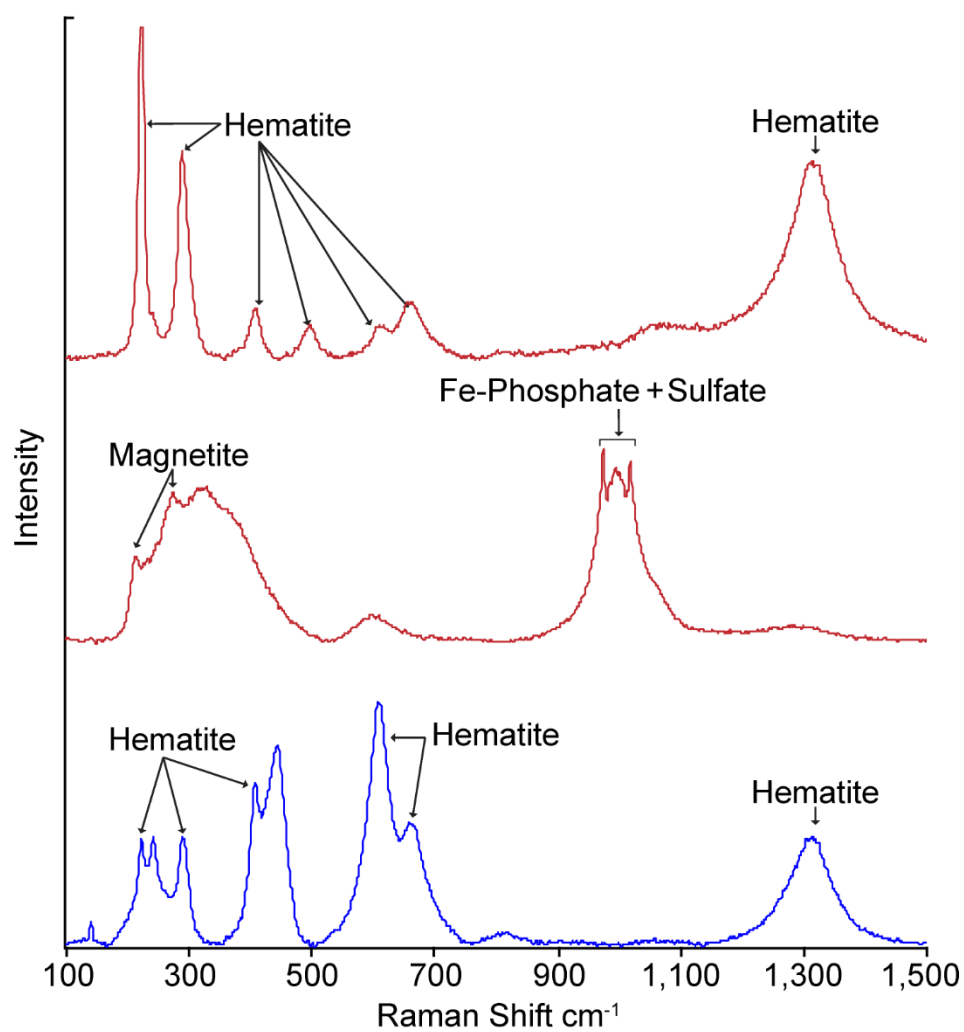
**Figure 2.24: Raman spectra from magnetite-hosted polycrystalline inclusions from Iron Springs (red) and Buena Vista (blue).**

Note that the spectrum in the middle of the figure shows overlapping Raman bands of Fe-phosphate and sulfate.
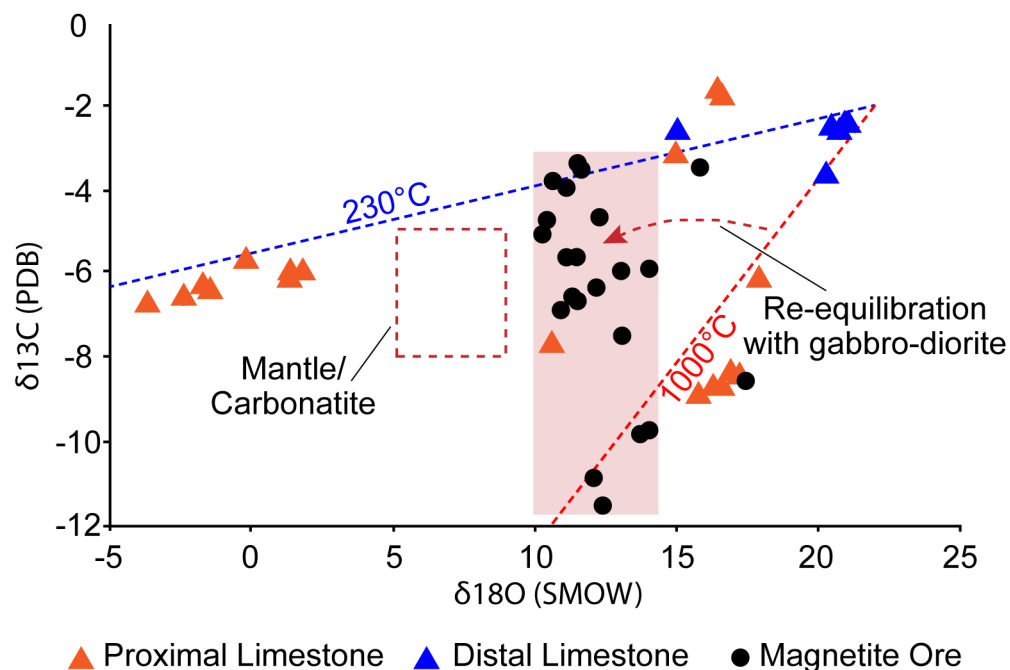
**Figure 2.25: C and O isotopic analyses of calcite separates from Buena Vista.**
Carbonate was sampled from both distal (blue triangles) and proximal (orange triangles) to an intrusive contact with gabbro-diorite, and from the magnetite ore body (locality BV3). Dashed lines represent Rayleigh distillation trends of decarbonation at 230 ºC (blue) and and 1000 ºC (orange), assuming a starting isotopic composition of distal limestone. Data from primary carbonate from magnetite ore (black circles) lie mostly along a narrow range of $\delta^{18}O$ values and a wide range of $\delta^{13}C$ values (highlighted with red rectangle). Note that this range lies outside normal mantle/carbonatite values (range outlined by square dotted line).
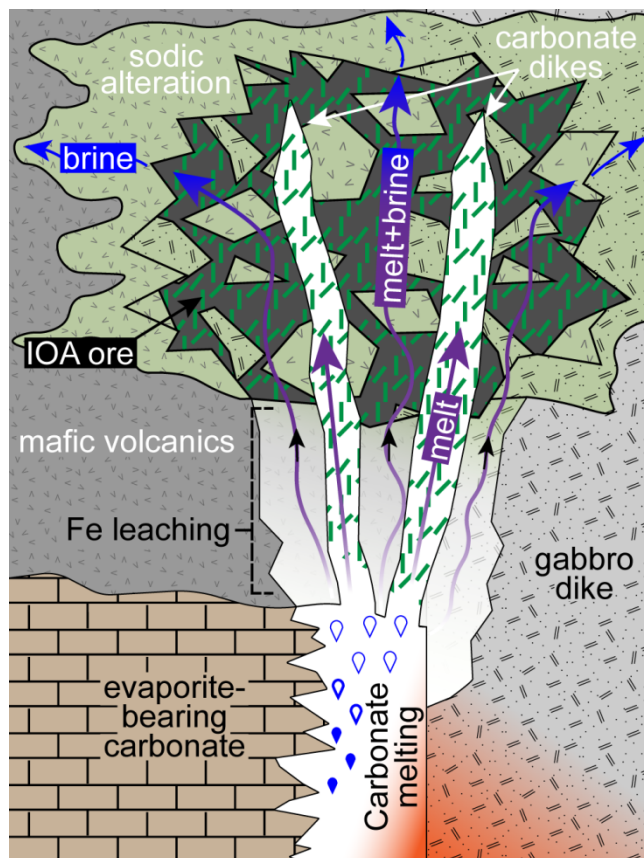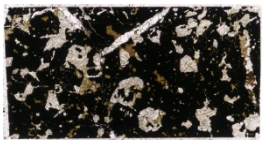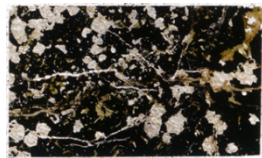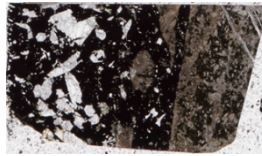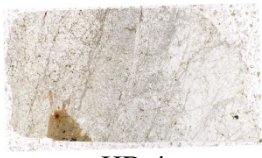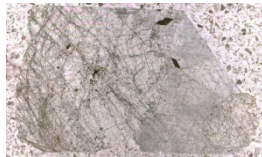
**Figure 2.26: Schematic cross section showing IOA formation via anatectic carbonate melting.**
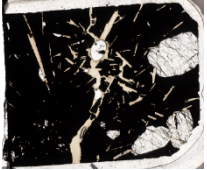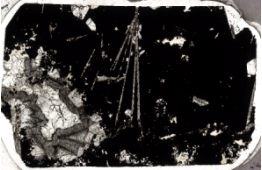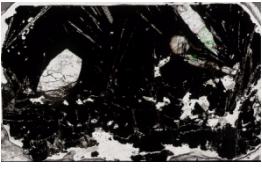
Carbonate melt is produced by partial melting of wet, evaporite-bearing carbonate rocks in response to magma intrusion. During formation of breccia and magnetite ore, brine unmixes from the carbonate melt and migrates outward into the country rock, forming a sodic alteration envelope. With continued heat flux from the magma, additional melting of carbonate leads to emplacement of apatite-rich, carbonate dikes.
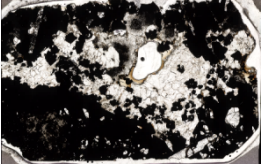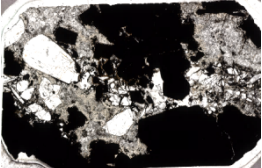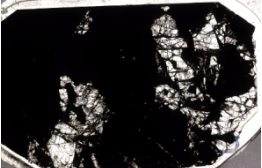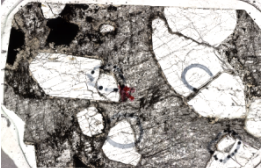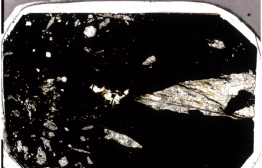
**Table 2.1: Descriptions of Buena Vista samples from this study.**
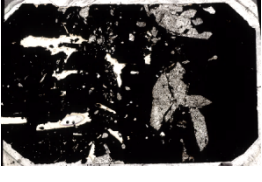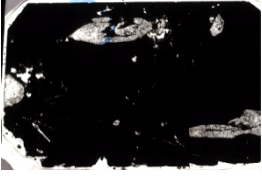
| Sample sections* | Location[†] | Description |
|---|---|---|
|  HB-1 | 39º58'25.65"N, 118º10'09.01"W BV1 | Magnetite (opaque) intergrown with subhedral to euhedral apatite (large clear areas), chlorite (patchy brown/green), and minor calcite (intergrown around the edges of apatite). Host rock does not appear in thin section. |
|  HB-2 | 39º58'25.65"N, 118º10'09.01"W BV1 | Magnetite (opaque) intergrown with subhedral to euhedral apatite (large clear areas), chlorite (patchy brown/green), and minor calcite (intergrown around the edges of apatite, and forming horizontal cracks). Most apatite in this sample has been cut perpendicular to the c-axis. Host rock does not appear in thin section. |
|  HUUS-04 | 39º58'25.65"N, 118º10'09.01"W BV1 | Magnetite (opaque) intergrown with subhedral to euhedral apatite (large clear areas). Most apatite in this sample are cut perpendicular to the c-axis. The right-hand portion of this section shows the contact between the magnetite-apatite vein and Na-altered mafic host-rock. |
|  HB-3 | 39º58'28.04"N, 118º10'1.57"W BV2 | Carbonate dike which crosscuts magnetite ore. Several generations of euhedral to anhedral apatite with minor anhedral potassium feldspar (brown-orange masses near the top of the image) and hematite (opaque masses associated with feldspars). |
|  HB-4 | 39º58'28.04"N, 118º10'01.57"W BV2 | Carbonate dike which crosscuts magnetite ore. Several generations of euhedral to anhedral apatite with minor anhedral potassium feldspar (brown-orange masses near the bottom of the image) and hematite (opaque/orange masses associated with feldspars). |
|  HB-5 | 39º58'28.04"N, 118º10'01.57"W BV2 | Carbonate dike which crosscuts magnetite ore. Euhedral apatite (left half of image and lower right corner) inter grown with clear calcite and actinolite (green rhombs near the top right). |

\* Each image is a digital scan of a polished thin section, 45 x 26 mm. †Location numbers refer to points labeled in Fig. S1.

**Table 2.2: Descriptions of Iron Springs samples from this study.**

| Sample sections* | Location[†] | Description |
|---|---|---|
|  UTMt-1-1-1 | 37°37'24.7116"N 113°24'2.3976"W IS1 | Tabular comb-textured magnetite-apatite dike cut perpendicular to outer margin: Euhedral magnetite (opaque) intergrown with comb-textured euhedral apatite (large clear areas) and actinolite (small acicular crystals along margin), and minor anhedral interstitial calcite (not visible in hand sample). |
|  UTMt-1-1-2 | 37°37'24.7116"N 113°24'2.3976"W IS1 | Tabular comb-textured magnetite-apatite dike cut perpendicular to outer margin: Euhedral magnetite (opaque) intergrown with comb-textured euhedral apatite (large clear areas) and actinolite (small acicular crystals along margin), and minor anhedral interstitial calcite (not visible in hand sample). |
|  UTPile1-1-1 | 37°36'51.6816"N 113°23'29.054"W IS2 | Tabular comb textured magnetite-apatite dike cut perpendicular to long axis showing calcite filled centerline: Euhedral magnetite (opaque) intergrown with minor euhdral apatite (large clear areas), and actinolite (acicular spray of crystals along upper margin) surrounding a vug filled with euhedral comb-textured / colloform calcite. |
|  UTPile1-1-2 | 37°36'51.6816"N 113°23'29.054"W IS2 | Tabular comb-textured magnetite-apatite dike cut perpendicular outer margin: Euhedral magnetite (opaque) intergrown with comb-textured euhedral apatite (large clear areas) and actinolite (small acicular crystals along upper margin), and minor anhedral interstitial calcite (not visible in hand sample). |
| | 37°36'51.6816"N 113°23'29.054"W | Tabular comb-textured magnetite-apatite dike cut perpendicular to long axis showing calcite filled centerline: Euhedral magnetite (opaque) intergrown with minor euhedral apatite (large clear areas), and |

| | | |
|---|---|---|
| UTPile1-2-1 | IS2 | actinolite (acicular spray of crystals along margin upper margin) surrounding a vug filled with euhedral comb-textured calcite. |
| UTMt-1-2-1 | 37°38'19.3092"N 113°22'6.5711"W IS3 (Iron Peak) | Tabular magnetite-apatite dike cut perpendicular to long axis showing intergrown apatite-calcite centerline: Euhedral comb-textured magnetite (opaque) surrounding a vug lined with euhedral apatite (large clear areas), open space-filling colloform calcite. |
| UTMt-1-2-2 | 37°38'19.3092"N 113°22'6.5711"W IS3 (Iron Peak) | Tabular magnetite-apatite dike cut perpendicular to long axis showing comb-textured apatite (large clear crystals). |
| UTMt-1-2-3 | 37°38'19.3092"N 113°22'6.5711"W IS3 (Iron Peak) | Intergrown apatite-calcite centerline of a magnetite-apatite dike: Euhedral apatite (large clear crystals) surrounded by subhedral-anhedral calcite (gray) and minor subhedral to anhedral magnetite (Opaque). |
| UTFis-1-1 | 37°44'15.8244" 113°10'54.7284"W IS4 (Corey fissure) | Tabular comb-textured magnetite-apatite dike cut perpendicular outer margin: Euhedral magnetite (opaque) intergrown with comb-textured euhedral apatite (large clear areas) and minor anhedral interstitial calcite (not visible in hand sample). |

| | | |
|---|---|---|
|  UTFis-1-2 | 37°44'15.8244" 113°10'54.7284"W IS4 (Corey fissure) | Tabular comb-textured magnetite-apatite dike cut perpendicular outer margin: Euhedral magnetite (opaque) intergrown with comb-textured euhedral apatite (large clear areas). |
|  UTFis-1-4 | 37°44'15.8244" 113°10'54.7284"W IS4 (Corey fissure) | Tabular comb-textured magnetite-apatite dike cut perpendicular outer margin: Euhedral magnetite (opaque) intergrown with comb-textured euhedral apatite (large clear areas) and minor anhedral interstitial calcite (not visible in hand sample). |
|  UTFis-2-1 | 37°44'15.8244" 113°10'54.7284"W IS4 (Corey fissure) | Tabular comb-textured magnetite-apatite dike cut perpendicular outer margin: Euhedral magnetite (opaque) intergrown with comb-textured euhedral apatite (large clear areas) and actinolite (small acicular crystals along margin), and minor anhedral interstitial calcite (not visible in hand sample). |

* Each image is a digital scan of a polished thin section, 45 x 26 mm. †Location numbers refer to points labeled in Fig. 2.2

**Table 2.3: Representative microthermometric data from high-temperature experiments on polycrystalline inclusions from the Iron Springs and Buena Vista IOA deposits, showing the first melting temperature ($T_{M1}$) and final melting temperature ($T_{Mf}$).**

Note: "n/a" denotes not observed or unclear, and "D" denotes inclusions that decrepitated during heating.

| Melt inclusions: Iron Springs | | | Melt inclusions: Buena Vista | | |
|---|---|---|---|---|---|
| n | $T_{M1}$ °C | $T_{Mf}$°C | n | $T_{M1}$°C | $T_{Mf}$°C |
| 1 | 270 | 840 | 1 | ~200 | 850 |
| 2 | 148 | D | 2 | ~200 | 865 |
| 3 | 73 | D | 3 | ~210 | n/a |
| 4 | 70 | D | 4 | ~290 | 870 |
| 5 | 167 | 785 | 5 | ~270 | 875 |
| 6 | 160 | 786 | 6 | n/a | 850 |
| 7 | 133 | 840 | 7 | ~230 | 875 |
| 8 | n/a | 821 | 8 | n/a | 720 |
| 9 | n/a | 845 | 9 | ~200 | n/a |
| 10 | n/a | 785 | 10 | ~250 | 744 |
| 11 | n/a | 840 | 11 | ~275 | <900 |
| 12 | n/a | 801 | 12 | n/a | <950 |
| 13 | 70 | D | | | |
| 14 | 70 | D | | | |
| 15 | n/a | 790 | | | |
| 16 | n/a | 785 | | | |

**Table 2.4: Representative microthermometric data of aqueous inclusions from the Iron Springs and Buena Vista IOA deposits.**

Table illustrates first melting ($T_{M1}$), ice melting ($T_{Mi}$), salt hydrate melting ($T_{Msh}$), vapor homogenization ($T_{HV}$), and halite melting ($T_{MH}$). Note: n/a = not observed.

| | Aqueous inclusions: Iron springs | | | | | | Aqueous inclusions: Buena Vista | | | | |
|---|---|---|---|---|---|---|---|---|---|---|---|
| n | $T_{M1}°C$ | $T_{Mi}°C$ | $T_{Msh}°C$ | $T_{HV}°C$ | $T_{MH}°C$ | n | $T_{M1}°C$ | $T_{Mi}°C$ | $T_{Msh}°C$ | $T_{HV}°C$ | $T_{MH}°C$ |
| 1 | n/a | -26 | n/a | n/a | n/a | 1 | -78 | -24 | +12 | +115 | +290 |
| 2 | ~-76 | -21 | +4 | n/a | n/a | 2 | -74 | -25 | +12 | +100 | +290 |
| 3 | ~-76 | -21 | +4 | n/a | n/a | 3 | -75 | -24 | +7 | +125 | +295 |
| 4 | n/a | n/a | +6 | n/a | n/a | 4 | -76 | -23 | +12 | +128 | +281 |
| 5 | n/a | n/a | +9 | n/a | n/a | 5 | -70 | -28 | +10 | +115 | +280 |
| 6 | n/a | -21 | n/a | n/a | n/a | 6 | -73 | -24 | +10 | n/a | n/a |
| 7 | ~-70 | n/a | +5 | n/a | n/a | 7 | -72 | -25 | +9 | +110 | +285 |
| 8 | n/a | -24 | +4 | +250 | n/a | 8 | n/a | -24 | n/a | n/a | n/a |
| 9 | n/a | n/a | +6 | +270 | n/a | 9 | -78 | -22 | +7 | +135 | +280 |
| 10 | n/a | -21 | +6 | n/a | n/a | 10 | n/a | n/a | n/a | +135 | +330 |
| 11 | ~-75 | -21 | n/a | n/a | n/a | 11 | -77 | -27 | +11 | n/a | +310 |
| 12 | n/a | -21 | +5 | +240 | +220 | 12 | n/a | n/a | n/a | +100 | +300 |
| 13 | n/a | -25 | +4 | +244 | +230 | 13 | n/a | n/a | n/a | +90 | +305 |
| 14 | n/a | -27 | +5 | +245 | +225 | 14 | n/a | n/a | n/a | +110 | n/a |
| 15 | n/a | n/a | +4.5 | n/a | n/a | 15 | n/a | n/a | n/a | +111 | n/a |
| 16 | n/a | n/a | +6.5 | n/a | n/a | 16 | n/a | -26 | +10 | +120 | +330 |
| 17 | ~-78 | -28 | +10 | n/a | n/a | 17 | n/a | n/a | n/a | +130 | +315 |
| 18 | n/a | -19 | +11 | +250 | n/a | 18 | n/a | n/a | n/a | +125 | +295 |
| 19 | n/a | n/a | +11 | n/a | n/a | 19 | n/a | -22 | n/a | +130 | +290 |
| 20 | n/a | n/a | +12 | n/a | n/a | 20 | -75 | -30 | +9 | +95 | +300 |
| 21 | n/a | n/a | n/a | n/a | +222 | 21 | -80 | -26 | n/a | +100 | +330 |
| 22 | n/a | n/a | n/a | +240 | +222 | | | | | | |
| 23 | n/a | n/a | n/a | n/a | +224 | | | | | | |
| 24 | n/a | n/a | n/a | +245 | +230 | | | | | | |

| Magnetite Ore | | Proximal Limestone | | Distal Limestone | |
|---|---|---|---|---|---|
| $\delta^{13}C$ (PDB) | $\delta^{18}O$ (SMOW) | $\delta^{13}C$ (PDB) | $\delta1^{8}O$ (SMOW) | $\delta^{13}C$ (PDB) | $\delta^{18}O$ (SMOW) |
| -3.7 | 10.6 | -6.1 | 17.9 | -2.6 | 15.0 |
| -3.9 | 11.1 | -6.6 | -2.4 | -2.6 | 20.7 |
| -5.0 | 10.3 | -8.9 | 15.8 | -3.6 | 20.2 |
| -3.3 | 11.5 | -8.7 | 16.3 | -2.7 | 20.9 |
| -3.5 | 11.6 | -6.1 | 1.3 | -2.7 | 20.7 |
| -4.7 | 10.4 | -5.9 | 1.4 | -2.5 | 20.5 |
| -3.5 | 15.8 | -5.9 | 1.7 | -2.4 | 21.0 |
| -5.7 | 11.2 | -6.2 | -1.8 | | |
| -5.6 | 11.1 | -6.4 | -1.7 | | |
| -5.6 | 11.3 | -8.5 | 17.1 | | |
| -6.3 | 12.2 | -8.4 | 16.9 | | |
| -6.5 | 11.4 | -8.7 | 16.6 | | |
| -6.8 | 10.8 | -3.1 | 14.9 | | |
| -6.6 | 11.5 | -6.7 | -3.6 | | |
| -5.8 | 13.9 | -5.7 | -0.2 | | |
| -5.9 | 13.0 | -1.8 | 16.5 | | |
| -11.5 | 12.3 | -1.7 | 16.4 | | |
| -8.5 | 17.3 | | | | |
| -9.7 | 13.9 | | | | |
| -9.8 | 13.6 | | | | |
| -10.9 | 12.0 | | | | |
| -4.7 | 12.2 | | | | |
| -7.5 | 12.9 | | | | |

**Table 2.5: Carbon and oxygen isotopic analyses from Buena Vista.**

Data includes analysis of fresh limestone (distal), limestone along the gabbro-diorite contact

(proximal), and magnetite ore from the Buena Vista system**.**

| Deposit/Location | Host rocks | References |
|---|---|---|
| Wernecke Breccia, Yukon Territory, Canada | Hosted in marine fine-grained sandstone, siltstone, and evaporite-bearing carbonates which are cross-cut by diorite-gabbrodiorite. | 1,2 |
| Bafq district (Chador-Malu, Se-Chahun, Choghart), Iran | Hosted in felsic volcanics, volcanogenic sediment, and evaporite-bearing carbonate and siliciclastic sedimentary rock. | 3-7 |
| Cloncurry district, Australia | Hosted in mafic-felsic volcanic rocks interbedded with siliciclastic and carbonate- and evaporite-bearing metasedimentary rocks. | 8-11 |
| China, Ningwu and Luzong basin | Hosted along the contact between subvolcanic gabbro-diorite and earlier volcanic rocks and evaporite-bearing carbonate and siliciclastic sediments. | 12-16 |
| China, Altay Orogenic belt | Hosted in calc-alkaline meta-volcanic rocks which cross-cut marble-bearing meta-sediments and are associated with mafic intrusive rocks which intrude carbonate strata | 17-19 |
| Peru, Marcona | Occurs mostly as discrete ore bodies which are surrounded by dacite and/or cross-cut metasediments and younger sandstones and limestones. | 20-23 |
| Mexico, Cerro de Mercado | Orebodies are interbedded with and/or cross cut rhyolite volcanic rocks and subvolcanic plutons. | 24 |
| California, Becks Springs | Hosted in limestone strata (either concordant with sedimentary bedding or cuts it at a low angle) which is intruded by diabase and gabbro-diorite dikes. | 25, 26 |
| Chile, El Laco | Orebody occurs as magnetite feeder dikes, strata-bound magnetite bodies interbedded with andesitic flows, and layered hematite-rich ash fall deposits. Mineralization is hosted in a volcanic complex that overlays thick evaporite-bearing sedimentary sequences. | 27-30 |
| Sweden, Kiruna | Ore body hosted in metavolcanics rocks which overlie and crosscut extension-related sequences of volcanics and evaporite-bearing chemical sediments. | 31-34 |

**Table 2.6: List of IOA districts that host iron oxide-apatite mineralization in which geologic context is consistent with anatexis of evaporate-bearing carbonate rocks.**

References are as follows (1) Kendrick et al., 2008; (2) Hunt et al., 2007; (3) Moore et al., 2003; (4) Sabet-Mobarhan-Tala et al., 2015; (5) Torab et al., 2008; (6) Bonvadi et al., 2011; (7) Jami et al., 2007; (8) Bertelli et al., 2010; (9) Baker et al., 2008; (10) Oliver et al., 2004; (11) Perring et al., 2000; (12) Li et al., 2015; (13) Wen et al., 2017; (14) Yu et al., 2015; (15) Yu et al., 2015; (16) Yu et al., 2011; (17) Chai et al., 2014; (18) Chai et al., 2009; (19) Shan et al., 2012; (20) Li et al., 2017; (21) Chen et al., 2011; (22) Chen et al., 2010; (23) Chen et al., 2010; (24) Lyons, 1988; (25) Calzia et al., 1988; (26) Lee et al., 2007; (27) Tornos et al., 2016; (28) Matthews et al., 1996; (29) Broman et al., 1999; (30) Mungall et al., 2018; (31) Frietsch et al., 1997; (32) Martinsson and Virkkunen, 2004; (33) Martinsson, 1997; (34) Gleeson and Smith, 2009

# Chapter 3: Iron oxide-apatite ore formed by Fe-rich sulfate melt at El Laco, Chile

### 3.1 Introduction

The El Laco system is a highly controversial example of the low-Ti magnetite-dominated systems known as Kiruna-type iron oxide-apatite (IOA) deposits. Kiruna-type systems are characterized by massive magnetite-apatite ± actinolite ore bodies, which commonly host overlapping geochemical and textures features suggestive of contrasting orthomagmatic (e.g. flow textures, layered magnetite sinter, vesiculated feeder dikes, columnar jointing) and hydrothermal (e.g massive magnetite replacement zones, comb-textures veins, pervasive alkali-calcic alteration) modes of formation (Nyström and Henríquez, 1994; Barton and Johnson, 1996; Li et al., 2015; Dare et al., 2015; Ovalle et al., 2015; Hofstra et al., 2016; Sillitoe and Burrows, 2002; Velasco et al., 2016; Tornos et al., 2017; Simon et al., 2018). The presence of these features in many systems has led to a robust debate about genetic models for these systems with some arguing for a hydrothermal origin (i.e. ore is formed either by direct precipitation or in-situ replacement by aqueous fluids) while others argue for a magmatic origin, (i.e. ore is crystallized directly from an iron-rich silicate melt, or an immiscible iron-oxide melt). El Laco is central to this debate as the Fe-oxide mineralization in this system has exceptionally well developed volcanic textures and a clear magmatic association but is also characterized by widespread hydrothermal alteration (Tornos et al., 2017). The former features indicate formation via subaerial volcanic-eruptive processes, whereas the latter attest to circulation of hot aqueous fluids. Still, the compositions and contributions of fluids and/or melts in this system are subject to intense debate, which epitomizes the wider debate regarding IOA genesis.

Here, we examine polycrystalline inclusions hosted in diopside-magnetite-anhydrite veins and dikes associated with massive magnetite ore bodies in the El Laco systems and build upon previous work with new compositional and microthermometric data. Diopside-magnetite-anhydrite veins and dikes host abundant assemblages of primary Fe-rich inclusions, representing the fluid(s) present during the formation of this system. Hence, our analyses represent direct sampling of fluids which likely transported and precipitated iron in this system. Analysis of fluid

and melt inclusions from hydrothermal and igneous environments has yielded direct evidence pertaining to the nature and evolution of fluid in these systems. Likewise, the analysis of polycrystalline inclusions from El Laco offers key evidence which illuminates a fundamental and hitherto unrecognize genetic mechanism for this system in which locally derived sulfate-oxide-[carbonate] melts play a central role.

## 3.2 Background

El Laco is a 35 km$^2$, Pliocene (5.3-1.6 Ma, Naranjo et el., 2010) volcanic complex situated in the Central Volcanic Zone (CVZ) in the northern Chilean Andes (Fig 3.1). The complex consists of porphyritic to massive, flow banded andesite and pyroclastic deposits which emanate out from a central volcanic edifice and have igneous textures indicative of subaerial eruptive processes (Sillitoe and Burrows, 2002). The andesites in the complex are compositionally close to trachyandesite and are chemically indistinguishable from the nearby Llullaillaco and Lascar volcanos (Matthews et al., 1994; 1999). The volcanic center is situated in an area that underwent exceptional crustal thickening during the Miocene (Zandt et al., 1994; Allmendinger et al., 1997; Trumbull et al., 1999) and is underlain by the alluvial conglomerates and siltstones of the Oligocene San Vicente formation, the sandstones, mudstones, limestones, and evaporites of late Cretaceous-tertiary Salta group, and Ordovician-Silurian age sedimentary basement rocks (Matthews et al 1996; Tornos et al., 2017). The crustal thickening and successive sequences of sedimentary rock underlaying the complex likely account for significant crustal contamination observed in the andesites in this system (Matthews et al., 1994; Zandt et al., 1994; Trumbull et al., 1999; Velasco et al., 2016).

Magnetite mineralization in the El Laco system is dominantly low Ti (<0.15 wt%), high V (90-2600 ppm), sub-horizontal stratabound orebodies and discordant subvertical feeder dikes which cross-cut the host andesite (Naranjo et al., 2010; Broughm et al., 2017). The stratabound orebodies are interbedded with the andesite flows and form semicircular, lobate structures which project outward from the central volcanic edifice and terminate into feeder dikes which extend under the complex (Velasco et al., 2016). The stratabound ores have abundant volcanic textures including flow structures, vesicles, columnar jointing, scoriaceous surfaces with pahoehoe banding, and pyroclastic deposits (Nyström and Henríquez, 1994; Naslund et al., 2002; LLedó, 2005; Nyström et al, 2016; Tornos et al., 2016). Along their bases, the stratabound ores overlie

brecciated andesite flows cemented with magnetite (Sillitoe and Burrows, 2002). The feeder dikes that connect with the bases of the stratabound orebodies also contain abundant magmatic textures such as columnar jointing, sharp contacts with host rocks, and vesiculated centerlines. In addition, many areas in this system are capped with layered sequences of friable hematite-rich ore that hosts rounded magnetite fragments interpreted to be volcanic bombs (Nyström and Henríquez, 1998).

Hydrothermal alteration forms a pervasive overprint throughout ~30-40% of the complex (Tornos et al., 2017) and consists of late acid alteration that overprints earlier alkali-calcic and propylitic alteration assemblages. The Alkali-calcic alteration is characterized by pervasive albitization and replacement of primary augite and enstatite-pigeonite by diopside and magnetite. In many cases (e.g., Pasos Blancos and Laco Norte), the alkali-calcic alteration is focused on areas showing pervasive brecciation, wherein fragments of host andesite are surrounded or replaced by course-grained diopside, anhydrite, Ti-poor magnetite, and scapolite. Alkali-calcic alteration is in turn overprinted by pervasive K-Ca alteration characterized by assemblages rich in sanidine, diopside, magnetite, scapolite, fluorapatite, and minor magnetite (Tornos et al., 2017).

Massive stratabound ore bodies, feeder dikes and zones of alkali-calcic alteration are commonly cross-cut by diopside-magnetite-anhydrite "veins." These veins are texturally similar to pegmatite dikes in that they contain well-developed unidirectional solidification textures defined by coarse, euhedral, graphic-textured diopside and magnetite that appear to have grown inward perpendicular to the vein margins that are in sharp contact with the heavily altered igneous host rocks. Along the central axis of each vein, diopside and magnetite are in contact with anhedral anhydrite with accessory pyrite and albite. These veins are the subject of the present study, and all of the crystalline phases observed within them host abundant assemblages of primary inclusions. Samples were collected via exploration drilling from a depth of ~200 m near the Pasos Blanco breccia pipe in the central region of the El Laco volcanic complex. Veins in this area occur along the upper boundary of a massive magnetite ore body and appear to be entirely intrusive, lacking a connection to or association with the magnetite feeder zones which grade into the extrusive, stratabound ore bodies near the surface. Furthermore, vein-hosted magnetite described in this study contains well-developed ilmenite exsolution lamellae and are identical to the "magnetite-α" variety identified by Ovalle et al. (2018). This magnetite is

inferred to be the "most magmatic" in character, on account of having the highest trace element content and being compositionally similar to magnetite found in orthomagmatic settings (Ovalle et al., 2018; Dare et al., 2015). This variety of magnetite is characterized by aggregates of titanomagnetite with well-developed ilmenite exsolution lamellae that are visible in EDS maps (Fig. 3.2).

## 3.3 Methods

### 3.3.1 Inclusion petrography and microthermometry

Diopside-magnetite-anhydrite samples examined in this study were prepared into doubly polished thick sections with an approximate thickness of 100-150 μm and examined using a petrographic microscope. Most of the data shown herein are from samples designated as LCO-252 and LCO-253. Inclusion petrography followed the methods described by Goldstein and Reynolds (1994) and focused on grouping inclusions into temporally distinct primary and secondary fluid inclusion assemblages (FIAs). The diopside- and albite-hosted polycrystalline inclusions characterized in this study were readily apparent from their granular appearance and birefringence in cross polarized light, which contrasted with that of the host (Fig. 3.3 c). Feldspar-bearing inclusions were differentiated from accessory albite mineral inclusions hosted in diopside on the basis of the presence of multiple phases and an unambiguous vapor phase. Petrography and chemical micro-analyses mostly focused on inclusions hosted in diopside and accessory albite, as these were the most abundant translucent phases that hosted clearly defined FIAs. However, observations were also recorded from inclusions hosted in magnetite and apatite, as these phases also host inclusions with similar phase assemblages as those observed in diopside and albite.

No aqueous liquid-rich inclusions were observed in this study and polycrystalline inclusions lacked a clear aqueous liquid phase at room temperature. As a result, low temperature (<0 °C) microthermomemtry was not conducted. All microthermometric observations were made between 20-1150°C using a Linkam TS1400XY stage calibrated using the critical point of $H_2O$, the α/β transition of quartz at 574 °C, and the melting point of NaCl at ~ 1bar (801 °C). Estimated precision and accuracy of the measurements at temperatures >500 °C is ±1 °C. Sample chips were heated only once in a continuous ramp at a rate of 10-30 °C/minute. Lower rates were

used when temperature was approaching that of the observed phases changes.  Results of microthermometric analysis are shown in table 3.1.

### 3.3.2 Raman Spectroscopy

Raman spectroscopy was used to identify individual phases in polycrystalline inclusions. At least 15 individual analysis were done of each inclusion to ascertain the phases present and constrain their spatial distribution and abundance. The Raman system consisted of a Thermo DXR2 dispersive Raman microscope and a 532nm laser with power range 0.1 – 10 coupled with a conventional microscope with x10 or x50 or x100 objectives. All reported Raman spectra in this study were collected using the x100 objective and a spot size of 0.7 µm. All spectra were acquired on unoriented grains using a laser power of 20 mW and two to three, 10-30 s exposures summed to the final reported spectra. Baseline subtraction and background reduction were applied using the and Fityk™ software package. Spectra were interpreted using the RRUFF database (Lafuente et al., 2016). High fluorescence background was not normally an issue during analysis, but when observed a fluorescence correction was applied using the Omnic spectral analysis software.

### 3.3.3 Scanning Electron Microscope – Energy Dispersive Spectroscopy (SEM-EDS)

Back-scattered electron (BSE) images, and energy-dispersive spectroscopy (EDS) were used to analyze the compositions of crystalline phases and solid residues in polycrystalline inclusions exposed at the sample surface by polishing (either intentional exposure subsequent to identification of an inclusion, or accidental exposure of inclusion in well-defined assemblages during sample preparation). The analyses were conducted at the Department of Earth and Atmospheric Sciences at the University of Alberta. The system consisted of a Zeiss EVO SEM with a LaB6 electron source and Bruker energy dispersive X-ray spectrometer (EDS) system with a silicon drift detector. The resolution was 123 eV and the window area was 10 mm$^2$. Analyses were carried out in variable pressure mode with a 100 µm aperture, an acceleration voltage of 20-25 kV, a beam current of 225-275 pA, and a 7-8.5 mm working distance. EDS

Element maps were collected using collection times of 10-30 min. None of the samples were carbon coated for this analysis.

## 3.4 Results

The samples examined in this study are dominantly composed of diopside, albite, and minor apatite intergrown with euhedral to subhedral magnetite. Diopside and albite host densely packed FIAs of primary (Fig. 3.4 a,b) and secondary (Fig. 3.4 c,d) inclusions ranging in size from 5 to 40 μm and commonly showing a characteristic negative crystal shape. Primary inclusions occur in two main compositional types, with paragenetically older inclusions having compositions more enriched in silicate components, whereas paragenetically younger inclusions exhibit more sulfate-rich compositions as described in more detail below.

Feldspar-bearing inclusions are composed primarily of anhydrite (~45 vol%), potassium feldspar (~20 vol%), albite (~20 vol%), quartz (~5 vol%), and Fe-Ti oxide (~5-15 vol%, either as mixed or discrete phases) (Fig 3.3 a,b;). Based on the relative phase proportions, the aggregate composition of the silicate phases in feldspar-bearing inclusions appears to be approximately rhyolitic with ~70-74% $SiO_2$. These inclusions appear to be paragenetically oldest and occur mostly in the cores of diopside crystals, where they are interspersed with clusters of coeval anhedral albite mineral inclusions. In backscatter electron (BSE) images, the silicate-dominated portions of these inclusions commonly show a pitted appearance. In EDS maps, individual pits contain high concentrations of Cl and are interpreted to represent halite crystals interspersed throughout each inclusion. In addition, areas rich in anhydrite commonly have an excavated appearance in BSE images but contain sulfate residue as well as significant P.

Inclusions lacking feldspar are composed of anhydrite (~70-75 vol%), hematite (~5-15 vol%), and additional alkali sulfate minerals (e.g. $Na_2Ca(SO_4)_2$) along with a vapor phase which fills the interstitial space between the translucent crystalline phases (Fig. 3.4 e). Raman analysis of the vapor phase in these inclusions showed no evidence of $CO_2$, $H_2S$, or $CH_4$. Primary FIAs of these inclusions occur either throughout the diopside host or in broad zones around the periphery of the host crystal (Fig. 3.4 b,d). Polycrystalline anhydrite-bearing inclusions also occur in secondary FIAs as discrete fracture-filling linear arrays which cross-cut primary assemblages (Fig. 3.4　c,d). Inclusions in secondary FIAs are identical to those observed in primary FIAs in terms of their phase ratios and physical shape/size, but are distinctive in that they occur together

with coeval vapor-rich inclusions in the same FIAs. Vapor-rich inclusions were not observed in any primary assemblages. While primarily observed in diopside, these inclusions were also observed in apatite and contained additional phases including allanite and natrite (Fig. 3.5).

Albite crystals intergrown with diopside and magnetite also contain abundant feldspar-bearing inclusions which have a similar phases assemblage to those observed in diopside. These latter inclusions are distinctive in that they have a more sinuous shape, lack albite as a discrete phase, and commonly contain pyrite in addition to Fe-Ti oxides (Fig. 3.3 a,c ). Also, the potassium feldspar in albite-hosted $PI_F$ inclusions does not occur as a single discrete subhedral-euhedral crystal as it does in diopside-hosted in feldspar-bearing inclusions, but instead appears to encapsulate a central region rich in sulfate, phosphate, chloride, iron and titanium. Furthermore, identical inclusions are also hosted in magnetite and contain distinct phases with compositions suggesting albite, anhydrite, phosphate, and magnesium-rich Ilmenite (Fig. 3.5) in the same volume proportions as those observed in diopside.

No aqueous liquid-rich inclusions were observed in this study, but have been previously reported by Broman et al. (1999) as being late stage and associated with polycrystalline inclusions rich in anhydrite and halite. Broman et al. (1999) also reported a continuum between aqueous and polycrystalline inclusions which might indicate a transition to hydrothermal condition later in the evolution of the El Laco system, which would coincide with the formation of alkali-calcic alteration.

High temperature microthermometry of feldspar-bearing and feldspar-absent inclusions showed consistent behavior, both within individual assemblages and between different assemblages and host minerals, and therefore are described together here (Fig. 3.6). The onset of melting was observed between ~400 and 470 °C and was apparent from the change in the shape and distribution of individual crystalline phases and the subtle coalescence of the vapor phase into a discrete rounded shape along the inclusions inner wall. With continued heating, the translucent portions of the crystal shrank, demonstrating that the bulk of the inclusions consisted of a single translucent phase (identified as anhydrite prior to heating via Raman analysis) along with 1-2 additional translucent crystals, an opaque crystal, and a vapor bubble. Final melting of all translucent crystalline phases occurred between 694-769 °C (median 724 °C) in primary inclusions and between 700-784 °C (median 782 °C) in secondary inclusions. Within any individual assemblage, the maximum range in final melting temperatures never exceeded 47 °C.

In many inclusions, opaque phases did not completely homogenize even at high temperatures. This is a common observation in silicate melt inclusions, and is commonly indicative of outward $H^+$ diffusion, which renders contents of the inclusion more oxidized and refractory than the original trapped liquid (Audétat and Günther, 1999). However, complete homogenization of opaque phases did occur in a limited number of inclusions, and was within 50 °C of the final melting temperature of the translucent phases. Liquid-vapor homogenization was difficult to observe due to reduced optical clarity of the host phases at temperatures >800 °C. However, when observed, liquid-vapor homogenization was variable and mostly occurred between 800 and 951 °C. These temperatures are in good agreement with temperatures of crystallization for pyroxenes (800-890 °C) in the El Laco systems determined via two pyroxene geothermometry (Naslund et al., 2002) and overlap the lower range of temperatures determined via $\Delta_{mt\text{-}di}$ oxygen isotope fractionation (900-1125 °C; Tornos et al., 2016). Upon quenching from high temperatures, the inclusions became granular in appearance, likely indicating the formation of a crystalline aggregate rather that a homogenous glass.

## 3.5 Discussion and conclusion

The volumetrically consistent phase assemblages and tightly constrained melting behavior of primary and secondary FIAs of polycrystalline inclusions provide strong evidence for the trapping of a homogenous liquid at magmatic conditions during the crystallization of magnetite, diopside, albite, and apatite in the El Laco system. Similar observations of polycrystalline inclusions in magmatic settings have been interpreted as direct evidence of the entrapment of aliquots of melt at high temperatures during the crystallization of phases in an igneous environment (Rodder, 1992). Here, too, we interpret the polycrystalline inclusions observed in El Laco as evidence of the formation of this system in an igneous setting and in association with orthomagmatic melts. However, the melts associated with the El Laco systems are distinctive in terms of their chemical compositions, which are dominantly sulfate-oxide±silicate with minor carbonate (as evidenced by the presence of natrite). In addition, phosphate and chloride also appear to be major constituents. Based on paragenetic relationships, feldspar-bearing inclusions appear to have been trapped early during the initial crystallization of diopside and albite, followed by the entrapment of inclusions which lack a significant silicate component. This was followed by the subsequent formation of fractures and the entrapment of

secondary FIAs of feldspar-absent polycrystalline as well as vapor-rich inclusions, likely in response to a decrease in pressure.

Key points of contention in our current understanding of the El Laco system include the nature of mineralizing fluids involved in iron transport, and the textural and geochemical observations that suggest contrasting orthomagmatic versus hydrothermal mechanisms of formation (Nyström and Henríquez, 1994; Sillitoe and Burrows, 2002; Dare et al., 2015; Ovalle et al., 2015; Velasco et al., 2016; Tornos et al., 2017; Simon et al., 2018). In considering the diversity of genetic models proposed for this system, one might consider how the fluid media invoked in the transport and precipitation of Fe in these models would be preserved. In the case of magmatic-hydrothermal models, the mineralizing fluid would be preserved as Fe-rich aqueous fluid inclusions in ore stage mineralization, similar to the halite- and chalcopyrite-bearing aqueous fluid inclusions observed in porphyry Cu deposits. Similarly, mineralizing fluids in orthomagmatic models involving immiscibility between Fe-P and silicate melts would be preserved as coeval silicate and Fe-rich melt inclusions. Aqueous, halite-bearing inclusions have been reported at El Laco (Broman et al 1999), and along with the pervasive hydrothermal alteration, provide evidence that aqueous fluids were present in this system at some point in its evolution. However, where reported, these inclusions appear to be late stage, and rarely show evidence of enrichment in Fe (i.e. Fe-oxide was rarely observed as part of a consistent room-temperature phase assemblage). Moreover, the hydrothermal alteration appears to overprint the system, and does not appear to be directly related to the formation of the magnetite ore bodies themselves (Tornos et al., 2017). This argues against a central role of aqueous fluids as a key medium for mobilizing and precipitating iron in this system. Aqueous fluids may contain up to several weight percent iron in the form of $FeCl_2$ at magmatic temperatures (Simon et al., 2004; Bell and Simon, 2011), but questions remain as to the mechanism of oxidizing $Fe^{2+}$ at the site of iron mineralization and/or mobilizing $Fe^{3+}$ in aqueous solution. In other studies, silicate glasses and aggregates of Fe-oxide, apatite and pyroxene occur as irregular masses along the boundaries of plagioclase crystals or as globules in resorbed plagioclase phenocrysts (Nasland et al., 2009; Tornos et al., 2016; Velasco et al.,2016, Tornos et al., 2017). On the basis of textural features, these have been interpreted as melt inclusions showing evidence for immiscibility between alkali-silicate melt formed as a result of the assimilation of P- and S-rich rocks (Larocque et al., 2000; Lledo, 2005). However, to our knowledge no coeval rhyolite and Fe-P melt inclusions that

display high-temperature melting behavior consistent with entrapment as two immiscible melts have been observed in mineral phases intergrown with the magnetite in this system. Furthermore, while several studies have demonstrated that conditions which might allow for the generation of Fe-P melts might occur at reasonable geologic temperatures (Lledo, 2005, Veksler, 2009; Hou et al., 2018), the existence of such melts remains controversial (Lindsey and Epler, 2017).

The data presented here indicate that the fluids involved in mobilizing and precipitating Fe-oxide in the El Laco system are neither aqueous chloride solutions, nor Fe- P melts. Rather, the main Fe-rich fluid hosted in the IOA mineralization in this system appears to have been an orthomagmatic fluid that evolved from an earlier composition dominated by silicate and sulfate to a later composition in which silicate is apparently absent. The key rationale underpinning this interpretation is that these inclusions 1) appear to be ubiquitously associated with primary Fe mineralization throughout the El Laco system; and 2) universally contain 5-15 vol% Fe-oxide and/or Fe-sulfide. This interpretation begs the question of the origin of the sulfate melts. One possibility is that the sulfate is a primary igneous component which became saturated in the melt over time as a result of fractionation. The fact that anhydrite is observed as a primary phase in dacitic pumice flows from the nearby Lascar volcano NW of El Laco (Matthew et al. 1994) might support this interpretation. However, sulfate is a major constituent of the mineralization at El Laco (Matthews 1993, Tornos et al., 2016) and can be up to 20 vol% of the mineralization and possibly higher in the diopside-magnetite-anhydrite veins that crosscut the ore body. While anhydrite can certainly occur as a primary igneous phase (Hutchinson and Dilles, 2019), it would be highly unusual for a magmatic system to fractionate towards a primary melt composition corresponding to a modal mineralogy of up to 20 vol% sulfate (Blount and Dickson, 1969). In addition, alkali sulfate species are highly soluble in aqueous chloride solutions at temperatures >750°C (Newton and Manning, 2005), which indicates that sulfate derived from an intermediate-felsic melt would likely be stripped from the melt as it underwent degassing. Instead, we posit that the abundant anhydrite in the veins, volcanic deposits, and melt inclusions described here results from the anatexis and assimilation of evaporite-bearing sediments by the andesite magmas during the formation of the volcanic system associated with the Fe mineralization. The assimilation of crustal sediments by magmas in the El Laco systems is robustly supported by a number of lines of evidence including systematic [18]O enrichment and high Zr and Nb content of host andesites (Harmon et al, 1984, Velasco et al., 2016), $^{87}Sr/^{86}Sr$ and $\varepsilon_{Ndi}$ signatures suggesting

magnetite ores have a more crustal signature than host andesites (Tornos et al., 2011;2017), and sedimentary xenoliths hosted in eruptive products of the nearby Lascar volcano (Matthews et al., 1996). Moreover, Tornos et al (2017) suggests that the ore-forming fluids are related to an "as yet undiscovered batch of highly contaminated igneous rock" which formed via interaction with the evaporite-bearing Salta Group which underlies the El Laco volcanic complex. The anatexis and assimilation of evaporite-bearing sediments would undoubtedly have led to the formation of such a reservoir of igneous rock, and the data presented here provide evidence in support of that process.

Experimental data show that in alkali-sulfate systems (i.e. $Na_2SO_4$-$CaSO_4$), melting can occur as low as 900 °C (Freyer et al., 1998; Freyer and Voigt, 2003;) and likely lower in the presence of excess $H_2O$ and NaCl and at higher pressures (Newton and Manning, 2005; Blount and Dickson, 1969). This is at or above the wet solidus temperatures of model silicate systems at low pressures (Tuttle and Bowen, 1958), which implies that anatexis of the evaporite units associated with the El Laco system could have occurred in response to the intrusion of the andesitic melt, either via heat flux or direct assimilation. This temperature is also at or below the temperature range of formation of diopside-magnetite-anhydrite veins inferred from $\Delta_{mt\text{-}di}$ oxygen isotope fractionation (900-1125°C; Tornos et al., 2016) and in the vicinity of liquid-vapor homogenization temperature of polycrystalline inclusions reported here. In addition, experimental evidence shows that at high $f_{O2}$, anhydrite can exist in equilibrium with andesitic-dacitic melt at 800-1040°C (Carroll and Rutherford 1987) and that Fe and other base metals would be strongly partitioned into the sulfate-rich phase (Lovering, 1982). This suggests that a sulfate melt in equilibrium with an andesitic melt would likely become highly enriched in Fe over time and thus become an effective medium for iron transport. Sulfate would also act as an oxidant, which would buffer the magmatic system at high $f_{O2}$ and account for the occurrence of $Fe^{3+}$ as the dominant iron species in the IOA ore (Wen et al., 2017). Taken together, these lines of evidence suggest that the conditions necessary to generate an Fe-rich sulfate melt existed in the El Laco system, and that such a process would account both for the orthomagmatic features and oxide-dominated nature of the mineralization in this system.

Evidence for the successive 1) mingling of sulfate melt with the andesite magmas, 2) accumulation of sulfate melt over time, and 3) generation of aqueous fluid via degassing of the sulfate melt can be found in the petrographic relationships between inclusions types presented

here. The formation of Fe-rich sulfate melts in the El Laco system starts with the assimilation of sedimentary material rich in anhydrite, potentially as well as halite and carbonate-evaporite layers, by andesitic melt during the formation of the volcanic complex (Fig. 3.7). This would have led to the formation of a sulfate-rich liquid, and/or assimilation and intermingling of sulfate within the intruding silicate melt. Such intermingling/assimilation is recorded by the feldspar-bearing inclusions observed in the cores of diopside and albite crystals described here. The breakdown of sulfate would have led to the oxidation of the silicate liquid and in turn driven the production of $Fe^{3+}$. With continued oxidation of the igneous system, the sulfate could have stably coexisted in equilibrium with the silicate melt, becoming more enriched in Fe, and being entrapped in crystalline phases as inclusions which are dominantly anhydrite and lack a significant silicate component. This interaction between the silicate melt and the sulfate liquid is recorded by O isotopes which indicate broad equilibration between the magnetite ore and the andesite in this system (Harmon et al., 1984; Tornos et al., 2016) and Fe isotopes and magnetite chemistry which suggest a magmatic origin for the magnetite mineralization (Knipping et al., 2015, Tornos et al., 2017). Over time, this sulfate-rich melt would have been extruded along with the coexisting silicate melt to form the sulfate-rich Fe-oxide flows interbedded with andesite (Tornos et al., 2017). With continued anatexis, the volume of sulfate melt would likely have increased and led to the formation of the diopside-magnetite-anhydrite veins that cross-cut the ore bodies. Subsequent cooling, depressurization, and degassing of the melt would have led to the generation of $H_2O$ vapor (trapped as vapor inclusions) and/or saline aqueous fluid which drove the formation of overprinting alkali-calcic and acid alteration (Fig. 3.7).

While seemingly novel, the observations presented here are by no means unique to the El Laco system. Recent studies of inclusions in IOA systems in Iron Springs, Utah and Buena Vista, Nevada (described in Chapter 2) have found similar observations, with the main difference being that the melts in those latter systems have higher concentrations of carbonate compared to the melts described here. Both latter systems exhibit textural features suggestive of an orthomagmatic origin like those observed in El Laco (e.g., columnar magnetite, vesiculated magnetite ore, dike-like magnetite bodies which cross-cut stratigraphy, etc.). In the case of Iron Springs, sulfate-[carbonate] melt inclusions identical to those described here are pervasive through the magnetite ore bodies (Bain et al., 2020; chapter 2). In the case of Buena Vista, melt inclusions are dominated by carbonates, but nonetheless contain abundant Ti and Fe-oxide (Bain

et al., 2020; chapter 2). Each of these IOA systems is associated with intrusive igneous complexes which cross-cut evaporite deposits and likely assimilated evaporite-bearing sedimentary rock; and indeed, so are many other IOA deposits around the world (Li et al., 2015; Wen et al., 2017; Bain et al., 2020). Hence, we argue that it is no coincidence that the primary ore-forming fluid phase in each of these systems is an unusual sulfate±carbonate-rich melt. Rather, these observations all point to a common model in which the anatexis and assimilation of evaporite-bearing sedimentary rocks plays a key role.

## 3.6 References

Allmendinger, R.W., Jordan, T.E., Kay, S.M., and Isacks, B.L., 1997, The evolution of the Altiplano-Puna plateau of the Central Andes: Annual Review of Earth and Planetary Sciences, v. 25, p. 139–174.

Audétat, A., and Günther, D., 1999, Mobility and $H_2O$ loss from fluid inclusions in natural quartz crystals: Contributions to mineral petrology, v. 137, p. 1-14.

Bain, W.M., Steele-MacInnis, M., Li, K., Li, L., Mazdab, F.K., and Marsh, E.E., 2020, A fundamental role of carbonate-sulfate melts in formation of iron oxide-apatite deposits, Nature Geoscience , *in press*

Barton, M.D., and Johnson, D.A., 1996, Evaporitic source model for igneous-related Fe oxide–(REE–Cu–Au–U) mineralization: Geology, v. 24, p. 259–262.

Barton, M.D., 2014, Iron Oxide(-Cu-Au-REE-P-Ag-Co) Systems: *In* Treatise on Geochemistry 2nd Edition, 515-541

Bell, A., and Simon, A.C., 2011, Evidence for the alteration of the $Fe3+/\sum Fe$ of silicate melt caused by the degassing of chlorine-bearing aqueous volatiles: Geology, v. 39, p. 499–502

Blount, C.W., and Dickson, W., 1969, The solubility of anhydrite ($CaSO4$) in $NaCl-H2O$ from 100 to 450°C and 1 to 1000 bars: Geochimica et Cosmochimica Acta, v. 33, p. 227-245

Broman, C., Nyström, J.O., Henriquez, F., and Elfman, M., 1999, Fluid inclusions in magnetite-apatite ore from a cooling magmatic system at El Laco, Chile: Journal of the Geological Society of Sweden, v. 121, p. 253–267.

Broughm, S., Hanchar, J.M., Tornos, F., Attersley, S., and Westhues, A., 2017, Mineral chemistry of magnetite from magnetite-apatite ores and their host rocks in Sweden and Chile: Mineralium Deposita, v. 52, p. 1223-1244.

Carroll, M.R., and Rutherford, M.J., 1987, The stability of igneous anhydrite: experimental results and implications for sulfur behavior in the 1982 El Chichon trachyandesite and other evolved magmas: Journal of Petrology, v. 28, p. 781–801.

Dare, S.A.S, Barnes, S. and Beaudoin, G., 2015, Did the massive magnetite "lava flows" of El Laco (Chile) form by magmatic or hydrothermal processes? New constraints from magnetite composition by LA-ICP-MS: Mineralium deposita, v. 50, p. 607-617.

Freyer, D., Voigt, W., and Köhnke, K., 1998, The phase diagram of the systems $Na_2SO_4$-$CaSO_4$: European Journal of Solid-State inorganic Chemistry. v. 35. p. 595-606.

Freyer, D., and Voigt, W., 2003. Crystallization and phase stability of $CaSO_4$ and $CaSO_4$-based salts: Chemical Monthly., v. 134, p. 693-719.

Goldstein, R. H., and Reynolds, T. J., 1993, Systematics of Fluid Inclusions in Diagenetic Minerals: SEPM Society for Sedimentary Geology.

Harmon, R., et al., 1984, Regional 0-, Sr-, and Pb-isotope relationships in late Cenozoic calc-alkaline lavas of the Andean Cordillera: Journal of the Geologic Society of London, v.141, p. 803–822.

Hofstra, A.H. *et al.,* 2016, Mineral thermometry and fluid inclusion studies of the Pea Ridge iron oxide-apatite-rare Earth element deposit, Mesoproterozoic St. Francois Mountains terrane, Southeast Missouri, USA: Economic Geology, v. 111, p. 1985-2016

Hou, T. *et al.,* 2018, Immiscible hydrous Fe-Ca-P melt and the origin of iron oxide-apatite ore deposits: Nature Communications. v. 9, p. 1-7

Johnson, D. A., and Barton, M. D., 2000, Time-space development of an external brine-dominated, igneous-driven hydrothermal system; Humboldt mafic complex, western Nevada: Society of Economic Geologists Guidebook Society of Economic Geologists Guidebook Series. v. 32, p. 127-144.

Lafuente, B., Downs, R. T., Yang, H., and Stone, N., 2016, the power of databases: The RRUFF project: in *Highlights in Mineralogical Crystallography*. 1-29.

Larocque, A.C.L., Stimac, J.A., Keith, J.D., and Huminicki, M.A.E., 2000, Evidence for open-system behavior in immiscible Fe-S-O liquids in silicate magmas: Implications for

contributions of metals and sulfur to ore-forming fluids: Canadian Mineralogist v. 38, p. 1233-1249.

Li, W., Audétat, A., and Zhang, J. 2015, The role of evaporites in the formation of magnetite–apatite deposits along the Middle and Lower Yangtze River, China: Evidence from LA-ICP-MS analysis of fluid inclusions: Ore Geology Reviews, v. 67, p. 264-278.

Lindsley, D., and Epler, N., 2017, Do Fe-Ti-oxide magmas exist? Probably not!: American Minerologist, v. 102, p. 2157–2169.

Lledo, H.L., 2005, Experimental Studies on the origin of iron deposits; and mineralization of Sierra La Bandera, Chile: unpub Dissertation, State University of New York at Binghamton. 271p.

Lovering, D.G., 1982, Molten Salt Technology

Matthews, S.J., 1993, El Laco magnetite lava, northern Chile: A REE-bearing iron oxide-phosphate magma. In: Rare earth minerals: chemistry, origin and ore deposits: p. 81–82. Mineralogical Society of Great Britain and Ireland and the Natural History Museum, London, Abstracts, 1-2 April 1993.

Matthews, S.J., Jones, A.P., and Beard, A.D., 1994, Buffering of melt oxygen fugacity by sulphur redox reactions in calc-alkaline magmas: Journal of the Geological Society, London v. 151, p. 815–823.

Matthews, S.J., Marquillas, R.A., Kemp, A.J., Grange, F.K., and Gardeweg, M.C., 1996, Active skarn formation beneath lascar volcano, northern Chile: a petrographic and geochemical study of xenoliths in eruption products: Journal of metamorphic geology. v.14, p. 509–530.

Matthews, S., Sparks, R., and Gardeweg, M., 1999, The Piedras Grandes-Soncor eruptions, Lascar ulcano, Chile: evolution of a zoned magma chamber in the Central Andean upper crust: Journal of Petrology. v. 40, p. 1891–1919.

Naslund, H.R., Henriquez, F., Nystr.m, J.O., Vivallo, W., and Dobbs, F.M., 2002, Magmatic iron ores and associated mineralisation; Examples from the Chilean High Andes and Coastal Cordillera, in Porter, T.M., ed., Hydrothermal Iron Oxide Copper-Gold and Related Deposits: A Global Perspective, Volume 2: Adelaide, Australia, PGC Publishing, p. 207–226.

Naranjo, J.A., Henríquez, F., and Nyström, J.O., 2010, Subvolcanic contact metasomatism at El Laco Volcanic Complex, Central Andes: Andean Geology, v. 37, p. 110–120.

Newton, R.C., and Manning, C.E., 2005, Solubility of Anhydrite, CaSO4, in NaCl-H2O solutions at high pressure and temperatures: applications to fluid-rock interactions: Journal of Petrology, v. 46, p 701-716.

Nyström, J. O. and Henríquez, F., 1994, Magmatic features of iron ores of the Kiruna type in Chile and Sweden: ore textures and magnetite geochemistry: Economic Geology. v. 89, p. 820–839.

Nyström, J.O., Henríquez, F., Naranjo, J.A., and Naslund, H.R., 2016, Magnetite spherules in pyroclastic iron ore at El Laco, Chile: American Mineralogist, v. 101, p. 587–595.

Ovalle, J.T. et al., 2018, Formation of massive iron deposits linked to explosive volcanic eruptions: Scientific Reports. v. 8. p. 1-11.

Roedder, E., 1992: Fluid inclusion evidence for immiscibility in magmatic differentiation: Geochimica et Cosmochimica Acta, v. 56, p. 5–20.

Sillitoe, R.H., and Burrows, D.R., 2002, New field evidence bearing on the origin of the El Laco magnetite deposit, northern Chile: Economic Geology and the Bulletin of the Society of Economic Geologists, v. 97, p. 1101–1109.

Simon, A.C., Pettke, T., Candela, P.A., Piccoli, P.M., and Heinrich, A.H., 2004, Magnetite solubility and iron transport in magmatic-hydrothermal environments: Geochimica et Cosmochimica Acta, v. 68, p. 4905–4914.

Simon, A. et al., 2018, Kiruna-type iron oxide-apatite (IOA) and iron oxide copper-gold (IOCG) deposits form be a combination of igneous and magmatic-hydrothermal processes: evidence from the Chilean iron belt: Society of Economic Geologist special publications, v. 21, p. 89-114.

Tornos, F., Velasco, F., Morata, D., Barra, F., and Rojo, M., 2011, The magmatic hydrothermal evolution of the El Laco deposit as tracked by melt inclusions and isotope data*: in* Barra, F., Reich, M., Campos, E., Tornos, F. (Eds.), Let's Talk Ore deposits, p. 345–3.

Tornos, F., Velasco, F., and Hanchar, J., 2016, Iron-rich melts, magmatic, magnetite, and superheated magmatic-hydrothermal systems: The El Laco deposit, Chile: Geology, v. 44, p. 427–430.

Tornos, F., Velasco, F., and Hanchar, J. M., 2017, The magmatic to magmatic hydrothermal evolution of the El Laco deposit (Chile) and its implications for the genesis of magnetite-apatite deposits: Economic Geology, v. 112, p. 1595–1628.

Trumbull, R.B., Wittenbrink, R., Hahne, K., Emmermann, R., Busch, W., Gerstenberger, H., and Siebel, W., 1999, Evidence for late Miocene to Recent contamination of arc andesites by crustal melts in the Chilean Andes (25–26°S) and its geodynamic implications: Journal of South American Earth Sciences, v. 12, p. 135–155.

Tuttle, O. F., and N. L. Bowen, 1958, Origin of granite in the light of experimental studies in the system $NaA1Si_3O_8$-$KA1Si_30_8$-$SiO_2$-$H_2O$: Geologic Society of America, v. 74, p. 153.

Veksler, I.V., 2009, Extreme iron enrichment and liquid immiscibility in mafic intrusions: experimental evidence revisited: Lithos. v. 111, p. 72-82.

Velasco, F., Tornos, F. and Hanchar, J.M., 2016, Immiscible iron- and silica-rich melts and magnetite geochemistry at the El Laco volcano (northern Chile): Evidence for a magmatic origin for the magnetite deposits: Ore geology reviews. v. 79, p. 346-366.

Wen, G., Bi, S., and Li, J., 2017, Role of evaporitic sulfates in iron skarn mineralization: a fluid inclusion and sulfur isotope study from the Xishimen deposit, Handan-Xingtai district, North China Craton: Mineralium Deposita. v. 52, p. 495-514.

Zandt, G., Velasco, A.A., and Beck, S.L., 1994, Composition and thickness of the southern Altiplano crust, Bolivia: Geology, v. 22, p. 1003–1006.
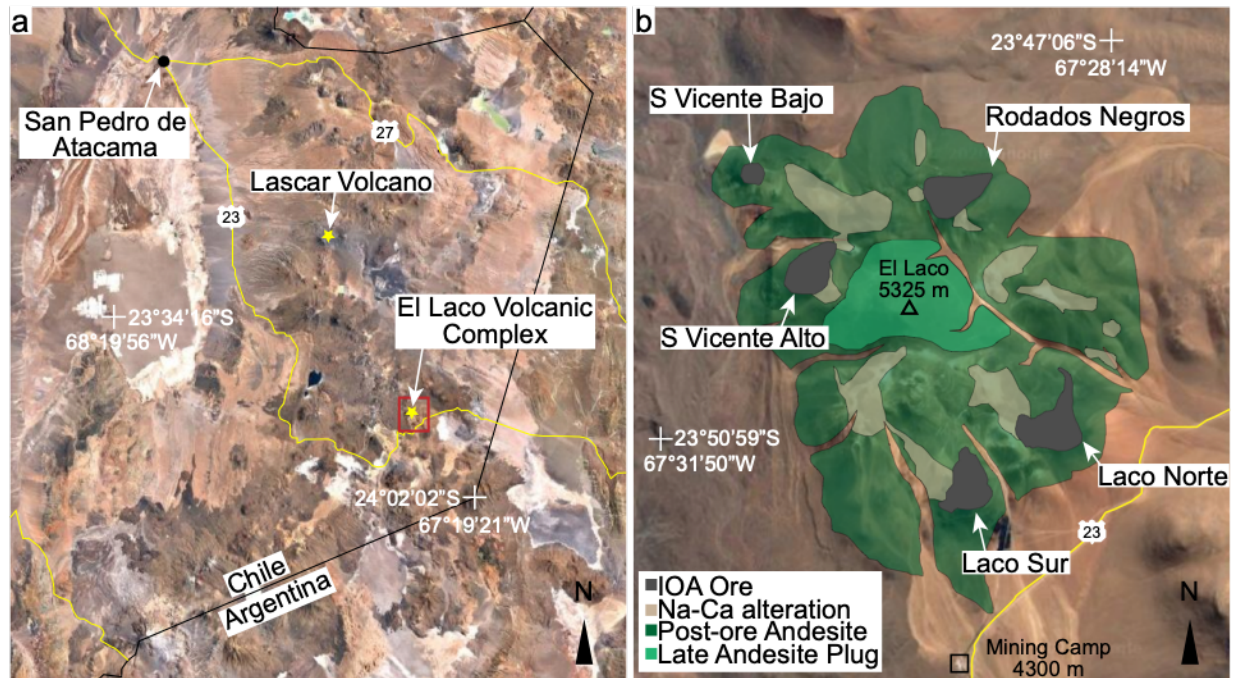
**Figure 3.1: Satellite photo and geologic map of the El Laco system**

(a) Satellite photo showing the Laco Volcanic Complex relative to the Lascar Volcano. (b) Satellite photo of El Laco Volcanic Complex with overlaid geologic map (after Tornos et al., 2016)
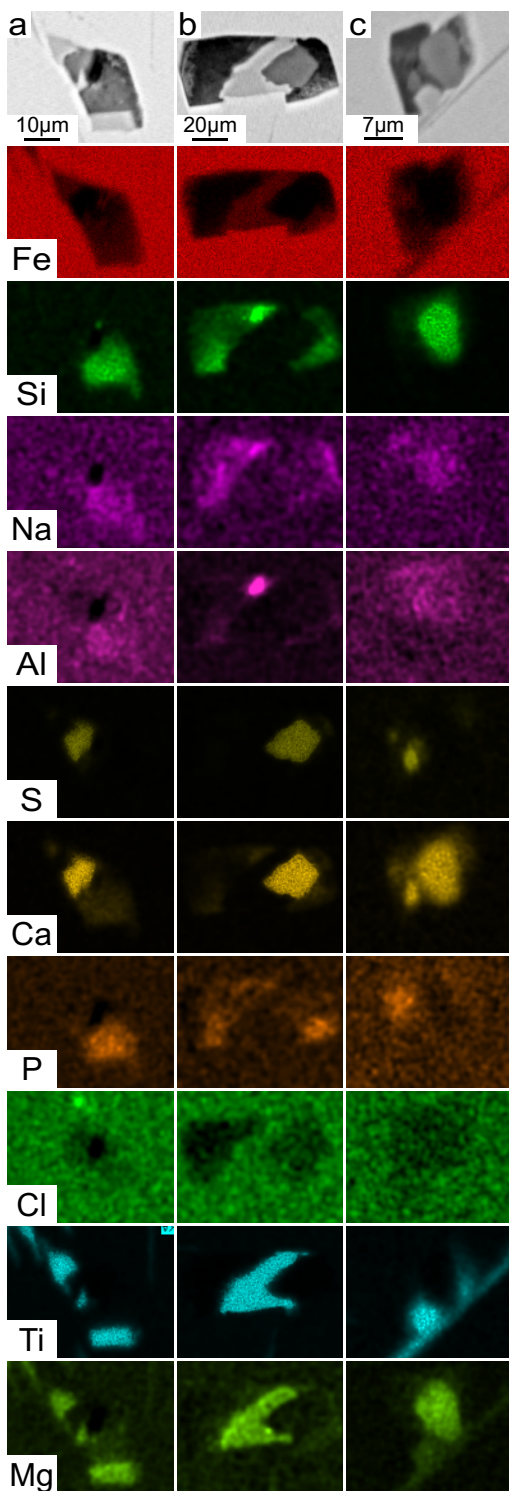
**Figure 3.2: Back scatter images and corresponding EDS maps showing magnetite-hosted polycrystalline inclusions.**

Individual inclusions have discreet Ca-S (Anhydrite), Si-Al-Na (Albite), Ti-Mg (Magnesium-bearing Ilmenite), and P (Apatite?) rich phases. Images shown here are taken from sample LCO-252.
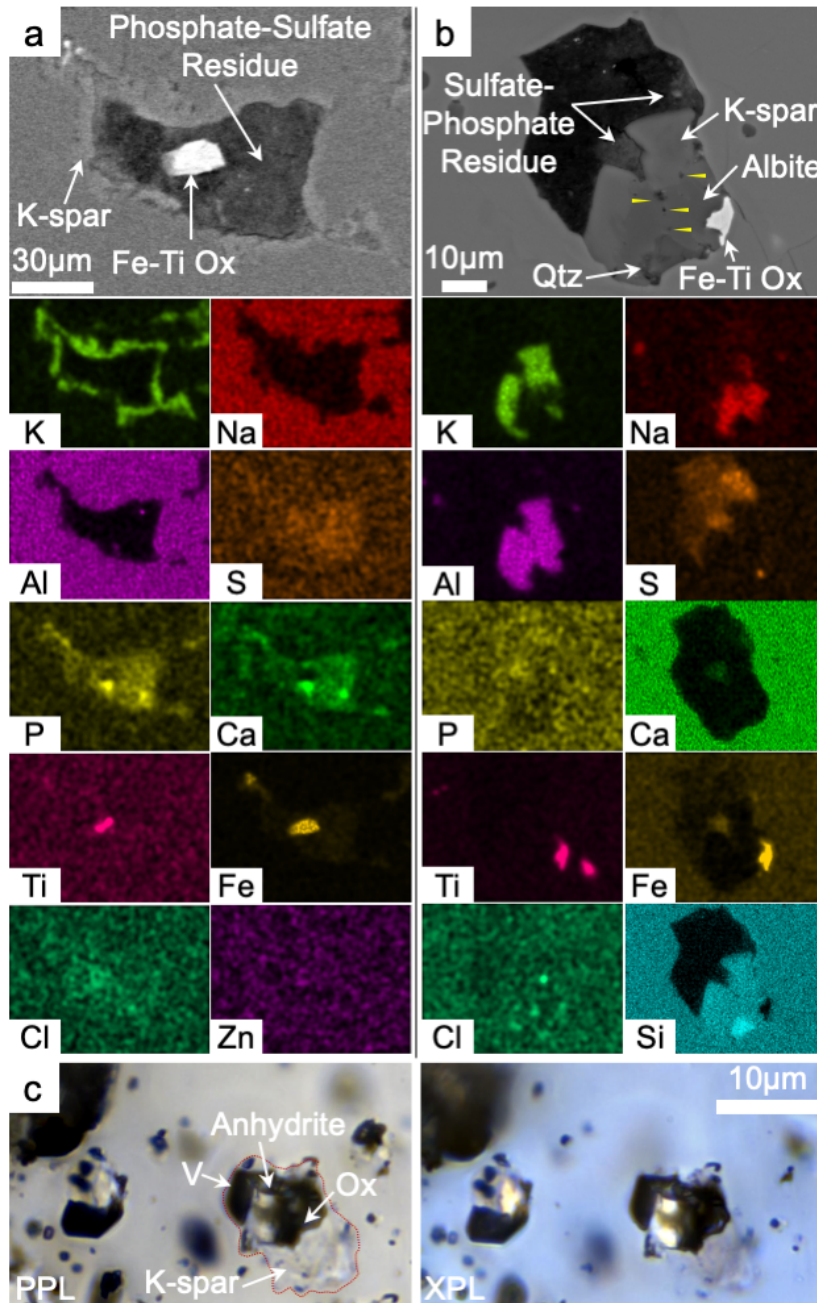
**Figure 3.3: Albite and diopside-hosted polycrystalline inclusions.**

a. Backscatter electron image of an exposed albite-hosted $PI_F$ inclusions and corresponding element maps. b: Backscatter electron image of an exposed diopside-hosted $PI_F$ inclusions and corresponding element maps. c: photomicrograph of albite-hosted $PI_F$ inclusions in plane-polarized light (PPL) and cross-polarized light (XPL). Images shown here are taken from sample LCO-253.
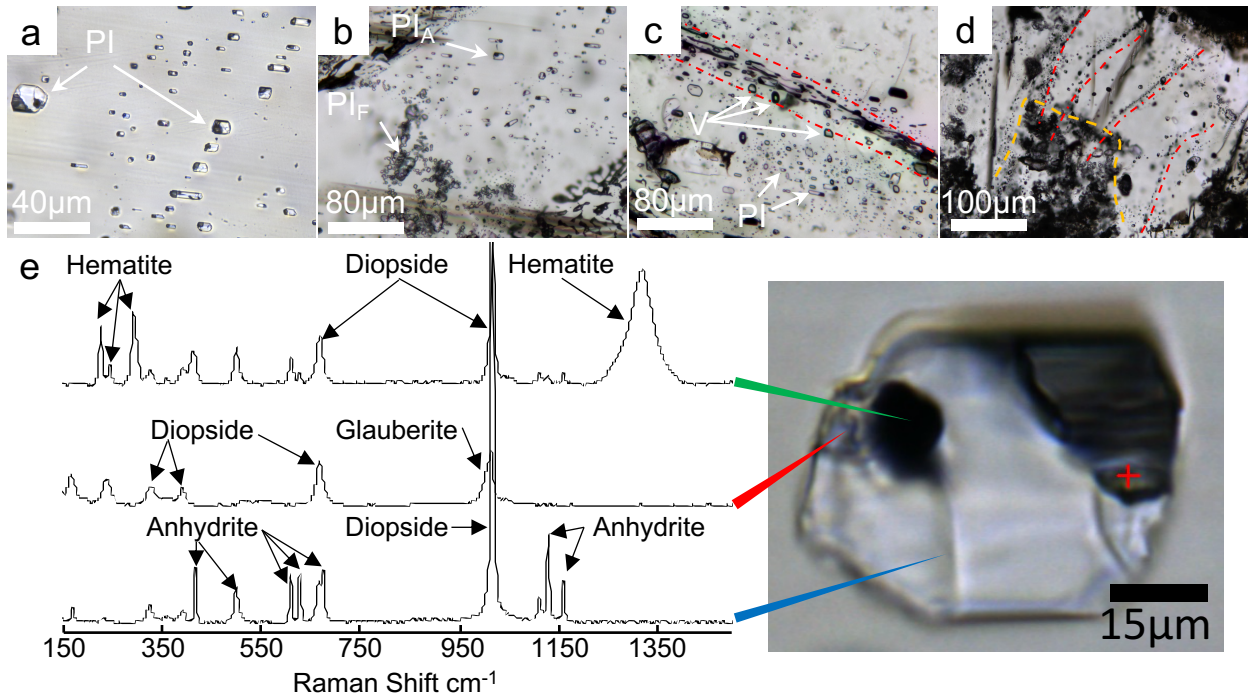
**Figure 3.4: Photomicrographs of inclusions hosted in diopside.**

a: Primary polycrystalline inclusions. b: Later primary non-feldspar-bearing ($PI_A$) inclusions alongside earlier primary felspar-bearing inclusions ($PI_F$). c,d: Secondary FIAs of coeval polycrystalline and vapor inclusions. e: Raman spectroscopy of a non-feldspar-bearing inclusion. Images shown in panels a-d are taken from sample LCO-252.
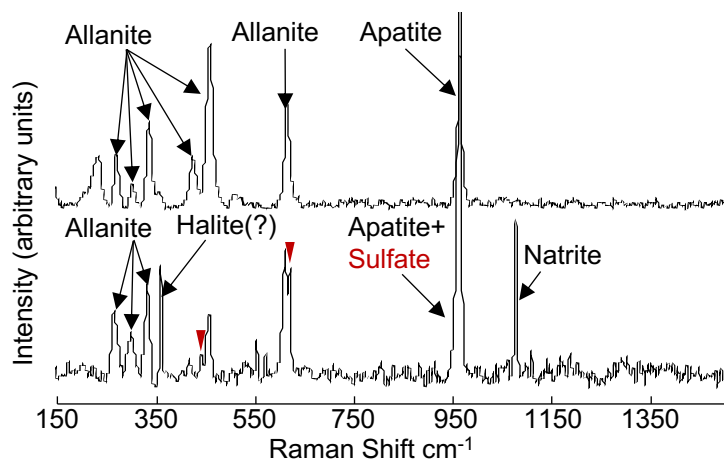
**Figure 3.5: Raman spectra from apatite hosted polycrystalline inclusions.**
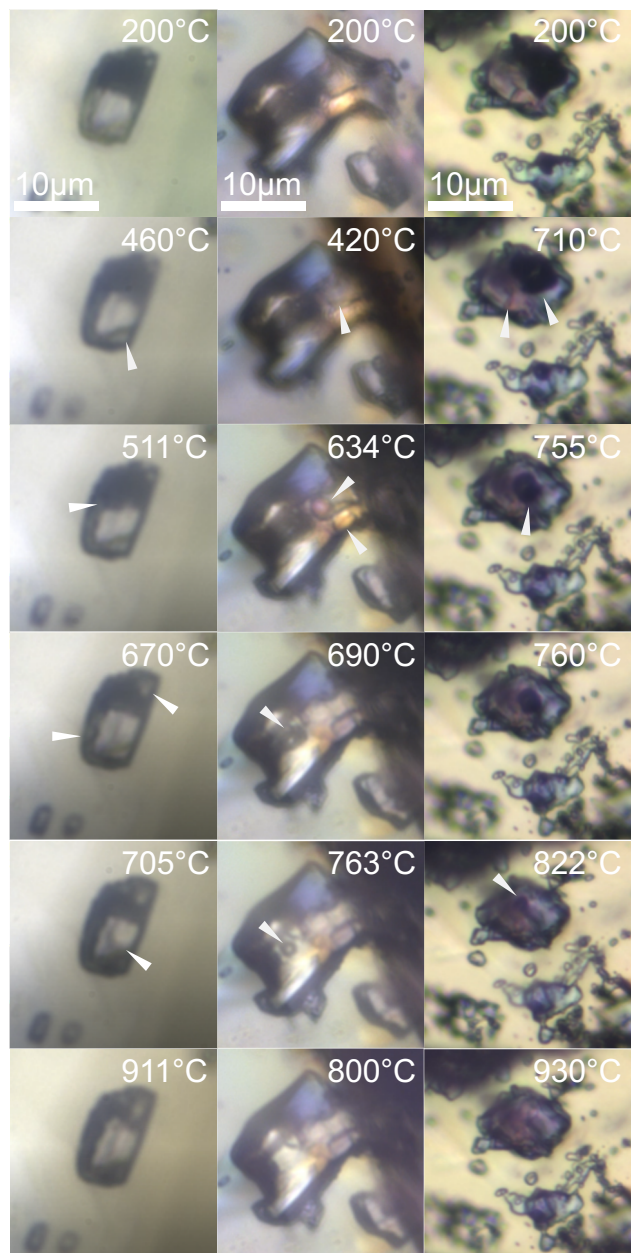
**Figure 3.6: High temperature microthermometry of polycrystalline inclusions**

Inclusions shown here are hosted in diopside from sample LCO-252.
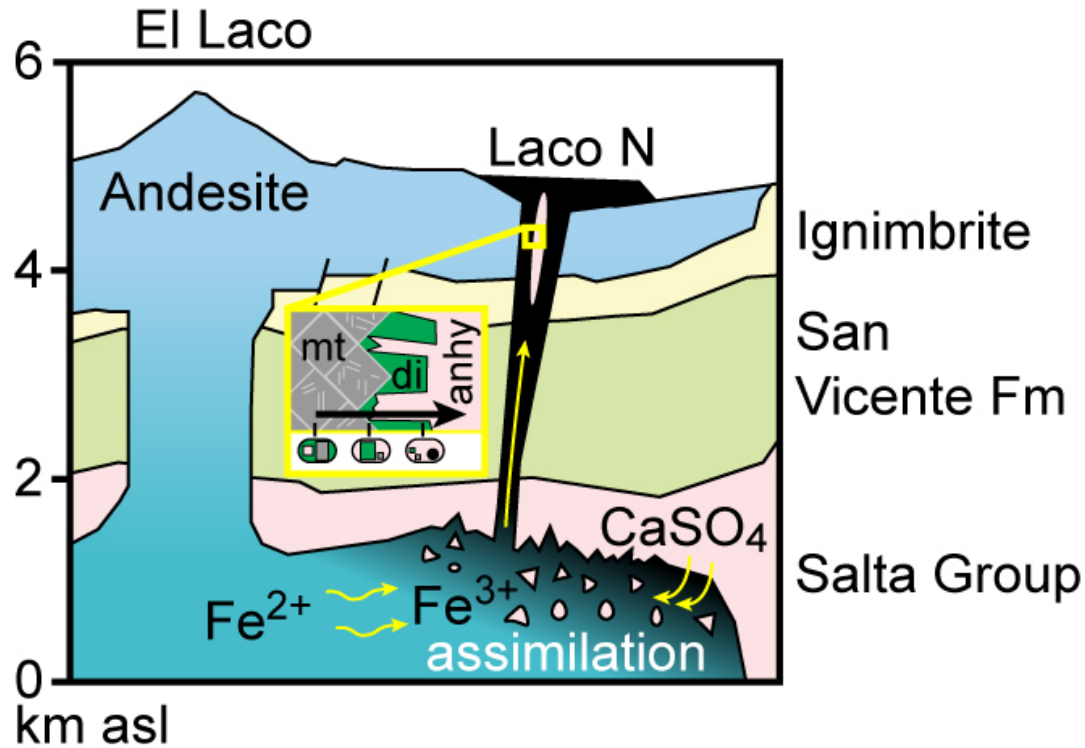
**Figure 3.7: Schematic model for the El Laco system.**

Andesite magmas underlying the El Laco volcanic complex assimilate/melt evaporite-bearing carbonate sediments. As carbonate-sulfate melt forms and mingles with the silicate magma $Fe^{2+}$ is oxidized to $Fe^{3+}$ and strongly partitions into the anatectic melt. Injection of the Fe-rich anatectic melt drives the formation of IOA ore bodies with volcanic features. The assimilation of evaporite-bearing carbonate sediments by the andesitic system at depth is evident from the sedimentary xenoliths present in the eruptive products of the nearby Lascar volcano.

**Table 3.1: Microthermometric data for primary and secondary FIAs reference in this study.**

Primary and Secondary inclusions are denoted by "P" and "S", respectively. Feldspar-bearing and non-feldspar-bearing inclusions are denoted by $PI_F$ and $PI_A$, respectively.

| n | FIA | Type | Host | $T_M\ 1^{st}$ | $T_M\ F$ | $T_H\ L\text{-}V$ |
|---|---|---|---|---|---|---|
| 1 | P FIA1 | $PI_A$ | Di | ~410 | 711 | - |
| 2 | P FIA1 | $PI_A$ | Di | - | 720 | - |
| 3 | P FIA1 | $PI_A$ | Di | - | 730 | - |
| 4 | P FIA1 | $PI_A$ | Di | - | 724 | - |
| 5 | P FIA2 | $PI_A$ | Di | ~346 | 700 | 805 |
| 6 | P FIA2 | $PI_A$ | Di | ~425 | 714 | 803 |
| 7 | P FIA2 | $PI_A$ | Di | - | 745 | - |
| 8 | P FIA3 | $PI_A$ | Di | - | 727 | 890 |
| 9 | P FIA3 | $PI_A$ | Di | - | 719 | 951 |
| 10 | P FIA3 | $PI_A$ | Di | - | 694 | 694 |
| 11 | P FIA3 | $PI_A$ | Di | - | 718 | - |
| 12 | P FIA3 | $PI_A$ | Di | - | 720 | - |
| 13 | P FIA4 | $PI_F$ | Ab | ~456 | 764 | 910 |
| 14 | P FIA4 | $PI_F$ | Ab | ~424 | 766 | 846 |
| 15 | P FIA4 | $PI_F$ | Ab | ~430 | 719 | 789 |
| 16 | P FIA5 | $PI_F$ | Ab | ~470 | 734 | >900 |
| 17 | P FIA5 | $PI_F$ | Ab | - | 760 | - |
| 18 | P FIA5 | $PI_F$ | Ab | - | 760 | - |
| 19 | P FIA5 | $PI_F$ | Ab | - | 769 | - |
| 20 | S FIA1 | $PI_A$ | Di | - | 764 | - |
| 21 | S FIA1 | $PI_A$ | Di | - | 784 | 940 |
| 22 | S FIA1 | $PI_A$ | Di | - | 782 | - |
| 23 | S FIA1 | $PI_A$ | Di | - | 782 | - |
| 24 | S FIA1 | $PI_A$ | Di | - | 782 | - |
| 25 | S FIA1 | $PI_A$ | Di | - | 782 | - |
| 26 | S FIA1 | $PI_A$ | Di | - | 782 | - |
| 27 | S FIA1 | $PI_A$ | Di | - | 782 | - |
| 28 | S FIA1 | $PI_A$ | Di | - | 782 | - |
| 29 | S FIA2 | $PI_A$ | Di | - | 720 | - |
| 30 | S FIA2 | $PI_A$ | Di | ~400 | 700 | 700 |
| 31 | S FIA2 | $PI_A$ | Di | - | 705 | - |

# Chapter 4: Fluids and melts at the magmatic-hydrothermal transition, recorded by unidirectional solidification textures at Saginaw Hill, Arizona, USA

## 4.1 Introduction

The previous chapters have illustrated how chemical and physical interactions between silicate magmas and sedimentary rocks can drive the formation of metal-rich mineralization. Here we examine a contrasting metal-rich system formed via the evolution of a silicate system which shows little to no evidence for crustal anatexis.

Fluids that form porphyry-type Cu mineralization are predominantly magmatic in origin, having exsolved from crystallizing, epizonal plutons of alkaline to calc-alkaline affinity and mostly intermediate (~andesitic) composition. By far the most available information on properties of such ore-forming fluids has been documented through analysis of fluid inclusions hosted in quartz veins. However, the properties of fluids in veins may have been affected by a variety of processes subsequent to exsolution, including phase separation (boiling), fluid-rock reactions, and precipitation of both ore and gangue minerals. Hence, the properties of fluid inclusions in veins which form distal from their magmatic-hydrothermal source likely do not represent the earliest exsolved fluids in these systems.

In recent years, much effort has been dedicated to improve our understanding of the nature of primary, exsolved magmatic fluids still in contact with their parental melt, for example by focusing on fluid inclusions hosted in miarolitic cavities (Audetat et al., 1998; 2000), or veins that host entrained droplets of silicate melt (Harris et al. 2003; Campos et al. 2006; Klemm et al. 2007; Zajacz et al., 2008; Li et al 2011; Stefanova et al., 2014; Rottier et al., 2016; Mernagh and Mavrogenes, 2018). In such cases, coeval assemblages of fluid and melt inclusions indicate that melt and fluid were in contact (and by inference, chemical equilibrium) at the time of trapping, and thus provide direct information on the process of fluid exsolution. Still, data of this type are

relatively scarce, and many questions remain. For example, how common is the direct exsolution of hypersaline, high-density brine, relative to the primary exsolution of single-phase, "intermediate density" type fluids that subsequently undergo boiling to produce brine and vapor? What factors drive systems toward either mode of fluid exsolution? Moreover, is the continuous exsolution of hydrothermal fluid a key factor for the formation of porphyry systems (Cline and Bodnar, 1991); or, is punctuated, repetitious and/or cyclic fluid release a more central process (Weis et al., 2012; Cloos and Sapiie, 2013; Mercer and Reed, 2013)? And how do these aforementioned questions relate to the concentration of economically important metals such as Cu?

Here, we provide new insights into the processes of fluid exsolution and release in the porphyry realm through analysis of fluid and melt inclusions hosted in unidirectional-solidification textures at Saginaw Hill, Arizona. We specifically target fluid and melt inclusions hosted in both monomineralic (hydrothermal) quartz bands, and in quartz phenocrysts in the corresponding aplitic (magmatic) bands. Results across multiple, time-resolved fluid inclusion assemblages between adjacent UST bands provide direct temporal constraints, allowing for an in-depth view of fluid exsolution and release. Our results reveal numerous new insights into processes at the magmatic-hydrothermal transition, including 1) direct exsolution of hypersaline brine; 2) extreme igneous fractionation tending towards peraluminous minimum-melt compositions; 3) intense partitioning of abundant Cu into the exsolving hydrothermal fluid phase; and 4) repetitious pressure build-up and catastrophic release. We by no means argue that any of these processes are ubiquitous at the magmatic-hydrothermal transition of all porphyry deposits. Rather, we suggest that our results provide exceptional examples of processes that *can* occur at the magmatic-hydrothermal transition of shallow calc-alkaline plutons.

## 4.2. Unidirectional Solidification Textures

Unidirectional solidification textures (also known as brain rock, ribbon rock, or USTs) are a common feature in the shallow apices of small intrusive bodies (Kirkham and Sinclair, 1988). USTs have been documented in a variety of magmatic-hydrothermal systems including porphyry Mo-W deposits (Carten et al., 1988; Lowenstern and Sinclair, 1996; Wilson et al., 2003; Seedorff and Einaudi, 2004), pegmatites (London 2009), and more rarely on the margins of felsic to intermediate plutons (Erdenbayer et al., 2014). These rocks are characterized by successive,

alternating bands of aplite and monomineralic quartz with euhedral terminations that invariably point inwards from the outer margin of the pluton (Fig 4.1). Lowenstern and Sinclair (1996) describe UST formation via exsolution and coalescence of aqueous hydrothermal fluids along the outer margins of degassing plutons. In this model, quartz crystals nucleate along the crystalline carapace, which forms the interface between the melt and country rock, and grow inward. The open-space-filling textures of euhedral quartz grains in such monomineralic bands indicate that quartz growth is not obstructed, suggesting growth into hydrothermal-fluid-filled space. Over time, the system episodically ruptures, either in response to fluid over-pressure or tectonic movement. As aqueous fluids vent outward into the country rock, the melt quenches to form a thin layer of aplite over top of the adjacent euhedral quartz band. At the same time, depressurization and cooling of the aqueous fluid as it circulates outward from the pluton results in resealing of fracture networks by quartz precipitation, allowing for subsequent re-pressurization of the system. The cycle then repeats, leading to the formation of sequential UST bands.

London (2009) presents a similar model for UST formation in granitic pegmatites. In his model, the large size, euhedral shape, and unidirectionality of crystalline phases are related to enrichment of fluxes (B, P, F) in the aqueous fluid, which allows for cooling below the solidus. Thermal gradients are steepest along the margins of the magma body, and this is where the viscosity of the melt is highest. The high viscosity of the melt delays the nucleation of crystalline phases, allowing for high degrees of undercooling and hence generating high chemical potentials (supersaturation) that subsequently drive rapid crystal growth as soon as the nucleation barrier is overcome. Hence, "normal," random nucleation of crystalline phases throughout the liquid is suppressed, favoring instead localized nucleation along the crystalline margins. Though discussed by London (2009) in the context of pegmatites, these processes likely also operate during the formation of successive bands of USTs in porphyry settings, for example in response to fluctuations of pressure related to fluid accumulation and release. In the latter context, the likely fluxes probably include key components of the ore-forming hydrothermal fluids, such as chloride salts (Veksler, 2004; Webster, 2004; Bodnar et al., 2014).

The models described above for the formation of USTs in crystallizing melts parallel the larger scale process of hydrothermal fluid flux involved in the formation of successive generations of quartz veins in porphyry systems. For instance, Cloos and Sapiie (2013) examined

the role of strike-slip faults in porphyry ore formation and described a cyclical process in which exsolution and release of metal-rich hydrothermal fluids are promoted by repeated pressurization and rupturing. These authors further reason that this physical process is likely a significant control on the formation and metal enrichment in porphyry systems, perhaps even outweighing the importance of metal-enriched magmas. Similarly, studies that have examined the thermal profiles of porphyry systems on the local scale (Mercer and Reed, 2013) describe the formation of quartz veining in porphyry systems as involving the flux of magmatic-hydrothermal fluids directly from a high temperature magmatic source at depth during repeated episodes of fracture formation. The parallels between the mechanisms for UST and porphyry deposit formation suggest that these models can be naturally linked, with the local-scale formation of UST bands recording the accumulation of hydrothermal fluids near the point of exsolution in the parental melt and directly prior to outward flux through the network of mineralized quartz veins.

**4.3 Geologic background**

The Saginaw Hill system is located directly southwest of Tucson, Arizona, along the western flank of the southernmost extension of the Tucson Mountains (Frank, 1970; Fig. 4.2). Saginaw Hill is a composite pluton composed primarily of the Saginaw Hill quartz latite porphyry and the Saginaw Mine quartz monzonite porphyry. Together, both lithologies share intrusive and fault contacts with the arkose-bearing limestone and greywacke units of the Cretaceous Amole Formation. Phenocrysts in the Saginaw Hill quartz latite porphyry are dominantly quartz (~15%), plagioclase (~12%), and orthoclase (~8%) surrounded by a quartz-rich groundmass. Total surface outcrop of the Saginaw Hill quartz latite porphyry covers an approximately rectangular area of ~0.3 km$^2$, but also includes several elongate dikes and lobate projections, some of which extend >1 km outward from its periphery. The Saginaw Mine quartz monzonite porphyry occurs as a few outcrops north of Saginaw Hill and intrudes the Saginaw Hill quartz latite porphyry at depth. Phenocrysts in the Saginaw Mine quartz monzonite porphyry are primarily plagioclase (~15%), orthoclase (~9%), and biotite (~1%) in a quartz-rich groundmass which is nearly identical to that of the Saginaw Hill quartz latite porphyry. Plagioclase in both lithologies is pervasively altered to kaolinite and montmorillonite associated with a pervasive, pyrite-rich sericitic overprint of Saginaw Hill and the surrounding area. The presence of pervasive sericitic alteration throughout the Saginaw Hill system indicates that a large hydrothermal system was

associated with the emplacement of both igneous bodies. In addition, several small porphyritic latite dikes crosscut both units and are distinctive in that they lack pervasive hydrothermal alteration and contain trace amounts of muscovite.

Uranium-lead ages of zircons from the Saginaw Hill quartz latite porphyry indicate an age of ~60±0.6 Ma (R.E. Greig, pers. commun., 2020), which is consistent with an estimated Laramide age based on cross-cutting relationships by Frank (1970). These ages are also similar to that of the Sierrita, Mission, and Silver Bell porphyry systems which are situated in relatively close proximity (<40 km; Fig. 4.2).

A several meter-thick, massive quartz vein extends NE-SW along the near-vertical Papago Queen fault, which runs through the center of the main Saginaw Hill quartz latite porphyry. This quartz vein grades northward and southward into abundant UST bands, which occur as near-vertically oriented, 3-15 mm-thick bands of euhedral to subhedral quartz separated by 3-10 mm-thick bands of fine-grained aplite (Fig. 4.1). Individual outcrops of USTs are in some cases up to several meters thick (5-10 m) and, unlike the well-documented USTs reported in silicic porphyry Mo deposits (Seedorff and Einaudi, 2004), exhibit a continuous, planar trace indicative of minimal post-emplacement deformation and fracturing. The aplite that truncates the individual monomineralic quartz bands is heavily sericitized. Outward from the UST bands, the Saginaw Hill quartz latite porphyry is crosscut by thin, comb-textured quartz veins which decrease in abundance with decreasing proximity to the main massive quartz vein.

The massive quartz vein that crosscuts the Saginaw Hill quartz latite porphyry is associated with sulfide mineralization, which occurs as disseminated and vein-hosted chalcopyrite and pyrite. Hence, several (now defunct) small-scale mines are present at Saginaw Hill and the surrounding area. The largest of these—the Papago Queen Mine—focused on the massive quartz vein itself. During its peak operation in the early 1900s, the Papago Queen Mine produced significant Cu and Ag, along with lesser Au. More recent drilling in this area has also revealed evidence of minor Mo mineralization, but failed to identify significant mineralization at depth. Several small carbonate-replacement deposits also occur along the northern margin of the Saginaw Hill quartz latite porphyry where it crosscuts limestone-bearing portions of the Amole Formation. These deposits (e.g., the Palo Verde Mine) are associated with the Palo Verde fault and produced significant Pb-Zn-Ag-Au and minor Cu. Farther north, the Saginaw Mine produced

both Cu and Au from disseminated mineralization associated with the Saginaw Hill quartz monzonite porphyry.

## 4.4 Methods

Samples of UST bands were collected from outcrop on the southern portion of the Saginaw Hill pluton. The UST bands in this area grade into the massive quartz vein which is the site of the Papago Queen Mine. Samples of UST quartz and aplite were prepared into 100 μm-thick, doubly-polished sections and characterized using a custom-built Olympus BX53M petrographic microscope. Petrographic analysis of fluid and melt inclusions focused on both monomineralic quartz UST bands and aplite-hosted quartz phenocrysts. Petrographic characterization of assemblages of coeval fluid and melt inclusions followed the methods detailed in Goldstein and Reynolds (1993).

Cathodoluminescence (CL) imaging of quartz UST bands and aplite-hosted quartz phenocrysts was used to discern growth zoning and healed fractures in quartz. The CL results were also used to differentiate primary versus secondary fluid inclusion assemblages, and to establish the overall paragenetic sequence of inclusion assemblages. Subsequent backscatter electron imaging (BSE), and energy dispersive spectroscopy (EDS) maps were used to characterize the compositions of melt inclusions. Cathodoluminescence imaging, backscatter electron imaging, and EDS analysis were carried out using a Zeiss EVO SEM with a LaB6 electron source. Acceleration voltage was set to 20-25 kV, beam current was 300-500 pA, and working distance was set at 7-8.5 mm. Images were collected in variable-pressure mode with a 100-mm aperture on uncoated samples using collection times that varied between 1-15 minutes.

Low-temperature microthermometry of fluid inclusions was conducted using a Linkam THMSG600 (-100-600 °C) stage calibrated using the triple point of $CO_2$ at -56.6 °C, the triple point of $H_2O$ at 0.0 °C, and the critical point of $H_2O$ at +374.1 °C. Estimated precision and accuracy of the temperature measurements is ±0.1 °C at subzero temperatures and ±0.5 °C at temperatures >100 °C. Salinity, density and isochore were interpreted from measured phase transition temperatures using the model of Steele-MacInnis et al. (2012)

High temperature (>500 °C) microthermometry of fluid and melt inclusions was conducted using a Linkam TS1400XY stage calibrated using the critical point of $H_2O$, the α/β transition of

quartz at 574 °C, and the melting point of NaCl at ~1 bar (801 °C). Estimated precision and accuracy of the measurements at temperatures >500 °C is ±1 °C.

Crystalline phases, vapor bubbles, and liquids within inclusions were analyzed by Raman spectroscopy using a Bruker SENTERRA instrument at MacEwan University. All Raman analyses used a 532 nm $Ar^+$ laser focused to a 1 μm spot through a 100x objective mounted on a standard petrographic microscope. All spectra were acquired on unoriented grains using a laser power of 20 mW and two to three, 5-30s exposures summed to the final reported spectra. Baseline subtraction and background reduction were applied using the Opus 6.1™ and Fityk™ software packages. Spectra were interpreted using the RRUFF database (Lafuente et al., 2016)

The major-element compositions of homogenized (glassy) melt inclusions were measured by electron microprobe analysis (EPMA) of the glass exposed at the surface of quartz chips after high-temperature microthermometry and quenching. Quartz chips containing melt inclusions were first heated to <900 °C, rapidly quenched (by instantaneously removing the chip from the high-temperature stage to ambient temperature), and then mounted in clear epoxy on glass slides. Samples were examined in situ with a binocular microscope in order to determine the orientation of the quartz chip and the position and depth of inclusions. The samples were then carefully ground and progressively polished to exposed homogenized inclusions at the surface of each sample.

Two sessions of EPMA were conducted to determine the composition of homogenized melt inclusions, as well as crystalline phases within unheated melt inclusions exposed at the surface of the samples. During the first session, quantitative compositional data were acquired using the wavelength dispersive spectrometers of a Cameca SX100 electron microprobe and Probe for EPMA software (Donovan et al., 2015). Twelve elements were analyzed (Na, Mg, Al, Si, P, S, Cl, K, Ca, Mn, Fe, and Cu; no other elements were observed by energy-dispersive X-ray spectrometry) with 15 kV accelerating voltage, 6 nA probe current, and beam diameters ranging from 1 to 5 μm. Total count times of 20 seconds were used for both peaks and backgrounds of the elements Na, Al, Si, K, and Fe, whereas 30 second count times were used for the remaining elements. The X-ray lines, diffraction crystals, and standards were: Na $K\alpha$, TAP, tugtupite; Mg $K\alpha$, TAP, pyrope; Al $K\alpha$, TAP, obsidian; Si $K\alpha$, TAP, obsidian; P $K\alpha$, PET, fluorapatite (intensity data aggregated from measurements on two spectrometers, Donovan et al., 2011); S $K\alpha$, PET, baryte; Cl $K\alpha$, PET, tugtupite; K $K\alpha$, PET, sanidine; Ca $K\alpha$, PET, diopside; Mn $K\alpha$,

LIF, spessartine; Fe $K\alpha$, LIF, hematite; and Cu $K\alpha$, LIF, copper. During the second session, thirteen elements were analyzed (Na, Mg, Al, Si, P, S, Cl, K, Ca, Mn, Fe, Cu and Zn; no other elements were observed by energy-dispersive X-ray spectrometry) with 15 kV accelerating voltage, 6 nA probe current, and 2 μm beam diameter. Total count times of 20 seconds were used for both peaks and backgrounds of the elements Na, Al, Si, K, and Fe, whereas 30 second count times were used for the remaining elements. The X-ray lines, diffraction crystals, and standards were: Na $K\alpha$, TAP, tugtupite; Mg $K\alpha$, TAP, pyrope; Al $K\alpha$, TAP, obsidian; Si $K\alpha$, TAP, quartz; P $K\alpha$, PET, fluorapatite (intensity data aggregated from measurements on two spectrometers, Donovan et al., 2011); S $K\alpha$, PET, baryte; Cl $K\alpha$, PET, tugtupite; K $K\alpha$, PET, sanidine; Ca $K\alpha$, PET, diopside; Mn $K\alpha$, LIF, spessartine; Fe $K\alpha$, LIF, hematite; Cu $K\alpha$, LIF, copper; and Zn $K\alpha$, LIF, willemite. Both sessions used time-dependent intensity corrections for Na (peak count times divided into five intervals) with Probe for EPMA software following Nielsen and Sigurdsson (1981). X-ray intensity data were reduced following Armstrong (1995). Oxygen equivalence of halogens was included in the data reduction. After analysis, data were filtered on the basis of total calculated abundances of oxides, and analyses that had abundances <90% were excluded from further consideration.

Laser ablation inductively coupled plasma mass spectrometry (LA-ICP-MS) was used to measure the major, minor and trace element composition of quartz UST bands, aplite-hosted quartz phenocrysts, and individual fluid and melt inclusions. The analyses were conducted using a GeoLas 193nm ArF Excimer laser with an adjustable circular aperture at the USGS Denver Inclusion Analysis Laboratory in Denver, Colorado, USA. The laser system was coupled with a ThermoFischer XSeries II mass spectrometer. The laser was set to 60% power with a 5 Hz pulse rate. Helium carrier gas was set to a flow rate of 400 cc and a round sample chamber was used during ablation. External standardization was done using the NIST612 and NIST610 reference materials. A maximum of 10 unknowns were bracketed with 3 analysis of each external standard during analytical sessions in order to correct for instrument drift. Three analytical sessions were conducted with element lists which included Li[7], B[11], Na[23], Al[27], Si[29], K[39], Ca[42], Ti[47], Mn[55], Fe[56], Fe[57], Cu[65], Zn[66], Rb[85], Sr[88], Mo[95], Ag[107], Sn[118], Cs[133], Ba[137], La[139], Ce[140], W[182], Au[197], Pb[208]. The latter two analytical sessions also included Be[9], As[75], Zr[90], Hf[178], Ta[181], Tl[205], and U[238]. In preliminary analyses, S[34] and Th[232] were also tested but were typically below the LOD and were excluded from all subsequent analysis.

Transient LA-ICP-MS signals were reduced using the SILLS software (Guillong at al., 2008). For aqueous brine inclusions, the internal standard was the average salinity in wt% NaCl equivalent determined for each assemblage by microthermometry and corrected for the contribution of major dissolved cations using the charge-balance procedure (Allan et al., 2005). Quantification of the silicate melt inclusions was carried out using the sum-to-100% oxide method (Halter et al., 2002, Leach and Hieftje, 2000), modified to account for the fact that $SiO_2$ in the melt inclusions could not be analyzed, owing to interference from the quartz host (specifically, by summing all other oxides to 31%, where the complementary 69% represents the estimated $SiO_2$ content based on analyses of bulk rock; R.E. Greig, pers. commun. 2020). In both cases, composition of the host quartz was determined (and host contribution to inclusion signals was corrected) using an internal standard for the quartz host of 100 wt% $SiO_2$. Finally, and as discussed below, the majority of analyzed melt inclusions showed evidence of having heterogeneously trapped muscovite and/or potassium feldspar; therefore, the final stage of data reduction for analysis of melt inclusions involved subtracting aliquots of stoichiometric muscovite and/or potassium feldspar in order to arrive at the estimated composition of the trapped silicate melt. This calculation approach is outlined in the Results section, below.

The Ti-in-quartz thermobarometer was used to calculate the temperature of formation for the quartz host of the analyzed inclusions using the calibration of Huang and Audétat (2012). This revised calibration of the original TitaniQ thermobarometer (Wark and Watson, 2006) relates the temperature of formation to Ti concentrations in quartz and pressure conditions during quartz formation. This calibration has been previously used to evaluate the temperatures of formation of the quartz in magmatic and magmatic-hydrothermal settings and has been shown to yield reasonable temperatures (Mercer and Reed, 2013). However, the accuracy of this calibration is greatly reduced under conditions of high quartz growth rates (Huang and Audétat, 2012), owing to chemical disequilibrium during rapid growth. Specifically, incorporation of trace element into the quartz structure is governed by solubility at low (slow) growth rates but become kinetically controlled at higher growth rates. Thus, the calibration is most accurate when applied to quartz crystals which display features indicative of slow, ordered growth (e.g., growth zonation) and which are grown in a magmatic environment (Huang and Audétat, 2012). As discussed in detail below, our interpretations of the Ti-in-quartz results consider both equilibrium formation temperatures, and periodic departures from equilibrium resulting from rapid growth, and we

evaluated the Ti-in-quartz results alongside other temperature constraints, such as fluid inclusion homogenization temperatures. Furthermore, the calibration of Huang and Audétat (2012) was constrained via experiments at rutile-saturated conditions (titania activity of 1). Thus, uncorrected, calculated temperatures represent *minimum* temperatures if $a_{TiO2}<1$. Activity of titania in silicic magmas is commonly on the order of ~0.5 (Watson et al., 2006) and tends towards 1 in exsolved magmatic-hydrothermal fluids (Mercer and Reed, 2013). Modal mineralogy of igneous phases in the Saginaw Hill stock (Frank, 1970) indicates an overall latite/monzonite composition and $a_{TiO2}$ >0.5, whereas hydrothermal alteration of the same rocks has generated secondary anatase suggesting $a_{TiO2}$ ~1. Hence, we estimated temperatures based on an assumed $a_{TiO2}$ between 0.5 and 1, which yields an estimated uncertainty on temperature of approximately ±40 °C (Mercer and Reed, 2013).

## 4.5 Results

*4.5.1 Petrography and CL imaging of quartz*

Cathodoluminescence imaging reveals that the monomineralic quartz bands contain two generations of quartz. The cores of monomineralic quartz bands are invariably composed of quartz that exhibits fine (>2μm), euhedral growth zones (Fig. 4.3). This generation is paragenetically the oldest, and is referred to as UST-bright. In transmitted light, growth-zoned crystals host abundant silicate melt inclusions which are dominantly <1 μm in size but up to >15 μm in some areas. As a result, areas with dense concentrations of melt inclusions in UST-bright quartz commonly exhibit a hazy, brown coloration. The large, sharply terminated crystals which form the tops of monomineralic quartz bands contain individual growth zones with a particularly bright CL response. In transmitted light, these areas host fine, brown bands of sub-micron melt inclusions or, less commonly, assemblages of 5-20 μm melt inclusions together with sparse coeval brine inclusions (Fig. 4.4).

Euhedral UST-bright quartz is commonly rimmed by quartz that exhibits widely spaced (50-100 μm), subhedral growth zones and/or a featureless gray response in CL (Fig. 4.3). This younger generation of quartz is referred to here as UST-dull, and occurs either as sinuous subhedral rims which truncate the growth zones of UST-bright quartz, or as thin sinuous trails

along healed fractures that appear to emanate outward from the base of the next overgrown aplite band. In transmitted light, UST-dull quartz is mostly clear and can be clearly distinguished from the brown, cloudy UST-bright quartz it surrounds and/or crosscuts.

Cathodoluminescence imaging of quartz phenocrysts in the aplite bands shows two distinct generations of quartz that resemble the two aforementioned generations of the UST bands. Quartz in phenocryst cores is characterized by a bright CL response and broad (1-3 μm), euhedral to subhedral growth zones (Fig. 4.5). This generation of quartz is referred to as Ph-bright, and like UST-bright quartz, has a brown, hazy appearance in transmitted light as a result of abundant silicate melt inclusions which range in size from <1μm to >15 μm. Quartz phenocrysts are invariably rimmed by quartz that has a uniform gray CL response, and commonly truncates the growth zones of the Ph-bright cores (Fig. 4.5). This quartz is referred to as Ph-dull, is mostly clear in transmitted light, and hosts evenly spaced fluid and melt inclusions. Collectively, the CL responses of the quartz phenocrysts in the aplite strongly resemble those of individual crystals found along the base of each monomineralic quartz band, suggesting similar formation mechanisms for both.

*4.5.2 Petrography of fluid and melt inclusions*

Each generation of quartz described in the previous section hosts well-constrained FIAs of fluid and melt inclusions. The abundance and character of inclusions varies with their occurrence in specific generations of quartz as described below (Table 4.1).

*4.5.2.1 Quartz UST bands*

Monomineralic quartz bands host abundant fluid and melt inclusions in well-defined coeval assemblages. Primary FIAs of silicate melt inclusions occur along the growth zones in UST-bright quartz (Fig. 4.4). Melt inclusions have an irregular or subhedral negative-crystal shape, range in size from <1 μm to >30 μm, are crystallized, and are hence easily distinguished by their birefringence in cross-polarized light. Phase proportions of melt inclusions are consistent throughout an assemblage and include several square or rectangular, translucent crystalline phases (50-70 vol%) and a large vapor bubble (30-50 vol%) at ambient temperature. Many inclusions are dominated by 1-2 rectangular crystals which comprise up to 50 vol% of the crystalline solids within the inclusion. In the cores of UST-bright quartz, <1 μm melt inclusions

comprise ~80-90% of the inclusions present and give the quartz a characteristic cloudy, brown appearance (Fig. 4.4). Surrounding the cores of UST-bright quartz, larger melt inclusions (up to >30μm) form well-defined linear arrays along primary growth zones (Fig. 4.4). Rare aqueous brine inclusions also occur alongside silicate melt inclusions in the same coeval assemblages throughout UST-bright quartz. Brine inclusions in UST-bright quartz are typically 5-10 μm in size and contain ~10-15 vol% vapor, a halite crystal,1-2 additional translucent birefringent crystals, and a round or triangular opaque grain. Vapor-rich inclusions were not observed in any UST-bright quartz.

UST-dull quartz hosts primary and pseudo-secondary FIAs dominated by brine inclusions and also hosting rare, coeval silicate melt inclusions, which are identical in appearance and phase proportions to the melt inclusions observed in UST-bright quartz (Fig. 4.4). Primary aqueous brine inclusions in UST-dull quartz range in size between 10 and 20 μm and show well-developed negative-crystal shapes. Phase ratios in the brine inclusions are identical within a given assemblage but varied between different assemblages. Aqueous brine inclusions typically contain 15-20 vol% liquid, ~15-30 vol% vapor, 25-35 vol% halite + sylvite, 5-10 vol% opaques, plus 1-2 additional translucent daughter crystals.

Abundant secondary FIAs of brine ± coeval vapor inclusions also occur in UST-dull quartz along planar arrays, which in some cases cross-cut UST-bright quartz (Fig. 4.4). Such secondary FIAs are particularly abundant in the euhedral apices of the UST bands. Within an individual FIA, brine inclusions have identical phase ratios which include liquid, vapor (20-25 vol%), halite±sylvite (20-25 vol%), 1-2 unidentified round translucent crystals with variable birefringence (5-20 vol%), plus a round or triangular opaque (2-5 vol%). Vapor-rich inclusions with up to ~85-95 vol% vapor commonly occur in coeval secondary assemblages alongside brine inclusions, but their presence is variable between FIAs.

### 4.5.2.2 Aplite-hosted quartz phenocrysts

The inclusions observed in the Ph-bright cores of quartz phenocrysts are remarkably similar to the FIAs observed in the UST-bright quartz. The Ph-bright quartz contains densely packed FIAs of silicate melt inclusions with coeval aqueous brine inclusions (Fig. 4.6). Silicate melt inclusions range in size from <1-30 μm and have consistent phase ratios of ~75-85 vol%

crystalline solids, ~15-23 vol% vapor, and a round of square opaque (~2%). The crystalline phases are discernible by their birefringence and are dominated by 1-2 rectangular phases which occupy ~50 vol% of each inclusion. Coeval brine inclusions (~5-15μm) contain liquid (~35 vol%), vapor (30 vol%), halite (30 vol%), and a round or triangular opaque grain (5 vol%).

The Ph-dull rims of quartz phenocrysts contain abundant coeval brine and vapor inclusions along with sparse silicate melt inclusions (Fig. 4.6). Brine inclusions range in size between 5 and 30μm and contain halite+sylvite (70-80 vol%), vapor (15-25 vol%), a round or square opaque (2-5 vol%), and liquid which fills the interstitial space between solid phases within the inclusions. Vapor-rich inclusions contain ~90-95 vol% vapor and a thin film of aqueous liquid around the periphery. Silicate melt inclusions in Ph-dull quartz are identical to the melt inclusions observed in the Ph-bright cores.

*4.5.3 Phase assemblage of the crystallized melt inclusions*

Melt inclusions in both the quartz UST bands and quartz phenocrysts show remarkably similar phase assemblages and volumetric phase ratios at ambient temperature, with SEM-EDS mapping consistently indicating discrete grains rich in K, Na, Al, Ca, Mg, P, and Fe (Fig. 4.7 and Fig. 4.8). Much of the silicate material in all the analyzed inclusions is composed of K-Al-rich phases corresponding to muscovite and K-feldspar. Raman analyses consistently indicate the presence of muscovite in the majority of melt inclusions (Fig. 4.9). Analyses by EPMA confirm that the K-Al-rich sheet silicate is muscovite *senso stricto*, containing minor Mg (0.02-0.005 apfu), $Mn^{2+}$ (0.015-0.007 apfu), and $Fe^{2+}$ (0.122-0.053 apfu; Table 4.2). EPMA analyses also confirm that the other (generally subordinate) K-Al-rich phase is K-feldspar, containing minor Na (0.036 apfu), S (0.01 apfu) and Ca (0.002 apfu; Table 4.2). Melt inclusions in both UST and phenocryst quartz also contain a Ca-rich silicate (plagioclase) and a discrete P-rich phase (apatite). Discrete grains of Fe-oxide (hematite) are also present. Phenocryst-hosted melt inclusions also commonly contain an additional Cl-rich phase (chloride salt) which is not observed in melt inclusions hosted in monomineralic quartz bands (salt; Fig. 4.8).

**4.6 Mineral phases in the brine inclusions**

Raman analyses of aqueous brine inclusions in monomineralic quartz bands and phenocrysts allows for the identification of grains other than halite+sylvite, including the

triangular opaque daughter crystals and aggregates of translucent to opaque grains. Raman spectra of the triangular opaque grains are consistent with chalcopyrite in all cases (Fig. 4.9). Spectra from aggregates of translucent to opaque grains are consistent with molybdenite, as well as occasional anatase (Fig. 4.9). In addition, the O-H stretching band of many brine inclusions shows a sharp, distinctive peak near 3450 cm$^{-1}$ (Fig. 4.9) consistent with structurally bound $H_2O$ in an Fe-rich chloride salt hydrate (Kodera et al., 2014).

## 4.7 Microthermometry

### 4.7.1 Monomineralic Quartz UST bands

Primary and pseudo-secondary FIAs of silicate melt inclusions in the UST-bright and UST-dull quartz show identical behavior during high temperature microthermometry. First melting, which is indicated by a change in shape and distribution of crystalline phases within inclusions, occurs at ~600-650 °C. At ~850-900 °C, ca. 85-90% of the volume of the inclusion abruptly melts, and a round vapor bubble along with a yellow crystalline mass is visible within each inclusion. With continued heating, the granular mass is absorbed into the silicate liquid. Complete homogenization by dissolution of the fluid bubble into the silicate liquid is rare and typically occurs at temperatures >1000 °C.

Low temperature microthermometry of primary and pseudo-secondary aqueous brine inclusions in UST-dull quartz does not result in any observable phase transitions between -130-+39 °C. However, between 40-45 °C, the liquid portion of the inclusion appears to abruptly shudder. This behavior and temperature range is consistent with abrupt decomposition of a salt hydrate (likely a sulfate; Walter et al., 2018); however, it is unclear whether such a salt hydrate was present at room temperature (prior to cooling) or nucleated during cooling. Continued heating of primary aqueous brine inclusions results in consistent homogenization via halite melting between 482 and 519 °C, corresponding to salinities between 55 and 62 wt% NaCl eq. Liquid-vapor homogenization (by disappearance of the vapor bubble) occurs prior to halite dissolution, and over a wide temperature range of 276-519 °C. Pseudo-secondary aqueous brine inclusions hosted in UST-dull quartz show similar behavior with liquid-vapor homogenization over a wide range (360-519 °C), followed by homogenization by halite melting between 441-550

°C, corresponding to salinities of 53-64 wt% NaCl eq. Opaque daughter crystals in both sets of brine inclusions commonly shank by ~60% during heating but do not completely homogenize even during heating to >600 °C, at which point most brine inclusions decrepitate. Homogenization of secondary vapor-rich inclusions is not observed because the liquid portion occupied a vanishingly thin film along the inclusion walls (Klyukin et al., 2019). A summary of microthermometric data from brine inclusions hosted in monomineralic quartz bands is provided in Tables 4.3, 4.4, 4.5.

### 4.7.2 *Quartz phenocrysts*

The microthermometric behavior of silicate melt inclusions in the Ph-bright cores and Ph-dull rims of individual phenocrysts is remarkably consistent throughout FIAs contained within single phenocrysts (Fig. 4.10) and between individual phenocrysts hosted within the same aplite band. During high-temperature experiments, most silicate melt inclusions show signs of melting at ~650-780 °C. In the case of melt inclusion assemblages that include large volume fractions of vapor prior to heating, melting of crystalline phases is observed as low as 100-200 °C with the formation of a translucent liquid phase and the coalescence of the vapor phase into a spherical bubble. In most FIAs, the silicate portion of inclusions is totally molten at 850-900 °C, and coexists with a volatile bubble that commonly persists to >1000 °C. In FIAs of silicate melt inclusions hosted in Ph-bright quartz, the oval area containing the volatile bubble commonly contains a white granular or square mass that appears to melt at 800-850 °C concurrent with the formation of a yellowish liquid that envelops a vapor bubble. Homogenization of the vapor phase into the yellowish liquid occurs at 900-950 °C. Above 1050 °C, inclusions shows signs of deformation (plasticity of the host) and were not heated further. Upon quenching, the immiscible liquid crystallizes to a black, granular mass within each bubble. This behavior is not observed in melt inclusions hosted in Ph-dull rims of quartz phenocrysts nor those in the monomineralic quartz bands.

The microthermometric behavior of brine inclusions in the same, coeval assemblages with silicate melt inclusions in Ph-bright quartz is consistent within an FIA and shows little variability between phenocryst-hosted brine inclusions within a single aplite band. The majority

of brine inclusions homogenize via vapor disappearance at 510-760 °C (avg. 640 °C). Halite melting occurs at 326-519 °C and indicates salinities between 42-62±7 wt% NaCl eq (avg. 50 wt% NaCl eq). In many cases, brine inclusions homogenize within <100°C of the onset of melting in coeval silicate melt inclusions.

Most brine inclusions in the Ph-dull rims of phenocrysts homogenize via vapor disappearance at temperatures between 375 and 791 °C, following halite melting between 300 and 761 °C. Salinities of brine inclusions hosted in Ph-dull quartz are mostly from 31 to 48 wt% NaCl eq., but are occasionally as high as 95 wt% NaCl eq. in inclusions that homogenize at >700 °C. Opaque phases in these inclusions typically shrink by ~60% during heating but do not fully dissolve. A summary of microthermometric data from brine inclusions hosted in quartz phenocrysts is shown in Tables 4.3 and 4.6

## 4.8 SEM-EDS and EPMA of homogenized melt inclusions

Energy dispersive spectroscopy maps of homogenized melt inclusions (Fig. 4.11) show that the glass in these inclusions is composed consistently of Al, K, Na, Ca, and Fe. In inclusions that still contain vapor and/or a salt globule prior to quenching, the inner walls of the bubble are commonly lined with discrete Cl- and Cu-rich phases after quenching.

The major-element compositions of homogenized melt inclusions, plus mineral grains within some unheated inclusions, are shown in Table 4.7. Analyses of crystalline solids in phenocryst-hosted melt inclusions show compositions corresponding to endmember muscovite and potassium feldspar (Table 4.7). These data points are plotted alongside data from homogenized melt inclusions and reference points representing endmember muscovite, orthoclase, and quartz in Fig. 4.12. Homogenized melt inclusions from monomineralic quartz bands and quartz phenocrysts have similar major-element compositions dominated by $SiO_2$, $Al_2O_3$, and $K_2O$, with lesser amounts of $CaO$, $Na_2O$, $MgO$, $FeO$ and $Cu_2O$, plus variable $P_2O_5$. Sulfur was above the limit of detection in only two analyses. In $K_2O$–$Al_2O_3$–$SiO_2$ space (Fig. 4.12a,b), all analyzed inclusions plot along well defined linear arrays that extend from bulk rock composition to those of muscovite, quartz and potassium feldspar. These trends are consistent with inclusions containing various proportions of trapped melt, muscovite, and orthoclase within all the analyzed silicate melt inclusions, as well as varying degrees of laboratory overheating (artificially high $SiO_2$, resulting from variable dissolution host quartz into the inclusion) and

interference from the host quartz during EPMA analysis. Nevertheless, the majority of analyses cluster around bulk rock composition of the Saginaw Hill stock (R.E. Greig, pers. commun., 2020) and hence likely reflect the least-contaminated melt compositions.


**4.9 Laser ablation ICP-MS analyses of inclusions**

Laser ablation data from individual brine and melt inclusions and host quartz are summarized in Table 4.8-4.14. The presence of particular elements in each inclusion was determined after examination of the time-resolved signal of each analysis, and the data presented here represent *only* those elements that showed unambiguous transient signals above the host matrix when the inclusion was breached (Fig. 4.13).

*4.9.1 Brine inclusions*

Brine inclusions have consistent compositions within a given assemblage, dominated by Na, K, Mn, and Fe. Phenocryst-hosted brine inclusions have median concentrations of Na, K, Mn, and Fe of 6 wt%, 3.5 wt%, 1 wt%, and 3.7 wt%, respectively. Copper, Pb, and Zn concentrations are variable but generally >1000 ppm and in some cases up to ~1 wt%. Brine inclusions hosted in monomineralic quartz bands have similar compositions dominated by Na, K, Mn, and Fe (median values of 8 wt%, 6 wt%, 1.5 wt%, and 5 wt%, respectively) and commonly contain Cu, Zn, and Pb in concentrations >1000 ppm. In one brine assemblage, Fe and Cu were notably higher with median concentrations of 15 wt% and ~1 wt%, respectively. However, the metal content of brine inclusions show very little variation with respect to paragenetic sequence (Fig. 4.14 - 4.16) with one exception being Cu which shows a subtle decrease in primary and pseudo-secondary inclusions in UST-dull quartz over time. This is the case in brine inclusions in both monomineralic quartz bands and phenocrysts which have similar metal content, but which differ in terms of their degree of fractionation with in a single UST band as indicated by Cs content (Audétat and Pettke, 2003).

*4.9.2 Melt inclusions*

Raw (uncorrected) LA- ICP-MS analyses of individual melt inclusions in quartz phenocrysts and monomineralic quartz bands indicate compositions that are commonly

anomalously rich in Al and K, similar to the results of EPMA analyses of homogenized melt inclusion glasses. In all cases, these melt inclusions with elevated Al and K plot along linear arrays that project from bulk rock towards the compositions of muscovite and potassium feldspar, indicating heterogeneous trapping of the latter two phases (Fig. 4.12). As such, we applied a mathematical correction to subtract aliquots of muscovite and/or K-feldspar from each raw analysis, to estimate the trace-element concentrations of the melt phase. To do so, we used the following constraints: The bulk (analytical) K and Al concentrations (and indeed, concentrations of any other element M) can be expressed by mass balance as $[M]_{bulk} = [M]_{melt}F_{melt} + [M]_{musc}F_{musc} + [M]_{ksp}F_{ksp}$, where [M] is concentration of element (M = K or Al) in ppm and $F_i$ is mass fraction of phase i (melt, musc = muscovite, and ksp = potassium feldspar). Setting the concentrations of K and Al in muscovite and potassium feldspar as the stoichiometric values, and those in melt according to the bulk rock composition (R.E. Greig, pers. commun., 2020), this creates a system of two equations with two unknowns ($F_{musc}$ and $F_{ksp}$, where $F_{melt} = 1 - F_{musc} - F_{ksp}$). We solved this system of equations by standard algebraic techniques, and then re-calculated the (corrected) trace element contents of the melt by subtracting the appropriate mass fractions of trapped muscovite and potassium feldspar. To correct for trace elements that are compatible with muscovite and potassium feldspar (particularly alkalis: Li, Rb, Cs), we assumed the average values for these two phases reported by Runyon et al. (2019). Summaries of both corrected and uncorrected data are shown in tables 4.9 and 4.10, and 4.11 and 4.12 and, respectively.

Melt inclusions hosted in both monomineralic quartz bands and quartz phenocrysts have similar trace element compositions and are described together here. After correction for trapped muscovite and potassium feldspar, the estimated concentrations of Al and K in the melt conform to the bulk rock compositions (8.6 wt% and 3.6 wt%, respectively). Metal concentrations are variable with Cu, Zn, and Mn all typically >1000 ppm (median concentrations of 1250 ppm, 1700 ppm, and 2720 ppm, respectively) and Pb and Mo commonly >100 ppm (median concentrations of 280 ppm, 240 ppm, respectively) when detected. Titanium and Na are present in most analysis and were in some cases as high as 5.8 wt% and 5.4 wt% (median values of 9000 ppm and ~2 wt%), respectively. Boron and Li are both commonly detected and in some analysis exceeded 1000 ppm (median concentrations of 1080 ppm and 600 ppm, respectively).

**4.10 Laser ablation ICP-MS analyses of quartz**

Generally, quartz phenocrysts and monomineralic quartz bands have very similar trace element compositions and mostly show little systematic variation with respect to quartz type or paragenetic sequence (Table 4.13).

*4.10.1 Phenocrysts*

The trace element contents of Ph-bright and Ph-dull quartz are virtually identical and were dominated by Al, K, and Ti (Fig. 4.13). Aluminum and K show wide ranges of 60-1600 ppm and 3-1800 ppm, respectively, and are typically higher in Ph-bright quartz (typically >100 ppm) compared to Ph-dull quartz. Titanium concentrations show little variation between phenocryst cores and rims and have an overall range of 50-590 ppm. Lithium is also detected in nearly all analyses but shows no systematic spatial variation and has a low range of 3-30 ppm. Sodium, Fe, and Mn are all highly variable.

*4.10.2 Monomineralic quartz bands*

The ranges of trace element concentrations for Al, K and Ti in UST-bright and UST-dull quartz show significant overlap. However, the range of concentrations of all trace elements in UST-dull quartz are typically more variable than in the corresponding UST-bright quartz within the same band, and consistently tend towards the higher end of each compositional range (Fig. 4.16). In most analyses, Al, K, and Ti in UST-bright quartz are 90-510, 4-630, and 90-470 ppm, respectively. UST-dull quartz shows similar Al, K, and Ti concentrations of 80-830, 40-570, and 110-590 ppm, respectively. However, concentrations of all trace elements are in some cases significantly higher, with quartz from one monomineralic band having K, Ti and Fe concentrations all exceeding 1000 ppm. Lithium is detected in all analysis and was mostly between 4-30 ppm.

*4.10.3 Ti-in-quartz thermobarometry*

An estimated emplacement depth of 0.5-1.5 km for Saginaw Hill (based on contact relationship between Saginaw Hill and extrusive lithologies in the Tucson Mountains; R.E. Greig, pers. commun., 2020) was used in order to evaluate the temperature of formation of

quartz in the Saginaw Hill system. Assuming a lithostatic pressure gradient, estimated ambient pressure of formation for Saginaw Hill is ~165-500 bar. For most analyses, these conditions yield a median range of minimum temperatures of 630-680 °C (overall range of 525-880 °C) and 690-740 °C (overall range of 565-1880 °C) for the crystallization of quartz phenocrysts and monomineralic quartz bands, respectively (Table 4.16). The overall larger range of temperatures for monomineralic quartz bands reflects the fact that trace element concentrations in these latter quartz grains were in some cases anomalously high and thus yielded temperatures >1000 °C. These temperatures are unreasonably high in comparison to the homogenization temperatures for silicate melt inclusions in the system and in excess of the $H_2O$-saturated granite solidus. Thus, these temperatures are not representative for this system and likely reflect high-quartz growth rates during formation. Excluding these outliers, the range in minimum temperatures for monomineralic quartz bands is more restricted, with a median value of 650-700 °C.

## 4.11 Discussion

### 4.11.1 Formation and preservation of USTs in a porphyry-Cu context

The petrologic characteristics of the quartz monzonite porphyry are generally similar to those associated with major porphyry-Cu-Au systems (Muntean and Einaudi, 2000; Koděra et al., 2014) – the main distinguishing feature of Saginaw Hill compared to more productive systems is its relatively small size. Following emplacement, the Saginaw Hill pluton underwent a period of active degassing, during which fluids accumulated, giving rise to a transition to a dominantly hydrothermal regime. A key line of evidence for this progressive transition is the inward zonation from comb textured veins, through UST bands, into a single massive quartz vein which runs through the apex of the main stock of Saginaw Hill quartz latite porphyry (Fig. 4.2; Frank, 1970). This transition in vein types arose from the progressive accumulation of hydrothermal fluid in this system as it crystallized, and parallels a transition from apparently lower-salinity fluids with lesser Cu contents, to later fluids that were highly saline and Cu rich. These overall trends in fluid salinities and metal contents are consistent with general predictions for shallow porphyries based on numerical modeling (Cline and Bodnar, 1991).

Early in its crystallization history, the Saginaw Hill quartz latite porphyry exsolved limited amounts of hydrothermal fluid which formed an outer zone of comb textured veins along the periphery of the system (Frank, 1970). These earliest veins are quite limited in extent at Saginaw Hill, suggesting relatively low volumes of hydrothermal fluid produced and expelled during this stage. As the front of crystallization progressed inward, increased fluid volumes led to the cyclic formation of UST bands. High fluid volumes seem to be a prerequisite for the formation of well-developed euhedral bands of monomineralic quartz (Lowenstern and Sinclair, 1996), and would be expected at high degrees of crystallinity and fractionation at late stage (Cline and Bodnar, 1991). As the degree of crystallinity and fractionation increases, the salinity and metal content of the exsolved fluids would concomitantly increase (Cline and Bodnar, 1991), evinced at Saginaw Hill by the presence of high-salinity, Cu-rich brine inclusions with fairly consistent compositions throughout all studied UST bands. During this UST stage, the system evidently cycles repeatedly between igneous crystallization and hydrothermal fluid release. Our results indicate that the melt composition (recorded by silicate melt inclusions in UST bands and quartz phenocrysts) and that of the exsolved brines remained essentially constant throughout this period, suggesting crystallization at approximately a eutectic liquid composition.

At the very late stages of fractionation, the final gasp of highly saline and metal-rich hydrothermal fluid was expelled from the system, giving rise to the massive, Cu-mineralized quartz vein which runs through the center of the system. This quartz vein was the site of significant flux of the most Cu rich (as well as Ag and Au rich) fluids, and it is the most Cu-rich feature in the Saginaw Hill system (as evidenced by the development of the Papago Queen mine along its eastern end). This latest-stage hydrothermal feature at Saginaw Hill may be considered analogous to the quartz core of a granitic pegmatite – the final pulse of silica-charged aqueous fluid, released with particularly high flux rate when the last remaining silicate melt was exhausted (London, 2009).

Unidirectional solidification textures are not commonly reported in porphyry-Cu-[Au] systems. This is likely due in part to the fact that the USTs in most porphyry systems would be hosted in the more fractionated portions of intrusive rocks that underlie the sulfide ore bodies and do not commonly host economic mineralization. As a result, areas which host USTs would not generally be the focus of exploration and development activities which would expose these features for study (Seedorff et al., 2008). Moreover, the intrusive phases which host USTs are

formed via multiple overprinting episodes of magma intrusion and hydrothermal fluid flux. During these episodes, any well-developed pre-existing UST bands would undergo significant deformation due to the high temperature conditions at depth, and in some cases might be wholly resorbed by paragenetically later intrusive phases. At Saginaw Hill, the small size, shallow emplacement, and essentially monogenetic character of the main mineralizing stock helped preserve UST bands. Thus, USTs in the Saginaw Hill system provide a somewhat unique snapshot of the evolution of a single, highly fractionated intrusive phase undergoing solidification and exsolution of metal-rich fluids.

*4.11.2 Temperature and pressure of formation of USTs at Saginaw Hill*

Homogenization temperatures of aqueous brine inclusions in the same assemblages with coeval vapor inclusions indicate trapping temperatures ranging from 510 to 760 °C, with a median value of 640 °C. This temperature is also in accord with temperatures estimated based on Ti-in-quartz phenocrysts (630-677 °C), which seem to be the most reliable of the Ti-in-quartz estimates based on fine zonation indicative of slow growth under magmatic conditions (Huang and Audétat, 2012; Mercer and Reed, 2013). Thus, an intermediate minimum value of ~650 °C seems to be a representative temperature of formation for USTs in the Saginaw hill system. This temperature is also identical to initial melting temperatures of silicate melt inclusions in the Ph-bright quartz, and consistent with fluid exsolution along the water-saturated solidus of a model haplogranitic melt (Holtz et al., 2001).

In evaluating the accuracy of the Ti-in-quartz results, the activity of titania must be considered. Several lines of evidence suggest that the values reported here based on an assumed $a_{TiO2} = 1$ are reasonable. Firstly, the Ti concentrations of melt inclusions analyzed here consistently exceed 1000 ppm, consistent with the compositions of melt inclusions from the Santa Rita pluton (New Mexico) reported by Huang and Audétat (2012), which those authors determined correspond to $a_{TiO2}$ between 0.88 and 1. Secondly, anatase is a product of hydrothermal alteration at Saginaw Hill, indicating that the hydrothermal fluid was in equilibrium with anatase. Thirdly, anatase is occasionally (inconsistently) observed within fluid inclusions in the UST samples, suggesting heterogeneous entrapment, which again indicates that the fluids were anatase-saturated. Collectively, these observations suggest that the calculated range of minimum temperatures based on Ti-in-quartz are likely close to the true temperatures of

formation. We also evaluated the potential impact of a lower hypothetical $a_{TiO2}$ for this system assuming a value of $a_{TiO2} = 0.5$ and the calibration of Thomas et al., (2010). The results differ by less than 40 °C on average compared to our calculations based on the calibration of Huang and Audétat, 2012 (Table 4.16). Thus, we interpret that the range of minimum temperatures calculated for quartz phenocrysts are representative of UST formation at ~650 °C at Saginaw Hill.

Pressure of UST formation at Saginaw Hill evidently varied repeatedly through the aforementioned process of gradual pressure buildup followed by violent release. During the stage of pressure buildup, petrographic evidence suggests that the exsolved magmatic-hydrothermal fluid was a single-phase brine, because coeval vapor-rich inclusions are absent from this stage. Based on a median brine salinity of 49 wt% NaCl eq., the minimum pressure required to sustain single-phase conditions was approximately 850 bar (Fig. 4.17), which places the conditions of fluid exsolution close to (though at temperatures still slightly below) the water-saturated solidus of a haplogranitic melt (Holtz et al., 2001). Pressure release by fracturing and fluid expulsion evidently drove the system below the liquid-vapor solvus, generating brine inclusions with coeval vapor. In some cases, evidence suggests that pressure dropped sufficiently to intersect the liquid-vapor-halite curve, which resulted in heterogeneous trapping of brine plus halite alongside coeval vapor-rich inclusions (Lecumberri-Sanchez et al., 2012; 2015; 2020). In the latter case, the phase equilibria correspond to pressures of ~300 bar or lower at 650 °C (Fig. 4.17). We infer that the upper pressure estimate of ~850 bar probably corresponds to pressures in excess of lithostatic, as required for hydraulic fracturing (Weis et al., 2012), whereas the lower estimate of <300 bar corresponds to hydrostatic pressure.

*4.11.3 Direct exsolution of hypersaline brine and boiling during dynamic pressure fluctuations*

The observation of coeval high salinity brine and melt inclusions in the cores of quartz phenocrysts in aplite bands within the Saginaw Hill quartz latite porphyry provides direct evidence for the exsolution of single phase brine from the silicate melt. This is interpretation is supported by the homogenization of brine inclusions and abrupt melting of silicate melt inclusions within <100 °C during high-temperature experiments.

The presence of abundant vapor inclusions and boiling assemblages in UST-dull and Ph-dull quartz indicates that a decrease in pressure coincides with the fracturing events which

truncate the growth of Ph-bright and UST-bright quartz. This decrease in pressure would have caused brine accumulated at the site of UST formation to intersect the liquid-vapor curve causing the formation of an immiscible vapor and an abrupt increase in brine salinity as high as to ~62±7 °C (Fig. 4.17). Concurrently, the solubility of quartz in the hydrothermal solution would also decrease as a result of decreasing pressure (Fig. 4.18), which would drive the rapid precipitation of UST-dull and Ph-Dull quartz. This is reflected in relatively high and variable trace element contents (and correspondingly high calculated minimum Ti-in-quartz temperatures) of both quartz generations, which we interpret as a result of high quartz growth rates. Furthermore, the majority of primary and pseudo-secondary inclusions in UST-dull and Ph-dull quartz homogenize by halite melting but show inconsistent liquid-vapor homogenization temperatures, consistent with the system having intersected the liquid-vapor-halite curve in response to the decrease in pressure (Lecumberri-Sanchez et al., 2012; 2015; 2020). This would result in the precipitation of halite at the site of UST formation and indicates that pressure conditions were reduced to <360 bar (Fig. 4.17). Both the precipitation of halite and the rapid growth of quartz would in turn effectively reseal the system by plugging the fluid pathways (Fournier, 1999; Rusk and Reed, 2002), allowing for fluid pressure to build up once again, and hence initiating a new cycle of fluid accumulation. Over time, the repetition of this process during UST formation resulted in an oscillatory pressure profile for the Saginaw Hill system (Fig. 4.18).

*5.11.4 Metal partitioning between melt and exsolved hydrothermal fluids*

Fig. 4.19 shows partition coefficients ($D=C_{Brine}/C_{Melt}$) calculated from corrected median concentrations of selected elements across all silicate melt and brine inclusions. These D values are also compared to D values for coeval high salinity brines and silicate melts reported by Zajacz et al. (2008) for the Mt. Malosa and Cuasso al Monte granites. These systems provide a reasonable comparison to Saginaw Hill, as the brines associated with these systems have a similar range in salinities (Mt. Malosa: 32-35 wt% NaCl; Cuasso al Monte: 53-69 wt%), occur alongside coeval vapor-rich inclusions in systems with highly fractionated igneous compositions, and are hosted in miarolitic cavities associated with late-stage degassing. Partition coefficients for most elements analyzed here are generally consistent with those reported by Zajacz et al. (2008). The main exceptions include Li, B, Ba, and Mo, which all showed D values significantly lower at Saginaw Hill compared to the other localities reported by Zajacz et al. (2008). Our

results are particularly unusual in the case of Li and B, which are generally expected to strongly partition into an exsolving aqueous fluid (Audétat and Pettke, 2003; Audétat, 2019). We do not have a definitive explanation of why these elements appear to have partitioned preferentially into the melt at Saginaw Hill, but we speculatively consider that this behavior may reflect the late, probably near-eutectic liquid fractionation, which at Saginaw Hill resembles a pegmatitic setting. In granitic pegmatites, Li and B are considered amongst the most important fluxing agents that allow for depression of the solidus (London, 2009). We surmise that at Saginaw Hill, these elements were retained in the late-stage melt in spite of significant degassing, as a result of fractionation towards such minimum-melt compositions.

*4.11.5 Throttling during fluid exsolution and release*

In their model for the formation of porphyry systems Cloos and Sapiie (2013) invoke throttling as a key mechanism which drives and sustains the exsolution of aqueous fluids. Throttling is an adiabatic, inenthapathic process in which a fluid within a restricted reservoir goes from a state of high pressure, low velocity, and restricted volume to a state of low pressure, high velocity, increased volume in response to the opening and venting of the reservoir. In calc-alkaline systems, throttling takes place when aqueous fluids which accumulated in the apices of the magmatic fluid reservoir (Cloos, 2001; Sillitoe, 2010) are allowed to vent during episodes of fracturing and subsequently expand into fracture networks above these systems. The main effects of throttling are to prevent the explosive eruption of the system in response to fluid over-pressure, and to focus the flow of exsolved hydrothermal fluids into a restricted volume where mineralization can be concentrated. Both are important as many calc-alkaline systems have the necessary geochemical properties to permit the formation of a large porphyry system (Cline and Bodnar, 1991) but lack the sustained, focused, and localized period of hydrothermal fluid flux needed to form an economic sulfide ore body (Pasteris, 1996). Throttling also helps sustain the exsolution of aqueous fluids over a prolonged period by repeatedly driving the calc-alkaline melt toward $H_2O$ saturation via adiabatic pressure reduction (Cloos, 2001). These periods of accelerated fluid exsolution in turn will efficiently strip metals from a crystalizing melt via the repeated separation of complex-rich (and metal-rich) aqueous solution from the melt.

The data presented here provide direct evidence for throttling during the growth of UST bands in the Saginaw Hill system (Fig. 4.18). UST-bright and Ph-bright quartz both have

relatively restricted trace element content and this along with the presence of well-developed growth zonation is consistent with the gradual growth of quartz relative to the more anhedral, trace element rich UST-dull Ph-dull quartz. These growth zones are defined by abundant assemblages of melt inclusions and coeval brine inclusions. The growth zonation in UST-bright and Ph-bright quartz is truncated by Ph-dull and UST-dull quartz, both of which show greater variability of trace element contents, in some cases up to very high (anomalous) values. For example, calculated Ti-in-quartz temperatures for some monomineralic quartz bands exceed 1000 °C; we do not consider these calculated values as representing true crystallization temperatures, and rather, we infer that these anomalously high values reflect chemical disequilibrium as a result of fast growth rates. This, together with the occurrence of abundant boiling assemblages, indicates that precipitation of Ph-dull and UST-dull quartz coincided with an abrupt drop in pressure, fluid boiling, and concomitant rapid quartz growth. Simultaneously, the pressure drop drove enhanced fluid exsolution from the silicate melt (Cloos, 2001), owing to the pressure dependence of $H_2O$ solubility (Burnham, 1997). At high degrees of igneous fractionation, the pressure drop would also give rise to higher concentrations of Cu in the exsolved fluid (Cline and Bodnar, 1991). Each individual UST band at Saginaw Hill displays this pattern, indicating that this process of fluid buildup and release was cyclic over the duration of UST formation.

Large quantities of aqueous fluid are needed to form economic accumulations of sulfide mineralization (Sillitoe, 2010). Thus, the number of times a system undergoes cycles of throttling (i.e. the number of times aqueous fluids are released) has a direct relationship to the size and scale of mineralization in any given system. The UST bands at Saginaw hill are ~5-10 m in thickness with each individual aplite and monomineralic quartz band having a median total thickness of ~15.5 mm. If each UST band represents a single cycle of throttling, then the Saginaw Hill system apparently underwent at least 300 to 650 individual cycles of pressure buildup and release. Numerical modeling indicates that a single pulse of fluid overpressure occurs on a timeframe of ~1/year (Weis et al., 2012). This in turn suggests that focused fluid flux in response to throttling occurred over ~300-650 years at Saginaw Hill – a relatively short time frame compared to larger, economic porphyry systems which may persist over tens of thousands of years (Mercer et al., 2015; Large et al., 2020). The very restricted time scale of focused fluid

flux at Saginaw Hill likely reflects the small size and shallow depth of emplacement of the Saginaw Hill stock.

*4.11.6 Fractionation, peraluminous minimum melt composition, and a link to porphyry roots*

Petrographic evidence and raw (uncorrected) EPMA and LA-ICP-MS data of melt inclusions provide abundant evidence of heterogeneous trapping of muscovite. Hence, our results indicate melt aluminum saturation indices (ASI; Zen, 1988; Frost and Frost 2008) in excess of 1, i.e. peraluminous liquid composition. This is somewhat unexpected because the bulk rock composition of the Saginaw Hill quartz latite porphyry is metaluminous. Hence, our results seem to suggest that this overall metaluminous pluton tended towards peraluminous liquid compositions at the high degrees of fractionation (evidently, near minimum-melt compositions) during UST formation.

The evolution of this system toward a late-stage, muscovite-saturated peraluminous composition is consistent with observations of late-stage, fractionated melts in the deep roots of porphyry systems (Seedorff et al., 2008; Runyon et al., 2017). Coarse-muscovite veins and alteration are common features in the mineralized portions of silicic porphyry Mo deposits, but are generally restricted to the unmineralized deep roots of more intermediate-composition, Cu-rich porphyries (Runyon et al., 2017, 2019). Paragenetic relationships, δD values of muscovite, and Al-in-hornblende thermobarometry consistently indicate that coarse-muscovite veins in the latter context record the very late-stage, highly fractionated portion of igneous evolution (i.e. after a high degree of crystallization). These observations suggest an igneous evolution towards muscovite saturation in the late stages. Saginaw Hill differs from the majority of porphyry Cu systems in which such features have been described, in that muscovite saturation seems to have taken place at the shallowest levels of the crystallizing cupola, where USTs formed. We interpret that the small size and shallow depth of emplacement of the Saginaw Hill pluton allowed for high degrees of fractionation even at the shallowest levels. Hence, in effect the "roots" of the magmatic system are essentially superimposed on the cupola, rather than being restricted to deeper levels.

**4.12 Conclusions**

The formation of UST bands took place relatively late in the paragenesis of Saginaw Hill, as is illustrated by the fairly consistent compositions of melt inclusions, suggesting fractionation to a near-eutectic composition. Moreover, the compositions of associated brine inclusions were fairly Cu-rich (as illustrated by the presence of abundant chalcopyrite in most brine inclusions, high Cu concentrations by LA-ICP-MS, and elevated Cu in the bubbles of melt inclusions) and highly saline, both of which would be expected with high degrees of crystallization, late in the evolution of a shallow pluton (Cline and Bodnar, 1991). In addition, the presence of abundant, heterogeneously trapped muscovite in melt inclusions indicates that this overall metaluminous system tended towards muscovite saturation late in its evolution. This is consistent with the observation of late-stage fluids in porphyry systems having highly fractionated, Al-enriched compositions which give rise to the formation of late-stage coarse-muscovite alteration in the roots of these system. In the case of Saginaw Hill, the small size and shallow depth allowed for these features to be superimposed on the mineralized cupola.

The paragenesis and composition of quartz-hosted fluid and melt inclusions in UST bands from Saginaw Hill are consistent with UST formation via rhythmic cycles of fluid exsolution, accumulation and release (i.e. throttling) from a highly-fractionated melt. Fluid exsolution took place at fairly stable temperatures conditions of ~650 °C, and pressures that ranged from ~850 to <300 bar. During the initial phase of each cycle, the silicate melt directly exsolved a single-phase, high-salinity brine. Accumulation of the exsolving fluid led to fluid overpressure and eventual rupturing, evinced by truncation of growth zones in UST-bright and Ph-bright quartz by fractures and quartz overgrowths. Rupturing in turn led to an abrupt decrease in pressure, which caused the hydrothermal fluid to boil and drove the rapid precipitation of quartz, evinced by the high and relatively variable trace element contents of UST-dull and Ph-dull quartz. Precipitation of quartz resealed the system and allowed for reestablishment of high fluid pressures. This subsequently initiated a new cycle of UST formation during a sustained period of fluid exsolution, accumulation, and release. Repetition of this cyclic process led to the formation of thick sequences of UST bands and gave rise to localized Cu-Ag-Au mineralization. Over a longer timeframe and on a larger scale, calc-alkaline composite plutons composed of multiple magmatic pulses that undergo otherwise similar processes of fluid release would give rise to large porphyry-type ore bodies; at Saginaw Hill, the limited size of the causative pluton

did not allow for such voluminous mineralization, but nevertheless permitted exceptional preservation of these features.

**4.13 References**

Allan, M.M., Yardley, B.W.D, Forbes, L.J., Shmulovich, K.I., Banks, D.A., and Shepherd, T.J., 2005, Validation of LA-ICP-MS fluid inclusion analysis with synthetic fluid inclusions: American Mineralogist, v. 90, p.1767-1775.

Armstrong, J.T., 1995, CITZAF: A package of correction programs for the quantitative electron microbeam X-ray-analysis of thick polished materials, thin-films, and particles: Microbeam Analysis v. 4, p. 177-200.

Audétat A. and Pettke, T., 2003, The magmatic-hydrothermal evolution of two barren granites: a melt and fluid inclusion study of the Rito del Medio and Canada Pinabete plutons in northern New Mexico (USA): Geochimica et Cosmochimica Acta, v. 67, p. 97–121.

Audétat, A., Günther, D., and Heinrich, C.A., 1998, Formation of a magmatic-hydrothermal ore deposit: Insights with LA-ICP-MS analysis of fluid inclusions: Science, v. 279 p. 2061-2094.

Audétat, A., Günther, D., and Heinrich, C.A., 2000, Causes for large-scale metal zonation around mineralized plutons: Fluid inclusion LA-ICP-MS evidence from the Mole Granite, Australia: Economic Geology, v. 95, p. 1563-1581.

Bodnar, R.J., Lecumberri-Sanchez, P., Moncada, D., and Steele-MacInnis, M., 2014, Fluid inclusions in Hydrothermal Ore Deposits: Treatise on Geochemistry, Second Edition v. 13, p. 119-142.

Burnham, C.W., and Davis, N.F., 1971, The role of H2O in silicate melts 1. P-V-T relations in the system $NaAlSi_3O_8$-$H_2O$ to 10 kilobars and 1000°C: American Journal of Science, v. 270, p. 54-79.

Campos, E.A., Touret, J.L.R., and Nikogosian, I., 2006, Magmatic fluid inclusions from the Zaldívar Deposit, Northern Chile: the role of early metal-bearing fluids in a porphyry copper system: Resource Geology, v. 56, p. 1–8.

Carten, R.B., Geraghty, E.P., Walker, B.M., and Shannon, J.R., 1988, Cyclic development of igneous features and their relationship to high-temperature hydrothermal features in the

Henderson porphyry molybdenum deposit, Colorado: Economic Geology, v. 83, p. 266-296.

Cline, J.S., and Bodnar, R.J., 1991, Can economic porphyry copper mineralization be generated by a typical calc-alkaline melt?: Journal of Geophysical Research, v. 96, p. 8113–8126

Cloos, M., 2001, Bubbling magma chambers, cupolas, and porphyry copper deposits: International Geology Review, v. 43, p. 285–311.

Cloos, M., and Sapiie, B., 2013, Porphyry copper deposits: strike–slip faulting and throttling cupolas: International Geology Review, v. 55, p. 43–65.

Donovan, J.J., Kremser, D., Fournelle, J.H., and Goemann, K., 2015, Probe for EPMA: Acquisition, automation and analysis, version 11: Eugene, Oregon, Probe Software, Inc., http://www.probesoftware.com.

Donovan, J.J., Lowers, H.A., and Rusk, B.G., 2011, Improved electron probe microanalysis of trace elements in quartz: American Mineralogist, v. 96, p. 274-282.

Erdenebayar, J., Ogata, T., Imai, A., and Sereenen, J., 2014, Textural and chemical evolution of unidirectional solidification textures in highly differentiated granitic rocks at Kharaatyagaan, central Mongolia: Resource Geology, v. 64, p. 283–300

Fournier, R.O., 1999, Hydrothermal processes related to movement of fluid from plastic into brittle rock in the magmatic-epithermal environment: Economic Geology, v. 94, p. 1193–1211.

Frank, T.R., 1970, Geology and mineralization in the Saginaw hill area, Pima County, Arizona: PhD Dissertation, The University of Arizona, Tucson AZ USA, 151 pp.

Frost, B.R., and Frost, C.D., 2008, A Geochemical Classification for Feldspathic Igneous Rocks: Journal of Petrology, v. 49, p. 1955-1969.

Goldstein, R.H., and Reynolds, T.J., 1994, Systematics of fluid inclusions in diagenetic minerals: SEPM Short Course, v. 31, p. 213.

Guillong, M., Meier, D. L., Allan, M.M., Heinrich, C.A., and Yardley, B.W., 2008, SILLS: A MATLAB-based program for the reduction of laser ablation ICP-MS data of homogeneous materials and inclusions: Mineralogical Association of Canada Short Course Series, v. 40, p. 328–333.

Halter W. E., Pettke T., Heinrich C.A., and Rothen-Rutishauser, B., 2002, Major to trace element analysis of melt inclusions by laser-ablation ICP-MS: methods of quantification: Chemical Geology, v. 183, p. 63–86.

Harris, A.C., Kamenetsky, V.S., White, N.C., van Achterbergh, E., and Ryan, C.G., 2004, Melt inclusions in veins: linking magmas and porphyry Cu Deposits: Science, v. 302, p. 2109-2111.

Holtz, F., Becker, A., Freise, M., and Johannes, W., 2001, The water-under- saturated and dry Qz-Ab-Or system revisited. Experimental results at very low water activities and geological implications: Contributions to Mineralogy and Petrology, v. 141, p. 347−357.

Huang, R., and Audétat, A., 2012, The titanium-in-quartz (TitaniQ) thermobarometer: a critical examination and re-calibration: Geochimica et Cosmochimica Acta, v. 84, p. 75–89.

Kirkham, R. V., and Sinclair, W. D., 1988, Comb quartz layers in felsic intrusions and their relationship to porphyry deposits: *in* Taylor, R. P. and Strong, D. F. (eds) Recent advances in the geology of granite-related mineral deposits: Canadian Institute of Mining and Metallurgy, Special Volume 39, p. 50-71

Klemm, L. M., Pettke, T., and Heinrich, C. A., 2008, Fluid and source magma evolution of the Questa porphyry Mo deposit, New Mexico, USA: Mineralium Deposita, v. 43, p. 533–552.

Klyukin, Y.I., Lecumberri-Sanchez, P., Steele-MacInnis, M., and Bodnar, R.J., 2019, Fluid inclusion phase ratios, compositions and densities, from ambient temperature to homogenization, based on PVTX properties of $H_2O$-NaCl: Earth-Science Reviews, v. 198, p. 1-16.

Koděra, P., Heinrich, C.A., Wälle, M., and Lexa, J. (2014) Magmatic salt melt and vapor: Extreme fluids forming porphyry gold deposits in shallow sub volcanic settings: Geology, v.42, p. 495-498.

Lafuente, B., Downs, R.T., Yang, H., and Stone, N., 2015, The power of databases: the RRUFF project: *in* Highlights in mineralogical crystallography, T Armbruster and R M Danisi, eds. Berlin, Germany, W. De Gruyter, 1-30.

Large, S.J.E., Wotzlaw, J.F., Guillong, M., von Quadt, A., and Heinrich, C.A., 2020, Resolving the timescales of magmatic and hydrothermal processes associated with porphyry deposit formation using zircon U–Pb petrochronology: Geochronology, v. 2, p. 209-230.

Leach, A.M., and Hieftje, G.M., 2000, Methods for shot-to-shot normalization in laser ablation with an inductively coupled plasma time-of-flight mass spectrometer: Journal of Analytical Atomic Spectrometry, v. 15, p. 1121–1124.

Lecumberri-Sanchez, P., Luo, M., Steele-MacInnis, M., Runyon, S.E., Sublett, D.M., Klyukin, Y., and Bodnar, R.J., 2020, Synthetic fluid inclusions XXII: Phase equilibria and microthermometric behavior of fluid inclusions trapped under vapor- and halite-saturated conditions: Geochimica et Cosmochimica Acta, v. 272, p. 78-92.

Lecumberri-Sanchez, P., Steele-MacInnis, M., and Bodnar, R.J., 2012, A numerical model to estimate trapping conditions of fluid inclusions that homogenize by halite disappearance: Geochimica et Cosmochimica Acta, v. 92, p. 14–22

Lecumberri-Sanchez, P., Steele-MacInnis, M., Weis, P., Driesner, T., Bodnar, R.J., 2015, Salt precipitation in magmatic-hydrothermal systems around upper-crustal plutons: Geology v. 43, p. 1063-1066.

Li, J.X., Li, G.M., Qin, K.Z., and Xiao, B., 2011, High-temperature magmatic fluid exsolved from magma at the Duobuza porphyry copper–gold deposit, Northern Tibet: Geofluids, v. 11, p. 134–143.

London, D., 2009, The origin of primary textures in granitic pegmatites: The Canadian Mineralogist. v. 47, p. 697–724.

Lowenstern, J.B., and Sinclair, W.D., 1996, Exsolved magmatic fluid and its role in the formation of comb-layered quartz at the Cretaceous Logtung W-Mo deposit, Yukon Territory, Canada: Transactions of the Royal Society of Edinburgh: Earth Sciences, v. 87, p. 291–303.

Mercer, C.N., and Reed, M.H., 2013, Porphyry Cu-Mo stock work formation by dynamic, transient hydrothermal pulses: mineralogic insights from the deposit at Butte, Montana: Economic Geology, v. 108, p. 1347–1377.

Mercer, C.N., Reed, M.H., and Mercer, C.M., 2015, Time Scales of Porphyry Cu Deposit Formation: Insights from Titanium Diffusion in Quartz: Economic Geology, v. 110, p. 587-602.

Mernagh, T.P., and Mavrogenes, J., 2019, Significance of high temperature fluids and melts in the Grasberg porphyry copper-gold deposit: Chemical Geology, v. 508, p. 210-224.

Muntean, J.L., and Einaudi, M.T., 2001, Porphyry gold deposits of the Refugio district, Maricunga belt, Northern Chile: Economic Geology, v. 95, p. 1445-1472.

Nielsen, C.H., and Sigurdsson, H., 1981, Quantitative methods for electron microprobe analysis of sodium in natural and synthetic glasses: American Mineralogist v. 66, p. 547-552.

Pasteris, J.D., 1996, Mount Pinatubo volcano and "negative" porphyry copper deposits: Geology, v. 24, p. 1075–1078.

Rottier, B., Kouzmanov, K., Bouvier, A.-S., Baumgartner, L.P., W.lle, M., Rezeau, H., Bendez.d, R., and Fontbot., L., 2016, Heterogeneous melt and hypersaline liquid inclusions in shallow porphyry type mineralization as markers of the magmatic-hydrothermal transition (Cerro de Pasco district, Peru): Chemical Geology, v. 447, p. 93–116.

Runyon, S.E., Seedorff, E., Barton, M.D., Steele-MacInnis, M., Lecumberri-Sanchez, P., and Mazdab, F.K., 2019, Coarse muscovite veins and alteration in porphyry systems: Ore Geology Reviews, v. 113, p. 1-32

Runyon, S.E., Steele-MacInnis, M., Seedorff, E., Lecumberri-Sanchez, P., and Mazdab, F.K., 2017, Coarse muscovite veins and alteration deep in the Yerington batholith, Nevada: insights into fluid exsolution in the roots of porphyry copper systems: Mineralium Deposita, v. 52, p. 463-470.

Seedorff, E., and Einaudi, M.T., 2004, Henderson porphyry molybdenum system, Colorado: I. Sequence and abundance of hydrothermal mineral assemblages, flow paths of evolving fluids, and evolutionary style: Economic Geology, v. 99, p. 3-37.

Sillitoe, R.H., 2010, Porphyry copper systems: Economic Geology, v. 105, p. 3–41

Steele-MacInnis, M., Lecumberri-Sanchez, P., and Bodnar, R. J., 2012, HokieFlincs_H$_2$O-NaCl: A Microsoft Excel spreadsheet for interpreting microthermometric data from fluid inclusions based on the PVTX properties of H$_2$O-NaCl: Computers and Geosciences, v. 49, p. 334–337.

Stefanova, E., Driesner, T., Zajacz, Z., Heinrich, C.A., Petrov, P., and Vasilev, Z., 2014, Melt and Fluid Inclusions in Hydrothermal Veins: The Magmatic to Hydrothermal Evolution of the Elatsite Porphyry Cu-Au Deposit, Bulgaria: Economic Geology, v. 109, p. 1359-1381

Thomas, J.B., Watson, E.B., Spear, F.S., Shemella, P.T., Nayak, S.K., and Lanzirotti, A., 2010, TitaniQ under pressure: the effect of pressure and temperature on the solubility of Ti in quartz: Contributions to Mineralogy and Petrology, v. 160, p. 743−759.

Veksler, I.V., 2004, Liquid immiscibility and its role at the magmatic–hydrothermal transition: a summary of experimental studies: Chemical Geology, v. 210, p. 7–31.

Walter, B.F., Steele-MacInnis, M., and Markl, G., 2017, Sulfate brines in fluid inclusions of hydrothermal veins: Compositional determinations in the system H2O-Na-Ca-Cl-SO4: Geochimica et Cosmochimica Acta, v. 209, p. 184-203.

Wark, D.A., and Watson, E.B., 2006, TitaniQ: A titanium-in-quartz geothermometer: Contributions to Mineralogy and Petrology, v. 152, p. 743–754.

Watson, E.B., Wark, D.A., and Thomas, J.B., 2006, Crystallization thermometers for zircon and rutile: Contribution to Mineral Petrology v. 151, p. 413–433.

Webster, J. D., 2004, The exsolution of magmatic hydrosaline chloride liquids: Chemical Geology, v. 210, p. 33–48.

Weis, P., Driesner, T., and Heinrich, C.A., 2012, Porphyry-Copper Ore Shells Form at Stable Pressure-Temperature Fronts Within Dynamic Fluid Plumes: Science, v. 338, p. 1613-1616.

Wilson, A.J., Cooke, D.R., and Harper, B.L., 2003, The Ridgeway gold-copper deposit: A high-grade alkalic porphyry deposit in the Lachlan fold belt, New South Wales, Australia: Economic Geology, 98, 1637–1666.

Zajacz, Z., Halter, W.E., Pettke, T., and Guillong, M., 2008, Determination of fluid/melt partition coefficients by LA-ICPMS analysis of co-existing fluid and silicate melt inclusions: Controls on element partitioning: Geochimica et Cosmochimica Acta, v. 72, p. 2169-2197.

Zen, E., 1988, Phase relations in peraluminous granitic rocks and their petrographic implications: Annual Review of Earth and Planetary Sciences, v. 16, p. 21-52
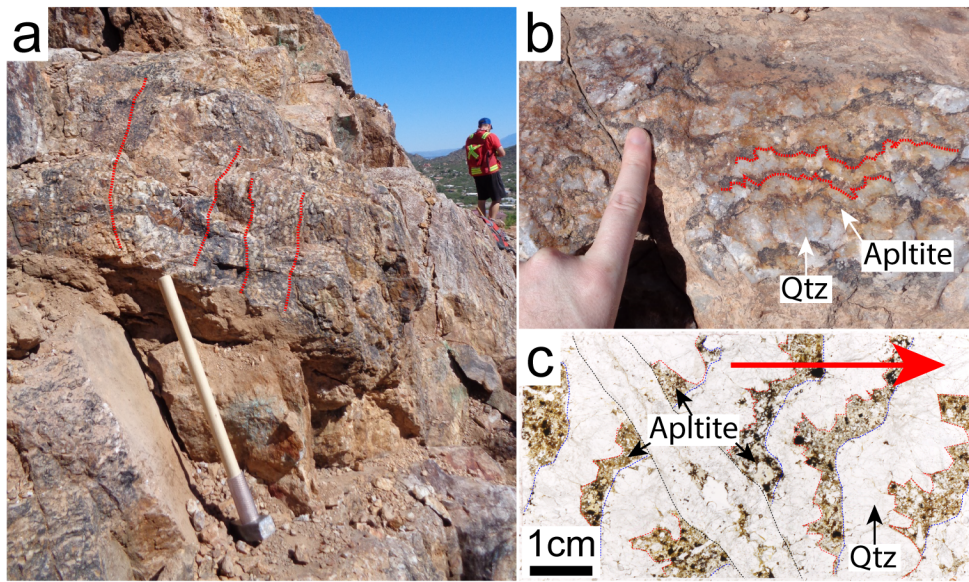
**Figure. 4.1: Unidirectional solidification textures (USTs).**

(a) Outcrops of USTs near the apex of Saginaw Hill. (b) Close up of UST outcrop. Individual monomineralic bands are out lined in red and show well developed euhedral terminations on individual quartz crystals. (c) Thick section showing monomineralic quartz (Qtz) bands overprinted by aplite. The red arrow denotes the solidification direction.
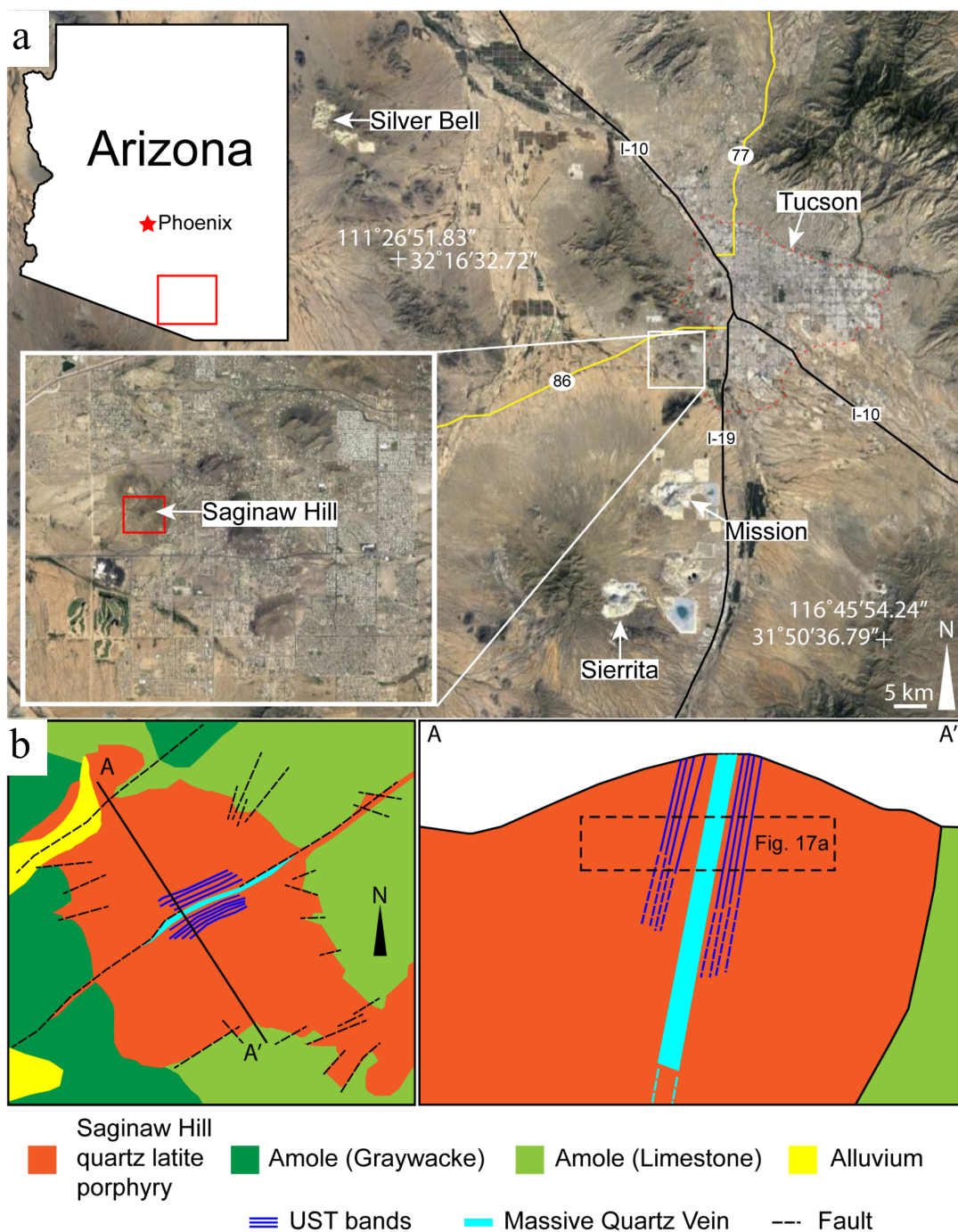
**Figure. 4.2: Map and cross section of the Saginaw Hill system**

(a) Satellite photo showing the location of Saginaw Hill relative to Tucson, Arizona, USA. The area outlined in red in the inset map shows Saginaw Hill as well as the approximate area of the geologic map shown in b. (b) Geologic map and corresponding cross-section of Saginaw Hill.

Fig
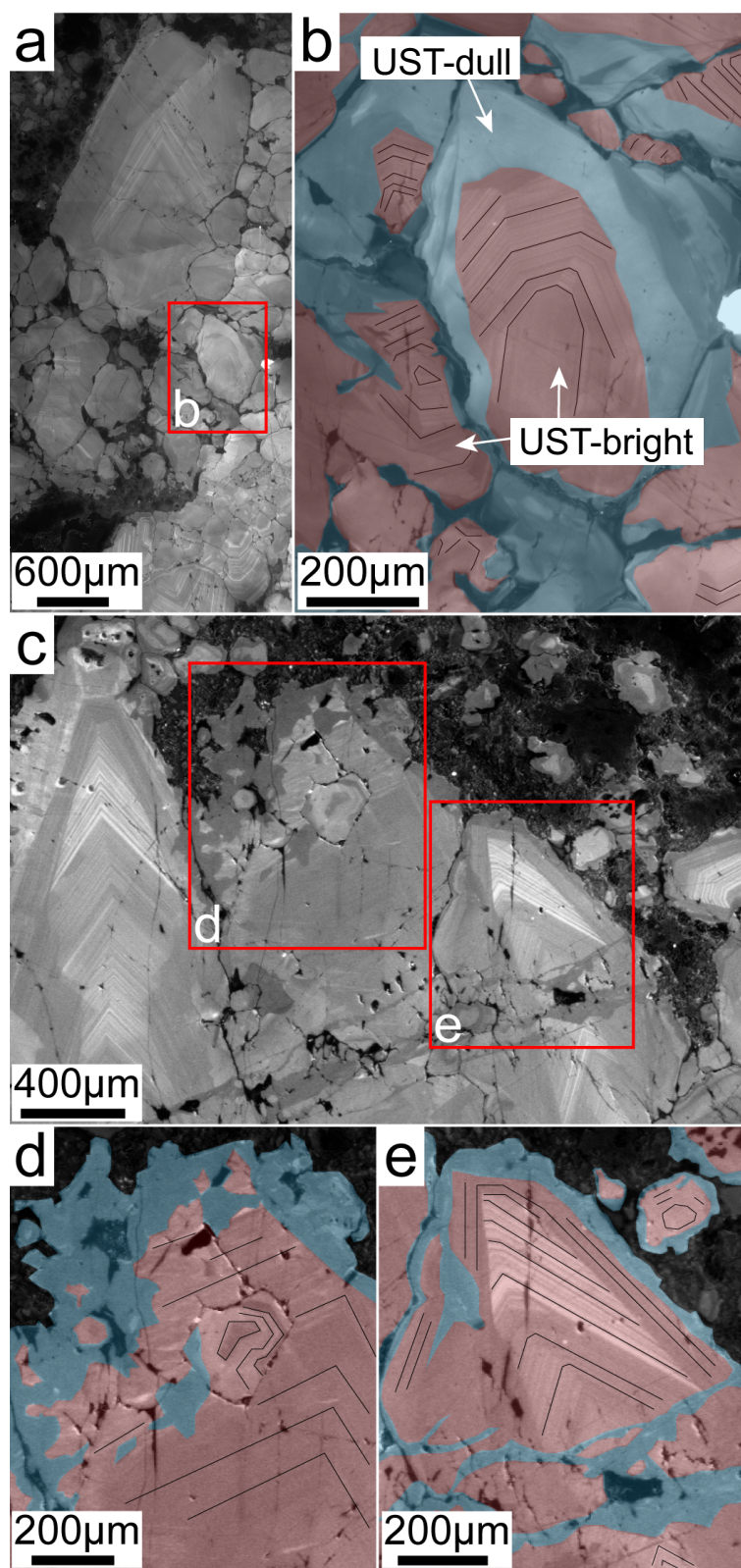
**Figure. 4.3: Annotated cathodoluminescence images of quartz in monomineralic quartz bands.**

(a) Raw cathodoluminescence image of a monomineralic quartz band. The area shown in panel b is outlined in red. (b) Annotated cathodoluminescence image showing UST-bright and UST-dull quartz. (c) Raw cathodoluminescence image of of the euhedral termination quartz crystal in a monomineralic quartz band. Areas shown in d and e are outlined in red. (d, e) Annotated cathodoluminescence image. All images are taken from sample SH-26.
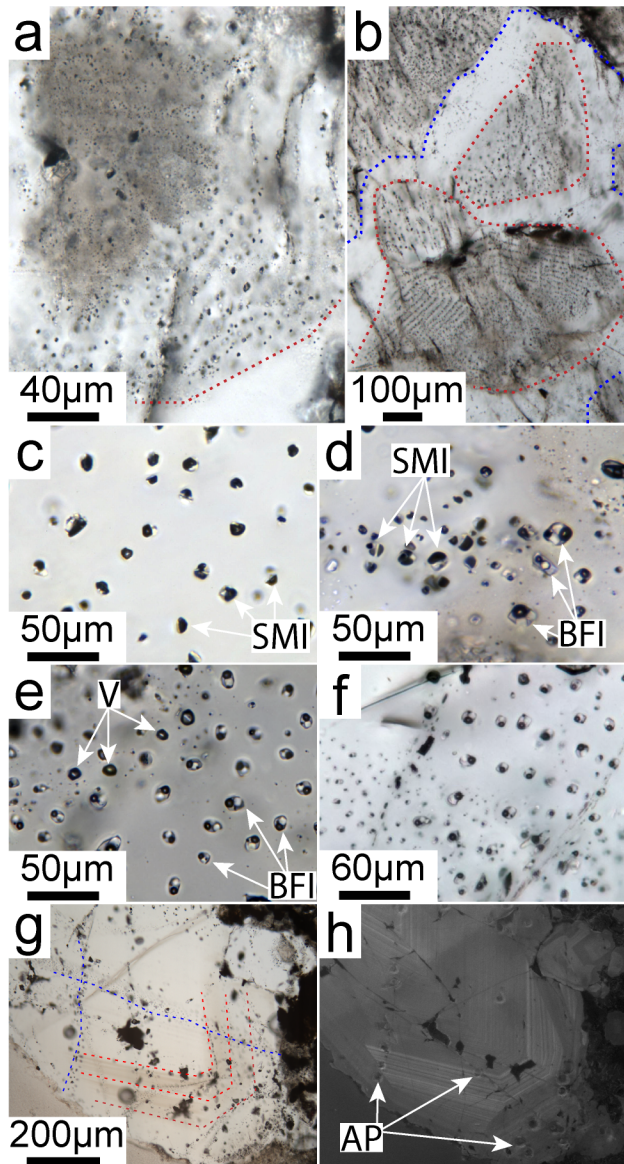
**Figure 4.4: Photomicrographs of inclusion hosted in monomineralic quartz bands.**

(a,b) UST-bright quartz with abundant primary assemblages of silicate melt and brine inclusions (outlined in red) rimed by UST-dull (outlined in blue). (c,d) primary silicate melt inclusions (SMI) and brine fluid inclusions (BFI). (e.f) Pseudo-secondary assemblages coexisting brine and vapor inclusions (V). (g) Cross cutting primary (denotd in red) and phsudo-secondary inclusions (denoted in blue), (h) Cathodoluminescence image of the area shown in panel "g" showing ablation pits (AP).
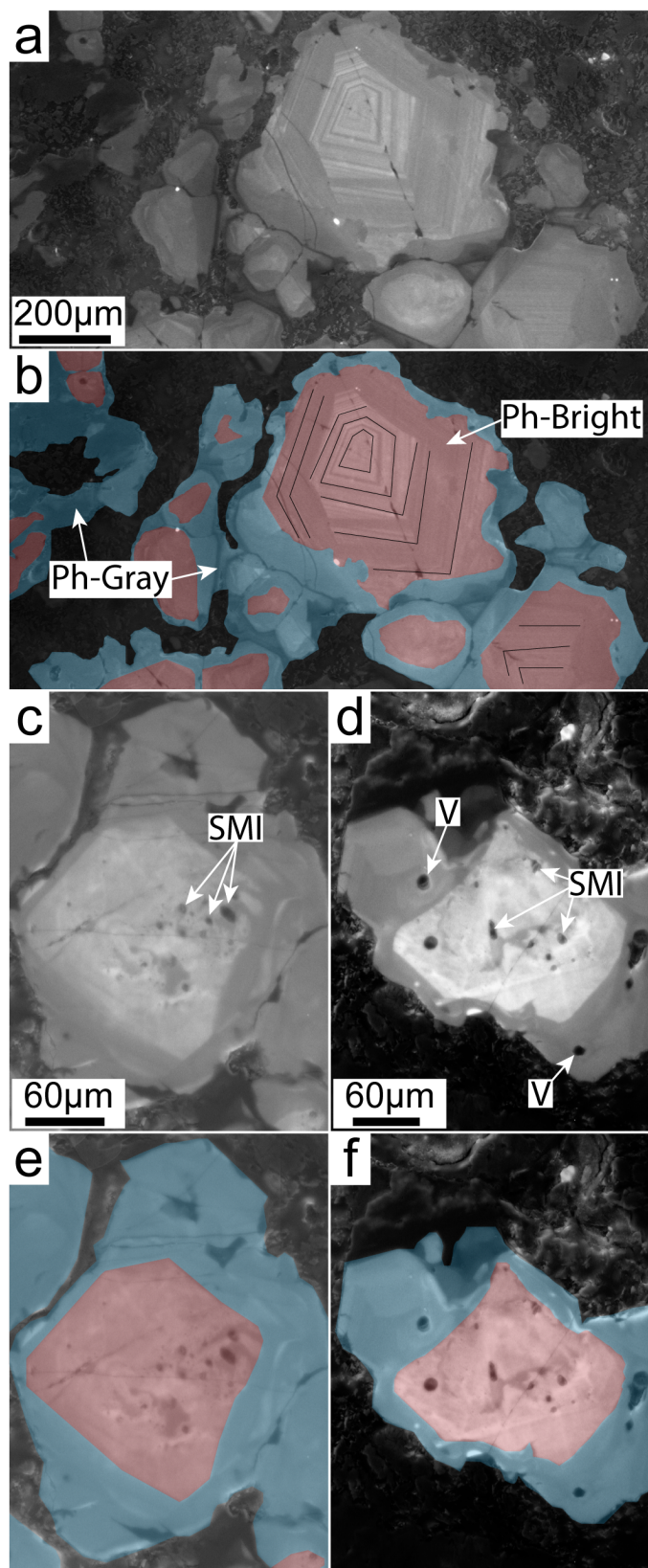
**Figure 4.5: Annotated cathodoluminescence images of quartz phenocrysts.**
(a) Raw cathodoluminescence image of quartz phenocrysts. (b) Annotated cathodoluminescence image showing Ph-bright and Ph-dull quartz. (c,d) Raw cathodoluminescence image of a quartz phenocrysts showing exposed silicate melt inclusions (SMI) and vapor inclusions (V). (e, f) Areas shown in c and d, respectively.
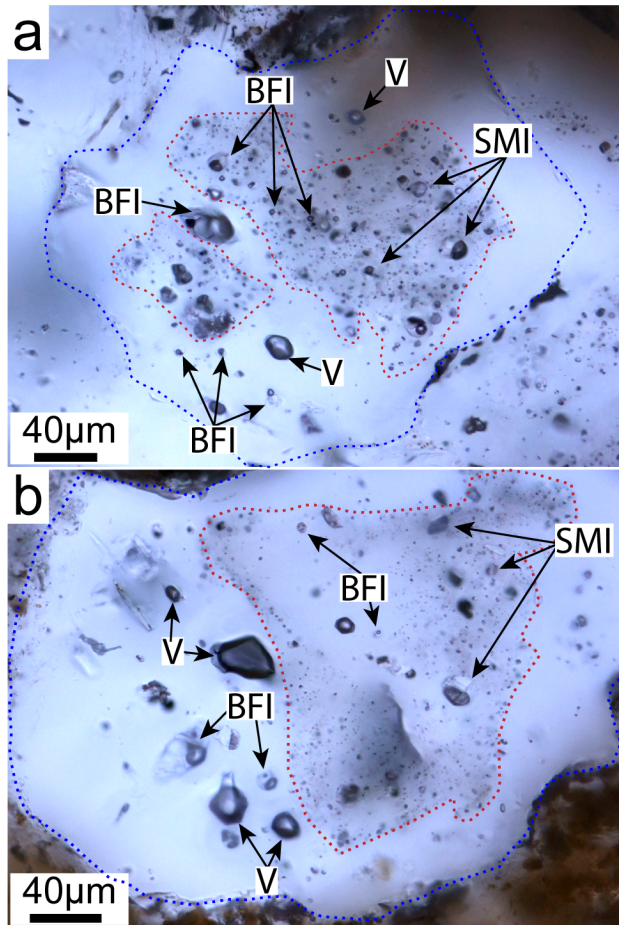
**Figure 4.6: Photomicrographs of quartz phenocrysts.**

(a,b) Coexisting brine (BFI) and silicate melt inclusions (SMI) in fractured Ph-bright quartz (outlined in red) rimed by Ph-dull quartz hosting coexisting brine and vapor (V) inclusions.
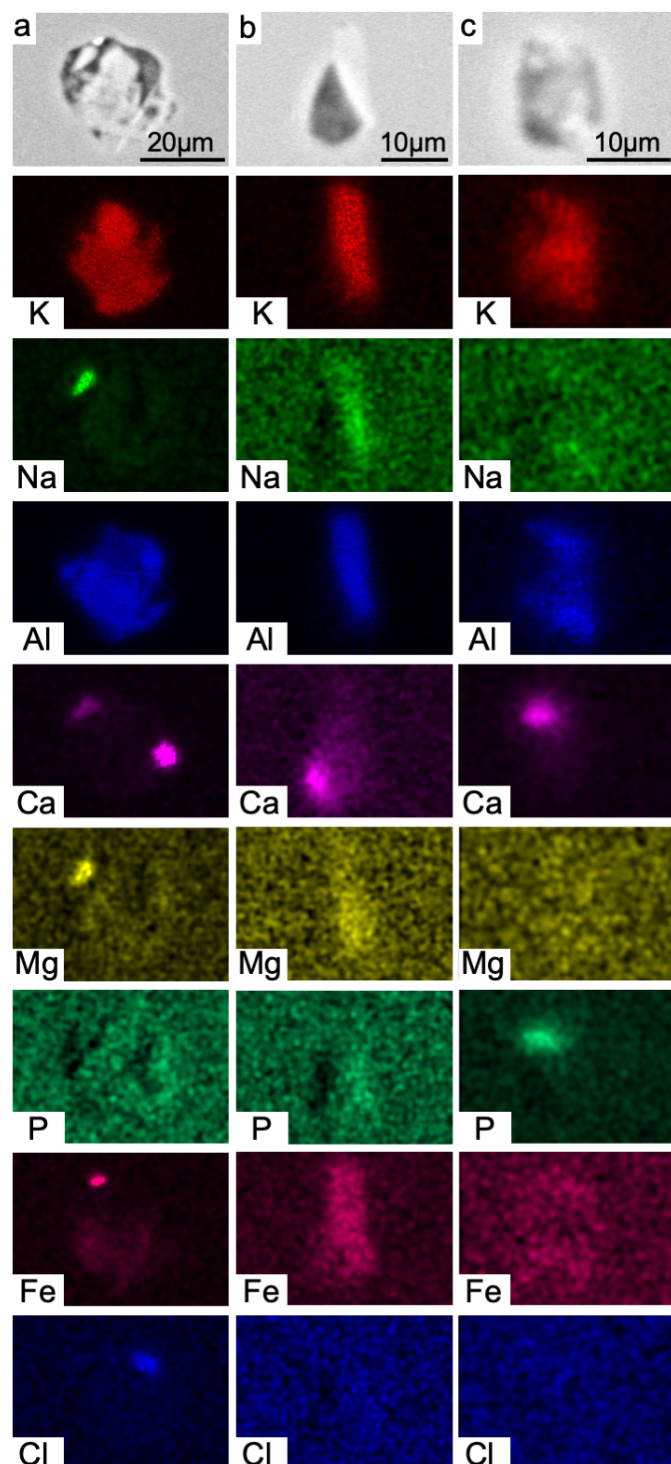
**Figure 4.7: Backscatter electron images of crystalline phases in exposed silicate melt inclusions with corresponding x-ray maps for selected elements.**
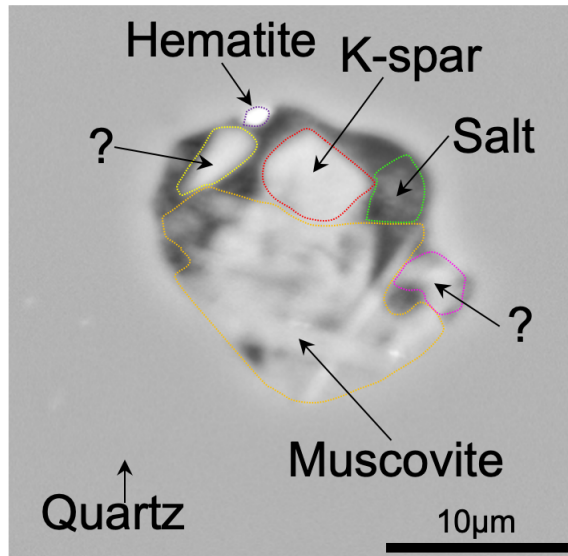
**Figure 4.8: Close-up backscatter electron image of an exposed silicate melt inclusions with labels for crystalline phase.**
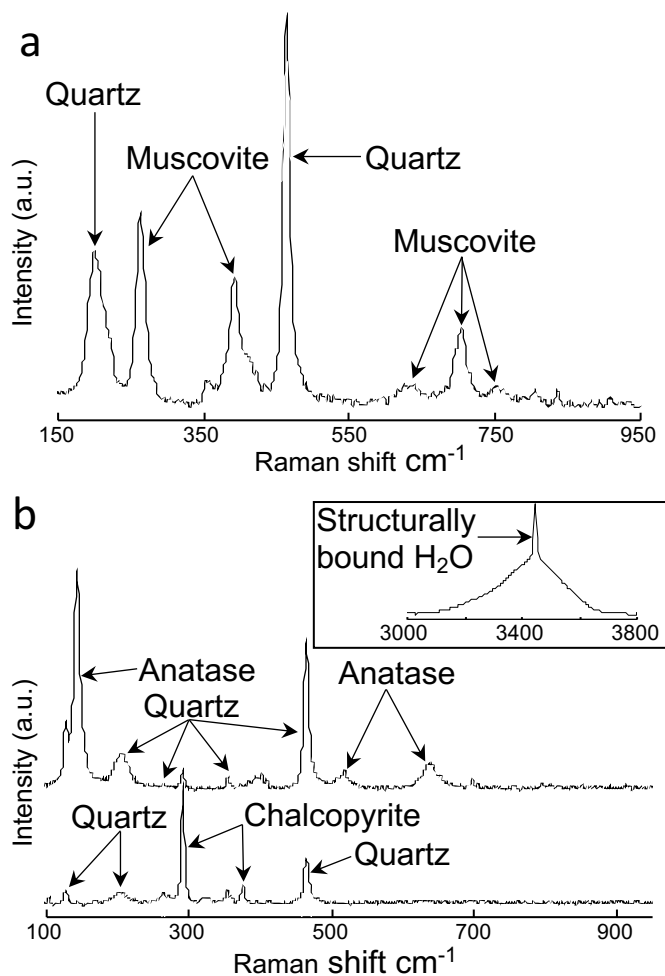
**Figure 4.9: Raman spectrum from solid phases in polycrystalline inclusions and brine inclusions.**

(a) Raman spectra of muscovite hosted in silicate melt inclusion in Ph-bright quartz. (b) Raman spectra from pseudo-secondary brine inclusion in UST-dull quartz. The inset spectra is consistent with the presence of Fe-bearing chloride salt hydrates.
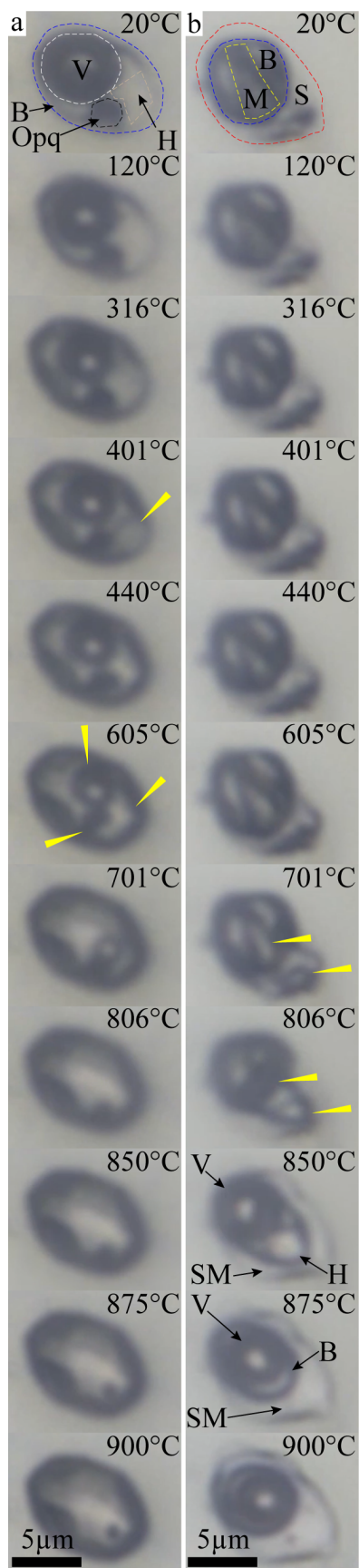
**Figure 4.10 Temperature series of coexisting brine and silicate melt inclusions during high temperature experiments.**

(a) Temperature series of brine inclusions showing vapor (V), brine (B), halite (H), and opaque (Opq) at room temperature. Yellow arrow indicates areas which show distinct melting behavior. (b) silicate melt inclusion showing silicate melt (S), a vapor bubble (B), and muscovite (M). Silicate melt (SM) is clearly apparent by 701°C.
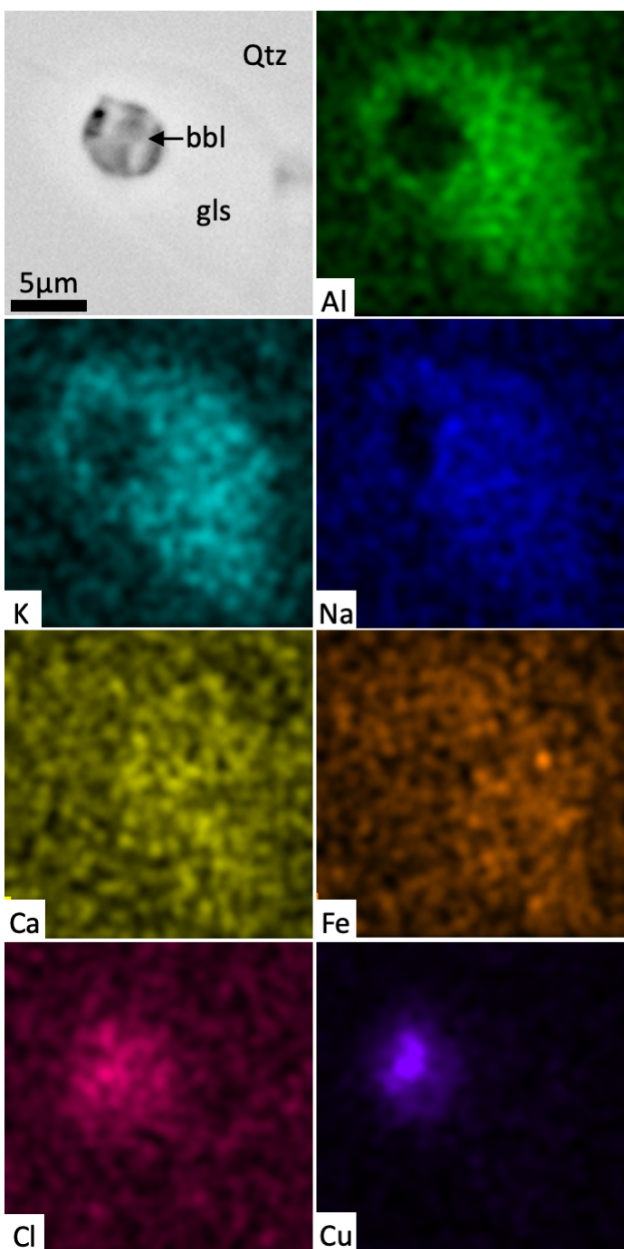
**Figure 4.11: Backscatter electron image of a homogenized silicate melt inclusions and corresponding x-ray maps for selected elements.**

Note presence of a chloride-rich vapor bubble (bbl) suspended in the quartz-hosted (Qtz) silicate glass(gls). The chloride also contains a distinct crystalline Cu-rich phase.
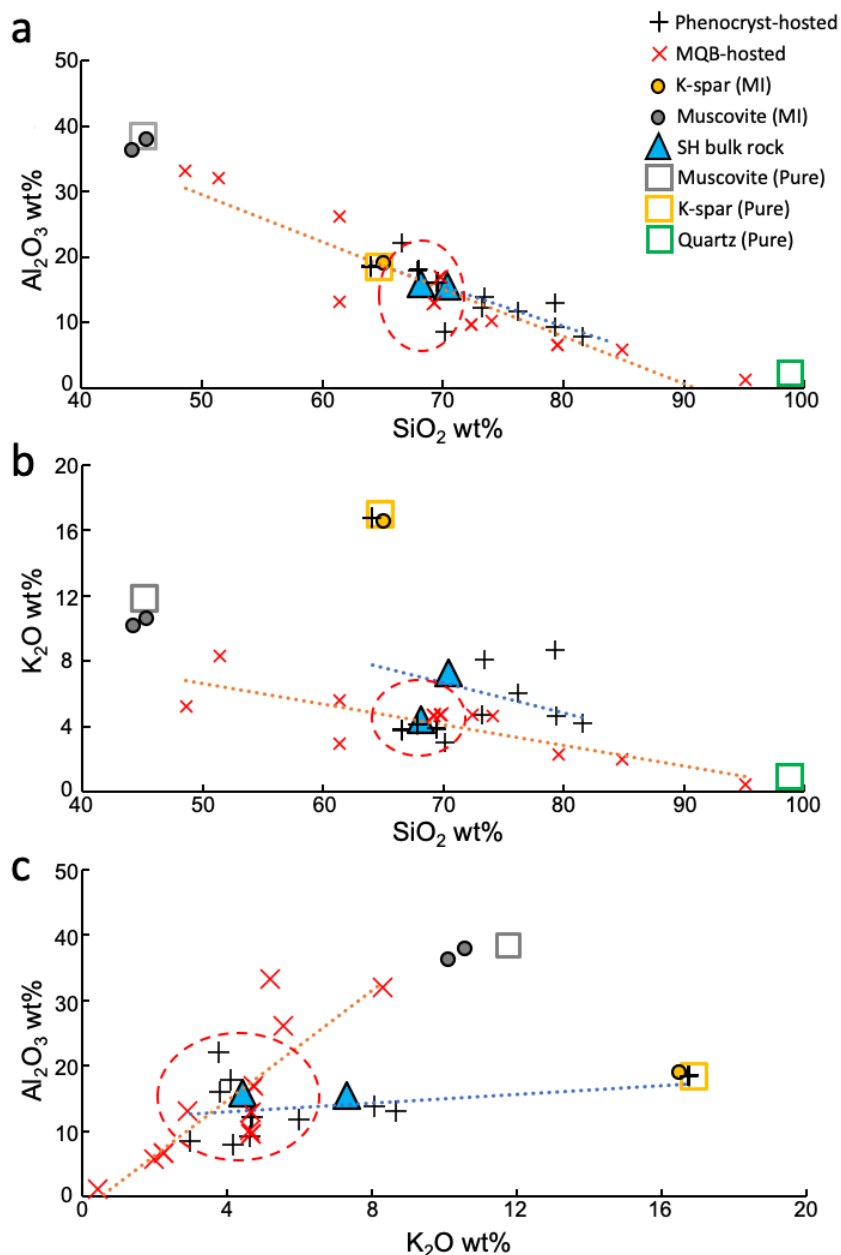
**Figure 4.12: Major element data from EPMA analyses of homogenized melt inclusions** hosted in quartz phenocrysts and monomineralic quartz bands (MQB) plotted along with crystalline potassium feldspar (K-spar) and muscovite in unheated inclusion, bulk rock data from Saginaw Hill (SH), and the endmember K-spar, muscovite and quartz (open squares). Trendlines for melt inclusion data from quartz phenocrysts and monomineralic quartz bands are shown in blue and orange, respectively. Inclusions showing the lowest amount of contamination by heterogeneously entrapped phases and the most representative melt compositions are circled in red.
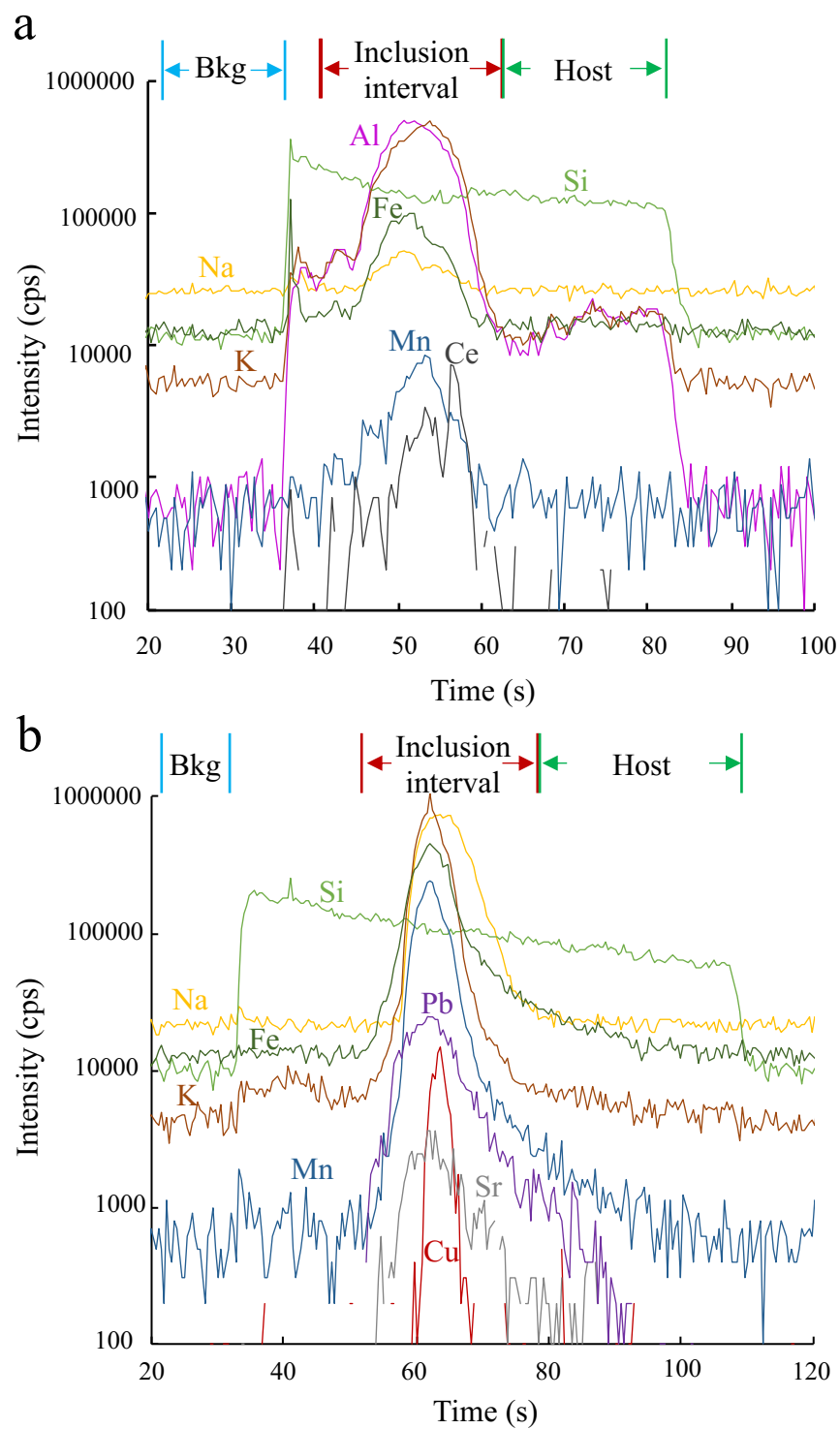
**Figure 4.13: Counts per second verses time plot for LA-ICPMS**

Transient signal is from the analysis of a single quartz hosted melt (a) and brine (b) inclusions.
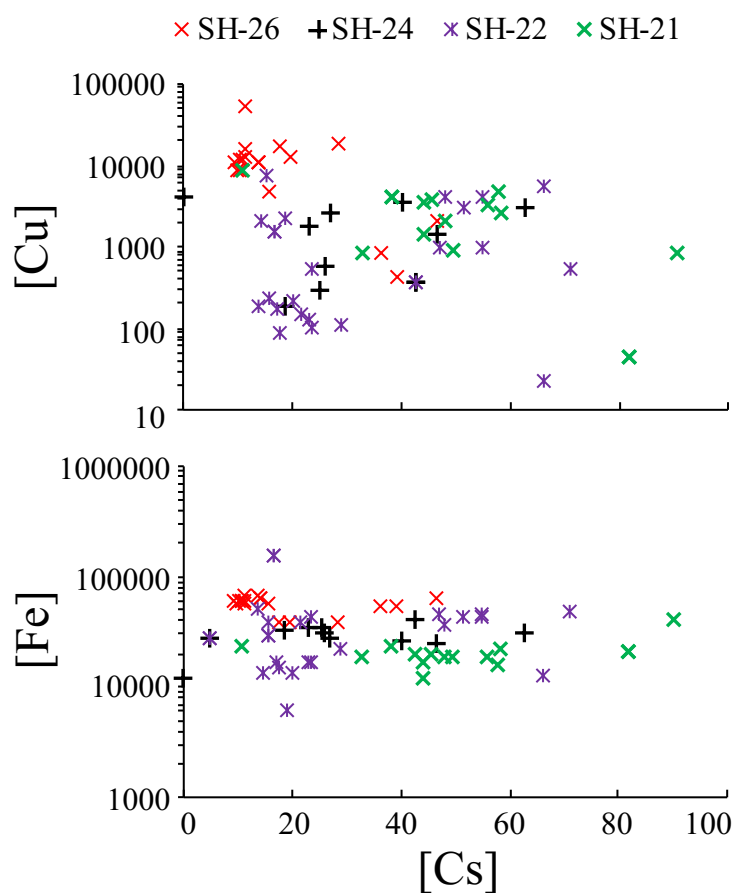
**Figure 4.14: Metal compositions of brine inclusions hosted in monomineralic quartz bands.**

Samples are arranged in paragenetic sequence from oldest to youngest in the figure legend.
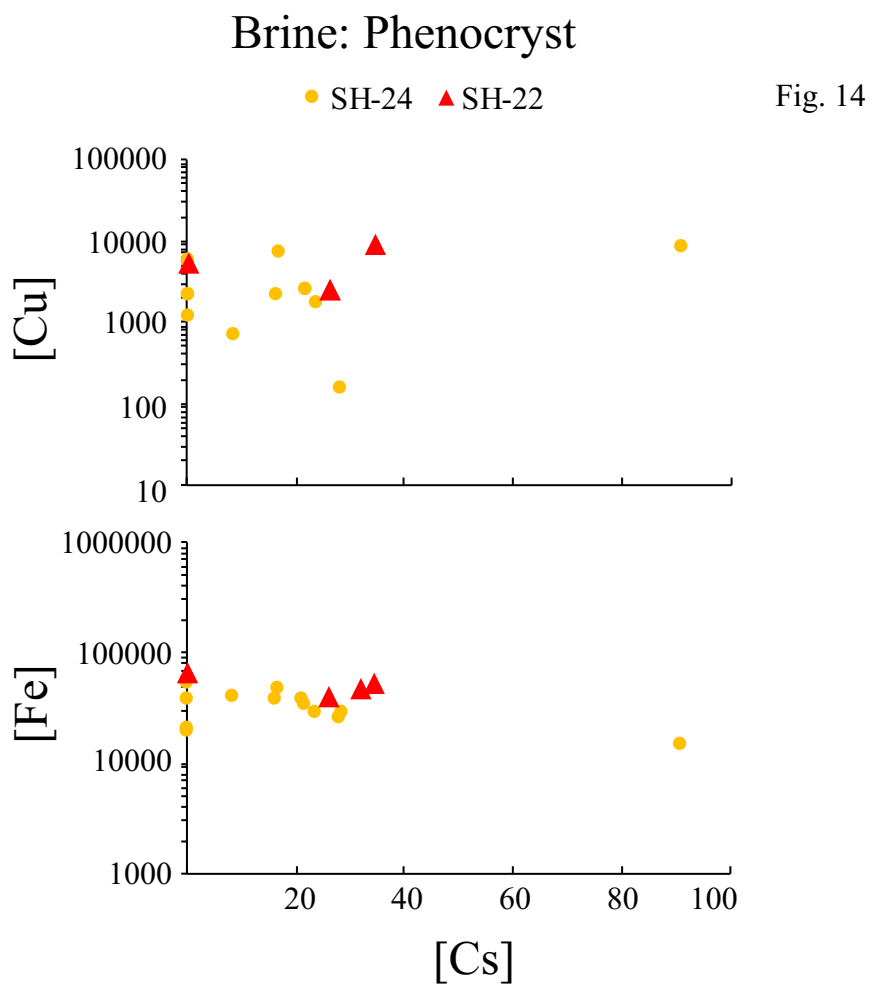
**Figure 4.15: Metal compositions of brine inclusions hosted in quartz phenocrysts.**

Samples are arranged in paragenetic sequence from oldest to youngest in the figure legend.
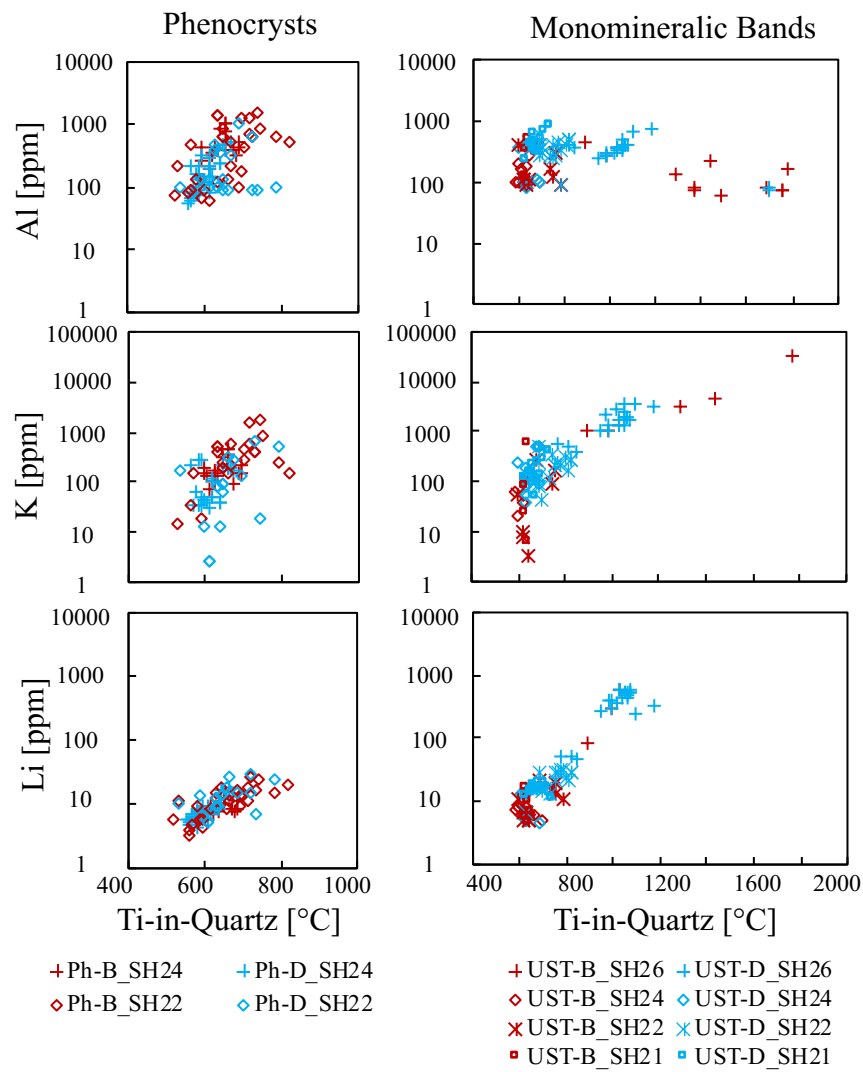
**Figure 4.16: Quartz trace element content compared to Ti-in-quartz temperatures.**

Data from Ph-bright (Ph-B) and UST-bright (UST-B) quartz are shown in red while data from

Ph-dull (Ph-D) and UST-dull (UST-D) are shown in blue.
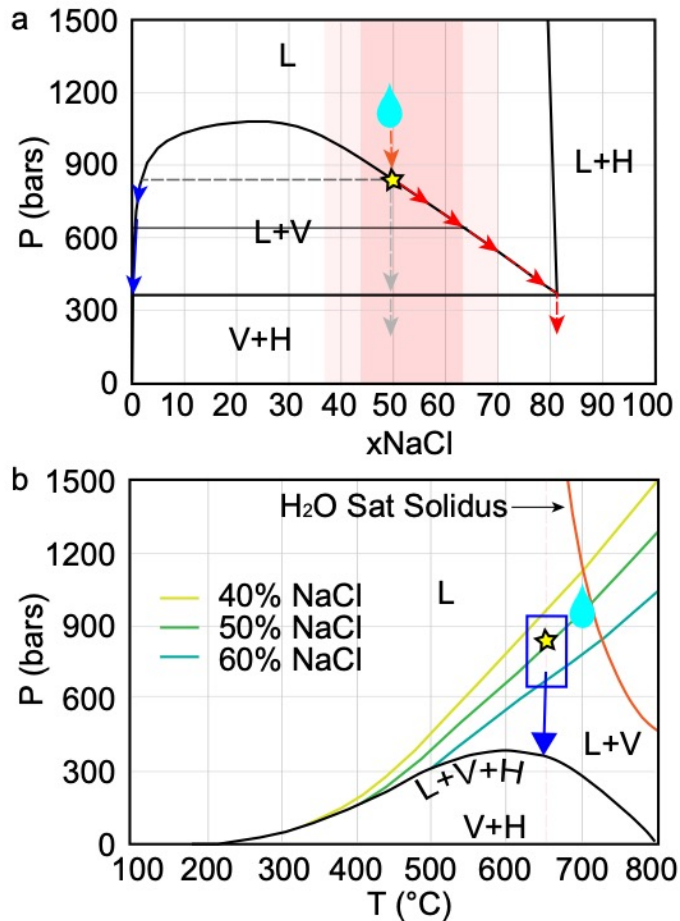
**Figure 4.17: Fluid evolution during UST formation.**

(a) P-X section through the $H_2O$-NaCl system showing the evolution of exsolved fluids. The range of salinities of brine from Ph-bright quartz is denoted by the red shaded area. Brines in Ph-bright quartz were trapped in the single-phase liquid field and P >850 bar. Episodic drops in pressure results in the intersection of the liquid-vapor (L+V) curve and immiscibility forming liquid (red path) and vapor (blue path). Pressure drops below ~370 bar would result in the precipitation of halite (H). (b) P-T section through the $H_2O$-NaCl system. The red dotted line shows the section depicted in "a". The blue box shows the P-T conditions recorded by brine inclusions hosted in Ph-bright quartz. The orange line depicts the $H_2O$ saturated granite solidus. Note that this boundary could be depressed to lower T conditions in the presence of abundant fluxes and that T conditions at the sight of UST formation are likely at subsolid us conditions (London, 2009).
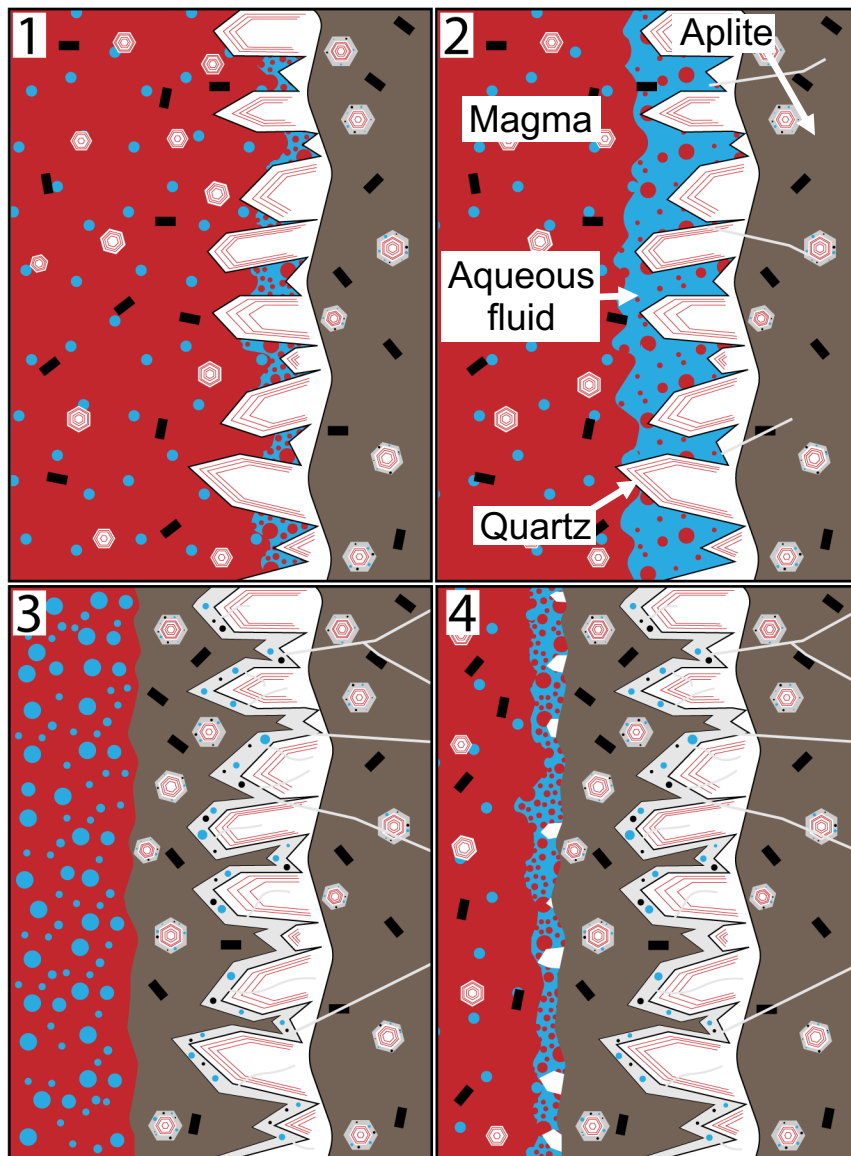
**Figure 4.18: Model of UST formation in the Saginaw Hill system.**

During the initial nucleation of Ph-bright and UST-bright quartz individual crystals entrap silicate melt (red) and small amounts of coexisting brine along well-developed growth zones (1). Overtime, brine accumulation along the site of UST formation leads to over-pressurization of the system and the formation of hydraulic fractures (2). Fracture formation results in the rapid depressurization of the system, liquid-vapor immiscibility, pressure quenching of aplite (brown), and the rapid growth of Ph-dull and UST-dull quartz (gray) which host abundant coeval vapor (black circles) and brine (blue circles). Concurrently the reduction in pressure drives fluid exsolution in the adjacent melt (3). Rapid precipitation of quartz leads to the resealing of the

system which reinitiates another cycle of gradual growth of UST-bright and Ph-bright quartz, accumulation of aqueous fluid along the systems periphery, and over-pressurization.
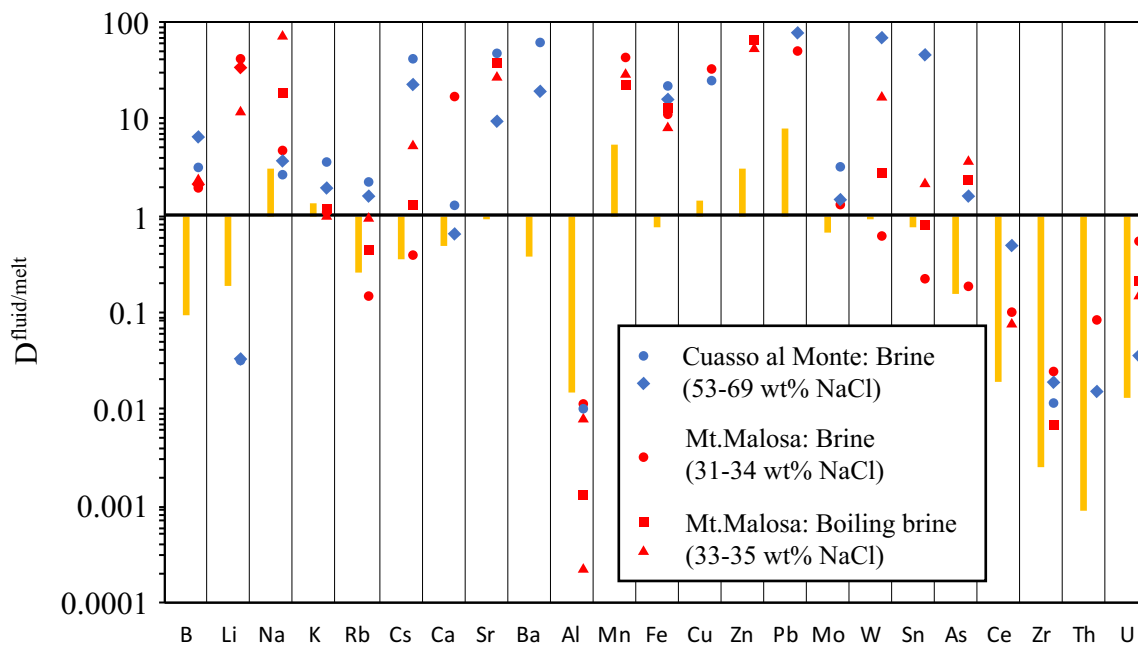
**Figure 4.19: Calculated partitioning coefficients for brine and melt inclusion in the Saginaw Hill system.**

Data from Saginaw Hill is shown as yellow bars alongside data points from high salinity brine reported by Zajacz et al., 2008.

**Table 4.1 Summary of inclusion petrography from Saginaw Hill**

| Location | Host quartz | FIA types | Distribution and occurrence of inclusion types |
|---|---|---|---|
| Phenocryst cores | Ph-bright | Silicate MI ±Brine | Primary FIAs in well-developed growth-zonation with a hazy brown coloration caused by disseminated <1μm melt inclusions |
| Phenocryst rims | Ph-Dull | Brine+Vapor ±Silicate Mi | Primary FIAs in randomly distributed in relatively clear quartz |
| Base and core of monomineralic quartz bands | UST-bright | Silicate MI ±Brine | Primary FIAs in well-developed growth-zonation with a hazy brown coloration caused by disseminated <1μm melt inclusions |
| Rims of monomineralic bands and fractures | UST-Dull | Brine+Vapor ±Silicate Mi | Primary FIAs in randomly distributed in relatively clear quartz and pseudo-secondary FIAs and fractures in primary quartz |

**Table 4.2. EPMA data from crystalline phases in an unhomogenized phenocryst-hosted melt inclusions and bulk rock data from Saginaw hill.**

| | Sample | MI K-spar | MI Muscovite | MI Muscovite | Bulk Saginaw Hill (Greig pres. commun.) | Bulk Saginaw Hill (Greig pres. commun.) |
|---|---|---|---|---|---|---|
| Wt% | $SiO_2$ | 65.1 | 45.4 | 44.2 | 68.2 | 70.4 |
| | $Al_2O_3$ | 19.0 | 37.9 | 36.2 | 15.9 | 15.6 |
| | FeO | | 1.0 | 2.2 | | |
| | $Cu_2O$ | | | | | |
| | MnO | | 0.3 | 0.1 | | |
| | MgO | | 0.1 | 0.2 | 0.9 | 0.3 |
| | CaO | 0.1 | | 0.0 | 1.9 | 2.5 |
| | $Na_2O$ | 0.4 | 0.5 | 1.0 | 4.3 | 2.3 |
| | $K_2O$ | 16.5 | 10.6 | 10.1 | 4.4 | 7.3 |
| | $P_2O_5$ | | | | 0.2 | 0.1 |
| | $SO_3$ | 0.0 | | | | |
| ppm | Cl | 0.0 | 0.0 | | | |
| | Total | 101.1 | 95.7 | 94.1 | 95.9 | 98.5 |
| | ASI* | | | | 1.0 | 1.0 |

**Table 4.3: Summarized microthermometric measurements from brine inclusions form Saginaw Hill.**

| | | $Tm_H$ | $Th_{L-V}$ | Salinity (wt% NaCl eq.) | $Pressure_H$ (bar) |
|---|---|---|---|---|---|
| Phenocryst rim (Ph-Dull) | Min | 300 | 372 | 31 | 372 |
| | Max | 483 | 791 | 48 | 791 |
| | Median | 410 | 675 | 38 | 465 |
| | STD | 60 | 166 | 7 | 178 |
| Phenocryst rim (Ph-Bright) | Min | 352 | 510 | 42 | 519 |
| | Max | 519 | 760 | 62 | 760 |
| | Median | 430 | 650 | 49 | 650 |
| | STD | 58 | 87 | 7 | 86 |
| Monomineralic Quartz (primary, UST-Dull) | Min | 482 | 276 | 55 | 482 |
| | Max | 519 | 519 | 62 | 519 |
| | Median | 504 | 424 | 60 | 504 |
| | STD | 15 | 70 | 2 | 15 |
| Monomineralic Quartz (Pseudo-secondary, UST-) | Min | 441 | 360 | 53 | 441 |
| | Max | 550 | 519 | 65 | 550 |
| | Median | 539 | 430 | 63 | 539 |
| | STD | 34 | 44 | 4 | 34 |

**Table 4.4: High temperature microthermometry data from primary brine inclusions hosted in UST-Dull quartz in monomineralic quartz bands**

| | $Tm_H$ | $Th_{L-V}$ | Salinity (wt% NaCl eq.) | Pressure$_H$ (bar) |
|---|---|---|---|---|
| Monomineralic Quartz (primary, UST-Dull) | 519 | 519 | 62 | 341 |
| | 519 | 519 | 62 | 341 |
| | 519 | 504 | 62 | 470 |
| | 504 | 464 | 60 | 634 |
| | 519 | 428 | 61 | 1151 |
| | 504 | 420 | 60 | 1036 |
| | 504 | 400 | 59 | 1311 |
| | 482 | 420 | 57 | 782 |
| | 482 | 276 | 55 | 4638 |
| | 482 | 392 | 57 | 1093 |

**Table 4.5 High temperature microthermometry data from Pseudo-secondary brine inclusions hosted in UST-Dull quartz in monomineralic quartz bands**

| | $Tm_H$ | $Th_{L-V}$ | Salinity (wt% NaCl eq.) | $Pressure_H$ (bar) | | $Tm_H$ | $Th_{L-V}$ | Salinity (wt% NaCl eq.) | $Pressure_H$ (bar) |
|---|---|---|---|---|---|---|---|---|---|
| Monomineralic Quartz (Pseudo-secondary, UST-Dull) | 500 | 460 | 60 | 627 | Monomineralic Quartz (Pseudo-secondary, UST-Dull) | 539 | 490 | 64 | 774 |
| | 539 | 385 | 63 | 2495 | | 519 | 570 | 62 | 406 |
| | 539 | 490 | 64 | 774 | | 519 | 570 | 62 | 406 |
| | 539 | 420 | 63 | 1659 | | 519 | 570 | 62 | 406 |
| | 539 | 397 | 63 | 2168 | | 519 | 504 | 62 | 470 |
| | 539 | 397 | 63 | 2168 | | 530 | 811 | 61 | 704 |
| | 539 | 490 | 64 | 774 | | 519 | 510 | 62 | 421 |
| | 539 | 490 | 63 | 1757 | | 519 | 519 | 62 | 341 |
| | 539 | 490 | 55 | 276 | | 519 | 483 | 62 | 629 |
| | 539 | 385 | 63 | 1659 | | 441 | 420 | 53 | 404 |
| | 539 | 506 | 63 | 1659 | | 441 | 700 | 50 | 696 |
| | 539 | 500 | 63 | 1659 | | 441 | 700 | 50 | 696 |
| | 539 | 372 | 63 | 2905 | | 441 | 700 | 50 | 696 |
| | 539 | 415 | 63 | 1757 | | 441 | 700 | 50 | 696 |
| | 467 | 506 | 55 | 338 | | 465 | 400 | 55 | 798 |
| | 539 | 420 | 63 | 1659 | | 465 | 400 | 55 | 798 |
| | 539 | 420 | 63 | 1659 | | 465 | 430 | 55 | 542 |
| | 539 | 420 | 63 | 1659 | | 450 | 400 | 53 | 649 |
| | 539 | 510 | 65 | 612 | | 465 | 450 | 56 | 393 |
| | 539 | 510 | 65 | 612 | | 550 | 430 | 65 | 1733 |
| | 539 | 420 | 63 | 1659 | | 465 | 430 | 55 | 542 |
| | 539 | 510 | 65 | 612 | | 465 | 430 | 55 | 542 |
| | 539 | 420 | 63 | 1659 | | 465 | 465 | 55 | 271 |
| | 539 | 420 | 63 | 1659 | | 465 | 430 | 55 | 542 |
| | 539 | 420 | 63 | 1659 | | 450 | 525 | 53 | 375 |
| | 539 | 490 | 64 | 774 | | 465 | 430 | 55 | 542 |
| | 539 | 360 | 63 | 3338 | | 465 | 525 | 55 | 369 |
| | 490 | 490 | 58 | 309 | | 500 | 525 | 60 | 355 |

**Table 4.6 High temperature microthermometry data from primary brine inclusions hosted in Ph-bright and Ph-dull quartz**

| | $Tm_H$ | $Th_{L-V}$ | Salinity (wt% NaCl eq.) | $Pressure_H$ (bar) |
|---|---|---|---|---|
| **Phenocryst rim (Ph-Dull)** | 431 | - | 31 | |
| | 300 | 372 | 38 | 145 |
| | 300 | 372 | 38 | 145 |
| | 300 | 372 | 38 | 145 |
| | 761 | 790 | 95 | 21 |
| | 761 | 790 | 95 | 21 |
| | 430 | 791 | 48 | 891 |
| | 380 | 764 | 43 | 913 |
| | 430 | - | 31 | - |
| | 483 | - | 32 | - |
| | 420 | - | 31 | - |
| | 400 | 465 | 47 | 289 |
| | 410 | 675 | 47 | 689 |
| **Phenocryst core (Ph-Bright)** | 436 | 760 | 49 | 760 |
| | 519 | 631 | 62 | 631 |
| | 400 | 540 | 47 | 540 |
| | 430 | 675 | 49 | 675 |
| | 352 | 650 | 42 | 650 |
| | 352 | 675 | 42 | 675 |
| | 519 | 510 | 62 | 519 |
| | 400 | 540 | 47 | 540 |
| | 436 | 760 | 49 | 760 |

**Table 4.7: EPMA data from homogenized melt inclusions hosted in quartz phenocrysts and monomineralic quartz bands.**

| | Sample | C2A2_MI3a | C2A2_MI1b | C3A1_MI3a | C2A2_MI2b | C1A4_MI1a | C3A1_MI1b | C3A1_MI3b | C1A4_MI2a | C1A4_MI3a | C1A1_MI1a | C3A1_MI2a |
|---|---|---|---|---|---|---|---|---|---|---|---|---|
| | | | | | | Phenocryst hosted | | | | | | |
| Wt% | $SiO_2$ | 67.9 | 79.3 | 69.4 | 76.2 | 73.2 | 81.6 | 66.6 | 64.1 | 70.1 | 73.5 | 79.3 |
| | $Al2O_3$ | 17.9 | 9.3 | 16.0 | 11.8 | 12.2 | 7.9 | 22.2 | 18.5 | 8.5 | 13.9 | 13.1 |
| | FeO | 2.4 | 0.5 | 1.0 | 0.5 | 0.7 | 1.3 | 1.5 | | 0.6 | 0.9 | 0.1 |
| | $Cu_2O$ | 1.2 | 0.4 | 1.7 | 0.6 | 2.5 | 1.3 | 1.5 | | 14.8 | 1.0 | 0.2 |
| | MnO | | | | | | 0.2 | | | | 0.3 | |
| | MgO | 0.2 | 0.0 | 0.1 | 0.1 | 0.1 | 0.1 | 0.1 | | 0.0 | 0.0 | |
| | CaO | 0.1 | 0.3 | 0.0 | 0.5 | 0.4 | 0.5 | 0.1 | 0.1 | 0.2 | 1.9 | 0.0 |
| | $Na_2O$ | 1.1 | 0.8 | 3.3 | 0.8 | 3.4 | 1.9 | 3.3 | 0.4 | 2.7 | 1.6 | 2.5 |
| | $K_2O$ | 4.1 | 4.6 | 3.8 | 6.0 | 4.7 | 4.2 | 3.8 | 16.8 | 3.0 | 8.1 | 8.7 |
| | $P_2O_5$ | | 0.0 | | | | | | | | 0.1 | |
| | $SO_3$ | 0.1 | | | | | | | | | | |
| ppm | Cl | 667.7 | 825.1 | 190.8 | 927.0 | 1050.9 | 1026.1 | | | 2541.8 | 3594.0 | 183.3 |
| | Total | 95.1 | 95.4 | 95.4 | 96.4 | 97.2 | 98.9 | 99.1 | 99.8 | 100.2 | 101.4 | 103.8 |
| | ASI* | 2.8 | 1.4 | 1.7 | 1.4 | 1.1 | 0.9 | 2.3 | 1.0 | 1.0 | 0.9 | 1.0 |

| | Sample | A1_MI1aa | A1_MI1ab | A1_MI1ac | A1_MI1ad | A2_MI2ba | A2_MI2ca | A2_MI3aa | A2_MI3ca | A1_MI2ab | A1_MI1ra | A1_MI1ae |
|---|---|---|---|---|---|---|---|---|---|---|---|---|
| | | | | | Monomineralic Quartz Band hosted | | | | | | | |
| Wt% | $SiO_2$ | 74.1 | 79.5 | 51.4 | 61.4 | 69.8 | 95.1 | 61.4 | 69.2 | 72.4 | 48.6 | 84.8 |
| | $Al_2O_3$ | 10.2 | 6.5 | 32.0 | 26.2 | 16.9 | 1.2 | 13.1 | 12.9 | 9.6 | 33.2 | 5.7 |
| | FeO | 0.6 | 1.5 | 2.2 | 1.5 | 1.3 | 0.1 | 1.3 | 1.3 | 0.7 | 1.7 | 0.4 |
| | $Cu_2O$ | 0.3 | 0.9 | | 0.2 | | | 0.1 | | | 0.1 | |
| | MnO | 0.1 | 0.2 | | 0.3 | 0.5 | | 0.4 | 0.7 | 0.4 | 0.3 | 0.2 |
| | MgO | 0.1 | 0.1 | 1.6 | 0.1 | 0.1 | | 0.2 | 0.1 | 0.0 | 0.1 | |
| | CaO | 0.4 | 0.6 | 0.1 | 0.0 | 0.6 | | 0.1 | 0.1 | 0.2 | 0.1 | 0.1 |
| | $Na_2O$ | 2.0 | 0.5 | 1.0 | 1.1 | 0.7 | 0.1 | 0.4 | 1.0 | 0.5 | 1.1 | 0.3 |
| | $K_2O$ | 4.6 | 2.3 | 8.3 | 5.6 | 4.8 | 0.4 | 2.9 | 4.7 | 4.7 | 5.2 | 2.0 |
| | $P_2O_5$ | | | | 1.6 | 2.8 | 0.4 | 3.5 | 3.8 | 2.4 | 1.8 | 1.5 |
| | $SO_3$ | | | | | | | | | | 0.1 | |
| ppm | Cl | 1797.4 | 1935.6 | 419.4 | | | | 969.8 | | 263.7 | 329.8 | 224.8 |
| | Total | 92.4 | 92.2 | 96.6 | 97.8 | 97.4 | 97.2 | 83.5 | 93.8 | 90.9 | 92.2 | 95.1 |
| | ASI* | 1.1 | 1.5 | 3.0 | 3.6 | 2.6 | 2.7 | 4.6 | 2.4 | 1.8 | 4.9 | 2.5 |

**Table 4.8: Summary of Brine inclusion composition from quartz phenocrysts and monmineralic quartz bands.**

| | Monomineralic quartz bands | | | | | | | Quartz Phenocrysts | | | | | |
|---|---|---|---|---|---|---|---|---|---|---|---|---|---|
| UST | Min | Max | Median | Average | STD | n | PH | Min | Max | Median | Average | STD | n |
| Li | 24 | 1291 | 101 | 278 | 395 | 16 | Li | 1173 | 1173 | 1173 | 1173 | 0 | 1 |
| B | 6 | 4701 | 72 | 268 | 799 | 34 | B | 50 | 657 | 432 | 369 | 221 | 5 |
| Na | 1073 | 120726 | 57844 | 55954 | 38224 | 70 | Na | 41707 | 101199 | 61881 | 64023 | 14841 | 18 |
| K | 8023 | 111462 | 60325 | 59454 | 23594 | 70 | K | 2734 | 65903 | 35569 | 35008 | 14172 | 18 |
| Mn | 3432 | 133944 | 15393 | 20969 | 18243 | 71 | Mn | 4598 | 23200 | 9129 | 10193 | 4406 | 18 |
| Fe | 6346 | 160002 | 34321 | 37586 | 22970 | 65 | Fe | 9233 | 56631 | 20064 | 22237 | 11021 | 18 |
| Cu | 22 | 52989 | 2162 | 4718 | 7651 | 64 | Cu | 157 | 9366 | 2507 | 4017 | 2819 | 15 |
| Zn | 2387 | 37751 | 6162 | 8223 | 6167 | 67 | Zn | 1509 | 11468 | 3336 | 4403 | 2782 | 17 |
| Rb | 114 | 2153 | 474 | 531 | 332 | 71 | Rb | 23 | 416 | 264 | 245 | 88 | 17 |
| Sr | 8 | 2756 | 324 | 417 | 463 | 71 | Sr | 54 | 826 | 208 | 253 | 188 | 18 |
| Mo | 4 | 1884 | 126 | 197 | 310 | 35 | Mo | 101 | 442 | 227 | 234 | 103 | 7 |
| Cs | 0 | 428 | 28 | 41 | 52 | 71 | Cs | 0 | 91 | 19 | 19 | 21 | 18 |
| Ba | 27 | 10446 | 1001 | 2223 | 2548 | 65 | Ba | 90 | 2145 | 556 | 678 | 500 | 14 |
| Pb | 879 | 9851 | 2355 | 2797 | 1696 | 70 | Pb | 636 | 2962 | 1265 | 1534 | 775 | 18 |

**Table 4.9: Summary of silicate melt inclusions hosted in monomineralic quartz bands (Uncorrected)**

| Monomineralic Quartz Hosted Melt Inclusions (uncorrected) | | | | | | |
|---|---|---|---|---|---|---|
| | Min | Max | Median | Average | STDEV.P | n |
| Li7 | 188 | 2449 | 498 | 705 | 666 | 9 |
| Be9 | 1381 | 1381 | 1381 | 1381 | 0 | 1 |
| B11 | 109 | 28901 | 1222 | 4387 | 8714 | 9 |
| Na23 | 4531 | 8870 | 6423 | 6700 | 1585 | 7 |
| Al27 | 195380 | 392001 | 315465 | 306341 | 48702 | 26 |
| K39 | 121678 | 343974 | 189486 | 209064 | 63059 | 26 |
| Ti47 | 1788 | 65440 | 8582 | 14465 | 16915 | 14 |
| Mn55 | 587 | 8058 | 1032 | 1849 | 1821 | 15 |
| Fe56 | 17783 | 74981 | 30320 | 31945 | 11032 | 20 |
| Fe57 | 1555 | 153935 | 23613 | 31180 | 31037 | 19 |
| Cu65 | 142 | 3135 | 1427 | 1537 | 1103 | 7 |
| Zn66 | 214 | 3870 | 2170 | 2034 | 1165 | 6 |
| As75 | 335 | 819 | 435 | 530 | 209 | 3 |
| Rb85 | 384 | 1261 | 816 | 815 | 219 | 25 |
| Sr88 | 39 | 399 | 249 | 258 | 91 | 24 |
| Zr90 | 95 | 363 | 237 | 233 | 98 | 16 |
| Mo95 | 145 | 699 | 217 | 320 | 225 | 4 |
| Ag107 | 42 | 409 | 397 | 283 | 170 | 3 |
| Sn118 | 7 | 726 | 223 | 295 | 288 | 4 |
| Cs133 | 2 | 51 | 28 | 26 | 14 | 11 |
| Ba137 | 575 | 4083 | 2105 | 2253 | 922 | 25 |
| La139 | 26 | 51199 | 146 | 3700 | 12046 | 24 |
| Ce140 | 71 | 595 | 219 | 231 | 107 | 25 |
| Hf178 | 6 | 17 | 8 | 10 | 5 | 3 |
| Ta181 | 2 | 7 | 5 | 5 | 2 | 3 |
| W182 | 179 | 179 | 179 | 179 | 0 | 1 |
| Au197 | 115 | 133 | 124 | 124 | 9 | 2 |
| Tl205 | 7 | 7 | 7 | 7 | 0 | 1 |
| Pb208 | 16 | 18792 | 105 | 1083 | 3968 | 21 |
| U238 | 7 | 42 | 17 | 19 | 10 | 10 |

**Table 4.10: Summary of silicate melt inclusions hosted in quartz phenocrysts (Uncorrected)**

| | Min | Max | Median | Average | STDEV.P | n |
|---|---|---|---|---|---|---|
| | | | Phenocryst Hosted Melt Inclusions (uncorrected) | | | |
| Li7 | 6.4 | 2159.2 | 163.1 | 430.0032 | 515.4002 | 31 |
| Be9 | 24.5 | 526.3 | 156.5 | 215.95 | 194.85 | 4 |
| B11 | 56.9 | 2663.1 | 529.1 | 718.6105 | 655.9563 | 38 |
| Na23 | 883.5 | 94965.6 | 9454.7 | 15970.75 | 19458.35 | 45 |
| Al27 | 183170 | 403369 | 322238.5 | 308976.8 | 50648.78 | 64 |
| K39 | 100841 | 333019 | 188464.5 | 203076.7 | 56768.26 | 64 |
| Ti47 | 718.4 | 29619.7 | 5293.65 | 6897.044 | 5833.123 | 34 |
| Mn55 | 677.2 | 47236.8 | 1750.4 | 3910.261 | 7336.702 | 51 |
| Fe56 | 7061.9 | 110142 | 37102.1 | 40644.87 | 20493.27 | 55 |
| Fe57 | 4895.8 | 330414 | 26257.3 | 32812.54 | 45531.58 | 52 |
| Cu65 | 6.7 | 17247.1 | 769.95 | 1630.517 | 3025.953 | 36 |
| Zn66 | 41.7 | 20694.6 | 909.6 | 2801.224 | 5035.802 | 33 |
| As75 | 18.7 | 1464.9 | 102.7 | 305.5375 | 414.8756 | 16 |
| Rb85 | 256.7 | 2166.1 | 988.25 | 1053.827 | 417.1678 | 62 |
| Sr88 | 15.5 | 2580.4 | 169.2 | 301.6068 | 436.8322 | 59 |
| Zr90 | 116.4 | 9336.3 | 607 | 845.9018 | 1233.376 | 55 |
| Mo95 | 31.5 | 3921.1 | 102.05 | 361.27 | 851.7256 | 20 |
| Ag107 | 8.6 | 2930.4 | 30.95 | 295.6429 | 752.4287 | 14 |
| Sn118 | 151.3 | 773 | 462.15 | 462.15 | 310.85 | 2 |
| Cs133 | 10 | 414.3 | 47.6 | 82.77674 | 93.8877 | 43 |
| Ba137 | 41.2 | 8207.9 | 1361.5 | 1664.488 | 1566.045 | 57 |
| La139 | 15.8 | 28306.8 | 154.6 | 1343.807 | 5192.427 | 59 |
| Ce140 | 19.6 | 1385.5 | 258.1 | 302.6049 | 254.0489 | 61 |
| Hf178 | 6.3 | 609.3 | 34.75 | 58.54211 | 97.22782 | 38 |
| Ta181 | 2.5 | 775.9 | 15.9 | 47.99118 | 128.6781 | 34 |
| W182 | 9.9 | 81.9 | 27.15 | 32.795 | 18.90837 | 20 |
| Au197 | 15.5 | 2705.5 | 20.4 | 913.8 | 1266.925 | 3 |
| Tl205 | 3.1 | 28.5 | 5.6 | 8.135714 | 6.390239 | 14 |
| Pb208 | 11.2 | 527584 | 125.1 | 10055.44 | 70434.71 | 55 |
| U238 | 2.5 | 404.2 | 30.8 | 44.66739 | 64.52424 | 46 |

**Table 4.11: Summary of silicate melt inclusions hosted in monomineralic quartz bands (Corrected)**

| | Min | Max | Median | Average | STDEV.P | n |
|---|---|---|---|---|---|---|
| Monomineralic Quartz Hosted Melt Inclusions (corrected) | | | | | | |
| Li7 | 127 | 1527 | 712 | 873 | 505 | 9 |
| Be9 | 1214 | 1214 | 1214 | 1214 | 0 | 1 |
| B11 | 369 | 9205 | 3286 | 3679 | 2671 | 7 |
| Na23 | 7824 | 32753 | 20245 | 18044 | 7894 | 7 |
| Al27 | 36848 | 109330 | 87453 | 84870 | 14918 | 22 |
| K39 | 31153 | 100541 | 37970 | 42305 | 15129 | 21 |
| Ti47 | 2671 | 36666 | 15161 | 18983 | 11038 | 14 |
| Mn55 | 175 | 26212 | 2807 | 4960 | 7060 | 14 |
| Fe56 | 25765 | 126046 | 69513 | 76859 | 32719 | 18 |
| Fe57 | 1333 | 89755 | 39879 | 40052 | 20693 | 18 |
| Cu65 | 237 | 4199 | 2680 | 2285 | 1165 | 7 |
| Zn66 | 508 | 5810 | 4542 | 3792 | 1978 | 6 |
| As75 | 729 | 2220 | 1312 | 1420 | 614 | 3 |
| Rb85 | 86 | 2328 | 998 | 1013 | 579 | 21 |
| Sr88 | 214 | 3311 | 543 | 724 | 767 | 14 |
| Zr90 | 110 | 1376 | 814 | 724 | 438 | 12 |
| Mo95 | 415 | 1041 | 523 | 626 | 248 | 4 |
| Ag107 | 71 | 1534 | 834 | 813 | 598 | 3 |
| Sn118 | 26 | 7724 | 419 | 2147 | 3228 | 4 |
| Cs133 | 15 | 152 | 64 | 62 | 42 | 9 |
| Ba137 | 47 | 9086 | 4801 | 4228 | 2562 | 19 |
| La139 | 65 | 72432 | 460 | 6976 | 19731 | 20 |
| Ce140 | 112 | 1490 | 488 | 603 | 337 | 21 |
| Hf178 | 22 | 53 | 32 | 36 | 13 | 3 |
| Ta181 | 5 | 26 | 20 | 17 | 9 | 3 |
| W182 | 575 | 575 | 575 | 575 | 0 | 1 |
| Au197 | 101 | 213 | 157 | 157 | 56 | 2 |
| Tl205 | 21 | 21 | 21 | 21 | 0 | 1 |
| Pb208 | 18 | 2699 | 278 | 470 | 619 | 19 |
| U238 | 18 | 78 | 47 | 49 | 19 | 9 |

**Table 4.12: Summary of silicate melt inclusions hosted in quartz phenocrysts (Corrected)**

| | Min | Max | Median | Average | STDEV.P | n |
|---|---|---|---|---|---|---|
| | | | Phenocryst Hosted Melt Inclusions (corrected) | | | |
| Li7 | 12 | 6076 | 214 | 1127 | 1538 | 24 |
| Be9 | 81 | 507 | 160 | 227 | 166 | 4 |
| B11 | 55 | 5320 | 658 | 1252 | 1241 | 34 |
| Na23 | 1652 | 54182 | 20017 | 21200 | 11907 | 41 |
| Al27 | 60384 | 122448 | 85353 | 87736 | 12244 | 55 |
| K39 | 9430 | 64532 | 35690 | 36350 | 8364 | 51 |
| Ti47 | 775 | 58331 | 6909 | 14645 | 15809 | 31 |
| Mn55 | 154 | 21439 | 2636 | 3761 | 3605 | 44 |
| Fe56 | 4402 | 197368 | 72990 | 77181 | 39311 | 48 |
| Fe57 | 275 | 84681 | 32987 | 38416 | 23077 | 40 |
| Cu65 | 9 | 7110 | 788 | 1825 | 2101 | 33 |
| Zn66 | 51 | 7253 | 1301 | 2033 | 1963 | 28 |
| As75 | 33 | 7066 | 138 | 844 | 1833 | 13 |
| Rb85 | 5 | 6078 | 1576 | 1737 | 1256 | 52 |
| Sr88 | 30 | 1771 | 265 | 454 | 465 | 27 |
| Zr90 | 55 | 6275 | 1354 | 1620 | 1251 | 47 |
| Mo95 | 15 | 7146 | 182 | 612 | 1691 | 16 |
| Ag107 | 6 | 2529 | 27 | 259 | 689 | 12 |
| Sn118 | 1013 | 1558 | 1286 | 1286 | 272 | 2 |
| Cs133 | 4 | 1330 | 69 | 151 | 240 | 38 |
| Ba137 | 40 | 9331 | 1803 | 2926 | 2673 | 29 |
| La139 | 11 | 82365 | 334 | 2704 | 12161 | 50 |
| Ce140 | 11 | 1829 | 552 | 632 | 501 | 52 |
| Hf178 | 4 | 533 | 58 | 96 | 111 | 33 |
| Ta181 | 2 | 256 | 28 | 50 | 57 | 28 |
| W182 | 12 | 132 | 46 | 51 | 31 | 17 |
| Au197 | 34 | 137 | 85 | 85 | 51 | 2 |
| Tl205 | 1 | 73 | 10 | 14 | 17 | 14 |
| Pb208 | 17 | 5153 | 276 | 697 | 1063 | 48 |
| U238 | 1 | 623 | 59 | 84 | 102 | 41 |

**Table 4.13: Laser Ablation-ICPMS data from quartz**

| | Li ppm | Na ppm | Al ppm | K ppm | Ti ppm | Mn ppm | Fe ppm | Huang and Audétat, 2012 (°C) P=0.165 b aTiO2=1 | Huang and Audétat, 2012 (°C) P=0.165 b aTiO2=0.5 | Thomas et al., 2010 (°C) P=0.165 b aTiO2=1 | Huang and Audétat, 2012 (°C) P=0.5 b aTiO2=1 | Huang and Audétat, 2012 (°C) P=0.5 b aTiO2=0.5 | Thomas et al., 2010 (°C) P=0.5 b aTiO2=0.5 |
|---|---|---|---|---|---|---|---|---|---|---|---|---|---|
| SH-26_UST-B | | | 74 | | 12369 | | 109 | 1752 | 2011 | 1733 | 1859 | 2132 | 1752 |
| SH-26_UST-B | | | 74 | | 12369 | | 109 | 1752 | 2011 | 1733 | 1859 | 2132 | 1752 |
| SH-26_UST-B | | | 87 | | 11034 | | 80 | 1689 | 1931 | 1674 | 1793 | 2048 | 1692 |
| SH-26_UST-B | | 31 | 162 | 35945 | 12861 | | | 1774 | 2039 | 1725 | 1883 | 2162 | 1744 |
| SH-26_UST-B | | | 63 | | 7246 | | 86 | 1488 | 1681 | 1481 | 1582 | 1785 | 1498 |
| SH-26_UST-B | | | 222 | 4850 | 6440 | | | 1439 | 1621 | 1430 | 1530 | 1721 | 1446 |
| SH-26_UST-B | | 42 | 140 | 3569 | 4300 | | | 1290 | 1440 | 1286 | 1373 | 1531 | 1301 |
| SH-26_UST-B | | | 79 | | 5327 | | | 1366 | 1531 | 1362 | 1453 | 1627 | 1377 |
| SH-26_UST-B | | | 81 | | 5399 | 25 | | 1371 | 1537 | 1367 | 1458 | 1633 | 1382 |
| SH-26_UST-B | 279 | | 280 | 1113 | 1411 | | 2567 | 987 | 1083 | 989 | 1054 | 1154 | 1001 |
| SH-26_UST-B | 562 | 41 | 393 | 1513 | 1696 | 880 | | 1029 | 1131 | 1030 | 1098 | 1205 | 1042 |
| SH-26_UST-B | 83 | 46 | 443 | 1074 | 874 | 79 | 408 | 890 | 971 | 894 | 952 | 1037 | 905 |
| SH-26_UST-D | | | 73 | | 11274 | | | 1701 | 1946 | 1685 | 1805 | 2063 | 1703 |
| SH-26_UST-D | 240 | 20 | 680 | 3624 | 2233 | 806 | 4849 | 1096 | 1210 | 1094 | 1169 | 1289 | 1107 |
| SH-26_UST-D | 319 | | 750 | 3412 | 3003 | | 1727 | 1178 | 1306 | 1175 | 1255 | 1390 | 1189 |
| SH-26_UST-D | 398 | 147 | 322 | 2375 | 1368 | 255 | 6402 | 980 | 1075 | 981 | 1047 | 1146 | 993 |
| SH-26_UST-D | 413 | 87 | 329 | 3654 | 1919 | 492 | 13883 | 1058 | 1165 | 1054 | 1129 | 1242 | 1067 |
| SH-26_UST-D | 399 | 67 | 288 | 1424 | 1408 | 398 | 3292 | 987 | 1082 | 987 | 1053 | 1154 | 999 |
| SH-26_UST-D | 562 | 41 | 393 | 1513 | 1696 | 880 | | 1029 | 1131 | 1030 | 1098 | 1205 | 1042 |
| SH-26_UST-D | 562 | 41 | 393 | 1513 | 1696 | 880 | | 1029 | 1131 | 1030 | 1098 | 1205 | 1042 |
| SH-26_UST-D | 518 | 25 | 370 | 1398 | 1911 | 406 | 2442 | 1057 | 1164 | 1057 | 1128 | 1240 | 1070 |
| SH-26_UST-D | 505 | 28 | 368 | 1999 | 1852 | | 2071 | 1050 | 1155 | 1050 | 1120 | 1231 | 1062 |
| SH-26_UST-D | 505 | 28 | 368 | 1999 | 1852 | | 2071 | 1050 | 1155 | 1050 | 1120 | 1231 | 1062 |
| SH-26_UST-D | 590 | | 427 | 1915 | 2047 | | | 1074 | 1184 | 1074 | 1146 | 1261 | 1087 |
| SH-26_UST-D | 470 | | 509 | 2537 | 1905 | | 2084 | 1056 | 1163 | 1056 | 1127 | 1239 | 1069 |
| SH-26_UST-D | 47 | | 376 | 441 | 682 | | | 846 | 920 | 850 | 905 | 984 | 861 |
| SH-26_UST-D | 53 | 39 | 411 | 581 | 429 | 31 | 196 | 771 | 836 | 776 | 826 | 894 | 786 |
| SH-26_UST-D | 263 | 19 | 242 | 1145 | 1196 | | 6513 | 952 | 1042 | 952 | 1017 | 1112 | 964 |
| SH-26_UST-D | 369 | 87 | 315 | 3163 | 1600 | 869 | 15482 | 1015 | 1115 | 1011 | 1083 | 1189 | 1023 |
| SH-26_UST-D | 521 | 17 | 410 | 1953 | 2013 | | | 1070 | 1179 | 1070 | 1141 | 1256 | 1083 |
| SH-26_UST-D | 521 | 17 | 410 | 1953 | 2013 | | | 1070 | 1179 | 1070 | 1141 | 1256 | 1083 |
| SH-26_UST-D | 50 | 32 | 406 | 520 | 572 | | 151 | 816 | 887 | 821 | 874 | 948 | 831 |
| SH-26_UST-D | 425 | 64 | 346 | 1753 | 1730 | 393 | 4094 | 1033 | 1136 | 1033 | 1103 | 1211 | 1046 |
| SH-26_UST-D | 279 | | 280 | 1113 | 1411 | | 2567 | 987 | 1083 | 989 | 1054 | 1154 | 1001 |
| SH-26_UST-D | | | 86 | | 11195 | 3 | 45 | 1697 | 1941 | 1681 | 1801 | 2058 | 1700 |

**Table 4.13 (Continued)**

| | Li ppm | Na ppm | Al ppm | K ppm | Ti ppm | Mn ppm | Fe ppm | Huang and Audétat, 2012 (°C) P=0.165 b aTiO2=1 | Huang and Audétat, 2012 (°C) P=0.165 b aTiO2=0.5 | Thomas et al., 2010 (°C) P=0.165 b aTiO2=1 | Huang and Audétat, 2012 (°C) P=0.5 b aTiO2=1 | Huang and Audétat, 2012 (°C) P=0.5 b aTiO2=0.5 | Thomas et al., 2010 (°C) P=0.5 b aTiO2=0.5 |
|---|---|---|---|---|---|---|---|---|---|---|---|---|---|
| SH-24_UST-B | 17 | 111 | 340 | 154 | 164 | 75 | 103 | 644 | 693 | 650 | 692 | 745 | 659 |
| SH-24_UST-B | 8 | | 130 | | 77 | | | 563 | 604 | 570 | 608 | 651 | 578 |
| SH-24_UST-B | 13 | 93 | 350 | 122 | 136 | 37 | 93 | 623 | 670 | 629 | 670 | 720 | 637 |
| SH-24_UST-B | 8 | | 98 | | 139 | | | 625 | 673 | 631 | 673 | 723 | 640 |
| SH-24_UST-B | 5 | | 97 | | 145 | | | 630 | 678 | 636 | 677 | 728 | 645 |
| SH-24_UST-B | 5 | | 288 | 157 | 159 | | | 640 | 690 | 647 | 689 | 741 | 655 |
| SH-24_UST-B | 7 | | 105 | | 151 | | | 634 | 683 | 640 | 682 | 733 | 649 |
| SH-24_UST-B | | | 183 | | 151 | | | 634 | 683 | 641 | 682 | 734 | 649 |
| SH-24_UST-B | 6 | | 368 | 135 | 184 | | | 657 | 708 | 663 | 706 | 760 | 672 |
| SH-24_UST-B | 6 | | 117 | | 152 | | | 635 | 683 | 641 | 683 | 734 | 650 |
| SH-24_UST-B | 6 | | 169 | | 114 | | | 604 | 649 | 610 | 650 | 698 | 619 |
| SH-24_UST-B | 6 | | 88 | | 136 | | | 622 | 670 | 629 | 670 | 719 | 637 |
| SH-24_UST-B | 5 | | 105 | | 137 | | | 623 | 671 | 630 | 671 | 721 | 638 |
| SH-24_UST-B | 5 | 297 | 104 | 509 | 240 | 109 | 540 | 690 | 745 | 696 | 741 | 799 | 705 |
| SH-24_UST-B | 8 | | 205 | 66 | 103 | | | 592 | 636 | 599 | 638 | 685 | 607 |
| SH-24_UST-B | 8 | | 90 | | 143 | | | 628 | 676 | 634 | 676 | 726 | 643 |
| SH-24_UST-B | 8 | | 103 | | 91 | | | 580 | 623 | 587 | 626 | 671 | 595 |
| SH-24_UST-B | 6 | | 103 | 41 | 130 | | | 617 | 664 | 624 | 664 | 714 | 632 |
| SH-24_UST-B | 8 | | 98 | 21 | 109 | | | 598 | 643 | 604 | 644 | 691 | 613 |
| SH-24_UST-B | 6 | | 106 | | 157 | | | 638 | 687 | 645 | 687 | 738 | 653 |
| SH-24_UST-D | 5 | | 82 | 43 | 145 | 28 | 97 | 630 | 678 | 636 | 678 | 728 | 645 |
| SH-24_UST-D | 16 | | 432 | 134 | 163 | | | 643 | 692 | 649 | 691 | 743 | 658 |
| SH-24_UST-D | 14 | 147 | 375 | 201 | 151 | 51 | 196 | 634 | 682 | 640 | 682 | 733 | 649 |
| SH-24_UST-D | 15 | | 427 | 154 | 177 | 42 | 103 | 652 | 703 | 659 | 702 | 755 | 667 |
| SH-24_UST-D | 13 | 91 | 385 | 249 | 109 | 108 | 321 | 599 | 644 | 605 | 645 | 692 | 614 |
| SH-24_UST-D | 5 | | 98 | | 127 | | | 615 | 661 | 621 | 662 | 711 | 630 |
| SH-24_UST-D | 5 | | 99 | 59 | 144 | 23 | 58 | 629 | 677 | 635 | 677 | 727 | 644 |
| SH-24_UST-D | 6 | | 88 | 87 | 145 | 51 | 208 | 630 | 678 | 636 | 677 | 728 | 644 |
| SH-24_UST-D | | 342 | 108 | 555 | 219 | 110 | 528 | 679 | 732 | 684 | 729 | 786 | 694 |
| SH-24_UST-D | 4 | 325 | 101 | 570 | 235 | 119 | 526 | 687 | 742 | 693 | 738 | 796 | 702 |
| SH-24_UST-D | 12 | | 418 | 121 | 145 | | | 629 | 677 | 636 | 677 | 728 | 644 |
| SH-24_UST-D | 18 | | 396 | 94 | 240 | | | 690 | 745 | 696 | 741 | 799 | 705 |

**Table 4.13 (Continued)**

| | Li ppm | Na ppm | Al ppm | K ppm | Ti ppm | Mn ppm | Fe ppm | Huang and Audétat, 2012 (°C) P=0.165 b aTiO2=1 | Huang and Audétat, 2012 (°C) P=0.165 b aTiO2=0.5 | Thomas et al., 2010 (°C) P=0.165 b aTiO2=1 | Huang and Audétat, 2012 (°C) P=0.5 b aTiO2=1 | Huang and Audétat, 2012 (°C) P=0.5 b aTiO2=0.5 | Thomas et al., 2010 (°C) P=0.5 b aTiO2=0.5 |
|---|---|---|---|---|---|---|---|---|---|---|---|---|---|
| SH-24_Ph-B | 8 | | 286 | 150 | 105 | 26 | 101 | 595 | 639 | 601 | 641 | 687 | 609 |
| SH-24_Ph-B | 6 | 352 | 123 | 146 | 112 | 52 | 136 | 602 | 647 | 608 | 648 | 696 | 617 |
| SH-24_Ph-B | 9 | | 412 | 133 | 146 | | 43 | 630 | 678 | 636 | 678 | 729 | 645 |
| SH-24_Ph-B | 8 | 209 | 860 | 342 | 162 | | 93 | 643 | 692 | 649 | 691 | 743 | 657 |
| SH-24_Ph-B | 9 | | 209 | 80 | 122 | | 47 | 610 | 656 | 617 | 657 | 705 | 625 |
| SH-24_Ph-B | 8 | 72 | 457 | 200 | 105 | | 54 | 595 | 639 | 601 | 641 | 687 | 609 |
| SH-24_Ph-B | 12 | | 523 | 228 | 243 | | 35 | 692 | 747 | 698 | 743 | 801 | 707 |
| SH-24_Ph-B | 9 | | 347 | 109 | 134 | | | 621 | 668 | 627 | 668 | 718 | 636 |
| SH-24_Ph-B | 10 | 175 | 370 | 180 | 133 | 15 | 97 | 620 | 667 | 627 | 668 | 717 | 635 |
| SH-24_Ph-B | 9 | | 438 | 167 | 239 | | 23 | 690 | 745 | 696 | 741 | 798 | 705 |
| SH-24_Ph-B | 11 | | 820 | 361 | 180 | | 77 | 655 | 706 | 661 | 704 | 757 | 670 |
| SH-24_Ph-B | 9 | | 406 | 98 | 207 | | | 671 | 724 | 677 | 721 | 777 | 686 |
| SH-24_Ph-B | 13 | | 1060 | 468 | 181 | | 76 | 656 | 706 | 661 | 705 | 758 | 670 |
| SH-24_Ph-B | 13 | | 1060 | 468 | 181 | | 76 | 656 | 706 | 661 | 705 | 758 | 670 |
| SH-24_Ph-B | 8 | | 340 | 158 | 230 | 21 | 77 | 685 | 739 | 691 | 736 | 793 | 700 |
| SH-24_Ph-B | 8 | 110 | 436 | 155 | 140 | | 40 | 626 | 673 | 632 | 673 | 723 | 640 |
| SH-24_Ph-B | 11 | | 392 | 207 | 180 | 58 | 97 | 655 | 705 | 661 | 704 | 757 | 670 |

**Table 4.13 (Continued)**

| | Li ppm | Na ppm | Al ppm | K ppm | Ti ppm | Mn ppm | Fe ppm | Huang and Audétat, 2012 (°C) P=0.165 b aTiO2=1 | Huang and Audétat, 2012 (°C) P=0.165 b aTiO2=0.5 | Thomas et al., 2010 (°C) P=0.165 b aTiO2=1 | Huang and Audétat, 2012 (°C) P=0.5 b aTiO2=1 | Huang and Audétat, 2012 (°C) P=0.5 b aTiO2=0.5 | Thomas et al., 2010 (°C) P=0.5 b aTiO2=0.5 |
|---|---|---|---|---|---|---|---|---|---|---|---|---|---|
| SH-24_Ph-D | 7 | 253 | 107 | 45 | 102 | 14 | 68 | 592 | 636 | 598 | 638 | 684 | 607 |
| SH-24_Ph-D | 10 | | 158 | 33 | 123 | | | 612 | 658 | 618 | 659 | 707 | 627 |
| SH-24_Ph-D | 5 | | 229 | 288 | 95 | | | 585 | 628 | 591 | 630 | 676 | 599 |
| SH-24_Ph-D | 6 | | 162 | 0 | 94 | | | 584 | 627 | 590 | 629 | 674 | 598 |
| SH-24_Ph-D | 8 | | 223 | 125 | 126 | | | 614 | 661 | 621 | 661 | 710 | 629 |
| SH-24_Ph-D | 5 | | 66 | 0 | 78 | 23 | 68 | 565 | 607 | 572 | 610 | 653 | 580 |
| SH-24_Ph-D | 6 | | 82 | 0 | 91 | | | 580 | 623 | 587 | 626 | 671 | 595 |
| SH-24_Ph-D | 9 | | 163 | 0 | 91 | | | 580 | 623 | 587 | 626 | 671 | 595 |
| SH-24_Ph-D | 8 | | 85 | 0 | 125 | | | 613 | 659 | 619 | 660 | 709 | 628 |
| SH-24_Ph-D | 7 | | 156 | 50 | 132 | | 36 | 619 | 666 | 625 | 666 | 716 | 634 |
| SH-24_Ph-D | 8 | | 113 | 0 | 122 | 8 | | 610 | 656 | 617 | 657 | 705 | 625 |
| SH-24_Ph-D | 14 | | 542 | 174 | 204 | | 39 | 670 | 723 | 676 | 720 | 775 | 685 |
| SH-24_Ph-D | 8 | | 85 | 0 | 92 | | | 581 | 624 | 587 | 626 | 671 | 596 |
| SH-24_Ph-D | 6 | | 311 | 113 | 127 | | | 615 | 661 | 621 | 662 | 711 | 629 |
| SH-24_Ph-D | 8 | 139 | 155 | 38 | 94 | | | 584 | 627 | 590 | 629 | 674 | 598 |
| SH-24_Ph-D | 9 | | 246 | 43 | 156 | | | 638 | 687 | 644 | 686 | 738 | 653 |
| SH-24_Ph-D | 9 | | 246 | 43 | 156 | | | 638 | 687 | 644 | 686 | 738 | 653 |
| SH-24_Ph-D | 7 | | 88 | 0 | 79 | | | 566 | 607 | 572 | 610 | 654 | 580 |
| SH-24_Ph-D | 7 | 46 | 105 | 64 | 85 | | | 574 | 616 | 580 | 618 | 663 | 588 |
| SH-24_Ph-D | 6 | | 225 | 237 | 77 | 56 | 263 | 564 | 605 | 570 | 608 | 651 | 578 |
| SH-24_Ph-D | 8 | | 345 | 305 | 99 | | 56 | 589 | 632 | 595 | 634 | 680 | 603 |
| SH-24_Ph-D | 8 | | 89 | 36 | 97 | | 58 | 586 | 630 | 593 | 632 | 677 | 601 |
| SH-24_Ph-D | 10 | 50 | 120 | 40 | 111 | 9 | 26 | 601 | 646 | 607 | 647 | 694 | 615 |
| SH-24_Ph-D | 6 | 65 | 55 | 0 | 72 | 16 | | 557 | 597 | 563 | 601 | 643 | 571 |
| SH-24_Ph-D | 5 | | 61 | 37 | 78 | 23 | 67 | 565 | 606 | 572 | 610 | 653 | 580 |
| SH-24_Ph-D | 20 | 88 | 518 | 213 | 196 | 15 | 95 | 665 | 717 | 671 | 714 | 769 | 680 |
| SH-24_Ph-D | 17 | 88 | 514 | 243 | 166 | 56 | 177 | 645 | 695 | 651 | 694 | 746 | 660 |
| SH-24_Ph-D | 18 | 93 | 508 | 212 | 181 | 36 | 164 | 655 | 706 | 661 | 705 | 758 | 670 |
| SH-24_Ph-D | 8 | 51 | 131 | 50 | 97 | 14 | 284 | 586 | 630 | 593 | 632 | 678 | 601 |
| SH-24_Ph-D | 6 | | 77 | 0 | 95 | 9 | | 585 | 628 | 591 | 630 | 676 | 599 |
| SH-24_Ph-D | 8 | | 75 | 0 | 80 | | | 568 | 609 | 574 | 612 | 656 | 582 |
| SH-24_Ph-D | 8 | | 199 | 51 | 125 | | | 613 | 660 | 620 | 660 | 709 | 628 |

**Table 4.13 (Continued)**

| | Li ppm | Na ppm | Al ppm | K ppm | Ti ppm | Mn ppm | Fe ppm | Huang and Audétat, 2012 (°C) P=0.165 b aTiO2=1 | Huang and Audétat, 2012 (°C) P=0.165 b aTiO2=0.5 | Thomas et al., 2010 (°C) P=0.165 b aTiO2=1 | Huang and Audétat, 2012 (°C) P=0.5 b aTiO2=1 | Huang and Audétat, 2012 (°C) P=0.5 b aTiO2=0.5 | Thomas et al., 2010 (°C) P=0.5 b aTiO2=0.5 |
|---|---|---|---|---|---|---|---|---|---|---|---|---|---|
| SH-22_UST-B | 26 | 15 | 486 | 117 | 815 | 5 | | 877 | 956 | 882 | 938 | 1022 | 893 |
| SH-22_UST-B | 16 | 52 | 474 | 279 | 885 | 42 | 72 | 892 | 974 | 897 | 954 | 1040 | 908 |
| SH-22_UST-B | 9 | 12 | 579 | 121 | 135 | | 7 | 622 | 669 | 628 | 669 | 719 | 636 |
| SH-22_UST-B | 10 | 3 | 313 | 28 | 100 | 7 | 6 | 590 | 634 | 596 | 636 | 682 | 604 |
| SH-22_UST-B | 7 | 7 | 108 | 10 | 134 | | | 621 | 668 | 627 | 668 | 718 | 636 |
| SH-22_UST-B | 5 | | 116 | 4 | 163 | | | 643 | 693 | 649 | 692 | 744 | 658 |
| SH-22_UST-B | 5 | 21 | 110 | 8 | 133 | | 18 | 620 | 667 | 626 | 667 | 716 | 635 |
| SH-22_UST-B | 6 | | 103 | | 144 | 10 | 8 | 629 | 677 | 635 | 677 | 727 | 644 |
| SH-22_UST-B | 6 | | 103 | | 144 | 10 | 8 | 629 | 677 | 635 | 677 | 727 | 644 |
| SH-22_UST-B | 11 | | 96 | | 468 | | | 784 | 850 | 789 | 840 | 910 | 800 |
| SH-22_UST-B | 16 | | 167 | 100 | 353 | | | 742 | 803 | 748 | 796 | 860 | 758 |
| SH-22_UST-B | 21 | | 368 | 291 | 219 | | | 679 | 732 | 685 | 729 | 786 | 694 |
| SH-22_UST-B | 19 | | 311 | 177 | 385 | | | 755 | 817 | 760 | 809 | 875 | 770 |
| SH-22_UST-B | 12 | | 123 | | 375 | | | 751 | 813 | 757 | 805 | 871 | 767 |
| SH-22_UST-B | 5 | | 90 | | 152 | | | 635 | 684 | 642 | 683 | 735 | 650 |
| SH-22_UST-B | 11 | 2 | 433 | 57 | 105 | | 7 | 595 | 639 | 601 | 641 | 687 | 609 |
| SH-22_UST-D | 6 | | 103 | | 144 | 10 | 8 | 629 | 677 | 635 | 677 | 727 | 644 |
| SH-22_UST-D | 32 | | 477 | 256 | 432 | 14 | | 772 | 837 | 777 | 827 | 896 | 787 |
| SH-22_UST-D | 23 | 245 | 396 | 331 | 522 | | | 801 | 870 | 806 | 858 | 931 | 817 |
| SH-22_UST-D | | | 96 | | 464 | | | 783 | 849 | 788 | 839 | 909 | 798 |
| SH-22_UST-D | 32 | 64 | 336 | 227 | 473 | 21 | 86 | 786 | 852 | 791 | 842 | 912 | 801 |
| SH-22_UST-D | 28 | | 269 | 220 | 403 | 56 | 154 | 761 | 825 | 767 | 816 | 883 | 777 |
| SH-22_UST-D | 21 | 235 | 245 | 216 | 380 | | | 753 | 816 | 759 | 807 | 873 | 768 |
| SH-22_UST-D | 29 | | 410 | 392 | 376 | 46 | 314 | 751 | 814 | 757 | 806 | 871 | 767 |
| SH-22_UST-D | 29 | | 518 | 286 | 594 | | | 822 | 894 | 827 | 880 | 955 | 838 |
| SH-22_UST-D | 29 | | 518 | 286 | 594 | | | 822 | 894 | 827 | 880 | 955 | 838 |
| SH-22_UST-D | 15 | 533 | 281 | 145 | 246 | 54 | 329 | 693 | 748 | 699 | 744 | 802 | 708 |
| SH-22_UST-D | 14 | 29 | 372 | 98 | 251 | 16 | 80 | 696 | 751 | 702 | 747 | 806 | 711 |
| SH-22_UST-D | 15 | 25 | 299 | 44 | 262 | 12 | 65 | 701 | 758 | 707 | 753 | 812 | 717 |
| SH-22_UST-D | 14 | 22 | 286 | 125 | 334 | 11 | | 734 | 795 | 740 | 788 | 851 | 750 |
| SH-22_UST-D | 22 | 9 | 520 | 189 | 565 | 4 | 13 | 814 | 885 | 819 | 872 | 946 | 829 |
| SH-22_UST-D | 16 | 35 | 477 | 77 | 170 | 24 | 23 | 648 | 698 | 654 | 697 | 749 | 663 |
| SH-22_UST-D | 29 | 500 | 414 | 529 | 236 | 184 | 492 | 688 | 743 | 693 | 739 | 797 | 702 |
| SH-22_UST-D | 17 | 19 | 594 | 259 | 239 | 15 | 67 | 690 | 745 | 695 | 741 | 799 | 705 |
| SH-22_UST-D | 16 | 3 | 351 | 82 | 232 | | 7 | 686 | 740 | 692 | 737 | 794 | 701 |

**Table 4.13 (Continued)**

| | Li ppm | Na ppm | Al ppm | K ppm | Ti ppm | Mn ppm | Fe ppm | Huang and Audétat, 2012 (°C) P=0.165 b aTiO2=1 | Huang and Audétat, 2012 (°C) P=0.165 b aTiO2=0.5 | Thomas et al., 2010 (°C) P=0.165 b aTiO2=1 | Huang and Audétat, 2012 (°C) P=0.5 b aTiO2=1 | Huang and Audétat, 2012 (°C) P=0.5 b aTiO2=0.5 | Thomas et al., 2010 (°C) P=0.5 b aTiO2=0.5 |
|---|---|---|---|---|---|---|---|---|---|---|---|---|---|
| SH-22_PH-B | 12 | | 720 | 597 | 294 | | 114 | 717 | 775 | 723 | 770 | 831 | 732 |
| SH-22_PH-B | 15 | 77 | 120 | 442 | 145 | 78 | 354 | 630 | 678 | 636 | 678 | 728 | 645 |
| SH-22_PH-B | 29 | | 666 | 441 | 315 | | | 726 | 786 | 732 | 779 | 842 | 742 |
| SH-22_PH-B | 17 | | 1609 | 1797 | 346 | | 299 | 739 | 800 | 744 | 793 | 857 | 754 |
| SH-22_PH-B | 19 | | 1375 | 1545 | 288 | 73 | 336 | 714 | 772 | 719 | 766 | 827 | 729 |
| SH-22_PH-B | 26 | | 911 | 852 | 362 | | 125 | 746 | 807 | 751 | 800 | 865 | 761 |
| SH-22_PH-B | 19 | 30 | 886 | 276 | 164 | 3 | 81 | 644 | 693 | 650 | 692 | 745 | 659 |
| SH-22_PH-B | 14 | 32 | 1384 | 574 | 149 | 8 | 106 | 633 | 681 | 639 | 681 | 732 | 647 |
| SH-22_PH-B | 14 | | 426 | 305 | 261 | | | 701 | 757 | 707 | 752 | 812 | 716 |
| SH-22_PH-B | 15 | | 566 | 584 | 199 | | | 667 | 719 | 673 | 717 | 772 | 682 |
| SH-22_PH-B | 12 | | 228 | 233 | 202 | | | 668 | 721 | 674 | 718 | 773 | 683 |
| SH-22_PH-B | 29 | | 666 | 441 | 315 | | | 726 | 786 | 732 | 779 | 842 | 742 |
| SH-22_PH-B | 10 | | 139 | 0 | 92 | | | 581 | 624 | 587 | 626 | 671 | 596 |
| SH-22_PH-B | 12 | | 216 | 0 | 55 | | | 532 | 570 | 539 | 575 | 615 | 547 |
| SH-22_PH-B | 6 | | 66 | 0 | 105 | | | 595 | 639 | 601 | 641 | 687 | 609 |
| SH-22_PH-B | 6 | 14 | 138 | 20 | 100 | | 22 | 589 | 633 | 596 | 635 | 681 | 604 |
| SH-22_PH-B | 3 | 19 | 81 | 37 | 73 | | 15 | 559 | 599 | 565 | 603 | 646 | 573 |
| SH-22_PH-B | 9 | 23 | 65 | 0 | 127 | | 22 | 615 | 662 | 621 | 662 | 711 | 630 |
| SH-22_PH-B | 14 | 32 | 1384 | 574 | 149 | 8 | 106 | 633 | 681 | 639 | 681 | 732 | 647 |
| SH-22_PH-B | 14 | 19 | 1284 | 486 | 255 | 5 | 69 | 698 | 754 | 703 | 749 | 808 | 713 |
| SH-22_PH-B | 11 | 52 | 636 | 193 | 166 | 4 | 42 | 645 | 695 | 651 | 694 | 746 | 660 |
| SH-22_PH-B | 11 | 52 | 636 | 193 | 166 | 4 | 42 | 645 | 695 | 651 | 694 | 746 | 660 |
| SH-22_PH-B | 9 | | 178 | 0 | 249 | 2 | | 695 | 750 | 701 | 746 | 805 | 710 |
| SH-22_PH-B | 21 | 14 | 518 | 161 | 586 | 3 | 35 | 820 | 891 | 825 | 878 | 953 | 835 |
| SH-22_PH-B | 5 | | 514 | 154 | 79 | 8 | 104 | 566 | 608 | 572 | 611 | 654 | 580 |
| SH-22_PH-B | 4 | 7 | 95 | 0 | 75 | | 61 | 561 | 601 | 567 | 605 | 648 | 575 |
| SH-22_PH-B | 5 | 6 | 90 | 0 | 106 | | | 596 | 640 | 602 | 642 | 689 | 611 |
| SH-22_PH-B | 17 | | 104 | 0 | 231 | | | 685 | 739 | 691 | 736 | 793 | 700 |
| SH-22_PH-B | 9 | | 136 | 164 | 186 | 30 | | 658 | 710 | 665 | 708 | 762 | 673 |
| SH-22_PH-B | 15 | 3 | 656 | 250 | 483 | 4 | 16 | 789 | 856 | 794 | 845 | 916 | 804 |
| SH-22_PH-B | 6 | 67 | 74 | 15 | 50 | 5 | | 523 | 561 | 530 | 566 | 605 | 537 |

**Table 4.13 (Continued)**

| | Li ppm | Na ppm | Al ppm | K ppm | Ti ppm | Mn ppm | Fe ppm | Huang and Audétat, 2012 (°C) P=0.165 b aTiO2=1 | Huang and Audétat, 2012 (°C) P=0.165 b aTiO2=0.5 | Thomas et al., 2010 (°C) P=0.165 b aTiO2=1 | Huang and Audétat, 2012 (°C) P=0.5 b aTiO2=1 | Huang and Audétat, 2012 (°C) P=0.5 b aTiO2=0.5 | Thomas et al., 2010 (°C) P=0.5 b aTiO2=0.5 |
|---|---|---|---|---|---|---|---|---|---|---|---|---|---|
| SH-22_PH-D | 16 | | 133 | 0 | 315 | | | 726 | 786 | 732 | 779 | 842 | 742 |
| SH-22_PH-D | 20 | | 369 | 337 | 187 | | | 659 | 710 | 665 | 708 | 762 | 674 |
| SH-22_PH-D | 15 | | 103 | 94 | 167 | | | 646 | 696 | 652 | 695 | 747 | 661 |
| SH-22_PH-D | 10 | 129 | 134 | 83 | 145 | | | 629 | 677 | 635 | 677 | 728 | 644 |
| SH-22_PH-D | 29 | | 402 | 309 | 204 | | | 670 | 722 | 676 | 719 | 775 | 685 |
| SH-22_PH-D | 16 | | 336 | 148 | 240 | | | 690 | 745 | 696 | 741 | 799 | 705 |
| SH-22_PH-D | 31 | | 1071 | 677 | 316 | | | 727 | 786 | 732 | 779 | 842 | 742 |
| SH-22_PH-D | 26 | | 654 | 539 | 481 | 23 | 104 | 788 | 855 | 793 | 844 | 915 | 804 |
| SH-22_PH-D | 15 | | 103 | 94 | 167 | | | 646 | 696 | 652 | 695 | 747 | 661 |
| SH-22_PH-D | 10 | 129 | 134 | 83 | 145 | | | 629 | 677 | 635 | 677 | 728 | 644 |
| SH-22_PH-D | 10 | 36 | 495 | 191 | 56 | 2 | 48 | 534 | 572 | 540 | 577 | 617 | 548 |
| SH-22_PH-D | 8 | | 105 | 19 | 348 | 6 | 5 | 740 | 801 | 746 | 794 | 858 | 756 |
| SH-22_PH-D | 13 | 9 | 154 | 14 | 151 | | 6 | 634 | 683 | 641 | 682 | 734 | 649 |
| SH-22_PH-D | 14 | 6 | 104 | 14 | 104 | 4 | 21 | 594 | 638 | 600 | 639 | 686 | 608 |
| SH-22_PH-D | 10 | 56 | 94 | 70 | 161 | 27 | 171 | 642 | 691 | 648 | 690 | 742 | 656 |
| SH-22_PH-D | 6 | 5 | 95 | 3 | 123 | | | 611 | 657 | 618 | 658 | 707 | 626 |
| SH-22_PH-D | 6 | 5 | 95 | 3 | 123 | | | 611 | 657 | 618 | 658 | 707 | 626 |

**Table 4.13 (Continued)**

| | Li ppm | Na ppm | Al ppm | K ppm | Ti ppm | Mn ppm | Fe ppm | Huang and Audétat, 2012 (°C) P=0.165 b aTiO2=1 | Huang and Audétat, 2012 (°C) P=0.165 b aTiO2=0.5 | Thomas et al., 2010 (°C) P=0.165 b aTiO2=1 | Huang and Audétat, 2012 (°C) P=0.5 b aTiO2=1 | Huang and Audétat, 2012 (°C) P=0.5 b aTiO2=0.5 | Thomas et al., 2010 (°C) P=0.5 b aTiO2=0.5 |
|---|---|---|---|---|---|---|---|---|---|---|---|---|---|
| SH-21_UST-B | 16 | 101 | 313 | 349 | 167 | 46 | 346 | 646 | 696 | 652 | 695 | 747 | 661 |
| SH-21_UST-B | 15 | 87 | 317 | 309 | 151 | 36 | 271 | 634 | 683 | 640 | 682 | 733 | 649 |
| SH-21_UST-B | 13 | 82 | 333 | 339 | 147 | 41 | 320 | 631 | 679 | 637 | 679 | 730 | 646 |
| SH-21_UST-B | 16 | 18 | 422 | 117 | 182 | 14 | 60 | 656 | 707 | 662 | 705 | 759 | 671 |
| SH-21_UST-B | 6 | 35 | 122 | 86 | 148 | 26 | 36 | 632 | 680 | 638 | 680 | 731 | 647 |
| SH-21_UST-B | 10 | 161 | 511 | 630 | 160 | 34 | 351 | 641 | 690 | 647 | 689 | 741 | 655 |
| SH-21_UST-B | 16 | | 332 | 121 | 147 | | | 631 | 680 | 637 | 679 | 730 | 646 |
| SH-21_UST-B | 10 | 41 | 108 | 24 | 149 | 21 | 78 | 633 | 681 | 639 | 681 | 732 | 648 |
| SH-21_UST-B | 7 | 3 | 91 | 7 | 169 | 3 | 10 | 648 | 698 | 654 | 696 | 749 | 662 |
| SH-21_UST-D | 14 | 71 | 418 | 163 | 175 | | | 651 | 702 | 657 | 700 | 753 | 666 |
| SH-21_UST-D | 16 | | 345 | 55 | 210 | | | 673 | 726 | 679 | 723 | 779 | 688 |
| SH-21_UST-D | 15 | 78 | 310 | 108 | 212 | 40 | 136 | 674 | 728 | 680 | 725 | 781 | 690 |
| SH-21_UST-D | 14 | 173 | 317 | 270 | 231 | 37 | 125 | 685 | 740 | 691 | 736 | 793 | 700 |
| SH-21_UST-D | 19 | 18 | 437 | 100 | 232 | | | 686 | 740 | 692 | 737 | 794 | 701 |
| SH-21_UST-D | 20 | | 489 | 142 | 265 | | | 703 | 760 | 709 | 755 | 814 | 718 |
| SH-21_UST-D | 15 | | 711 | 290 | 290 | | | 715 | 773 | 721 | 767 | 828 | 730 |
| SH-21_UST-D | 11 | 33 | 833 | 400 | 342 | 5 | 42 | 738 | 798 | 743 | 791 | 855 | 753 |
| SH-21_UST-D | 11 | 33 | 833 | 400 | 342 | 5 | 42 | 738 | 798 | 743 | 791 | 855 | 753 |
| SH-21_UST-D | 16 | | 444 | 155 | 195 | | 41 | 664 | 716 | 670 | 714 | 769 | 679 |
| SH-21_UST-D | 12 | 94 | 227 | 122 | 146 | 34 | 128 | 630 | 678 | 636 | 678 | 729 | 645 |
| SH-21_UST-D | 12 | 94 | 227 | 122 | 146 | 34 | 128 | 630 | 678 | 636 | 678 | 729 | 645 |
| SH-21_UST-D | 17 | 6 | 593 | 240 | 196 | 1 | 23 | 665 | 717 | 671 | 715 | 769 | 680 |
| SH-21_UST-D | 15 | | 333 | 90 | 199 | | 11 | 666 | 719 | 673 | 716 | 771 | 682 |

**Table 4.14: Laser Ablation-ICPMS data from brines. (All data in ppm, Uncorrected)**

| Sample Name | FIA | Li7 | B11 | Na23 | Mg24 | K39 | Ca44 | Mn55 | Fe56 | Fe57 | Cu65 |
|---|---|---|---|---|---|---|---|---|---|---|---|
| SH-26_MQB_FI1 | UST | 117.4 | 43.1 | 34110.6 | 196.6 | 105504 | - | 14088.5 | 95698.3 | 38440.6 | 17677.9 |
| SH-26_MQB_FI2 | UST | 1231.5 | 4701.1 | 13032.1 | 263 | 38071.5 | - | 9595.5 | 128083 | 45355.5 | 2445.1 |
| SH-26_MQB_FI3 | UST | - | - | 7758.3 | 105.8 | 8023.1 | - | 6095.5 | 160869 | 69606.7 | 52988.7 |
| SH-26_MQB_FI4 | UST | - | - | 6559 | 109.4 | 33650.2 | - | 10952.4 | 163243 | 60285.1 | 15841.9 |
| SH-26_MQB_FI5 | UST | - | - | 5841 | - | 35817.7 | - | 38212.5 | 145885 | 54768.9 | 428 |
| SH-26_MQB_FI6 | UST | - | - | 4491.9 | 91.7 | 39904.8 | - | 13979.1 | 163769 | 59845.8 | 11651.3 |
| SH-26_MQB_FI7 | UST | - | 82.1 | 4211.5 | 63.4 | 38867.9 | - | 14324.1 | 156637 | 65856.4 | 10599.8 |
| SH-26_MQB_FI8 | UST | - | - | 4189.3 | 880 | 48586 | - | 72181.9 | - | - | - |
| SH-26_MQB_FI9 | UST | - | - | 4083.1 | 111.3 | 39479.7 | - | 14454.5 | 161152 | 61470.8 | 10923.9 |
| SH-26_MQB_FI10 | UST | - | - | 4077.7 | 116.3 | 35182.3 | - | 14021.1 | 165430 | 61808.1 | 11578.3 |
| SH-26_MQB_FI11 | UST | - | - | 3989.3 | 102.9 | 41340.7 | - | 15187.4 | 161039 | 59121.7 | 12496.9 |
| SH-26_MQB_FI12 | UST | 24.4 | 45.8 | 3663 | 108.2 | 43017.4 | - | 9515.2 | 159002 | 67377.8 | 10835.8 |
| SH-26_MQB_FI13 | UST | 33.6 | 72.1 | 3271.6 | 106.7 | 48552.9 | 609.5 | 10062.7 | 161344 | 59573.6 | 8586.8 |
| SH-26_MQB_FI14 | UST | - | - | 2968.7 | - | 25651.2 | - | 64528.2 | 80307.3 | 28819.4 | 93.2 |
| SH-24_MQB_FI1 | UST | - | - | 118323 | - | 33375.9 | - | 12961 | 50471.6 | 34321.3 | 294.2 |
| SH-24_MQB_FI2 | UST | - | 91.1 | 94890.3 | - | 72171 | - | 14127.9 | 36182 | 24569.5 | 1414 |
| SH-24_MQB_FI3 | UST | - | 41.2 | 90136.5 | - | 64448.7 | 22890.4 | 15859.9 | 40290.6 | 27129.7 | 3406.6 |
| SH-24_MQB_FI4 | UST | - | 201.1 | 89329.8 | - | 63143.8 | - | 15648.8 | 43733 | 28611.4 | 2604.1 |
| SH-24_MQB_FI5 | UST | - | - | 84606.9 | - | 38395.6 | 22613.3 | 25363.9 | 51964.1 | 35839.3 | 1753.1 |
| SH-24_MQB_FI6 | UST | 53.8 | 101.1 | 79911.1 | - | 81190.2 | - | 18217.4 | 45871.6 | 31176.3 | 3065.4 |
| SH-24_MQB_FI7 | UST | - | - | 79856.7 | - | 52896.8 | - | 18419.4 | 47345.2 | 32052.5 | 571.9 |
| SH-24_MQB_FI8 | UST | - | 175.6 | 62362.6 | - | 64087 | - | 22388.5 | 60651.5 | 40891.8 | 355.4 |
| SH-24_MQB_FI9 | UST | - | - | 52893.3 | - | 37034 | - | 16275.6 | 46846 | 27833.2 | - |
| SH-22_MQB_FI1 | UST | - | 35.1 | 114344 | - | 73722.7 | - | 22272.1 | 48944.9 | - | - |
| SH-22_MQB_FI2 | UST | - | 15.4 | 111640 | - | 86843.9 | - | 23142.6 | 13787 | - | 5597.1 |
| SH-22_MQB_FI3 | UST | - | 71.2 | 86935.8 | - | 39639.4 | - | 15683.9 | 50200.9 | 50977.5 | 189.8 |
| SH-22_MQB_FI4 | UST | - | - | 77186.9 | - | 27864.6 | - | 11306 | 87577.3 | 13717.3 | 214.4 |
| SH-22_MQB_FI5 | UST | - | - | 70290.8 | - | 33088.7 | - | 11084.9 | 41413.8 | 13698.9 | 2068.4 |
| SH-22_MQB_FI6 | UST | - | 227.4 | 66727.9 | - | 38787.4 | - | 17286.1 | 71642.6 | 16771.2 | 123.6 |
| SH-22_MQB_FI7 | UST | - | - | 65715.3 | - | 32015.8 | 25832.3 | 14392.4 | 87705.9 | 16785.9 | 168.7 |
| SH-22_MQB_FI8 | UST | - | - | 61992.2 | - | 57715.4 | 27671.1 | 17457 | 58982.4 | 39344.9 | 148.6 |
| SH-22_MQB_FI9 | UST | - | - | 61519 | - | 59568.4 | - | 15393.3 | 34522.5 | 17525.4 | 514.9 |
| SH-22_MQB_FI10 | UST | - | 126.9 | 60858.5 | - | 54480.8 | - | 17188 | 49507.7 | 43419.6 | 102.4 |
| SH-22_MQB_FI11 | UST | - | 1240.5 | 60128.2 | - | 31483 | 27325 | 15031.8 | 84341.1 | 15495.7 | 85.2 |
| SH-22_MQB_FI12 | UST | - | - | 58243.2 | - | 82157.8 | - | 17821.7 | 60187.7 | 44278.8 | 4027.5 |
| SH-22_MQB_FI13 | UST | - | 53.6 | 57444.3 | - | 56078.3 | 30749.5 | 18046.5 | 59484.1 | 40305.2 | 237.5 |
| SH-22_MQB_FI14 | UST | - | 186.3 | 56875.6 | - | 111462 | - | 20382.9 | 49956.7 | 36537.8 | 4126.3 |
| SH-22_MQB_FI15 | UST | - | 190.4 | 52665.2 | - | 73938.6 | - | 32146.3 | 77684.2 | 22208.1 | 106.3 |
| SH-22_MQB_FI16 | UST | - | - | 52360.6 | - | 100382 | 8382.6 | 20867.6 | 58725.7 | 47003.2 | 981.4 |
| SH-22_MQB_FI17 | UST | 99.9 | 110.7 | 51186.3 | - | 97896.6 | 13009.1 | 19054.1 | 58487.7 | 44914.2 | 2961.9 |
| SH-22_MQB_FI18 | UST | - | 231.1 | 50669.4 | - | 33751.8 | 64847.4 | 38732.8 | 14956.6 | 12601.1 | 21.6 |
| SH-22_MQB_FI19 | UST | - | - | 45752.8 | - | 94899 | 17973.1 | 19235.6 | 59300.2 | 46564.6 | 995.4 |

**Table 4.14 (Continued)**

| Sample Name | FIA | Li7 | B11 | Na23 | Mg24 | K39 | Ca44 | Mn55 | Fe56 | Fe57 | Cu65 |
|---|---|---|---|---|---|---|---|---|---|---|---|
| SH-22_MQB_FI20 | UST | - | 6.2 | 37229.9 | - | 34500.3 | - | 8641.6 | 10458.9 | 160002 | 1473.3 |
| SH-22_MQB_FI21 | UST | - | 23.3 | 35345.7 | - | 96388.7 | 57203.2 | 57971.1 | 27118.2 | - | - |
| SH-22_MQB_FI22 | UST | - | 330.8 | 33326.1 | - | 102266 | 11280.4 | 19641.5 | 65959.6 | 49807.8 | 529.7 |
| SH-22_MQB_FI23 | UST | - | - | 30708 | - | 74600.8 | - | 3432.3 | 17103.8 | 6345.5 | 2186.2 |
| SH-21_MQB_FI1 | UST | - | 30.8 | 120726 | 40 | 61236.3 | - | 15556.3 | 39720.4 | 18618.3 | 890.6 |
| SH-21_MQB_FI2 | UST | 124.2 | 54.9 | 117735 | 579.2 | 68507.5 | - | 10741.6 | 33717.5 | 12474.2 | 3630.5 |
| SH-21_MQB_FI3 | UST | 72.8 | 47.2 | 113039 | 270.7 | 65207.6 | 7829.7 | 14139.2 | 42697 | 19138 | 2035 |
| SH-21_MQB_FI4 | UST | - | 67.7 | 109047 | 71.9 | 63326.4 | - | 15293.1 | 41082.5 | 19083.5 | 827.4 |
| SH-21_MQB_FI5 | UST | - | 195.2 | 108882 | - | 77945.7 | - | 15243.4 | 44889.9 | 16498.3 | 4665.3 |
| SH-21_MQB_FI6 | UST | 101.1 | - | 105689 | 59.2 | 70702.1 | - | 13688 | 42201.9 | 19846.3 | 3721.1 |
| SH-21_MQB_FI7 | UST | - | - | 102083 | - | 68928 | - | 15226.4 | 49429 | 24106.2 | 3970.3 |
| SH-21_MQB_FI8 | UST | - | - | 101622 | - | 70180.7 | - | 14208.5 | 43114.8 | 20649.5 | - |
| SH-21_MQB_FI9 | UST | - | - | 96129.3 | 37.7 | 63243.8 | - | 15525.8 | 49879.2 | 22391 | 2675.1 |
| SH-21_MQB_FI10 | UST | 1291.3 | - | 94916.5 | 133.4 | 64024.5 | - | 12790.4 | 47640.6 | 16868.8 | 1417.3 |
| SH-21_MQB_FI11 | UST | - | 23.3 | 81682.1 | 178.4 | 79784.2 | 21540.9 | 10677.8 | 51803.6 | 23463.1 | 8774 |
| SH-21_MQB_FI12 | UST | 593.1 | - | 36907.6 | 177.4 | 61080.7 | - | 41277.8 | 52367.8 | 21551.1 | 43.9 |
| SH-21_MQB_FI13 | UST | 181 | 65.6 | 27246.4 | 226.9 | 104972 | 28289.7 | 19611.4 | 61169.5 | - | - |
| SH-21_MQB_FI14 | UST | - | - | 9482.9 | 3928.8 | 53667.6 | - | 32685.6 | 74417.7 | 42623 | 838.6 |
| SH-24_Ph_FI1 | Ph | - | - | 101199 | - | 18532.5 | - | 9797 | 19185.2 | 11955 | 5602.5 |
| SH-24_Ph_FI2 | Ph | - | - | 72996.5 | - | 31669.4 | - | 10591.1 | 28447.9 | 17922.7 | 1761.4 |
| SH-24_Ph_FI3 | Ph | - | - | 69215 | - | 32850.9 | - | 8160.6 | 19902.6 | 12678.5 | 2173.9 |
| SH-24_Ph_FI4 | Ph | - | - | 67432 | - | 36061.6 | - | 15169.6 | 37716.7 | 23173.4 | - |
| SH-24_Ph_FI5 | Ph | - | 516.6 | 66005.1 | - | 43849.1 | - | 11370 | 37047.6 | 20661.6 | 1144.7 |
| SH-24_Ph_FI6 | Ph | - | - | 63158.7 | - | 35076.7 | - | 10876.6 | 36400.3 | 19466.2 | 2180.6 |
| SH-24_Ph_FI7 | Ph | - | 657.2 | 56274.3 | - | 13407.8 | - | 5278 | 14373.5 | 9233 | 8385.7 |
| SH-24_Ph_FI8 | Ph | - | - | 55090.3 | - | 43527.4 | - | 8035.3 | 46739 | 29810.8 | 7507.1 |
| SH-24_Ph_FI9 | Ph | - | - | 52781.3 | - | 33365.2 | - | 8461.7 | 38756.4 | 24742.5 | 707 |
| SH-24_Ph_FI10 | Ph | - | - | 41707 | - | 36986.3 | - | 6217.6 | 54503.9 | 32150.3 | 5387 |
| SH-24_Ph_FI11 | Ph | - | - | 93400.2 | - | 48260.3 | - | 13011.1 | 32757.3 | 22347.2 | 2507 |
| SH-24_Ph_FI12 | Ph | - | - | 56010.4 | - | 24798.8 | - | 23199.6 | 27468.8 | 16249.8 | - |
| SH-24_Ph_FI13 | Ph | - | - | 48680.6 | - | 49632.8 | - | 4598.4 | 52756.3 | 36965.9 | 5443.6 |
| SH-22_Ph_FI1 | Ph | 1172.5 | - | 70131 | - | 47999.4 | - | 7377.7 | 45319.5 | 21205 | - |
| SH-22_Ph_FI2 | Ph | - | 187.4 | 53594.3 | - | 36873.4 | - | 7605.5 | 53130.6 | 15695.3 | 9366 |
| SH-22_Ph_FI3 | Ph | - | - | 48530.6 | - | 28609.2 | - | 13768.5 | 66341.8 | 56630.6 | 5491.7 |

**Table 4.14 (Continued)**

| Sample Name | FIA | Zn66 | Rb85 | Sr88 | Mo95 | Cs133 | Ba137 | Ce140 | W182 | Tl205 | Pb208 |
|---|---|---|---|---|---|---|---|---|---|---|---|
| SH-26_MQB_FI1 | UST | 6715.3 | 495.7 | 119.5 | 348.5 | 17.8 | 51.4 | 66.5 | 22.8 | - | 1853.1 |
| SH-26_MQB_FI2 | UST | 5062.4 | 1281.6 | 230 | 56.3 | 428.1 | 254.9 | 42.2 | - | - | 1146.1 |
| SH-26_MQB_FI3 | UST | 6041.3 | 142.8 | 7.6 | 446.8 | 11.3 | - | - | - | - | 878.8 |
| SH-26_MQB_FI4 | UST | 5286.1 | 621.5 | 67.3 | 104.4 | 11.3 | 268 | 61.2 | 46.8 | - | 1365.6 |
| SH-26_MQB_FI5 | UST | 6001.7 | 854.9 | 233.4 | - | 39.3 | 4678.7 | - | 38.4 | - | 2702.5 |
| SH-26_MQB_FI6 | UST | 4545.2 | 629.7 | 35.7 | 113.1 | 10.9 | - | 46.6 | - | - | 1248.4 |
| SH-26_MQB_FI7 | UST | 4675.4 | 464.3 | 33.9 | 125.5 | 14.1 | 29.1 | 35.4 | - | - | 1186.8 |
| SH-26_MQB_FI8 | UST | - | 1355.7 | 1708.2 | - | 0 | - | - | - | - | 7587.6 |
| SH-26_MQB_FI9 | UST | 4402.7 | 787.4 | 41.6 | 171.8 | 9.4 | 48.3 | 55.6 | 40 | - | 1185.6 |
| SH-26_MQB_FI10 | UST | 4599.4 | 687.3 | 37 | 163.5 | 10.5 | - | 49 | - | - | 1223.1 |
| SH-26_MQB_FI11 | UST | 4498 | 624 | 26.1 | 153 | 11.3 | - | 38.4 | - | - | 1036.3 |
| SH-26_MQB_FI12 | UST | 4436.1 | 648.6 | 34.1 | 95.2 | 13.8 | - | 56.1 | - | - | 1238.9 |
| SH-26_MQB_FI13 | UST | 5845.8 | 846.2 | 44 | 78.8 | 10.1 | 167.9 | 47.3 | - | - | 1250.9 |
| SH-26_MQB_FI14 | UST | 12731.5 | 670.8 | 1182.1 | - | 116.9 | 2416.2 | - | 408.4 | - | 5469.3 |
| SH-24_MQB_FI1 | UST | 6789.6 | 235.6 | 259.6 | - | 25.4 | 2167.6 | - | - | - | 2190.6 |
| SH-24_MQB_FI2 | UST | 4487 | 547.1 | 349.3 | 4.4 | 46.9 | 1366.5 | 6 | 27 | 18.9 | 4478.6 |
| SH-24_MQB_FI3 | UST | 8250.3 | 375.4 | 554 | - | 40.1 | 1138.9 | 0.7 | 13.5 | 13.5 | 4059 |
| SH-24_MQB_FI4 | UST | 4301 | 411.9 | 291.6 | 12.4 | 27.1 | 1087.4 | 2.9 | 26.8 | 8.7 | 3258 |
| SH-24_MQB_FI5 | UST | 4793.8 | 447.5 | 472.2 | - | 23.2 | 619 | - | 72.2 | - | 2965.9 |
| SH-24_MQB_FI6 | UST | 6162 | 643.1 | 433.4 | 35.8 | 63 | 1418.4 | 3.2 | 58.7 | 15.1 | 5648.2 |
| SH-24_MQB_FI7 | UST | 4798.6 | 322.2 | 324.9 | - | 26.2 | 3056.8 | - | 52.4 | 11.8 | 2344.5 |
| SH-24_MQB_FI8 | UST | 5368.1 | 465.2 | 415.3 | - | 42.6 | 4173.1 | - | 20.4 | 15.3 | 2766.8 |
| SH-24_MQB_FI9 | UST | 5631.4 | 236.7 | 323.7 | - | 5 | 2509.6 | - | 10.5 | 13.9 | 2215.3 |
| SH-22_MQB_FI1 | UST | 5693.4 | 460.9 | 631.2 | - | 47.2 | 4377.1 | - | - | - | 3890.1 |
| SH-22_MQB_FI2 | UST | - | 499.4 | 464.1 | 1884 | 66.2 | 1077.8 | - | 403.7 | 13.9 | 5109.2 |
| SH-22_MQB_FI3 | UST | 11646.1 | 201.5 | 308.9 | - | 14 | 3329.5 | 7.8 | 22.3 | 5.2 | 1444.4 |
| SH-22_MQB_FI4 | UST | 25153.7 | 261.3 | 301.3 | - | 20.2 | 10445.5 | 1.4 | 21 | 5.8 | 1765.4 |
| SH-22_MQB_FI5 | UST | 7060.7 | 228.6 | 200.6 | 447.8 | 14.6 | 991.6 | - | - | - | - |
| SH-22_MQB_FI6 | UST | 12809.5 | 335.1 | 475.4 | - | 23.2 | 7557.7 | - | 29.7 | 10.3 | 2364.8 |
| SH-22_MQB_FI7 | UST | 21983.8 | 267.1 | 413.9 | - | 17.5 | 10333.3 | - | 36.8 | 12.8 | 2246.6 |
| SH-22_MQB_FI8 | UST | 7206 | 279.4 | 292.3 | - | 21.9 | 4075.7 | 5.3 | 21.5 | - | 1313.7 |
| SH-22_MQB_FI9 | UST | 5833.8 | 324.9 | 798.2 | - | 23.5 | 3727.7 | - | - | - | 2036.4 |
| SH-22_MQB_FI10 | UST | 8732.4 | 222.3 | 289.6 | - | 23.6 | 4424.2 | 13.2 | 21.2 | - | 1392.2 |
| SH-22_MQB_FI11 | UST | 21220.7 | 276.9 | 402.3 | - | 17.9 | 8780.9 | - | 60 | 9 | 2268.8 |
| SH-22_MQB_FI12 | UST | 7815 | 473.9 | 341.6 | 164.7 | 55.1 | 958.2 | 15.9 | 105.8 | 9.6 | 2376.3 |
| SH-22_MQB_FI13 | UST | 9511.9 | 215.4 | 278.1 | - | 15.7 | 4379.9 | 16.8 | - | 3.2 | 1348.8 |
| SH-22_MQB_FI14 | UST | 5256.5 | 624.1 | 533 | 139.4 | 48.2 | 964.2 | 4.9 | 99.7 | 16.3 | 4017.3 |
| SH-22_MQB_FI15 | UST | 5448.8 | 453.3 | 726 | - | 29.1 | 4178.1 | 3.4 | 32.6 | 5.9 | 3398.5 |
| SH-22_MQB_FI16 | UST | 6654.2 | 561.5 | 298.5 | 52.3 | 47.1 | 792.8 | 21.3 | 23.8 | 11.9 | 2227.1 |
| SH-22_MQB_FI17 | UST | 5913.7 | 538.4 | 292.6 | 150.5 | 51.4 | 817.9 | 10.3 | 70.3 | 7.3 | 2024.5 |
| SH-22_MQB_FI18 | UST | 37751 | 527.7 | 2148.1 | - | 66.1 | 2125.9 | - | 1.2 | 17.5 | 5675.6 |
| SH-22_MQB_FI19 | UST | 7010.2 | 547.4 | 333.4 | 92.9 | 54.8 | 922.8 | 22.7 | 72.8 | 8.1 | 2201.6 |

**Table 4.14 (Continued)**

| Sample Name | FIA | Zn66 | Rb85 | Sr88 | Mo95 | Cs133 | Ba137 | Ce140 | W182 | Tl205 | Pb208 |
|---|---|---|---|---|---|---|---|---|---|---|---|
| SH-22_MQB_FI20 | UST | 22315.9 | 221.7 | 175.9 | - | 16.8 | 365.2 | - | 50.4 | 4.3 | 1710.8 |
| SH-22_MQB_FI21 | UST | - | 525 | 1033.7 | - | 36.2 | 4888.2 | 1.7 | 133 | 29.7 | 4130.8 |
| SH-22_MQB_FI22 | UST | 14187.5 | 713.6 | 695.3 | 205.2 | 71.2 | 967.1 | 40.4 | 141 | 11.4 | 3378.4 |
| SH-22_MQB_FI23 | UST | 2797.6 | 276 | 120.3 | - | 19 | 145.2 | 11.7 | 56.6 | - | 1336.9 |
| SH-21_MQB_FI1 | UST | 5030.9 | 446.2 | 345.2 | 48 | 49.7 | 878.8 | 2.6 | 20.5 | - | 2861.5 |
| SH-21_MQB_FI2 | UST | 5529.9 | 350.5 | 201.5 | - | 44.2 | 614.4 | 5.6 | 50.9 | - | 2614.8 |
| SH-21_MQB_FI3 | UST | 5862.6 | 476 | 353.9 | 88.2 | 48.4 | 821.9 | 7.9 | - | - | 2745.7 |
| SH-21_MQB_FI4 | UST | 4240.6 | 388.3 | 330.7 | - | 33.1 | 1205.4 | - | 49.8 | - | 3015.6 |
| SH-21_MQB_FI5 | UST | 9382.3 | 403.6 | 264.8 | - | 57.9 | 803.3 | - | 142.9 | - | 3515.5 |
| SH-21_MQB_FI6 | UST | 6404 | 440.1 | 337.1 | 42.2 | 45.7 | 754.3 | 10.8 | 80.6 | - | 2536.2 |
| SH-21_MQB_FI7 | UST | 7859.6 | 552.5 | 409.5 | 129.1 | 38.4 | 754.1 | 0.3 | 174.9 | - | 3191.1 |
| SH-21_MQB_FI8 | UST | 6405.6 | 484.9 | 378.8 | - | 42.7 | 866 | 6.7 | - | - | 2452.1 |
| SH-21_MQB_FI9 | UST | 7234.6 | 489.7 | 351.3 | 83.4 | 58.4 | 992.4 | 13.2 | 84.2 | - | 2782.4 |
| SH-21_MQB_FI10 | UST | 6607.7 | 113.7 | 358.8 | - | 44.2 | 849.7 | 49.4 | 54.6 | - | 2901.7 |
| SH-21_MQB_FI11 | UST | 3819.9 | 282 | 290.8 | 118.4 | 11 | 1001.4 | 17.9 | 60.8 | - | 1069.1 |
| SH-21_MQB_FI12 | UST | 25222.3 | 239.9 | 1355.2 | - | 82.1 | 2259.7 | - | - | - | 6529.1 |
| SH-21_MQB_FI13 | UST | 11831.2 | 665.1 | 533.3 | - | 68.2 | 1292.5 | - | 27.6 | - | 4336.5 |
| SH-21_MQB_FI14 | UST | 10732.5 | 798.9 | 788.2 | 42.8 | 90.5 | 2048 | 26.9 | 379.4 | - | 4309.7 |
| SH-24_Ph_FI1 | Ph | 11118.2 | - | 126.3 | - | 0 | 772.1 | - | - | - | 2366.5 |
| SH-24_Ph_FI2 | Ph | 3185.6 | 295.8 | 235.7 | - | 23.8 | 402.3 | - | 46 | - | 2339.5 |
| SH-24_Ph_FI3 | Ph | 3336.3 | 182.1 | 330.5 | 201 | 0 | 499.1 | - | 95.9 | - | 1989.2 |
| SH-24_Ph_FI4 | Ph | 5427.4 | 329.9 | 224.3 | - | 21.1 | 2145.2 | - | - | - | 1497.5 |
| SH-24_Ph_FI5 | Ph | 4397.4 | 294.9 | 266.3 | - | 0 | 1015.7 | - | - | - | 2565.3 |
| SH-24_Ph_FI6 | Ph | 2220.3 | 278.1 | 181.7 | - | 16.4 | 686.3 | 17.8 | 29.1 | 14.7 | 2377.2 |
| SH-24_Ph_FI7 | Ph | 1509.3 | 205.2 | 523 | 255.5 | 90.8 | 103.6 | - | - | 4.4 | 878.3 |
| SH-24_Ph_FI8 | Ph | 4377.6 | 264.4 | 157.3 | 227 | 16.6 | 1015.6 | 80.7 | 156.5 | - | 816.3 |
| SH-24_Ph_FI9 | Ph | 4953.6 | 121.1 | 139.6 | 101.2 | 8.3 | 551 | 8.9 | 28.8 | - | 692.9 |
| SH-24_Ph_FI10 | Ph | 1650.6 | 292.5 | 91.1 | - | 0 | - | 19.7 | - | - | 757.9 |
| SH-24_Ph_FI11 | Ph | 2932.7 | 337.6 | 317.2 | - | 21.9 | 338.4 | - | 69.1 | - | 2962.2 |
| SH-24_Ph_FI12 | Ph | 11468 | 177 | 825.9 | - | 28.4 | 954.7 | - | - | 20.8 | 2485.8 |
| SH-24_Ph_FI13 | Ph | 3292.2 | 215 | 113.5 | - | 0 | - | - | - | - | 1009.6 |
| SH-22_Ph_FI1 | Ph | - | 241.8 | 59.3 | - | 32.2 | - | 41.1 | - | - | 636.2 |
| SH-22_Ph_FI2 | Ph | 5337.9 | 222.4 | 54 | 441.5 | 34.3 | 89.6 | 89.3 | 143.6 | - | 861 |
| SH-22_Ph_FI3 | Ph | 2694.9 | 275.4 | 211.8 | 275.6 | 0 | - | - | - | - | 823.4 |

**Table 4.15: Laser Ablation-ICPMS data from silicate melt inclusions (Corrected)**

| Sample Name | FIA | SiO2 | TiO2 | Al2O3 | FeO | MnO | CaO | Na2O | K2O | |
|---|---|---|---|---|---|---|---|---|---|---|
| SH-24_MQB_MI1 | UST | 69.00 | - | 18.08 | 5.93 | 0.57 | - | - | 4.82 | Wt % |
| SH-24_MQB_MI3 | UST | 69.00 | - | 15.92 | 8.17 | - | - | - | 4.25 | Wt % |
| SH-24_MQB_MI4 | UST | 69.00 | - | 15.14 | 11.55 | - | - | - | 4.04 | Wt % |
| SH-24_MQB_MI5 | UST | 69.00 | - | 18.44 | 6.18 | 0.38 | - | - | 4.92 | Wt % |
| SH-24_MQB_MI6 | UST | 69.00 | 4.18 | 17.17 | 3.05 | - | - | - | 4.58 | Wt % |
| SH-24_MQB_MI7 | UST | 69.00 | 1.27 | 18.65 | 4.35 | 0.08 | - | - | 4.97 | Wt % |
| SH-24_MQB_MI8 | UST | 69.00 | 0.45 | 16.56 | 7.00 | - | - | - | 4.42 | Wt % |
| SH-24_MQB_MI9 | UST | 69.00 | 1.76 | 18.13 | 3.71 | 0.19 | - | - | 4.83 | Wt % |
| SH-24_MQB_MI10 | UST | 69.00 | 1.57 | 17.15 | 3.91 | 0.14 | - | 2.92 | 4.57 | Wt % |
| SH-24_MQB_MI11 | UST | 69.00 | 1.45 | 17.58 | 2.89 | 0.16 | - | 2.75 | 4.69 | Wt % |
| SH-24_Ph_MI2 | Ph | 69.00 | 7.41 | 17.14 | - | 0.83 | - | - | 3.01 | Wt % |
| SH-24_Ph_MI3 | Ph | 69.00 | - | 16.31 | 9.46 | 0.41 | - | - | 4.35 | Wt % |
| SH-24_Ph_MI4 | Ph | 69.00 | - | 19.11 | 2.48 | - | - | - | 5.10 | Wt % |
| SH-24_Ph_MI5 | Ph | 69.00 | - | 15.06 | 1.54 | 2.77 | - | 5.70 | 4.02 | Wt % |
| SH-24_Ph_MI6 | Ph | 69.00 | - | 15.92 | 0.84 | 0.74 | 6.41 | 3.00 | 3.43 | Wt % |
| SH-24_Ph_MI7 | Ph | 69.00 | 1.07 | 16.38 | 3.77 | 0.71 | - | 3.08 | 4.37 | Wt % |
| SH-24_Ph_MI8 | Ph | 69.00 | 2.87 | 17.06 | 3.56 | 0.33 | - | 2.21 | 4.55 | Wt % |
| SH-24_Ph_MI9 | Ph | 69.00 | 1.25 | 16.36 | 5.38 | 0.32 | - | 1.31 | 4.36 | Wt % |
| SH-24_Ph_MI11 | Ph | 69.00 | 0.13 | 15.10 | 2.45 | 1.03 | - | 7.30 | 4.03 | Wt % |
| SH-24_Ph_MI12 | Ph | 69.00 | 0.64 | 15.70 | 3.84 | 0.83 | - | 4.50 | 4.19 | Wt % |
| SH-24_Ph_MI13 | Ph | 69.00 | - | 15.66 | 3.67 | 1.02 | - | 4.50 | 4.18 | Wt % |
| SH-24_Ph_MI14 | Ph | 69.00 | - | 21.44 | 3.20 | - | - | 5.83 | - | Wt % |
| SH-24_Ph_MI15 | Ph | 69.00 | 0.37 | 15.20 | 1.96 | 0.11 | 7.16 | 1.83 | 4.05 | Wt % |
| SH-24_Ph_MI16 | Ph | 69.00 | - | 15.46 | 5.43 | 0.70 | - | 3.67 | 4.12 | Wt % |
| SH-24_Ph_MI17 | Ph | 69.00 | 0.37 | 15.45 | 5.17 | 1.10 | - | 3.03 | 4.12 | Wt % |
| SH-24_Ph_MI18 | Ph | 69.00 | - | 16.90 | 3.51 | 0.26 | - | 4.44 | 4.51 | Wt % |
| SH-24_Ph_MI19 | Ph | 69.00 | 0.14 | 15.81 | - | 0.02 | 8.58 | 1.78 | 4.22 | Wt % |
| SH-24_Ph_MI20 | Ph | 69.00 | 0.65 | 16.99 | 4.02 | 0.25 | - | 3.53 | 4.53 | Wt % |
| SH-24_Ph_MI21 | Ph | 69.00 | 0.48 | 14.50 | 4.47 | 0.33 | 5.78 | 0.55 | 4.52 | Wt % |
| SH-24_Ph_MI23 | Ph | 69.00 | 1.15 | 22.11 | 1.50 | 0.12 | - | 3.51 | 1.14 | Wt % |
| SH-24_Ph_MI24 | Ph | 69.00 | - | 15.34 | 0.35 | 0.02 | - | 0.54 | 4.09 | Wt % |

**Table 4.15 (Continued)**

| Sample Name | FIA | SiO2 | TiO2 | Al2O3 | FeO | MnO | CaO | Na2O | K2O | |
|---|---|---|---|---|---|---|---|---|---|---|
| SH-22_MQB_MI2 | UST | 69.00 | 6.12 | 15.31 | - | - | - | - | 3.75 | Wt % |
| SH-22_MQB_MI3 | UST | 69.00 | 2.69 | 16.75 | 5.71 | - | - | - | 4.47 | Wt % |
| SH-22_MQB_MI4 | UST | 69.00 | - | 20.65 | - | 3.39 | - | - | - | Wt % |
| SH-22_MQB_MI5 | UST | 69.00 | 5.74 | 6.96 | 5.09 | - | - | - | 12.11 | Wt % |
| SH-22_MQB_MI6 | UST | 69.00 | 5.97 | 15.22 | 5.18 | 0.38 | - | - | 4.06 | Wt % |
| SH-22_MQB_MI7 | UST | 69.00 | - | 11.85 | 8.98 | 0.12 | - | 1.92 | 7.34 | Wt % |
| SH-22_MQB_MI8 | UST | 69.00 | - | 18.25 | 0.17 | - | - | 4.41 | 4.87 | Wt % |
| SH-22_MQB_MI9 | UST | 69.00 | 4.79 | 15.60 | - | 0.35 | - | 2.73 | 4.16 | Wt % |
| SH-22_MQB_MI10 | UST | 69.00 | 3.76 | 11.72 | 5.96 | 0.43 | - | 1.05 | 7.49 | Wt % |
| SH-22_MQB_MI11 | UST | 69.00 | 2.37 | 16.48 | 3.89 | 0.64 | - | 1.25 | 4.39 | Wt % |
| SH-22_Ph_MI1 | Ph | 69.00 | - | 15.20 | 9.75 | 0.47 | - | - | 4.05 | Wt % |
| SH-22_Ph_MI2 | Ph | 69.00 | 9.73 | 15.27 | - | 0.72 | - | - | 4.07 | Wt % |
| SH-22_Ph_MI3 | Ph | 69.00 | 0.84 | 15.30 | - | - | - | - | 4.08 | Wt % |
| SH-22_Ph_MI4 | Ph | 69.00 | - | 23.13 | - | - | - | - | - | Wt % |
| SH-22_Ph_MI5 | Ph | 69.00 | 0.84 | 17.28 | 1.59 | 0.26 | - | 5.47 | 4.61 | Wt % |
| SH-22_Ph_MI6 | Ph | 69.00 | - | 15.05 | - | 0.23 | 9.50 | 1.09 | 4.01 | Wt % |
| SH-22_Ph_MI7 | Ph | 69.00 | 1.50 | 15.30 | 7.59 | 0.15 | - | 1.81 | 4.08 | Wt % |
| SH-22_Ph_MI8 | Ph | 69.00 | - | 15.24 | 9.14 | 0.42 | - | 1.32 | 4.06 | Wt % |
| SH-22_Ph_MI9 | Ph | 69.00 | 0.62 | 13.40 | 10.90 | 0.05 | - | 0.22 | 5.61 | Wt % |
| SH-22_Ph_MI10 | Ph | 69.00 | 2.25 | 15.33 | 7.69 | 0.61 | - | - | 4.09 | Wt % |
| SH-22_Ph_MI11 | Ph | 69.00 | - | 15.73 | 10.84 | 0.59 | - | - | 3.62 | Wt % |
| SH-22_Ph_MI12 | Ph | 69.00 | - | 22.43 | 7.19 | - | - | - | - | Wt % |
| SH-22_Ph_MI13 | Ph | 69.00 | 5.27 | 17.36 | - | 0.37 | - | - | 4.63 | Wt % |
| SH-22_Ph_MI14 | Ph | 69.00 | 8.91 | 18.50 | - | - | - | - | 1.69 | Wt % |
| SH-22_Ph_MI15 | Ph | 69.00 | 5.89 | 17.28 | - | - | - | - | 4.61 | Wt % |
| SH-22_Ph_MI16 | Ph | 69.00 | - | 18.17 | 5.64 | - | - | 0.48 | 4.85 | Wt % |
| SH-22_Ph_MI17 | Ph | 69.00 | 1.10 | 15.30 | 7.07 | 0.15 | - | 2.39 | 4.08 | Wt % |
| SH-22_Ph_MI18 | Ph | 69.00 | - | 16.67 | - | 0.10 | - | 3.81 | 4.45 | Wt % |
| SH-22_Ph_MI19 | Ph | 69.00 | 3.46 | 15.25 | - | 1.37 | - | 3.78 | 4.07 | Wt % |
| SH-22_Ph_MI20 | Ph | 69.00 | 2.84 | 17.36 | - | 0.17 | - | 4.50 | 4.63 | Wt % |
| SH-22_Ph_MI21 | Ph | 69.00 | 1.44 | 16.92 | 3.79 | 0.27 | - | 2.59 | 4.51 | Wt % |
| SH-22_Ph_MI22 | Ph | 69.00 | - | 15.45 | 8.68 | 0.28 | - | 1.74 | 4.12 | Wt % |
| SH-22_Ph_MI23 | Ph | 69.00 | 1.32 | 11.41 | 7.29 | 0.36 | - | 1.46 | 7.77 | Wt % |
| SH-22_Ph_MI24 | Ph | 69.00 | 0.98 | 17.96 | 1.56 | 0.47 | - | 3.17 | 4.79 | Wt % |
| SH-22_Ph_MI25 | Ph | 69.00 | - | 16.12 | 7.64 | 0.21 | - | 1.97 | 4.30 | Wt % |
| SH-22_Ph_MI26 | Ph | 69.00 | 1.04 | 18.34 | - | 0.35 | - | 4.83 | 4.89 | Wt % |
| SH-22_Ph_MI27 | Ph | 69.00 | 3.12 | 17.53 | 0.04 | - | - | 3.24 | 4.67 | Wt % |
| SH-22_Ph_MI28 | Ph | 69.00 | - | 17.71 | 4.53 | 0.27 | - | 2.87 | 4.72 | Wt % |
| SH-22_Ph_MI29 | Ph | 69.00 | - | 12.54 | 8.25 | 0.41 | - | 1.50 | 6.72 | Wt % |
| SH-22_Ph_MI30 | Ph | 69.00 | 6.94 | 15.45 | - | - | - | 2.70 | 4.12 | Wt % |
| SH-22_Ph_MI31 | Ph | 69.00 | - | 12.03 | 6.58 | 0.69 | - | 1.84 | 7.31 | Wt % |
| SH-22_Ph_MI32 | Ph | 69.00 | - | 17.80 | 3.89 | 0.32 | - | 1.55 | 4.75 | Wt % |

**Table 4.15 (Continued)**

| Sample Name | FIA | Li7 | Be9 | B11 | Cu65 | Zn66 | As75 | Rb85 | Sr88 | Zr90 | |
|---|---|---|---|---|---|---|---|---|---|---|---|
| SH-24_MQB_MI1 | UST | - | - | - | - | - | - | 491.47 | 1351.07 | 1321.28 | ppm |
| SH-24_MQB_MI3 | UST | 127.07 | - | 4265.39 | - | 5809.62 | - | 922.04 | 364.52 | - | ppm |
| SH-24_MQB_MI4 | UST | - | - | - | - | - | - | 459.19 | - | - | ppm |
| SH-24_MQB_MI5 | UST | 447.62 | - | - | - | - | - | 86.24 | 568.05 | 1030.71 | ppm |
| SH-24_MQB_MI6 | UST | - | - | - | 2679.71 | 5369.60 | - | 1159.07 | 311.13 | 810.20 | ppm |
| SH-24_MQB_MI7 | UST | 334.20 | - | 368.65 | 1473.51 | - | - | 1375.62 | 637.22 | 1375.66 | ppm |
| SH-24_MQB_MI8 | UST | - | - | 3285.86 | 4199.25 | - | 2220.18 | 137.42 | 532.83 | 983.40 | ppm |
| SH-24_MQB_MI9 | UST | - | - | 2348.20 | - | 3713.86 | - | 1887.41 | 682.94 | 403.79 | ppm |
| SH-24_MQB_MI10 | UST | - | - | - | - | - | - | 1029.54 | 412.39 | 817.82 | ppm |
| SH-24_MQB_MI11 | UST | - | - | 1465.06 | - | - | - | 1036.11 | 553.55 | 1112.92 | ppm |
| SH-24_Ph_MI2 | Ph | 4435.20 | - | - | - | - | - | 1469.16 | 1003.98 | 1304.55 | ppm |
| SH-24_Ph_MI3 | Ph | - | - | - | - | - | - | - | - | 1042.83 | ppm |
| SH-24_Ph_MI4 | Ph | - | - | - | - | - | 7066.16 | 4910.71 | 80.06 | 3657.37 | ppm |
| SH-24_Ph_MI5 | Ph | 63.63 | - | 575.07 | - | 7252.69 | 46.93 | 309.37 | 1149.35 | 98.73 | ppm |
| SH-24_Ph_MI6 | Ph | - | - | - | 729.87 | 1698.67 | - | - | 1036.85 | - | ppm |
| SH-24_Ph_MI7 | Ph | 29.17 | - | 260.56 | 5293.89 | 2700.34 | 32.52 | 632.55 | 176.22 | 1851.21 | ppm |
| SH-24_Ph_MI8 | Ph | - | - | - | - | - | - | 740.37 | - | 1440.94 | ppm |
| SH-24_Ph_MI9 | Ph | - | - | 1448.21 | 299.27 | 1225.01 | 753.74 | 2454.24 | - | 2682.16 | ppm |
| SH-24_Ph_MI11 | Ph | - | - | 64.32 | 1284.04 | 3645.86 | 47.13 | 565.65 | 131.10 | 421.34 | ppm |
| SH-24_Ph_MI12 | Ph | 127.61 | - | 58.97 | 2716.41 | 3391.29 | - | 1121.77 | 97.76 | 1448.37 | ppm |
| SH-24_Ph_MI13 | Ph | - | - | - | 5303.69 | 4891.38 | - | 420.81 | 383.92 | 2406.94 | ppm |
| SH-24_Ph_MI14 | Ph | 1577.47 | - | - | - | - | - | 281.37 | 215.23 | - | ppm |
| SH-24_Ph_MI15 | Ph | 88.87 | - | - | - | - | - | 704.97 | - | 460.94 | ppm |
| SH-24_Ph_MI16 | Ph | - | - | - | 5843.30 | 3787.17 | - | 944.31 | - | 1353.81 | ppm |
| SH-24_Ph_MI17 | Ph | - | - | - | 7109.73 | 3243.38 | - | 1619.15 | - | 1035.97 | ppm |
| SH-24_Ph_MI18 | Ph | - | - | 1539.62 | 9.09 | 1376.50 | - | 1403.03 | - | 2796.76 | ppm |
| SH-24_Ph_MI19 | Ph | - | - | - | 42.16 | 137.62 | 42.29 | 4.93 | 1770.51 | 191.44 | ppm |
| SH-24_Ph_MI20 | Ph | 61.02 | 184.87 | 597.09 | 1959.35 | 1077.25 | 104.05 | 1008.92 | 254.16 | 826.33 | ppm |
| SH-24_Ph_MI21 | Ph | 30.72 | - | 55.46 | 441.31 | 582.04 | - | 120.75 | 341.58 | 54.75 | ppm |
| SH-24_Ph_MI23 | Ph | - | - | 795.14 | 337.25 | - | - | 920.16 | 264.89 | 5616.47 | ppm |
| SH-24_Ph_MI24 | Ph | - | - | 545.27 | 208.08 | - | - | 424.91 | 34.52 | 313.60 | ppm |

**Table 4.15 (Continued)**

| Sample Name | FIA | Li7 | Be9 | B11 | Cu65 | Zn66 | As75 | Rb85 | Sr88 | Zr90 | |
|---|---|---|---|---|---|---|---|---|---|---|---|
| SH-22_MQB_MI2 | UST | 1330.90 | - | - | 1780.57 | - | - | - | - | - | ppm |
| SH-22_MQB_MI3 | UST | 602.37 | - | - | - | - | - | 853.09 | 213.85 | - | ppm |
| SH-22_MQB_MI4 | UST | - | - | - | - | - | - | 2328.32 | 3311.45 | - | ppm |
| SH-22_MQB_MI5 | UST | - | 1213.93 | - | 2716.36 | 1928.58 | - | 810.20 | - | 146.80 | ppm |
| SH-22_MQB_MI6 | UST | - | - | - | - | - | - | 643.48 | - | - | ppm |
| SH-22_MQB_MI7 | UST | 1526.90 | - | - | - | - | - | 1709.15 | - | 346.06 | ppm |
| SH-22_MQB_MI8 | UST | 1377.33 | - | 4813.32 | - | 508.24 | 1312.43 | 997.91 | 626.50 | - | ppm |
| SH-22_MQB_MI9 | UST | - | - | 9205.04 | - | - | - | 1052.77 | - | - | ppm |
| SH-22_MQB_MI10 | UST | - | - | - | 237.00 | - | 728.75 | 2037.45 | - | 234.99 | ppm |
| SH-22_MQB_MI11 | UST | - | - | - | 2905.56 | 5423.46 | - | 840.80 | 248.00 | - | ppm |
| SH-22_Ph_MI1 | Ph | - | - | 3063.39 | - | - | - | 2686.98 | - | - | ppm |
| SH-22_Ph_MI2 | Ph | - | - | - | 787.98 | - | - | 3117.25 | - | 2686.03 | ppm |
| SH-22_Ph_MI3 | Ph | 6075.90 | - | - | - | - | - | 3320.79 | - | - | ppm |
| SH-22_Ph_MI4 | Ph | - | - | - | 5538.39 | - | - | 2300.86 | - | 6274.74 | ppm |
| SH-22_Ph_MI5 | Ph | - | 80.78 | 202.65 | - | 263.69 | 251.58 | 2067.75 | - | 2759.78 | ppm |
| SH-22_Ph_MI6 | Ph | 195.27 | - | 1846.73 | 93.42 | 120.64 | - | 1207.50 | - | 1881.14 | ppm |
| SH-22_Ph_MI7 | Ph | 147.06 | - | 670.23 | 161.10 | - | - | 1186.25 | - | 1029.81 | ppm |
| SH-22_Ph_MI8 | Ph | 232.50 | - | 567.92 | 1224.44 | 545.48 | 138.25 | 2257.37 | - | 402.99 | ppm |
| SH-22_Ph_MI9 | Ph | 12.33 | 134.91 | 147.04 | 26.45 | 196.15 | - | 490.84 | - | - | ppm |
| SH-22_Ph_MI10 | Ph | - | - | - | 1383.07 | - | - | 2127.93 | - | 1260.01 | ppm |
| SH-22_Ph_MI11 | Ph | - | - | - | 717.80 | - | - | 334.13 | - | - | ppm |
| SH-22_Ph_MI12 | Ph | - | - | 394.01 | 4983.60 | 4928.35 | - | 548.25 | 722.60 | - | ppm |
| SH-22_Ph_MI13 | Ph | 2783.45 | - | 3940.17 | 3655.52 | - | - | 813.22 | 344.97 | 2473.96 | ppm |
| SH-22_Ph_MI14 | Ph | 2898.25 | - | 1590.16 | 1329.78 | - | 1270.50 | 475.65 | 93.92 | 761.47 | ppm |
| SH-22_Ph_MI15 | Ph | - | - | 5319.76 | 1174.57 | - | - | 2596.83 | 350.28 | 2870.10 | ppm |
| SH-22_Ph_MI16 | Ph | - | - | - | - | - | - | 2301.14 | 646.65 | 2519.14 | ppm |
| SH-22_Ph_MI17 | Ph | - | - | 2031.07 | - | 343.18 | - | 1099.93 | - | 284.10 | ppm |
| SH-22_Ph_MI18 | Ph | - | - | - | 65.06 | - | - | 1509.82 | 172.81 | 1810.51 | ppm |
| SH-22_Ph_MI19 | Ph | 1923.07 | - | 1236.30 | - | 5890.47 | - | 2593.14 | - | 1526.91 | ppm |
| SH-22_Ph_MI20 | Ph | 741.91 | - | 291.54 | - | 1588.84 | - | 6078.09 | - | 1055.38 | ppm |
| SH-22_Ph_MI21 | Ph | - | 507.45 | 1614.44 | - | 51.50 | 97.84 | 2564.41 | 127.01 | 1013.16 | ppm |
| SH-22_Ph_MI22 | Ph | 161.80 | - | 481.16 | 1587.06 | 276.83 | - | 1783.75 | - | 588.96 | ppm |
| SH-22_Ph_MI23 | Ph | 1046.63 | - | 1441.04 | - | 264.27 | - | 1618.25 | - | 897.07 | ppm |
| SH-22_Ph_MI24 | Ph | - | - | 1083.49 | 212.95 | 956.29 | - | 2638.57 | 29.66 | 1835.51 | ppm |
| SH-22_Ph_MI25 | Ph | - | - | 257.30 | - | - | - | 3591.51 | - | 673.18 | ppm |
| SH-22_Ph_MI26 | Ph | 33.16 | - | 646.03 | - | 312.22 | - | 1892.13 | 395.74 | 2307.98 | ppm |
| SH-22_Ph_MI27 | Ph | 972.85 | - | 1995.41 | 385.80 | - | 779.19 | 4822.86 | - | 2317.04 | ppm |
| SH-22_Ph_MI28 | Ph | 84.65 | - | - | 4608.95 | - | - | - | - | 655.96 | ppm |
| SH-22_Ph_MI29 | Ph | 1623.56 | - | 574.70 | - | - | - | 2198.84 | - | 1337.19 | ppm |
| SH-22_Ph_MI30 | Ph | - | - | - | - | 3286.17 | 345.82 | 1560.85 | 142.29 | 1071.33 | ppm |
| SH-22_Ph_MI31 | Ph | 1693.45 | - | 3721.04 | 506.83 | - | - | 2434.82 | - | 1353.69 | ppm |
| SH-22_Ph_MI32 | Ph | - | - | 2910.30 | - | - | - | 1865.13 | 583.35 | 1860.21 | ppm |

**Table 4.15 (Continued)**

| Sample Name | FIA | Mo95 | Ag107 | Sn118 | Cs133 | Ba137 | La139 | Ce140 | Hf178 | Ta181 | |
|---|---|---|---|---|---|---|---|---|---|---|---|
| SH-24_MQB_MI1 | UST | - | 1534.31 | - | 91.09 | 7506.98 | 510.06 | 694.96 | - | - | ppm |
| SH-24_MQB_MI3 | UST | - | - | - | - | 1605.91 | 65.10 | 300.35 | - | - | ppm |
| SH-24_MQB_MI4 | UST | 415.29 | - | - | - | 993.47 | - | - | - | - | ppm |
| SH-24_MQB_MI5 | UST | - | - | 26.41 | - | 6396.78 | 105.63 | 282.89 | - | - | ppm |
| SH-24_MQB_MI6 | UST | - | - | - | - | 5386.15 | 522.58 | 716.06 | - | - | ppm |
| SH-24_MQB_MI7 | UST | 1040.75 | - | - | 16.44 | 4801.28 | 521.80 | 996.95 | 32.15 | 26.27 | ppm |
| SH-24_MQB_MI8 | UST | - | - | - | - | 3899.15 | 466.64 | 488.04 | - | - | ppm |
| SH-24_MQB_MI9 | UST | 585.76 | - | - | - | 4843.92 | 476.49 | 880.28 | 22.22 | 20.34 | ppm |
| SH-24_MQB_MI10 | UST | - | - | - | 19.91 | 2913.22 | 299.81 | 658.52 | - | - | ppm |
| SH-24_MQB_MI11 | UST | - | - | - | 67.78 | 4298.47 | 523.00 | 858.56 | 52.65 | 5.39 | ppm |
| SH-24_Ph_MI2 | Ph | - | - | - | - | 9330.94 | 147.03 | 834.95 | - | - | ppm |
| SH-24_Ph_MI3 | Ph | - | - | - | - | 1687.49 | 387.15 | 474.41 | - | - | ppm |
| SH-24_Ph_MI4 | Ph | 7146.41 | - | - | - | 7296.53 | 1207.26 | 1672.48 | - | - | ppm |
| SH-24_Ph_MI5 | Ph | - | 18.60 | - | 42.87 | 2105.09 | 11.28 | 31.61 | - | - | ppm |
| SH-24_Ph_MI6 | Ph | 22.08 | 8.76 | - | 10.71 | 961.64 | 11.80 | 11.45 | - | - | ppm |
| SH-24_Ph_MI7 | Ph | 71.34 | - | - | 11.49 | - | 465.19 | 787.09 | 103.47 | 102.60 | ppm |
| SH-24_Ph_MI8 | Ph | - | - | - | 45.15 | - | 384.21 | 556.57 | 50.78 | 37.80 | ppm |
| SH-24_Ph_MI9 | Ph | 414.76 | - | - | 624.94 | 1140.88 | 1049.63 | 1829.40 | 103.96 | 39.06 | ppm |
| SH-24_Ph_MI11 | Ph | 89.94 | 25.90 | - | 44.01 | 625.44 | 36.46 | 45.30 | 13.92 | 4.62 | ppm |
| SH-24_Ph_MI12 | Ph | 193.78 | 23.17 | - | 80.40 | - | 140.72 | 307.57 | 58.16 | 86.13 | ppm |
| SH-24_Ph_MI13 | Ph | - | - | - | 4.09 | 1862.53 | 61.49 | 86.49 | 51.60 | 101.06 | ppm |
| SH-24_Ph_MI14 | Ph | - | - | 1557.90 | - | 95.69 | - | - | - | - | ppm |
| SH-24_Ph_MI15 | Ph | - | - | - | - | - | 312.91 | 915.20 | 24.70 | 45.45 | ppm |
| SH-24_Ph_MI16 | Ph | 87.78 | - | - | 109.08 | - | 195.52 | 321.40 | 95.29 | - | ppm |
| SH-24_Ph_MI17 | Ph | 303.16 | - | - | 48.59 | - | 155.89 | 440.26 | 32.04 | 68.11 | ppm |
| SH-24_Ph_MI18 | Ph | 197.86 | - | - | 274.38 | - | 193.10 | 329.40 | 249.13 | 67.23 | ppm |
| SH-24_Ph_MI19 | Ph | - | - | - | 6.36 | 1324.32 | 81.30 | 109.38 | 6.88 | 2.73 | ppm |
| SH-24_Ph_MI20 | Ph | 82.13 | - | - | 44.90 | 485.77 | 36.69 | 54.81 | 65.03 | 24.39 | ppm |
| SH-24_Ph_MI21 | Ph | 14.82 | 6.07 | - | - | 1210.56 | 27.38 | 73.00 | 3.76 | 2.16 | ppm |
| SH-24_Ph_MI23 | Ph | - | - | - | 30.38 | - | 494.71 | 1036.12 | 265.34 | 140.11 | ppm |
| SH-24_Ph_MI24 | Ph | - | - | - | 23.77 | - | 121.48 | 156.83 | - | 14.27 | ppm |

**Table 4.15 (Continued)**

| Sample Name | FIA | Mo95 | Ag107 | Sn118 | Cs133 | Ba137 | La139 | Ce140 | Hf178 | Ta181 | |
|---|---|---|---|---|---|---|---|---|---|---|---|
| SH-22_MQB_MI2 | UST | - | - | - | - | - | - | 338.32 | - | - | ppm |
| SH-22_MQB_MI3 | UST | - | - | - | - | 9086.23 | 180.00 | 874.42 | - | - | ppm |
| SH-22_MQB_MI4 | UST | - | - | 7724.48 | - | 7281.11 | 1115.50 | 1489.81 | - | - | ppm |
| SH-22_MQB_MI5 | UST | - | - | - | - | 255.43 | 157.43 | 318.82 | - | - | ppm |
| SH-22_MQB_MI6 | UST | - | - | - | - | - | 418.85 | 180.47 | - | - | ppm |
| SH-22_MQB_MI7 | UST | - | - | - | 44.40 | 744.35 | 275.53 | 557.96 | - | - | ppm |
| SH-22_MQB_MI8 | UST | - | - | - | 152.02 | 5952.49 | 1095.65 | 1153.95 | - | - | ppm |
| SH-22_MQB_MI9 | UST | 460.85 | - | 195.11 | 87.60 | - | 413.66 | 372.26 | - | - | ppm |
| SH-22_MQB_MI10 | UST | - | 70.80 | 643.22 | 64.44 | 47.04 | 261.10 | 476.52 | - | - | ppm |
| SH-22_MQB_MI11 | UST | - | - | - | - | 6405.12 | 453.03 | 443.24 | - | - | ppm |
| SH-22_Ph_MI1 | Ph | - | - | - | - | - | 1719.84 | 392.81 | - | - | ppm |
| SH-22_Ph_MI2 | Ph | - | - | - | - | 1477.36 | 614.54 | 1435.53 | - | - | ppm |
| SH-22_Ph_MI3 | Ph | - | - | - | - | - | - | - | - | - | ppm |
| SH-22_Ph_MI4 | Ph | - | - | 1013.20 | 119.78 | - | 259.83 | 863.86 | 385.06 | 255.81 | ppm |
| SH-22_Ph_MI5 | Ph | - | 28.36 | - | 78.92 | - | 252.24 | 449.41 | 96.94 | 57.04 | ppm |
| SH-22_Ph_MI6 | Ph | - | - | - | 302.43 | - | 77.85 | 122.20 | 52.17 | 23.44 | ppm |
| SH-22_Ph_MI7 | Ph | - | 37.53 | - | 25.38 | 39.98 | 27.74 | 63.66 | 42.62 | 10.59 | ppm |
| SH-22_Ph_MI8 | Ph | - | 45.86 | - | 112.91 | - | 31.79 | 153.00 | - | - | ppm |
| SH-22_Ph_MI9 | Ph | - | 6.36 | - | 50.50 | - | 55.63 | 80.80 | 11.13 | 1.51 | ppm |
| SH-22_Ph_MI10 | Ph | - | - | - | 85.11 | 2386.75 | 485.88 | 700.13 | 117.71 | - | ppm |
| SH-22_Ph_MI11 | Ph | - | - | - | - | 912.36 | - | 112.87 | - | - | ppm |
| SH-22_Ph_MI12 | Ph | - | 63.58 | - | - | - | 45.53 | 78.13 | - | - | ppm |
| SH-22_Ph_MI13 | Ph | - | - | - | - | 3985.34 | 355.52 | 912.98 | - | - | ppm |
| SH-22_Ph_MI14 | Ph | - | - | - | - | 1643.16 | - | 445.83 | - | - | ppm |
| SH-22_Ph_MI15 | Ph | - | - | - | - | 3030.82 | 649.54 | 1373.13 | 72.04 | - | ppm |
| SH-22_Ph_MI16 | Ph | - | - | - | - | 7567.38 | 541.39 | 1803.56 | 172.99 | - | ppm |
| SH-22_Ph_MI17 | Ph | - | - | - | 59.94 | 61.13 | 84.12 | 186.99 | 12.87 | 7.25 | ppm |
| SH-22_Ph_MI18 | Ph | - | - | - | 32.00 | 5720.65 | 422.18 | 812.95 | 75.10 | - | ppm |
| SH-22_Ph_MI19 | Ph | - | - | - | 51.82 | 5458.77 | 453.03 | 675.75 | - | - | ppm |
| SH-22_Ph_MI20 | Ph | - | - | - | 503.66 | - | 424.13 | 812.97 | - | - | ppm |
| SH-22_Ph_MI21 | Ph | 247.91 | - | - | 488.23 | - | 860.54 | 1192.75 | 48.70 | 13.91 | ppm |
| SH-22_Ph_MI22 | Ph | - | 314.46 | - | 18.60 | - | 29.67 | 46.58 | 38.13 | 8.12 | ppm |
| SH-22_Ph_MI23 | Ph | - | - | - | 53.82 | 2246.70 | 207.35 | 410.00 | 34.85 | - | ppm |
| SH-22_Ph_MI24 | Ph | - | - | - | 193.57 | - | 1001.89 | 1406.82 | 87.67 | 16.70 | ppm |
| SH-22_Ph_MI25 | Ph | - | - | - | 171.08 | - | 457.14 | 547.32 | - | - | ppm |
| SH-22_Ph_MI26 | Ph | - | - | - | 45.20 | - | 4874.62 | 708.57 | 56.93 | 18.98 | ppm |
| SH-22_Ph_MI27 | Ph | 260.85 | - | - | 1329.70 | - | 743.27 | 1418.74 | - | 44.35 | ppm |
| SH-22_Ph_MI28 | Ph | - | 2529.20 | - | - | - | - | - | - | - | ppm |
| SH-22_Ph_MI29 | Ph | 170.22 | - | - | 126.11 | 3561.75 | 415.80 | 830.03 | 81.79 | - | ppm |
| SH-22_Ph_MI30 | Ph | 326.00 | - | - | 111.17 | 6540.87 | 290.28 | 981.93 | - | - | ppm |
| SH-22_Ph_MI31 | Ph | 158.77 | - | - | 187.95 | 1803.14 | 581.53 | 827.85 | 85.94 | 22.22 | ppm |
| SH-22_Ph_MI32 | Ph | - | - | - | 90.68 | 8709.95 | 683.54 | 968.16 | - | - | ppm |

**Table 4.15 (Continued)**

| Sample Name | FIA | W182 | Au197 | Tl205 | Pb208 | Th232 | U238 | |
|---|---|---|---|---|---|---|---|---|
| SH-24_MQB_MI1 | UST | - | - | - | 307.16 | - | 74.63 | ppm |
| SH-24_MQB_MI3 | UST | - | - | - | 1538.96 | - | - | ppm |
| SH-24_MQB_MI4 | UST | - | - | - | 546.74 | - | - | ppm |
| SH-24_MQB_MI5 | UST | - | - | - | 103.63 | - | - | ppm |
| SH-24_MQB_MI6 | UST | - | - | - | 178.17 | - | 78.32 | ppm |
| SH-24_MQB_MI7 | UST | - | - | - | 328.92 | - | 47.04 | ppm |
| SH-24_MQB_MI8 | UST | - | - | - | - | - | - | ppm |
| SH-24_MQB_MI9 | UST | - | - | - | 232.03 | - | 56.50 | ppm |
| SH-24_MQB_MI10 | UST | - | - | - | 163.51 | - | 41.51 | ppm |
| SH-24_MQB_MI11 | UST | - | - | 21.25 | 168.73 | - | 57.09 | ppm |
| SH-24_Ph_MI2 | Ph | - | - | - | 223.22 | - | - | ppm |
| SH-24_Ph_MI3 | Ph | - | - | - | 245.48 | - | 178.23 | ppm |
| SH-24_Ph_MI4 | Ph | - | - | - | 1334.92 | - | 622.96 | ppm |
| SH-24_Ph_MI5 | Ph | - | - | 12.96 | 3386.00 | - | 1.14 | ppm |
| SH-24_Ph_MI6 | Ph | 14.08 | - | 2.63 | 1197.93 | - | - | ppm |
| SH-24_Ph_MI7 | Ph | 57.04 | - | 5.39 | 486.06 | - | 71.13 | ppm |
| SH-24_Ph_MI8 | Ph | - | - | - | 115.09 | - | 88.58 | ppm |
| SH-24_Ph_MI9 | Ph | - | - | - | 225.08 | - | - | ppm |
| SH-24_Ph_MI11 | Ph | 23.56 | - | 5.42 | 935.97 | - | 4.34 | ppm |
| SH-24_Ph_MI12 | Ph | 81.82 | - | 5.67 | 747.35 | - | 32.78 | ppm |
| SH-24_Ph_MI13 | Ph | 39.43 | - | - | 952.03 | - | 17.91 | ppm |
| SH-24_Ph_MI14 | Ph | - | - | - | - | - | - | ppm |
| SH-24_Ph_MI15 | Ph | - | - | - | 33.16 | - | 10.11 | ppm |
| SH-24_Ph_MI16 | Ph | 86.27 | - | - | 753.87 | - | 45.95 | ppm |
| SH-24_Ph_MI17 | Ph | 80.63 | - | - | 796.31 | - | 49.33 | ppm |
| SH-24_Ph_MI18 | Ph | - | - | - | 291.87 | - | 21.89 | ppm |
| SH-24_Ph_MI19 | Ph | - | - | - | 90.15 | - | 14.75 | ppm |
| SH-24_Ph_MI20 | Ph | 39.48 | - | 12.31 | 290.54 | - | 117.98 | ppm |
| SH-24_Ph_MI21 | Ph | 12.46 | - | - | 127.52 | - | 1.27 | ppm |
| SH-24_Ph_MI23 | Ph | 70.23 | - | - | 209.30 | - | 128.69 | ppm |
| SH-24_Ph_MI24 | Ph | - | - | - | 91.96 | - | 16.46 | ppm |

**Table 4.15 (Continued)**

| Sample Name | FIA | W182 | Au197 | Tl205 | Pb208 | Th232 | U238 | |
|---|---|---|---|---|---|---|---|---|
| SH-22_MQB_MI2 | UST | - | - | - | - | - | - | ppm |
| SH-22_MQB_MI3 | UST | - | - | - | - | - | - | ppm |
| SH-22_MQB_MI4 | UST | - | - | - | 2698.89 | - | - | ppm |
| SH-22_MQB_MI5 | UST | - | 101.18 | - | 99.86 | - | 36.48 | ppm |
| SH-22_MQB_MI6 | UST | - | - | - | 468.58 | - | - | ppm |
| SH-22_MQB_MI7 | UST | - | 213.18 | - | 148.43 | - | - | ppm |
| SH-22_MQB_MI8 | UST | - | - | - | 728.61 | - | 28.17 | ppm |
| SH-22_MQB_MI9 | UST | 575.07 | - | - | 277.59 | - | - | ppm |
| SH-22_MQB_MI10 | UST | - | - | - | 175.58 | - | 17.57 | ppm |
| SH-22_MQB_MI11 | UST | - | - | - | 330.59 | - | - | ppm |
| SH-22_Ph_MI1 | Ph | - | - | - | - | - | - | ppm |
| SH-22_Ph_MI2 | Ph | - | - | - | - | - | - | ppm |
| SH-22_Ph_MI3 | Ph | - | - | - | - | - | - | ppm |
| SH-22_Ph_MI4 | Ph | - | 136.61 | 72.99 | 1810.77 | - | 161.39 | ppm |
| SH-22_Ph_MI5 | Ph | 52.10 | - | 12.20 | 210.69 | 478.43 | 47.15 | ppm |
| SH-22_Ph_MI6 | Ph | - | - | - | 77.40 | - | 23.59 | ppm |
| SH-22_Ph_MI7 | Ph | 24.79 | - | - | - | - | 44.49 | ppm |
| SH-22_Ph_MI8 | Ph | - | - | 7.98 | 224.29 | - | 9.06 | ppm |
| SH-22_Ph_MI9 | Ph | - | - | 0.95 | 17.05 | 53.29 | 59.27 | ppm |
| SH-22_Ph_MI10 | Ph | - | - | - | 318.08 | - | 99.50 | ppm |
| SH-22_Ph_MI11 | Ph | - | - | - | - | - | - | ppm |
| SH-22_Ph_MI12 | Ph | - | - | - | 4152.23 | - | - | ppm |
| SH-22_Ph_MI13 | Ph | - | - | - | 216.35 | - | 33.96 | ppm |
| SH-22_Ph_MI14 | Ph | - | - | - | 362.24 | - | - | ppm |
| SH-22_Ph_MI15 | Ph | - | - | - | 363.01 | - | 195.87 | ppm |
| SH-22_Ph_MI16 | Ph | - | - | - | 282.31 | - | 117.73 | ppm |
| SH-22_Ph_MI17 | Ph | - | - | - | 132.11 | - | 4.87 | ppm |
| SH-22_Ph_MI18 | Ph | - | - | - | 199.35 | - | - | ppm |
| SH-22_Ph_MI19 | Ph | - | - | - | 2546.44 | - | 64.76 | ppm |
| SH-22_Ph_MI20 | Ph | - | - | - | 252.99 | 29.64 | 106.56 | ppm |
| SH-22_Ph_MI21 | Ph | - | - | - | 187.41 | - | - | ppm |
| SH-22_Ph_MI22 | Ph | 20.72 | - | 6.63 | 18.57 | - | - | ppm |
| SH-22_Ph_MI23 | Ph | - | - | 15.74 | 166.77 | - | 36.77 | ppm |
| SH-22_Ph_MI24 | Ph | 64.54 | - | - | 310.52 | - | 163.13 | ppm |
| SH-22_Ph_MI25 | Ph | 46.29 | - | 25.05 | 202.41 | 112.43 | 77.16 | ppm |
| SH-22_Ph_MI26 | Ph | - | - | - | 176.77 | 209.23 | 46.44 | ppm |
| SH-22_Ph_MI27 | Ph | - | - | - | 291.00 | 544.62 | 195.71 | ppm |
| SH-22_Ph_MI28 | Ph | - | - | - | - | - | - | ppm |
| SH-22_Ph_MI29 | Ph | - | - | - | 257.29 | - | 52.51 | ppm |
| SH-22_Ph_MI30 | Ph | 131.63 | - | - | 268.97 | 59.73 | 82.94 | ppm |
| SH-22_Ph_MI31 | Ph | - | - | - | 366.27 | - | 77.91 | ppm |
| SH-22_Ph_MI32 | Ph | - | - | - | 473.01 | - | 68.39 | ppm |

**Table 4.16: Laser Ablation-ICPMS data from silicate melt inclusions (Raw, Uncorrected)**

| Sample Name | FIA | SiO2 | TiO2 | Al2O3 | FeO | MnO | CaO | Na2O | K2O | |
|---|---|---|---|---|---|---|---|---|---|---|
| SH-24_MQB_MI1 | UST | 69.00 | - | 62.60 | 3.06 | 0.23 | - | - | 19.96 | Wt % |
| SH-24_MQB_MI3 | UST | 69.00 | - | 59.64 | 6.44 | - | - | - | 23.02 | Wt % |
| SH-24_MQB_MI4 | UST | 69.00 | - | 50.52 | 19.81 | - | - | - | 20.49 | Wt % |
| SH-24_MQB_MI5 | UST | 69.00 | - | 63.77 | 3.06 | 0.18 | - | - | 20.21 | Wt % |
| SH-24_MQB_MI6 | UST | 69.00 | 1.80 | 66.01 | 2.54 | - | - | - | 24.71 | Wt % |
| SH-24_MQB_MI7 | UST | 69.00 | 0.53 | 65.70 | 2.56 | 0.10 | - | - | 23.74 | Wt % |
| SH-24_MQB_MI8 | UST | 69.00 | 0.30 | 44.46 | 3.54 | - | - | - | 14.66 | Wt % |
| SH-24_MQB_MI9 | UST | 69.00 | 0.65 | 62.53 | 2.28 | 0.12 | - | - | 24.43 | Wt % |
| SH-24_MQB_MI10 | UST | 69.00 | 0.73 | 59.35 | 2.60 | 0.12 | - | 1.04 | 22.62 | Wt % |
| SH-24_MQB_MI11 | UST | 69.00 | 0.64 | 62.45 | 2.18 | 0.12 | - | 0.87 | 24.38 | Wt % |
| SH-24_Ph_MI2 | Ph | 69.00 | 1.86 | 56.28 | - | 0.26 | - | - | 16.82 | Wt % |
| SH-24_Ph_MI3 | Ph | 69.00 | - | 63.03 | 5.43 | 0.24 | - | - | 28.21 | Wt % |
| SH-24_Ph_MI4 | Ph | 69.00 | - | 60.90 | 1.63 | - | - | - | 25.84 | Wt % |
| SH-24_Ph_MI5 | Ph | 69.00 | - | 45.74 | 3.62 | 6.10 | - | 12.54 | 15.35 | Wt % |
| SH-24_Ph_MI6 | Ph | 69.00 | - | 59.58 | 2.28 | 1.31 | 10.97 | 5.14 | 15.82 | Wt % |
| SH-24_Ph_MI7 | Ph | 69.00 | 0.80 | 60.75 | 3.45 | 0.47 | - | 1.77 | 19.80 | Wt % |
| SH-24_Ph_MI8 | Ph | 69.00 | 1.18 | 59.32 | 2.41 | 0.18 | - | 0.78 | 24.07 | Wt % |
| SH-24_Ph_MI9 | Ph | 69.00 | 0.78 | 60.15 | 3.78 | 0.22 | - | 0.67 | 25.63 | Wt % |
| SH-24_Ph_MI11 | Ph | 69.00 | 0.26 | 46.88 | 4.53 | 1.81 | - | 12.80 | 20.66 | Wt % |
| SH-24_Ph_MI12 | Ph | 69.00 | 0.64 | 55.01 | 4.02 | 0.72 | - | 3.65 | 21.44 | Wt % |
| SH-24_Ph_MI13 | Ph | 69.00 | - | 54.84 | 3.59 | 0.81 | - | 3.37 | 23.40 | Wt % |
| SH-24_Ph_MI14 | Ph | 69.00 | - | 76.19 | 3.30 | - | - | 2.89 | 20.15 | Wt % |
| SH-24_Ph_MI15 | Ph | 69.00 | 0.62 | 52.49 | 3.45 | 0.18 | 10.84 | 2.77 | 22.46 | Wt % |
| SH-24_Ph_MI16 | Ph | 69.00 | - | 43.05 | 4.42 | 0.53 | - | 2.60 | 19.55 | Wt % |
| SH-24_Ph_MI17 | Ph | 69.00 | 0.31 | 48.56 | 3.92 | 0.76 | - | 2.04 | 28.19 | Wt % |
| SH-24_Ph_MI18 | Ph | 69.00 | - | 64.43 | 2.70 | 0.17 | - | 1.70 | 23.65 | Wt % |
| SH-24_Ph_MI19 | Ph | 69.00 | 0.31 | 65.72 | 1.14 | 0.09 | 7.85 | 1.63 | 20.55 | Wt % |
| SH-24_Ph_MI20 | Ph | 69.00 | 0.47 | 64.45 | 3.05 | 0.18 | - | 1.52 | 23.82 | Wt % |
| SH-24_Ph_MI21 | Ph | 69.00 | 1.03 | 38.34 | 9.51 | 0.70 | 12.28 | 1.18 | 16.54 | Wt % |
| SH-24_Ph_MI23 | Ph | 69.00 | 0.56 | 67.35 | 2.03 | 0.12 | - | 1.02 | 19.10 | Wt % |
| SH-24_Ph_MI24 | Ph | 69.00 | - | 66.19 | 1.59 | 0.09 | - | 0.88 | 20.67 | Wt % |

**Table 4.16 (Continued)**

| Sample Name | FIA | SiO2 | TiO2 | Al2O3 | FeO | MnO | CaO | Na2O | K2O | |
|---|---|---|---|---|---|---|---|---|---|---|
| SH-22_MQB_MI2 | UST | 69.00 | 1.12 | 49.45 | 3.11 | - | - | - | 17.54 | Wt % |
| SH-22_MQB_MI3 | UST | 69.00 | - | 59.53 | - | 0.40 | - | - | 17.72 | Wt % |
| SH-22_MQB_MI4 | UST | 69.00 | 6.53 | 36.91 | 5.83 | - | - | - | 40.56 | Wt % |
| SH-22_MQB_MI5 | UST | 69.00 | 3.37 | 48.21 | 3.02 | 0.22 | - | - | 37.53 | Wt % |
| SH-22_MQB_MI6 | UST | 69.00 | - | 47.29 | 5.66 | 0.08 | - | 1.20 | 41.44 | Wt % |
| SH-22_MQB_MI7 | UST | 69.00 | - | 66.39 | 1.55 | - | - | 1.13 | 22.89 | Wt % |
| SH-22_MQB_MI8 | UST | 69.00 | 1.54 | 47.27 | 0.20 | 0.13 | - | 0.85 | 32.58 | Wt % |
| SH-22_MQB_MI9 | UST | 69.00 | 2.25 | 46.79 | 3.61 | 0.26 | - | 0.63 | 41.24 | Wt % |
| SH-22_MQB_MI10 | UST | 69.00 | 1.32 | 58.55 | 3.04 | 0.38 | - | 0.61 | 22.32 | Wt % |
| SH-22_MQB_MI11 | UST | 69.00 | - | 44.19 | 4.66 | 0.23 | - | - | 34.81 | Wt % |
| SH-22_Ph_MI1 | Ph | 69.00 | 3.06 | 46.27 | - | 0.23 | - | - | 38.32 | Wt % |
| SH-22_Ph_MI2 | Ph | 69.00 | 0.43 | 65.58 | - | - | - | - | 33.97 | Wt % |
| SH-22_Ph_MI3 | Ph | 69.00 | - | 73.08 | 0.85 | - | - | - | 21.42 | Wt % |
| SH-22_Ph_MI4 | Ph | 69.00 | 0.41 | 61.68 | 1.61 | 0.14 | - | 1.66 | 27.42 | Wt % |
| SH-22_Ph_MI5 | Ph | 69.00 | - | 62.66 | - | 0.36 | 12.76 | 1.46 | 22.22 | Wt % |
| SH-22_Ph_MI6 | Ph | 69.00 | 1.16 | 50.23 | 5.95 | 0.13 | - | 1.35 | 33.08 | Wt % |
| SH-22_Ph_MI7 | Ph | 69.00 | - | 48.22 | 6.99 | 0.32 | - | 0.97 | 32.55 | Wt % |
| SH-22_Ph_MI8 | Ph | 69.00 | 2.40 | 58.68 | 42.52 | 0.20 | - | 0.87 | 27.81 | Wt % |
| SH-22_Ph_MI9 | Ph | 69.00 | 1.00 | 48.47 | 3.49 | 0.27 | - | - | 38.90 | Wt % |
| SH-22_Ph_MI10 | Ph | 69.00 | - | 44.61 | 14.67 | 0.80 | - | - | 12.15 | Wt % |
| SH-22_Ph_MI11 | Ph | 69.00 | 0.12 | 65.83 | 4.17 | - | - | - | 17.51 | Wt % |
| SH-22_Ph_MI12 | Ph | 69.00 | 2.26 | 67.44 | 1.41 | 0.23 | - | - | 21.53 | Wt % |
| SH-22_Ph_MI13 | Ph | 69.00 | 4.94 | 68.55 | 0.63 | - | - | - | 18.99 | Wt % |
| SH-22_Ph_MI14 | Ph | 69.00 | 1.69 | 68.19 | 0.77 | - | - | - | 21.18 | Wt % |
| SH-22_Ph_MI15 | Ph | 69.00 | - | 66.57 | 2.88 | - | - | 0.12 | 23.99 | Wt % |
| SH-22_Ph_MI16 | Ph | 69.00 | 0.92 | 49.32 | 5.96 | 0.13 | - | 1.91 | 31.20 | Wt % |
| SH-22_Ph_MI17 | Ph | 69.00 | - | 60.83 | 1.05 | 0.11 | - | 1.39 | 20.95 | Wt % |
| SH-22_Ph_MI18 | Ph | 69.00 | 1.23 | 46.63 | - | 0.49 | - | 1.34 | 39.25 | Wt % |
| SH-22_Ph_MI19 | Ph | 69.00 | 0.96 | 61.51 | 0.97 | 0.11 | - | 1.27 | 26.93 | Wt % |
| SH-22_Ph_MI20 | Ph | 69.00 | 0.86 | 65.16 | 3.15 | 0.20 | - | 1.19 | 21.99 | Wt % |
| SH-22_Ph_MI21 | Ph | 69.00 | - | 51.50 | 5.64 | 0.19 | - | 1.05 | 32.78 | Wt % |
| SH-22_Ph_MI22 | Ph | 69.00 | 0.90 | 44.61 | 5.01 | 0.25 | - | 0.99 | 39.34 | Wt % |
| SH-22_Ph_MI23 | Ph | 69.00 | 0.52 | 66.79 | 1.99 | 0.23 | - | 0.99 | 22.75 | Wt % |
| SH-22_Ph_MI24 | Ph | 69.00 | - | 62.30 | 4.83 | 0.16 | - | 0.98 | 28.77 | Wt % |
| SH-22_Ph_MI25 | Ph | 69.00 | 0.40 | 61.15 | 0.95 | 0.14 | - | 0.97 | 22.66 | Wt % |
| SH-22_Ph_MI26 | Ph | 69.00 | 1.01 | 60.78 | 1.13 | - | - | 0.88 | 27.09 | Wt % |
| SH-22_Ph_MI27 | Ph | 69.00 | - | 65.13 | 2.72 | 0.15 | - | 0.82 | 23.26 | Wt % |
| SH-22_Ph_MI28 | Ph | 69.00 | - | 46.12 | 4.28 | 0.21 | - | 0.77 | 40.12 | Wt % |
| SH-22_Ph_MI29 | Ph | 69.00 | 1.94 | 45.92 | - | - | - | 0.71 | 20.37 | Wt % |
| SH-22_Ph_MI30 | Ph | 69.00 | - | 44.50 | 2.51 | 0.26 | - | 0.69 | 39.69 | Wt % |
| SH-22_Ph_MI31 | Ph | 69.00 | - | 67.65 | 2.63 | 0.17 | - | 0.46 | 24.48 | Wt % |

**Table 4.16 (Continued)**

| Sample Name | FIA | Li7 | Be9 | B11 | Cu65 | Zn66 | As75 | Rb85 | Sr88 | Zr90 | |
|---|---|---|---|---|---|---|---|---|---|---|---|
| SH-24_MQB_MI1 | UST | - | - | - | - | - | - | 683.40 | 392.90 | 352.30 | ppm |
| SH-24_MQB_MI3 | UST | 187.70 | - | 2808.50 | - | 3870.10 | - | 1006.10 | 348.40 | - | ppm |
| SH-24_MQB_MI4 | UST | - | - | - | - | - | - | 921.80 | - | - | ppm |
| SH-24_MQB_MI5 | UST | 259.50 | - | - | - | - | - | 589.30 | 172.80 | 257.60 | ppm |
| SH-24_MQB_MI6 | UST | - | - | - | 1036.50 | 2145.90 | - | 955.10 | 223.90 | 312.40 | ppm |
| SH-24_MQB_MI7 | UST | 225.30 | - | 108.60 | 379.30 | - | - | 889.50 | 249.00 | 350.90 | ppm |
| SH-24_MQB_MI8 | UST | - | - | 1222.20 | 1551.90 | - | 819.30 | 407.20 | 230.20 | 362.90 | ppm |
| SH-24_MQB_MI9 | UST | - | - | 636.40 | - | 1057.30 | - | 981.40 | 298.30 | 107.20 | ppm |
| SH-24_MQB_MI10 | UST | - | - | - | - | - | - | 815.80 | 248.20 | 291.60 | ppm |
| SH-24_MQB_MI11 | UST | - | - | 474.70 | - | - | - | 799.00 | 291.40 | 350.90 | ppm |
| SH-24_Ph_MI2 | Ph | 1129.10 | - | - | - | - | - | 843.70 | 239.90 | 292.80 | ppm |
| SH-24_Ph_MI3 | Ph | - | - | - | - | - | - | - | - | 479.20 | ppm |
| SH-24_Ph_MI4 | Ph | - | - | - | - | - | 1151.30 | 1251.80 | 164.70 | 595.90 | ppm |
| SH-24_Ph_MI5 | Ph | 161.20 | - | 1266.80 | - | 15960.80 | 103.20 | 762.10 | 2580.40 | 217.10 | ppm |
| SH-24_Ph_MI6 | Ph | 32.10 | - | - | 1251.10 | 2954.10 | - | 313.80 | 1783.40 | - | ppm |
| SH-24_Ph_MI7 | Ph | 141.50 | - | 162.80 | 3047.20 | 1624.00 | 18.70 | 843.40 | 143.40 | 1064.50 | ppm |
| SH-24_Ph_MI8 | Ph | - | - | - | - | - | - | 688.40 | 103.70 | 510.80 | ppm |
| SH-24_Ph_MI9 | Ph | - | - | 744.70 | 154.20 | 678.90 | 382.10 | 1634.00 | 154.00 | 1359.70 | ppm |
| SH-24_Ph_MI11 | Ph | - | - | 115.00 | 2251.10 | 6402.60 | 82.60 | 1075.00 | 373.10 | 738.50 | ppm |
| SH-24_Ph_MI12 | Ph | 190.50 | - | 56.90 | 2206.60 | 2801.80 | - | 1244.70 | 185.60 | 1175.40 | ppm |
| SH-24_Ph_MI13 | Ph | - | - | - | 3969.60 | 3705.40 | - | 626.10 | 430.80 | 1800.60 | ppm |
| SH-24_Ph_MI14 | Ph | 949.80 | - | - | - | - | - | 782.20 | 125.00 | - | ppm |
| SH-24_Ph_MI15 | Ph | 179.70 | - | - | - | - | - | 1240.90 | 96.40 | 697.80 | ppm |
| SH-24_Ph_MI16 | Ph | - | - | - | 4146.60 | 2717.40 | - | 877.00 | 87.10 | 960.40 | ppm |
| SH-24_Ph_MI17 | Ph | - | - | - | 4771.40 | 2199.50 | - | 1243.30 | 190.90 | 695.10 | ppm |
| SH-24_Ph_MI18 | Ph | - | - | 604.40 | 6.70 | 602.90 | - | 1041.40 | 88.40 | 1073.20 | ppm |
| SH-24_Ph_MI19 | Ph | - | - | - | 41.70 | 198.40 | 38.70 | 492.40 | 1651.70 | 175.20 | ppm |
| SH-24_Ph_MI20 | Ph | 154.20 | 79.60 | 270.40 | 846.80 | 536.90 | 44.80 | 926.40 | 205.70 | 355.80 | ppm |
| SH-24_Ph_MI21 | Ph | 65.30 | - | 117.90 | 938.20 | 1237.40 | - | 256.70 | 815.30 | 116.40 | ppm |
| SH-24_Ph_MI23 | Ph | 91.50 | - | 246.00 | 101.30 | - | - | 863.50 | 93.50 | 1623.50 | ppm |
| SH-24_Ph_MI24 | Ph | - | - | 908.00 | 345.00 | - | - | 1079.70 | 93.20 | 516.30 | ppm |

**Table 4.16 (Continued)**

| Sample Name | FIA | Li7 | Be9 | B11 | Cu65 | Zn66 | As75 | Rb85 | Sr88 | Zr90 | |
|---|---|---|---|---|---|---|---|---|---|---|---|
| SH-22_MQB_MI2 | UST | 318.80 | - | - | - | - | - | 694.30 | 137.90 | - | ppm |
| SH-22_MQB_MI3 | UST | - | - | 1210.80 | - | - | - | 783.50 | 327.40 | - | ppm |
| SH-22_MQB_MI4 | UST | - | 1381.00 | - | 3090.20 | 2194.00 | - | 921.70 | 62.80 | 167.00 | ppm |
| SH-22_MQB_MI5 | UST | - | - | - | - | - | - | 384.20 | 196.50 | - | ppm |
| SH-22_MQB_MI6 | UST | 952.60 | - | - | - | - | - | 1066.30 | 240.00 | 215.90 | ppm |
| SH-22_MQB_MI7 | UST | 498.40 | - | 1245.30 | - | 213.50 | 335.40 | 818.10 | 226.90 | - | ppm |
| SH-22_MQB_MI8 | UST | - | - | 2871.80 | - | - | - | 453.80 | 286.50 | - | ppm |
| SH-22_MQB_MI9 | UST | - | - | - | 141.60 | - | 435.40 | 1217.30 | 247.60 | 140.40 | ppm |
| SH-22_MQB_MI10 | UST | - | - | - | 1426.50 | 2720.20 | - | 833.20 | 222.50 | - | ppm |
| SH-22_MQB_MI11 | UST | - | - | 1433.20 | - | - | - | 1278.00 | 171.40 | - | ppm |
| SH-22_Ph_MI1 | Ph | - | - | - | 246.70 | - | - | 995.90 | 337.70 | 840.50 | ppm |
| SH-22_Ph_MI2 | Ph | 2159.20 | - | - | - | 20694.60 | - | 1497.00 | - | - | ppm |
| SH-22_Ph_MI3 | Ph | - | - | 2663.10 | 831.40 | - | - | 1026.10 | 15.50 | 937.00 | ppm |
| SH-22_Ph_MI4 | Ph | - | 24.50 | 72.70 | - | 141.70 | 76.30 | 1042.80 | 119.80 | 837.00 | ppm |
| SH-22_Ph_MI5 | Ph | 355.00 | - | 2491.00 | 127.80 | 215.00 | - | 1978.70 | 82.50 | 2527.60 | ppm |
| SH-22_Ph_MI6 | Ph | 133.80 | - | 502.60 | 120.80 | - | - | 977.70 | 126.20 | 768.40 | ppm |
| SH-22_Ph_MI7 | Ph | 190.90 | - | 421.80 | 905.60 | 414.10 | 102.20 | 1741.90 | 171.10 | 297.90 | ppm |
| SH-22_Ph_MI8 | Ph | 48.10 | 526.30 | 573.60 | 103.20 | 765.20 | - | 1914.80 | 59.70 | - | ppm |
| SH-22_Ph_MI9 | Ph | - | - | - | 607.60 | - | - | 957.80 | 376.90 | 553.40 | ppm |
| SH-22_Ph_MI10 | Ph | - | - | - | 931.30 | - | - | 670.40 | - | - | ppm |
| SH-22_Ph_MI11 | Ph | - | - | 161.50 | 1853.50 | 1913.10 | - | 767.20 | 284.20 | - | ppm |
| SH-22_Ph_MI12 | Ph | 1232.40 | - | 1547.30 | 1424.70 | - | - | 894.50 | 170.50 | 961.70 | ppm |
| SH-22_Ph_MI13 | Ph | 1685.90 | - | 858.40 | 708.50 | - | 673.40 | 828.00 | 66.10 | 403.60 | ppm |
| SH-22_Ph_MI14 | Ph | - | - | 1331.30 | 294.20 | - | - | 1262.60 | 111.00 | 709.20 | ppm |
| SH-22_Ph_MI15 | Ph | - | - | - | - | - | - | 1124.20 | 247.90 | 629.10 | ppm |
| SH-22_Ph_MI16 | Ph | - | - | 1627.70 | - | 289.50 | - | 980.60 | 202.00 | 227.30 | ppm |
| SH-22_Ph_MI17 | Ph | - | - | - | 27.00 | - | - | 1050.10 | 124.90 | 663.00 | ppm |
| SH-22_Ph_MI18 | Ph | 684.10 | - | 439.20 | - | 2092.70 | - | 925.20 | 476.20 | 542.30 | ppm |
| SH-22_Ph_MI19 | Ph | 320.60 | - | 94.10 | - | 513.30 | - | 2146.90 | 122.90 | 299.10 | ppm |
| SH-22_Ph_MI20 | Ph | - | 233.40 | 756.80 | - | 101.90 | 45.00 | 1706.20 | 116.60 | 466.00 | ppm |
| SH-22_Ph_MI21 | Ph | 133.50 | - | 294.00 | 958.30 | 187.50 | - | 1214.10 | 160.50 | 355.30 | ppm |
| SH-22_Ph_MI22 | Ph | 711.70 | - | 979.90 | - | 179.70 | - | 1100.40 | 311.60 | 610.00 | ppm |
| SH-22_Ph_MI23 | Ph | 19.30 | - | 352.60 | 69.90 | 381.20 | - | 1383.30 | 71.50 | 571.60 | ppm |
| SH-22_Ph_MI24 | Ph | 6.40 | - | 138.50 | - | - | - | 2166.10 | 99.10 | 335.90 | ppm |
| SH-22_Ph_MI25 | Ph | 136.70 | - | 142.90 | - | 136.80 | - | 879.10 | 170.00 | 462.20 | ppm |
| SH-22_Ph_MI26 | Ph | 372.70 | - | 555.60 | 107.90 | 41.70 | 212.60 | 1728.40 | 126.80 | 632.20 | ppm |
| SH-22_Ph_MI27 | Ph | 163.10 | - | - | 1313.10 | - | - | 469.70 | - | 186.40 | ppm |
| SH-22_Ph_MI28 | Ph | 831.70 | - | 294.40 | - | - | - | 1126.40 | 370.80 | 685.00 | ppm |
| SH-22_Ph_MI29 | Ph | - | - | - | - | 909.60 | 90.90 | 718.90 | 169.20 | 281.60 | ppm |
| SH-22_Ph_MI30 | Ph | 632.50 | - | 1389.80 | 189.30 | - | - | 909.40 | 329.10 | 505.60 | ppm |
| SH-22_Ph_MI31 | Ph | - | - | 883.00 | - | - | - | 1105.90 | 264.10 | 554.90 | ppm |

**Table 4.16 (Continued)**

| Sample Name | FIA | Mo95 | Ag107 | Sn118 | Cs133 | Ba137 | La139 | Ce140 | Hf178 | Ta181 | |
|---|---|---|---|---|---|---|---|---|---|---|---|
| SH-24_MQB_MI1 | UST | - | 409.10 | - | 36.60 | 2709.50 | 136.00 | 185.30 | - | - | ppm |
| SH-24_MQB_MI3 | UST | - | - | - | - | 1752.30 | 42.70 | 197.00 | - | - | ppm |
| SH-24_MQB_MI4 | UST | 699.20 | - | - | - | 2099.90 | - | - | - | - | ppm |
| SH-24_MQB_MI5 | UST | - | - | 6.60 | 7.40 | 2320.40 | 26.40 | 70.70 | - | - | ppm |
| SH-24_MQB_MI6 | UST | - | - | - | - | 2887.50 | 201.50 | 276.10 | - | - | ppm |
| SH-24_MQB_MI7 | UST | 272.30 | - | - | 16.20 | 2032.80 | 133.10 | 254.30 | 8.20 | 6.70 | ppm |
| SH-24_MQB_MI8 | UST | - | - | - | - | 1922.70 | 172.20 | 180.10 | - | - | ppm |
| SH-24_MQB_MI9 | UST | 161.60 | - | - | 1.50 | 2092.70 | 126.50 | 233.70 | 5.90 | 5.40 | ppm |
| SH-24_MQB_MI10 | UST | - | - | - | 17.10 | 1774.80 | 106.90 | 234.80 | - | - | ppm |
| SH-24_MQB_MI11 | UST | - | - | - | 31.90 | 2152.50 | 164.90 | 270.70 | 16.60 | 1.70 | ppm |
| SH-24_Ph_MI2 | Ph | - | - | - | - | 2718.80 | 33.00 | 187.40 | - | - | ppm |
| SH-24_Ph_MI3 | Ph | - | - | - | - | 1639.30 | 177.90 | 218.00 | - | - | ppm |
| SH-24_Ph_MI4 | Ph | 1170.10 | - | - | - | 2037.30 | 196.70 | 272.50 | - | - | ppm |
| SH-24_Ph_MI5 | Ph | - | 40.90 | - | 96.10 | 4837.80 | 24.80 | 69.50 | - | - | ppm |
| SH-24_Ph_MI6 | Ph | 41.80 | 15.00 | - | 25.40 | 2030.80 | 20.20 | 19.60 | - | - | ppm |
| SH-24_Ph_MI7 | Ph | 47.10 | - | - | 17.30 | 97.00 | 267.50 | 452.60 | 59.50 | 59.00 | ppm |
| SH-24_Ph_MI8 | Ph | - | - | - | 25.50 | 660.70 | 136.20 | 197.30 | 18.00 | 13.40 | ppm |
| SH-24_Ph_MI9 | Ph | 215.20 | - | - | 325.50 | 1361.50 | 532.10 | 927.40 | 52.70 | 19.80 | ppm |
| SH-24_Ph_MI11 | Ph | 158.70 | 45.40 | - | 79.00 | 1501.90 | 63.90 | 79.40 | 24.40 | 8.10 | ppm |
| SH-24_Ph_MI12 | Ph | 161.50 | 18.80 | - | 72.70 | 97.70 | 114.20 | 249.60 | 47.20 | 69.90 | ppm |
| SH-24_Ph_MI13 | Ph | - | - | - | 10.00 | 2062.40 | 46.00 | 64.70 | 38.60 | 75.60 | ppm |
| SH-24_Ph_MI14 | Ph | - | - | 773.00 | - | 828.30 | - | - | - | - | ppm |
| SH-24_Ph_MI15 | Ph | - | - | - | - | - | 473.70 | 1385.50 | 37.40 | 68.80 | ppm |
| SH-24_Ph_MI16 | Ph | 64.90 | - | - | 82.00 | 370.60 | 138.70 | 228.00 | 67.60 | - | ppm |
| SH-24_Ph_MI17 | Ph | 205.40 | - | - | 36.10 | 454.70 | 104.60 | 295.40 | 21.50 | 45.70 | ppm |
| SH-24_Ph_MI18 | Ph | 82.30 | - | - | 116.50 | - | 74.10 | 126.40 | 95.60 | 25.80 | ppm |
| SH-24_Ph_MI19 | Ph | - | - | - | 16.70 | 1842.70 | 74.40 | 100.10 | 6.30 | 2.50 | ppm |
| SH-24_Ph_MI20 | Ph | 41.60 | - | - | 30.30 | 984.60 | 15.80 | 23.60 | 28.00 | 10.50 | ppm |
| SH-24_Ph_MI21 | Ph | 31.50 | 12.90 | - | - | 2765.90 | 58.20 | 155.20 | 8.00 | 4.60 | ppm |
| SH-24_Ph_MI23 | Ph | - | - | - | 22.10 | 41.20 | 143.00 | 299.50 | 76.70 | 40.50 | ppm |
| SH-24_Ph_MI24 | Ph | - | - | - | 47.60 | 322.60 | 200.00 | 258.20 | - | 23.50 | ppm |

**Table 4.16 (Continued)**

| Sample Name | FIA | Mo95 | Ag107 | Sn118 | Cs133 | Ba137 | La139 | Ce140 | Hf178 | Ta181 | |
|---|---|---|---|---|---|---|---|---|---|---|---|
| SH-22_MQB_MI2 | UST | - | - | - | - | 3874.70 | 65.40 | 317.70 | - | - | ppm |
| SH-22_MQB_MI3 | UST | - | - | 726.40 | - | 1370.70 | 104.90 | 140.10 | - | - | ppm |
| SH-22_MQB_MI4 | UST | - | - | - | - | 1032.30 | 179.10 | 362.70 | - | - | ppm |
| SH-22_MQB_MI5 | UST | - | - | - | - | 945.90 | 235.80 | 101.60 | - | - | ppm |
| SH-22_MQB_MI6 | UST | - | - | - | 27.70 | 1485.10 | 171.90 | 348.10 | - | - | ppm |
| SH-22_MQB_MI7 | UST | - | - | - | 51.40 | 2315.10 | 280.00 | 294.90 | - | - | ppm |
| SH-22_MQB_MI8 | UST | 145.20 | - | 60.80 | 30.10 | 574.60 | 128.90 | 116.00 | - | - | ppm |
| SH-22_MQB_MI9 | UST | - | 42.30 | 384.30 | 38.50 | 1046.30 | 156.00 | 284.70 | - | - | ppm |
| SH-22_MQB_MI10 | UST | - | - | - | - | 3842.60 | 222.00 | 217.20 | - | - | ppm |
| SH-22_MQB_MI11 | UST | - | - | - | - | 528.60 | 804.30 | 183.70 | - | - | ppm |
| SH-22_Ph_MI1 | Ph | - | - | - | - | 1495.50 | 192.30 | 449.20 | - | - | ppm |
| SH-22_Ph_MI2 | Ph | 3921.10 | - | - | - | - | - | - | - | - | ppm |
| SH-22_Ph_MI3 | Ph | - | - | 151.30 | 33.10 | 356.70 | 38.80 | 129.00 | 57.50 | 38.20 | ppm |
| SH-22_Ph_MI4 | Ph | - | 8.60 | - | 33.20 | 98.80 | 76.50 | 136.30 | 29.40 | 17.30 | ppm |
| SH-22_Ph_MI5 | Ph | - | - | - | 414.30 | - | 104.60 | 164.20 | 70.10 | 31.50 | ppm |
| SH-22_Ph_MI6 | Ph | - | 28.00 | - | 21.00 | 893.70 | 20.70 | 47.50 | 31.80 | 7.90 | ppm |
| SH-22_Ph_MI7 | Ph | - | 33.90 | - | 85.10 | 726.80 | 23.50 | 113.10 | - | - | ppm |
| SH-22_Ph_MI8 | Ph | - | 24.80 | - | 197.00 | 115.40 | 217.00 | 315.20 | 43.40 | 5.90 | ppm |
| SH-22_Ph_MI9 | Ph | - | - | - | 37.90 | 2083.90 | 213.40 | 307.50 | 51.70 | - | ppm |
| SH-22_Ph_MI10 | Ph | - | - | - | - | 1470.50 | - | 146.20 | - | - | ppm |
| SH-22_Ph_MI11 | Ph | - | 23.60 | - | - | 464.50 | 16.90 | 29.00 | - | - | ppm |
| SH-22_Ph_MI12 | Ph | - | - | - | - | 2295.20 | 138.20 | 354.90 | - | - | ppm |
| SH-22_Ph_MI13 | Ph | - | - | - | - | 1570.70 | - | 236.30 | - | - | ppm |
| SH-22_Ph_MI14 | Ph | - | - | - | - | 1518.20 | 160.50 | 339.30 | 17.80 | - | ppm |
| SH-22_Ph_MI15 | Ph | - | - | - | - | 2710.40 | 135.20 | 450.40 | 43.20 | - | ppm |
| SH-22_Ph_MI16 | Ph | - | - | - | 50.20 | 857.40 | 67.30 | 149.60 | 10.30 | 5.80 | ppm |
| SH-22_Ph_MI17 | Ph | - | - | - | 22.80 | 2801.60 | 154.60 | 297.70 | 27.50 | - | ppm |
| SH-22_Ph_MI18 | Ph | - | - | - | 18.50 | 2987.40 | 160.90 | 240.00 | - | - | ppm |
| SH-22_Ph_MI19 | Ph | - | - | - | 152.20 | 812.10 | 120.20 | 230.40 | - | - | ppm |
| SH-22_Ph_MI20 | Ph | 120.70 | - | - | 236.30 | 545.60 | 395.80 | 548.60 | 22.40 | 6.40 | ppm |
| SH-22_Ph_MI21 | Ph | - | 189.70 | - | 14.30 | 744.50 | 17.90 | 28.10 | 23.00 | 4.90 | ppm |
| SH-22_Ph_MI22 | Ph | - | - | - | 36.60 | 2470.80 | 141.00 | 278.80 | 23.70 | - | ppm |
| SH-22_Ph_MI23 | Ph | - | - | - | 72.80 | 173.20 | 312.00 | 438.10 | 27.30 | 5.20 | ppm |
| SH-22_Ph_MI24 | Ph | - | - | - | 93.70 | 214.30 | 228.10 | 273.10 | - | - | ppm |
| SH-22_Ph_MI25 | Ph | - | - | - | 20.20 | 540.20 | 976.20 | 141.90 | 11.40 | 3.80 | ppm |
| SH-22_Ph_MI26 | Ph | 76.40 | - | - | 372.00 | 506.20 | 202.80 | 387.10 | - | 12.10 | ppm |
| SH-22_Ph_MI27 | Ph | - | 718.70 | - | - | - | - | - | - | - | ppm |
| SH-22_Ph_MI28 | Ph | 87.20 | - | - | 64.60 | 2840.30 | 213.00 | 425.20 | 41.90 | - | ppm |
| SH-22_Ph_MI29 | Ph | 89.60 | - | - | 36.10 | 2359.80 | 76.30 | 258.10 | - | - | ppm |
| SH-22_Ph_MI30 | Ph | 59.30 | - | - | 70.20 | 1697.00 | 217.20 | 309.20 | 32.10 | 8.30 | ppm |
| SH-22_Ph_MI31 | Ph | - | - | - | 39.30 | 3426.70 | 203.90 | 288.80 | - | - | ppm |

**Table 4.16 (Continued)**

| Sample Name | FIA | W182 | Au197 | Tl205 | Pb208 | Th232 | U238 | |
|---|---|---|---|---|---|---|---|---|
| SH-24_MQB_MI1 | UST | - | - | - | 81.90 | - | 19.90 | ppm |
| SH-24_MQB_MI3 | UST | - | - | - | 1009.40 | - | - | ppm |
| SH-24_MQB_MI4 | UST | - | - | - | 918.00 | - | - | ppm |
| SH-24_MQB_MI5 | UST | - | - | - | 25.90 | - | - | ppm |
| SH-24_MQB_MI6 | UST | - | - | - | 68.70 | - | 30.20 | ppm |
| SH-24_MQB_MI7 | UST | - | - | - | 83.90 | - | 12.00 | ppm |
| SH-24_MQB_MI8 | UST | - | - | - | - | - | - | ppm |
| SH-24_MQB_MI9 | UST | - | - | - | 61.60 | - | 15.00 | ppm |
| SH-24_MQB_MI10 | UST | - | - | - | 58.30 | - | 14.80 | ppm |
| SH-24_MQB_MI11 | UST | - | - | 6.70 | 53.20 | - | 18.00 | ppm |
| SH-24_Ph_MI2 | Ph | - | - | - | 50.10 | - | - | ppm |
| SH-24_Ph_MI3 | Ph | - | - | - | 112.80 | - | 81.90 | ppm |
| SH-24_Ph_MI4 | Ph | - | - | - | 217.50 | - | 101.50 | ppm |
| SH-24_Ph_MI5 | Ph | - | - | 28.50 | 7445.80 | - | 2.50 | ppm |
| SH-24_Ph_MI6 | Ph | 24.10 | - | 4.50 | 2050.10 | - | - | ppm |
| SH-24_Ph_MI7 | Ph | 32.80 | - | 3.10 | 279.50 | - | 40.90 | ppm |
| SH-24_Ph_MI8 | Ph | - | - | - | 40.80 | - | 31.40 | ppm |
| SH-24_Ph_MI9 | Ph | - | - | - | 114.10 | - | - | ppm |
| SH-24_Ph_MI11 | Ph | 41.30 | - | 9.50 | 1640.50 | - | 7.60 | ppm |
| SH-24_Ph_MI12 | Ph | 66.40 | - | 4.60 | 606.50 | - | 26.60 | ppm |
| SH-24_Ph_MI13 | Ph | 29.50 | - | - | 712.20 | - | 13.40 | ppm |
| SH-24_Ph_MI14 | Ph | - | - | - | - | - | - | ppm |
| SH-24_Ph_MI15 | Ph | - | - | - | 50.20 | - | 15.30 | ppm |
| SH-24_Ph_MI16 | Ph | 61.20 | - | - | 534.80 | - | 32.60 | ppm |
| SH-24_Ph_MI17 | Ph | 54.10 | - | - | 534.30 | - | 33.10 | ppm |
| SH-24_Ph_MI18 | Ph | - | - | - | 112.00 | - | 8.40 | ppm |
| SH-24_Ph_MI19 | Ph | - | - | - | 82.50 | - | 13.50 | ppm |
| SH-24_Ph_MI20 | Ph | 17.00 | - | 5.30 | 125.10 | - | 50.80 | ppm |
| SH-24_Ph_MI21 | Ph | 26.50 | - | - | 271.10 | - | 2.70 | ppm |
| SH-24_Ph_MI23 | Ph | 20.30 | - | - | 60.50 | - | 37.20 | ppm |
| SH-24_Ph_MI24 | Ph | - | - | - | 151.40 | - | 27.10 | ppm |

**Table 4.16 (Continued)**

| Sample Name | FIA | W182 | Au197 | Tl205 | Pb208 | Th232 | U238 | |
|---|---|---|---|---|---|---|---|---|
| SH-22_MQB_MI2 | UST | - | - | - | - | - | - | ppm |
| SH-22_MQB_MI3 | UST | - | - | - | 253.80 | - | - | ppm |
| SH-22_MQB_MI4 | UST | - | 115.10 | - | 113.60 | - | 41.50 | ppm |
| SH-22_MQB_MI5 | UST | - | - | - | 263.80 | - | - | ppm |
| SH-22_MQB_MI6 | UST | - | 133.00 | - | 92.60 | - | - | ppm |
| SH-22_MQB_MI7 | UST | - | - | - | 186.20 | - | 7.20 | ppm |
| SH-22_MQB_MI8 | UST | 179.20 | - | - | 86.50 | - | - | ppm |
| SH-22_MQB_MI9 | UST | - | - | - | 104.90 | - | 10.50 | ppm |
| SH-22_MQB_MI10 | UST | - | - | - | 162.00 | - | - | ppm |
| SH-22_MQB_MI11 | UST | - | - | - | - | - | - | ppm |
| SH-22_Ph_MI1 | Ph | - | - | - | - | - | - | ppm |
| SH-22_Ph_MI2 | Ph | - | - | - | - | - | - | ppm |
| SH-22_Ph_MI3 | Ph | - | 20.40 | 10.90 | 270.40 | - | 24.10 | ppm |
| SH-22_Ph_MI4 | Ph | 15.80 | - | 3.70 | 63.90 | 145.10 | 14.30 | ppm |
| SH-22_Ph_MI5 | Ph | - | - | - | 104.00 | - | 31.70 | ppm |
| SH-22_Ph_MI6 | Ph | 18.50 | - | - | - | - | 33.20 | ppm |
| SH-22_Ph_MI7 | Ph | - | - | 5.90 | 165.80 | - | 6.70 | ppm |
| SH-22_Ph_MI8 | Ph | - | - | 3.70 | 66.50 | 207.90 | 231.20 | ppm |
| SH-22_Ph_MI9 | Ph | - | - | - | 139.70 | - | 43.70 | ppm |
| SH-22_Ph_MI10 | Ph | - | - | - | - | - | - | ppm |
| SH-22_Ph_MI11 | Ph | - | - | - | 1541.30 | - | - | ppm |
| SH-22_Ph_MI12 | Ph | - | - | - | 84.10 | - | 13.20 | ppm |
| SH-22_Ph_MI13 | Ph | - | - | - | 192.00 | - | - | ppm |
| SH-22_Ph_MI14 | Ph | - | - | - | 89.70 | - | 48.40 | ppm |
| SH-22_Ph_MI15 | Ph | - | - | - | 70.50 | - | 29.40 | ppm |
| SH-22_Ph_MI16 | Ph | - | - | - | 105.70 | - | 3.90 | ppm |
| SH-22_Ph_MI17 | Ph | - | - | - | 73.00 | - | - | ppm |
| SH-22_Ph_MI18 | Ph | - | - | - | 904.40 | - | 23.00 | ppm |
| SH-22_Ph_MI19 | Ph | - | - | - | 71.70 | 8.40 | 30.20 | ppm |
| SH-22_Ph_MI20 | Ph | - | - | - | 86.20 | - | - | ppm |
| SH-22_Ph_MI21 | Ph | 12.50 | - | 4.00 | 11.20 | - | - | ppm |
| SH-22_Ph_MI22 | Ph | - | - | 10.70 | 113.40 | - | 25.00 | ppm |
| SH-22_Ph_MI23 | Ph | 20.10 | - | - | 96.70 | - | 50.80 | ppm |
| SH-22_Ph_MI24 | Ph | 23.10 | - | 12.50 | 101.00 | 56.10 | 38.50 | ppm |
| SH-22_Ph_MI25 | Ph | - | - | - | 35.40 | 41.90 | 9.30 | ppm |
| SH-22_Ph_MI26 | Ph | - | - | - | 79.40 | 148.60 | 53.40 | ppm |
| SH-22_Ph_MI27 | Ph | - | - | - | - | - | - | ppm |
| SH-22_Ph_MI28 | Ph | - | - | - | 131.80 | - | 26.90 | ppm |
| SH-22_Ph_MI29 | Ph | 34.60 | - | - | 70.70 | 15.70 | 21.80 | ppm |
| SH-22_Ph_MI30 | Ph | - | - | - | 136.80 | - | 29.10 | ppm |
| SH-22_Ph_MI31 | Ph | - | - | - | 141.10 | - | 20.40 | ppm |

# Chapter 5: Conclusions

This thesis reports the results of investigations into the nature of mineralizing fluids in iron oxide-apatite (IOA) deposits and at the magmatic-hydrothermal transition of a small Cu-Ag-Au porphyry system. In both cases, identification and analysis of coeval fluid and melt inclusions provides a basis for understanding fluid sources and evolution in these systems. Through a combination of petrographic characterization and *in situ* chemical analysis, I have constrained the types, compositions and physical/chemical properties of mineralizing fluid at the time of entrapment during the formation of various features in these systems. These factors are important controls of the size and composition of base-metal mineralization in these systems and thus provide insight in the underlying factors with drive the evolution of these systems.

In **Chapter 2**, I examined the Buena Vista and Iron Springs IOA deposits. In both deposits, I observed nearly identical populations of Fe-rich carbonate-sulfate melt inclusions and coeval brines. At Buena Vista, these melt inclusions are dominated by carbonate with minor sulfate, whereas sulfate dominates at Iron Springs. Nevertheless, the high Fe contents of these melts, as well as their ubiquitous occurrence throughout the paragenesis and the absence of other Fe-rich fluid inclusion types, indicate that the main mineralizing fluids in both systems were carbonate-sulfate melts. The most likely source of the carbonate-sulfate melts was likely through anatexis of evaporite-bearing sedimentary rocks that were intruded by the silicate magmas associated with these systems. This is indicated both by cross-cutting relationships as well as by C-O and isotopes of carbonates in the Buena Vista system. These observations indicate that the Buena Vista and Iron Springs systems were formed by primarily *igneous* processes, in which 1) intruding silicate melt generated a carbonate-sulfate-rich liquid by melting and assimilation of wet, evaporite-bearing chemical-sedimentary rocks; 2) the newly-formed melt became enriched in $Fe^{3+}$ by equilibration with the mafic-to-intermediate silicate melt and volcanic country rock, and by subsequent oxidation of ferrous to ferric iron, as a result of the high $f_{O2}$ buffered by the oxidized carbon and sulfur species in the liquid; and 3) the circulation and cooling of the carbonate-sulfate fluids drove crystallization of Fe-oxide (magnetite) as well as immiscible separation of an aqueous fluid that circulated outward and formed a large envelope of Na-Ca alteration. Over time, the sustained generation of carbonate-sulfate liquid and the accumulation of spent ore fluid in the deposit led to the formation of carbonate dikes and veins which

commonly crosscut the ore bodies. While this model can be clearly applied to Buena Vista and Iron Springs, I argue that it is likely that it also applies to other IOA systems more broadly. This inference is based on the fact that the igneous intrusions associated with many IOA systems cross-cut evaporite-bearing sediments and show unambiguous evidence of crustal assimilation. This model is significantly different from the previous orthomagmatic, magmatic-hydrothermal, and amagmatic hydrothermal models that have been typically attributed to IOA systems. As such, it represents a novel mechanism for IOA formation that reconciles the presence of overlapping orthomagmatic and hydrothermal features in IOA systems more generally.

In **Chapter 3**, I examined the nature of mineralizing fluids in the El Laco deposit in northern Chile. Diopside, magnetite, albite, and apatite from pegmatitic diopside-magnetite-anhydrite veins which cap massive magnetite ore bodies in the deepest parts of the system contain abundant polycrystalline melt inclusions that resemble those described in chapter 2. The compositions of inclusions at El Laco vary with relative position within the host phases, with inclusions in the cores of diopside crystals containing albite-orthoclase-anhydrite-hematite whereas inclusions near the rims of the same grains are dominantly sulfate-hematite in composition. Similar to the Iron Springs system, the main mineralizing fluid at El Laco appears to be a sulfate-rich melt derived from the anataxis of sulfate- and carbonate-rich sedimentary strata. This is indicated both by 1) the crosscutting nature of the anhydrite intrusions which feed the El Laco system and evaporite-bearing carbonate strata at depth; and 2) the transition of inclusion compositions from the cores to the rims of host minerals, which indicate an early mixture of sulfate and silicate components, that tends towards more sulfate-rich (silicate-poor) liquid compositions later in the paragenesis. I argue that the similarities in mineralizing fluid compositions observed at El Laco compared to the Buena Vista and Iron Spring systems (chapter 2) is not a coincidence. Rather, this suggests a common genetic model for these systems, in which the generation of carbonate- and/or sulfate-rich melt by anatexis and assimilation of chemical sediments plays a central role.

In **Chapter 4**, I examined the nature and evolution of melts and exsolved fluids at the magmatic-hydrothermal transition of a small porphyry-Cu deposit at Saginaw Hill, Arizona. Unidirectional solidification textures in the Saginaw Hill quartz latite porphyry host abundant assemblages of coeval fluid and melt inclusions. The cores of quartz crystals throughout the UST bands have relatively low trace-element contents and host coeval silicate melt and high-salinity

brine inclusions, consistent with direct exsolution of high-salinity Cu-rich brine. In contrast, the rims of UST quartz have variable and relatively high trace-element contents and host abundant coeval brine and vapor inclusions consistent with liquid-vapor immiscibility at lower pressures compared to the respective quartz cores. This transition from dominantly coeval silicate melt inclusions and brine in the cores, to coeval brine and vapor in the rims, suggests that the Saginaw Hill system underwent a cyclic process during UST formation characterized by an initial stage of relatively slow quartz growth during brine exsolution, accumulation, and development of fluid overpressure; followed by an abrupt episode of depressurization, fluid release, and rapid quartz precipitation. This cyclic process took place at relatively stable temperatures (consistently ~650 °C) late in the magmatic evolution, and melt inclusion data indicate that the melt was at this stage highly fractionated and tending toward muscovite saturation. Our results indicate that the degassing of the Saginaw Hill systems was an episodic process defined by repetitious cycles of fluid accumulation, over-pressurization, fluid release, and depressurization (i.e throttling) of brine exsolved directly form the silicate melt. The small size and shallow depth of formation for this system likely drove the melt toward a highly fractionated composition which in turn drove the active exsolution of brines. Though this system hosts only minor amounts of mineralization, the processes that operated in the Saginaw Hill system likely also occur in larger porphyry-systems on larger scales, at greater depths, and during multiple pulses of magma emplacement. As such, I suggest that direct exsolution of brine, and evolution of that brine via throttling, are important processes that affect metal partitioning at the magmatic-hydrothermal transition and the evolution of mineralizing fluid during outward flux from degassing magmas.

The evolution and chemical character of mineralizing fluids are key factors controlling the formation of metal-rich deposits. In IOA systems the key medium for iron transport appears to be a fluid which departs form the conventional paradigm in most systems: a highly reactive carbonate-sulfate melt generated by crustal anataxis. Such a fluid would effectively partition and mobilize Fe- and thus would account for many of the enigmatic features of IOA systems. The conditions which would allow for the formation of anatectic carbonate-sulfate melt are likely quite common. This suggests that fluids of this type might drive the formation of a much broader range of metal-rich systems beyond IOA deposits -particularly those enriched in lithophile elements (e.g. REEs). Similarly, in porphyry-Cu systems, the direct exsolution of brine from highly fractionated silicate melt appears to be a fundamental process. The chloride-rich nature of

the exsolved brines is directly related to Cu partitioning at the magmatic-hydrothermal transition, and their exsolution and release into a hydrothermal system is a function of dynamic pressure fluctuations and fractionation of the silicate system. On a larger scale, the model presented here for fluid exsolution at Saginaw Hill illustrates a fundamental process involved in the formation of economic magmatic-hydrothermal systems generally. Thus, the processes I characterize in IOA and porphyry-Cu systems represent key mechanisms governing the size and scale of mineralization in a broad range of economic systems.

# Bibliography

Allan, M.M., Yardley, B.W.D, Forbes, L.J., Shmulovich, K.I., Banks, D.A., and Shepherd, T.J., 2005, Validation of LA-ICP-MS fluid inclusion analysis with synthetic fluid inclusions: American Mineralogist, v. 90, p.1767-1775.

Allmendinger, R.W., Jordan, T.E., Kay, S.M., and Isacks, B.L., 1997, The evolution of the Altiplano-Puna plateau of the Central Andes: Annual Review of Earth and Planetary Sciences, v. 25, p. 139–174.

Anenburg, M., Burnham, A.D., and Mavrogenes, J.A., 2018, REE redistribution textures in altered fluorapatite: Symplectites veins, and phosphate-silicate-carbonate assemblages from the Nolans Bore P-REE-Th deposit, Northern Territory, Australia: Canadian Mineralogist, v. 56, p. 331-354.

Armstrong, J.T., 1995, CITZAF: A package of correction programs for the quantitative electron microbeam X-ray-analysis of thick polished materials, thin-films, and particles: Microbeam Analysis v. 4, p. 177-200.

Audétat A. and Pettke, T., 2003, The magmatic-hydrothermal evolution of two barren granites: a melt and fluid inclusion study of the Rito del Medio and Canada Pinabete plutons in northern New Mexico (USA): Geochimica et Cosmochimica Acta, v. 67, p. 97–121.

Audétat, A., and Günther, D., 1999, Mobility and H2O loss from fluid inclusions in natural quartz crystals: Contributions to mineral petrology, v. 137, p. 1-14.

Audétat, A., and Günther, D., 1999, Mobility and H2O loss from fluid inclusions in natural quartz crystals: Contributions to Mineral Petrology, v. 137, p. 1-14.

Audétat, A., Günther, D., and Heinrich, C.A., 1998, Formation of a magmatic-hydrothermal ore deposit: Insights with LA-ICP-MS analysis of fluid inclusions: Science, v. 279 p. 2061-2094.

Audétat, A., Günther, D., and Heinrich, C.A., 2000, Causes for large-scale metal zonation around mineralized plutons: Fluid inclusion LA-ICP-MS evidence from the Mole Granite, Australia: Economic Geology, v. 95, p. 1563-1581.

Bain, W.M., Steele-MacInnis, M., Li, K., Li, L., Mazdab, F.K., and Marsh, E.E., 2020, A fundamental role of carbonate-sulfate melts in formation of iron oxide-apatite deposits, Nature Geoscience , in press

Baker, T. et al., 2008, Mixed messages in iron oxide–copper–gold systems of the Cloncurry district, Australia: insights from PIXE analysis of halogens and copper in fluid inclusions: Mineralium Deposita, v. 43, p. 599-608.

Barton, M.D., 2014, Iron Oxide(-Cu-Au-REE-P-Ag-Co) Systems: in Treatise on Geochemistry 2nd Edition, p. 515-541.

Barton, M.D., and Johnson, D.A., 1996, Evaporitic source model for igneous-related Fe oxide–(REE–Cu–Au–U) mineralization, Geology, v. 24, p. 259–262.

Bell, A., and Simon, A.C., 2011, Evidence for the alteration of the $Fe3+/\sum Fe$ of silicate melt caused by the degassing of chlorine-bearing aqueous volatiles: Geology, v. 39, p. 499–502

Bertelli, M., and Baker, T., 2010, A fluid inclusion study of the Suicide Ridge Breccia Pipe, Cloncurry district, Australia: Implication for Breccia Genesis and IOCG mineralization: Precambrian Research, v. 179, p. 69-87.

Blount, C.W., and Dickson, W., 1969, The solubility of anhydrite ($CaSO4$) in $NaCl$-$H2O$ from 100 to 450°C and 1 to 1000 bars: Geochimica et Cosmochimica Acta, v. 33, p. 227-245

Bodnar, R.J., Lecumberri-Sanchez, P., Moncada, D., and Steele-MacInnis, M., 2014, Fluid inclusions in Hydrothermal Ore Deposits: in Treatise on Geochemistry, Second Edition v. 13, p. 119-142.

Bonyadi, Z., Davidson, G.J., Mehrabi, B., Meffre, S., and Ghazban, F., 2011, Significance of apatite REE depletion and monazite inclusions in the brecciated Se–Chahun iron oxide–apatite deposit, Bafq district, Iran: Insights from paragenesis and geochemistry: Chemical Geology, v. 281. p. 253-269.

Broman, C., Nystr.m, J.O., Henriquez, F., and Elfman, M., 1999, Fluid inclusions in magnetite-apatite ore from a cooling magmatic system at El Laco, Chile: Journal of the Geologic Society of Sweden, v. 121, p. 253–267.

Broughm, S., Hanchar, J.M., Tornos, F., Attersley, S., and Westhues, A., 2017, Mineral chemistry of magnetite from magnetite-apatite ores and their host rocks in Sweden and Chile: Mineralium Deposita, v. 52, p. 1223-1244.

Bullock, K.C., 1970, Iron deposits of Utah: Utah Geological and Mineralogical Survey Bulletin. v. 88, p. 101.

Burnham, C.W., 1997, Magmas and hydrothermal fluids, in Barnes, H.L., ed., Geochemistry of hydrothermal ore deposits (third edition): New York, John Wiley and Sons, p. 63–123.

Burnham, C.W., and Davis, N.F., 1971, The role of H2O in silicate melts 1. P-V-T relations in the system NaAlSi3O8-H2O to 10 kilobars and 1000°C: American Journal of Science, v. 270, p. 54-79.

Calzia, J.P., Frisken, J.G., Jachens, R.C., McMahon, A.B., and Rumsey, C.M., 1988, Mineral resources of the Kingston Range Wilderness study area, San Bernardino County, California: USGS Bulletin, v. 1709-D.

Campos, E.A., Touret, J.L.R., and Nikogosian, I., 2006, Magmatic fluid inclusions from the Zaldívar Deposit, Northern Chile: the role of early metal-bearing fluids in a porphyry copper system: Resource Geology, v. 56, p. 1–8.

Carroll, M.R., and Rutherford, M.J., 1987, The stability of igneous anhydrite: experimental results and implications for sulfur behavior in the 1982 El Chichon trachyandesite and other evolved magmas: Journal of Petrology, v. 28, p. 781–801.

Carten, R.B., Geraghty, E.P., Walker, B.M., and Shannon, J.R., 1988, Cyclic development of igneous features and their relationship to high-temperature hydrothermal features in the Henderson porphyry molybdenum deposit, Colorado: Economic Geology, v. 83, p. 266-296.

Carter, L. B., and Dasgupta, R., 2016, Effect of melt composition on crustal carbonate assimilation: Implications for the transition from calcite consumption to skarnification and associated CO2 degassing: Geochemistry, Geophysics, Geosystems, v. 17, p. 3893–3916.

Chacko, T., Mayeda, T.K., Clayton, R.N., and Goldsmith, J.T., 1991, Oxygen and carbon isotope fractionations between CO2 and calcite: Geochimica et Cosmochimica Acta, v. 55, p. 2867-2882.

Chai, F. et al., 2009, Geochronology of metarhyolites from the Kangbutiebao Formation in the Kelang basin, Altay Mountains, Xinjiang: Implications for the tectonic evolution and metallogeny: Gondwana Research, v. 16, p. 189-200.

Chai, F. et al., 2014, The Abagong apatite-rich magnetite deposit in the Chinese Altay Orogenic Belt: a Kiruna-type iron deposit: Ore Geology Reviews, v. 57, p. 482-497.

Chen, H. et al., 2010, Evolution of the giant Marcona-Mina Justa iron oxide-copper-gold district, south-central Peru: Economic Geology, v. 105, p. 155-185.

Chen, H., Clark, A. H., and Kyser, T. K., 2010, The Marcona magnetite deposit, Ica, south-central Peru: A product of hydrous, iron oxide-rich melts?: Economic Geology, v. 105, p. 1441-1456.

Chen, H., Kyser, T.K., and Clark, A.H., 2011, Contrasting fluids and reservoirs in the contiguous Marcona and Mina Justa iron oxide–Cu (–Ag–Au) deposits, south-central Perú: Mineralium Deposita, v. 46, p. 677-706.

Cline, J.S., and Bodnar, R.J., 1991, Can economic porphyry copper mineralization be generated by a typical calc-alkaline melt?: Journal of Geophysical Research, v. 96, p. 8113–8126

Cloos, M., 2001, Bubbling magma chambers, cupolas, and porphyry copper deposits: International Geology Review, v. 43, p. 285–311.

Cloos, M., and Sapiie, B., 2013, Porphyry copper deposits: strike–slip faulting and throttling cupolas: International Geology Review, v. 55, p. 43–65.

Dare, S.A.S, Barnes, S. and Beaudoin, G., 2015, Did the massive magnetite "lava flows" of El Laco (Chile) form by magmatic or hydrothermal processes? New constraints from magnetite composition by LA-ICP-MS: Mineralium deposita, v. 50, p. 607-617.

Donovan, J.J., Kremser, D., Fournelle, J.H., and Goemann, K., 2015, Probe for EPMA: Acquisition, automation and analysis, version 11: Eugene, Oregon, Probe Software, Inc., http://www.probesoftware.com.

Donovan, J.J., Lowers, H.A., and Rusk, B.G., 2011, Improved electron probe microanalysis of trace elements in quartz: American Mineralogist, v. 96, p. 274-282.

Durand, C., Baumgartner, L. P., and Marquer, D., 2015, Low melting temperature for calcite at 100 bars on the join CaCO3-H2O – some geological implications: Terra Nova.v. 27, p. 364-369.

Eiler, J.M., 2001, Oxygen isotope variations of basaltic lavas and upper mantle rocks: Reviews in Mineral Geochemistry, .v. 43, p. 319-364.

Erdenebayar, J., Ogata, T., Imai, A., and Sereenen, J., 2014, Textural and chemical evolution of unidirectional solidification textures in highly differentiated granitic rocks at Kharaatyagaan, central Mongolia: Resource Geology, v. 64, p. 283–300

Ferrero, S., 2012, Microstructures of melt inclusions in anatectic metasedimentary rocks: Journal of Metamorphic Geology, v. 30, p. 303–322.

Floess, D., Baumgartner, L. P., and Vonlanthen, P., 2015, An observational and thermodynamic investigation of carbonate partial melting: Earth and Planetary Science Letters, v. 409, p. 147-156.

Fournier, R.O., 1999, Hydrothermal processes related to movement of fluid from plastic into brittle rock in the magmatic-epithermal environment: Economic Geology, v. 94, p. 1193–1211.

Frank, T.R., 1970, Geology and mineralization in the Saginaw hill area, Pima County, Arizona: PhD Dissertation, The University of Arizona, Tucson AZ USA, 151 pp.

Freyer, D., and Voigt, W., 2003. Crystallization and phase stability of CaSO4 and CaSO4-based salts: Chemical Monthly., v. 134, p. 693-719.

Freyer, D., Voigt, W., and Köhnke, K., 1998, The phase diagram of the systems Na2SO4-CaSO4: European Journal of Solid-State inorganic Chemistry. v. 35. p. 595-606.

Frezzotti, M.L., Tecce, F., and Casagli, A., 2012, Raman spectroscopy for fluid inclusion analysis: Journal of Geochemical Exploration, v. 112, p. 1-20.

Frietsch R., Tuisku P., Martinsson O., and Perdahl J. A., 1997, Early Proterozoic Cu–(Au) and Fe ore deposits associated with regional Na–Cl metasomatism in northern Fennoscandia: Ore Geology Reviews, v. 12, p. 1–34.

Frost, B.R., and Frost, C.D., 2008, A Geochemical Classification for Feldspathic Igneous Rocks: Journal of Petrology, v. 49, p. 1955-1969.

Fulignati, P., Kamenetsky, V. S., Marianelli, P., Sbrana, A., and Mernagh, T. P., Melt inclusion record of immiscibility between silicate, hydrosaline, and carbonate melts: Applications to skarn genesis at Mount Vesuvius: Geology, v. 29, p. 1043-1046

Ganino, C., Arndt, N. T., Chauvel, C., Jean, A., and Athurion, C., 2013, Melting of carbonate wall rocks and formation of the heterogeneous aureole of the Panzhihua intrusion, China: Geoscience Frontiers, v. 4, p. 535-546.

Giebel, R.J., Marks, M.A.W., Gauert, C.D.K., and Markl, G. A., 2019, model for the formation of carbonatite-phoscorite assemblages based on the compositional variations of mica and apatite from the Palabora Carbonatite Complex, South Africa: Lithos v. 324-325, p. 89-104.

Giuliani, A. et al., 2012, Nature of alkali-carbonate fluids in the sub-continental lithospheric mantle: Geology, v. 40, p. 967-970.

Gleeson, S.A., and Smith, M.P., 2009, The sources and evolution of mineralising fluids in iron oxide–copper–gold systems, Norrbotten, Sweden: Constraints from Br/Cl ratios and stable Cl isotopes of fluid inclusion leachates: Geochimica et Cosmochimica Acta, v. 73, p. 5658-5672.

Goldstein, R. H., and Reynolds, T. J., 1993, Systematics of Fluid Inclusions in Diagenetic Minerals: SEPM Society for Sedimentary Geology.

Gozzi, F. et al., 2014, Primary magmatic calcite reveals origin from crustal carbonate: Lithos, v. 190, p. 191-203.

Gregory, H. E., and Moore, E. C., 1931, The Kaiparowits region, a geographic and geologic reconnaissance of parts of Utah and Arizona: U.S. Geol. Survey Prof. Paper v. 164, p. 161 p.

Guillong, M., Meier, D. L., Allan, M.M., Heinrich, C.A., and Yardley, B.W., 2008, SILLS: A MATLAB-based program for the reduction of laser ablation ICP-MS data of homogeneous materials and inclusions: Mineralogical Association of Canada Short Course Series, v. 40, p. 328–333.

Halter W. E., Pettke T., Heinrich C.A., and Rothen-Rutishauser, B., 2002, Major to trace element analysis of melt inclusions by laser-ablation ICP-MS: methods of quantification: Chemical Geology, v. 183, p. 63–86.

Harmon, R., et al., 1984, Regional 0-, Sr-, and Pb-isotope relationships in late Cenozoic calc-alkaline lavas of the Andean Cordillera: Journal of the Geologic Society of London, v.141, p. 803–822.

Harris, A.C., Kamenetsky, V.S., White, N.C., van Achterbergh, E., and Ryan, C.G., 2004, Melt inclusions in veins: linking magmas and porphyry Cu Deposits: Science, v. 302, p. 2109-2111.

Heinrich, C.A., and Candela, P.A., 2014, Fluids and Ore Formation in the Earth's Crust: in Treatise on Geochemistry, Second Edition v. 13, p. 1-23.

Hofstra, A.H. et al., 2016, Mineral thermometry and fluid inclusion studies of the Pea Ridge iron oxide-apatite-rare Earth element deposit, Mesoproterozoic St. Francois Mountains terrane, Southeast Missouri, USA: Economic Geology, v. 111, p. 1985-2016

Holtz, F., Becker, A., Freise, M., and Johannes, W., 2001, The water-under- saturated and dry Qz-Ab-Or system revisited. Experimental results at very low water activities and geological implications: Contributions to Mineralogy and Petrology, v. 141, p. 347−357.

Hou, T. et al., 2018 Immiscible hydrous Fe-Ca-P melt and the origin of iron oxide-apatite ore deposits: Nature Communications, v. 9, p. 1-7.

Hsu, H.S., DeVan, J.H., and Howell, M., 1987, Corrosion of iron in molten carbonates at 650 °C: Journal of the Electrochemical Society, v. 134, p. 3038-3043.

Huang, R., and Audétat, A., 2012, The titanium-in-quartz (TitaniQ) thermobarometer: a critical examination and re-calibration: Geochimica et Cosmochimica Acta, v. 84, p. 75–89.

Hunt, J.A., Baker,T., and Thorkelson, D.J., 2007, A Review of iron oxide copper-gold deposits, with focus on the Wernecke breccias, Yukon, Canada, as an example of a non-magmatic end member and implications for IOCG genesis and classification: Exploration and Mining Geology, v. 16, p. 209-232.

Jami, M., Dunlop, A.C., and Cohen, D.R., 2007, Fluid inclusion and stable isotope study of the Esfordi apatite-magnetite deposit, Central Iran: Economic Geology, v. 102. p. 1111-1128.

Johnson, D. A., 2000, Studies of Iron-Oxide (Cu–REE–Au–Co–Ag–Ni–U) Mineralization and associated sodic alteration in the Great Basin: 277. PhD Dissertation, University of Arizona.

Johnson, D. A., and Barton, M. D., 2000, Time-space development of an external brine-dominated, igneous-driven hydrothermal system; Humboldt mafic complex, western Nevada: Society of Economic Geologists Guidebook Society of Economic Geologists Guidebook Series. v. 32, p. 127-144.

Jones, A. P., Genge, M., and Carmody, L., 2013, Carbonate melts and carbonatites: Reviews in Mineral geochemistry, v. 75, p. 289-322.

Jonsson, E. et al., 2013 Magmatic origin of giant 'Kiruna-type' apatite-iron-oxide ores in central Sweden: Scientific Reports, v. 3, p. 1-8.

Kenderes, S.M., and Appold, M.S., 2017, Fluorine concentrations of ore fluids in the Illinois-Kentucky district: evidence from SEM-EDS analysis of fluid inclusion decrepitate: Geochimica et Cosmochimica Acta, v. 210, p. 132-151 (2017).

Kendrick, M.A. Honda, M., Gillen, D., Baker, T., and Phillips, D., 2008, New constraints on regional brecciation in the Wernecke Mountains, Canada, from He, Ne, Ar, Kr, Xe, Cl, Br and I in fluid inclusions: Chemical Geology, v. 255, p. 33-46.

Kirkham, R. V., and Sinclair, W. D., 1988, Comb quartz layers in felsic intrusions and their relationship to porphyry deposits: in Taylor, R. P. and Strong, D. F. (eds) Recent advances in the geology of granite-related mineral deposits: Canadian Institute of Mining and Metallurgy, Special Volume 39, p. 50-71

Klemm, L. M., Pettke, T., and Heinrich, C. A., 2008, Fluid and source magma evolution of the Questa porphyry Mo deposit, New Mexico, USA: Mineralium Deposita, v. 43, p. 533–552.

Klyukin, Y.I., Lecumberri-Sanchez, P., Steele-MacInnis, M., and Bodnar, R.J., 2019, Fluid inclusion phase ratios, compositions and densities, from ambient temperature to homogenization, based on PVTX properties of H2O-NaCl: Earth-Science Reviews, v. 198, p. 1-16.

Knipping, J.L., Fiege, A., Simon, A.C., Oeser, M., Reich, M., and Bilenker. L.D., 2019, In-situ iron isotope analyses reveal igneous and magmatic-hydrothermal growth of magnetite at the Los Colorados Kiruna-type iron oxide-apatite deposit, Chile: American Mineralogist, v. 104, p. 471-484.

Koděra, P., Heinrich, C.A., Wälle, M., and Lexa, J., 2014, Magmatic salt melt and vapor: Extreme fluids forming porphyry gold deposits in shallow sub volcanic settings: Geology, v.42, p. 495-498.

Kontak, D., 2004, Analysis of evaporate mounds as a complement to fluid-inclusion thermometric data: case studies from granitic environments in Nova Scotia and Peru: Canadian Mineralogist, v. 42, p. 1315-1329,

Lafuente, B., Downs, R. T., Yang, H., and Stone, N., 2016, the power of databases: The RRUFF project: in Highlights in Mineralogical Crystallography. 1-29.

Lafuente, B., Downs, R.T., Yang, H., and Stone, N., 2015, The power of databases: the RRUFF project: in Highlights in mineralogical crystallography, T Armbruster and R M Danisi, eds. Berlin, Germany, W. De Gruyter, 1-30.

Large, S.J.E., Wotzlaw, J.F., Guillong, M., von Quadt, A., and Heinrich, C.A., 2020, Resolving the timescales of magmatic and hydrothermal processes associated with porphyry deposit formation using zircon U–Pb petrochronology: Geochronology, v. 2, p. 209-230.

Larocque, A.C.L., Stimac, J.A., Keith, J.D., and Huminicki, M.A.E., 2000, Evidence for open-system behavior in immiscible Fe-S-O liquids in silicate magmas: Implications for contributions of metals and sulfur to ore-forming fluids: Canadian Mineralogist v. 38, p. 1233-1249.

Leach, A.M., and Hieftje, G.M., 2000, Methods for shot-to-shot normalization in laser ablation with an inductively coupled plasma time-of-flight mass spectrometer: Journal of Analytical Atomic Spectrometry, v. 15, p. 1121–1124.

Lecumberri-Sanchez, P., Luo, M., Steele-MacInnis, M., Runyon, S.E., Sublett, D.M., Klyukin, Y., and Bodnar, R.J., 2020, Synthetic fluid inclusions XXII: Phase equilibria and microthermometric behavior of fluid inclusions trapped under vapor- and halite-saturated conditions: Geochimica et Cosmochimica Acta, v. 272, p. 78-92.

Lecumberri-Sanchez, P., Steele-MacInnis, M., and Bodnar, R.J., 2012, A numerical model to estimate trapping conditions of fluid inclusions that homogenize by halite disappearance: Geochimica et Cosmochimica Acta, v. 92, p. 14-22.

Lecumberri-Sanchez, P., Steele-MacInnis, M., Weis, P., Driesner, T., Bodnar, R.J., 2015, Salt precipitation in magmatic-hydrothermal systems around upper-crustal plutons: Geology v. 43, p. 1063-1066.

Lee, C.A. et al., 2007, Trace-element composition of Fe-rich residual liquids formed by fractional crystallization: Implications for the Hadean magma ocean: Geochimica et Cosmochimica Acta, v. 71, p. 3601-3615.

Lentz, D.R., 1998, Late-tectonic U-Th-Mo-REE skarn and carbonatitic vein-dyke systems in the southwestern Grenville Province: A pegmatite-related pneumatolytic model linked to marble melting: in Mineralized Intrusion-related Skarn Systems (Lentz, D.R., ed.): Mineralogical Association of Canada, Short Course v. 26, p. 519-657.

Lentz, D.R., 1999, Carbonatite genesis: A reexamination of the role of intrusion-related pneumatolytic skarn processes in limestone melting: Geology. v. 27, p. 335-338.

Li, J.X., Li, G.M., Qin, K.Z., and Xiao, B., 2011, High-temperature magmatic fluid exsolved from magma at the Duobuza porphyry copper–gold deposit, Northern Tibet: Geofluids, v. 11, p. 134–143.

Li, R. et al., 2017, Ore fluid evolution in the giant Marcona Fe-(Cu) deposit, Perú: Evidence from in-situ sulfur isotope and trace element geochemistry of sulfides: Ore Geology Reviews, v. 86, p. 624-638.

Li, W., Audétat, A., and Zhang, J. 2015, The role of evaporites in the formation of magnetite–apatite deposits along the Middle and Lower Yangtze River, China: Evidence from LA-ICP-MS analysis of fluid inclusions: Ore Geology Reviews, v. 67, p. 264-278.

Lindsley, D., and Epler, N., 2017, Do Fe-Ti-oxide magmas exist? Probably not!: American Mineralogist, v. 102, p. 2157–2169.

Lledo, H.L., 2005, Experimental Studies on the origin of iron deposits; and mineralization of Sierra La Bandera, Chile: unpub Dissertation, State University of New York at Binghamton. 271p.

London, D., 2009, The origin of primary textures in granitic pegmatites: The Canadian Mineralogist. v. 47, p. 697–724.

Lovering, D.G., 1982, Molten Salt Technology

Lowenstern, J.B., and Sinclair, W.D., 1996, Exsolved magmatic fluid and its role in the formation of comb-layered quartz at the Cretaceous Logtung W-Mo deposit, Yukon Territory, Canada: Transactions of the Royal Society of Edinburgh, Earth Sciences, v. 87, p. 291–303.

Lyons, J.I., 1988, Volcanogenic Iron Oxide Deposits, Cerro De Mercado and Vicinity, Durango, Mexico: Economic Geology, v.83, p. 1886-1906

Martinsson O., 1997, Tectonic Setting and Metallogeny of the Kiruna Greenstones: PhD Thesis, Luleå University of Technology, v. 19.

Martinsson O., and Virkkunen R., 2004, Apatite iron ores in the Gällivare, Svappavaara, and Jukkasjaärvi areas: Society of Geologic Geologist, Guidebook Series v. 33, p. 167–172.

Matthews, S., Sparks, R., and Gardeweg, M., 1999, The Piedras Grandes-Soncor eruptions, Lascar ulcano, Chile: evolution of a zoned magma chamber in the Central Andean upper crust: Journal of Petrology. v. 40, p. 1891–1919.

Matthews, S.J., 1993, El Laco magnetite lava, northern Chile: A REE-bearing iron oxide-phosphate magma. in Rare earth minerals: chemistry, origin and ore deposits: p. 81–82. Mineralogical Society of Great Britain and Ireland and the Natural History Museum, London, Abstracts, 1-2 April 1993.

Matthews, S.J., Jones, A.P., and Beard, A.D., 1994, Buffering of melt oxygen fugacity by sulphur redox reactions in calc-alkaline magmas: Journal of the Geological Society, London v. 151, p. 815–823.

Matthews, S.J., Marquillas, R.A., Kemp, A.J., Grange, F.K., and Gardeweg, M.C., 1996, Active skarn formation beneath lascar volcano, northern Chile: A petrographic and geochemical study of xenoliths in eruption products: Journal of Metamorphic Geology, v. 14, p. 509-530.

McCrea, J.M., 1950, On the isotopic chemistry of carbonates and paleotemperature scale: Journal of Chemical Physics, v. 18, p. 849-857.

McDonough, W.F., and Sun, S., 1994, The Composition of the Earth: Chemical Geology, v. 120, p. 223-253.

Mercer, C.N., and Reed, M.H., 2013, Porphyry Cu-Mo stock work formation by dynamic, transient hydrothermal pulses: mineralogic insights from the deposit at Butte, Montana: Economic Geology, v. 108, p. 1347–1377.

Mercer, C.N., Reed, M.H., and Mercer, C.M., 2015, Time Scales of Porphyry Cu Deposit Formation: Insights from Titanium Diffusion in Quartz: Economic Geology, v. 110, p. 587-602.

Mernagh, T.P., and Mavrogenes, J., 2019, Significance of high temperature fluids and melts in the Grasberg porphyry copper-gold deposit: Chemical Geology, v. 508, p. 210-224.

Moore, F., and Modabberi, S., 2003, Origin of Choghart iron oxide deposit, Bafq mining district, central Iron: New isotopic and geochemical evidence: Journal of Science, v. 14, p. 259-269.

Mungall, J.E., 2014, Geochemistry of Magmatic Ore Deposits: in Treatise on Geochemistry, Second Edition v. 13, p. 195-215.

Mungall, J.E., Long, K., Brenan, J.M., Smythe, D., and Nuslund, H.R., 2018, Immiscible shoshonitic and Fe-P-oxide melts preserved in unconsolidated tephra at El Laco volcano, Chile: Geology. v. 46, p. 255-258.

Muntean, J.L., and Einaudi, M.T., 2001, Porphyry gold deposits of the Refugio district, Maricunga belt, Northern Chile: Economic Geology, v. 95, p. 1445-1472.

Naranjo, J.A., Henríquez, F., and Nyström, J.O., 2010, Subvolcanic contact metasomatism at El Laco Volcanic Complex, Central Andes: Andean Geology, v. 37, p. 110–120.

Naslund, H.R., Henriquez, F., Nystr.m, J.O., Vivallo, W., and Dobbs, F.M., 2002, Magmatic iron ores and associated mineralisation; Examples from the Chilean High Andes and Coastal Cordillera, in Porter, T.M., ed., Hydrothermal Iron Oxide Copper-Gold and Related Deposits: A Global Perspective, Volume 2: Adelaide, Australia, PGC Publishing, p. 207–226.

Newton, R.C., and Manning, C.E., 2005, Solubility of Anhydrite, CaSO4, in NaCl-H2O solutions at high pressure and temperatures: applications to fluid-rock interactions: Journal of Petrology, v. 46, p 701-716.

Nielsen, C.H., and Sigurdsson, H., 1981, Quantitative methods for electron microprobe analysis of sodium in natural and synthetic glasses: American Mineralogist v. 66, p. 547-552.

Nyström, J. O. and Henríquez, F., 1994, Magmatic features of iron ores of the Kiruna type in Chile and Sweden: ore textures and magnetite geochemistry: Economic Geology. v. 89, p. 820–839.

Nyström, J.O., Henríquez, F., Naranjo, J.A., and Naslund, H.R., 2016, Magnetite spherules in pyroclastic iron ore at El Laco, Chile: American Mineralogist, v. 101, p. 587–595.

Oliver, N.H.S. et al., 2004, Modeling the role of sodic alteration in the genesis of iron oxide-copper-gold deposits, eastern Mount Isa Block, Australia: Economic Geology v. 99, p. 1145-1176.

Ovalle, J.T. et al., 2018, Formation of massive iron deposits linked to explosive volcanic eruptions: Scientific Reports. v. 8. p. 1-11.

Palmer, D.A.S., and Williams-Jones, A.S., 1996, Genesis of the Carbonatite-hosted fluorite deposit at Amba Dogar, India: Evidence from fluid inclusions, stable isotopes, and whole rock-mineral geochemistry: Economic Geology, v. 91, p. 934-950.

Pasteris, J.D., 1996, Mount Pinatubo volcano and "negative" porphyry copper deposits: Geology, v. 24, p. 1075–1078.

Perring, C.S., Pollard, P.J., Dong, G., Nunn, A.J., and Blake, K.L., 2000, The Lightning Creek Sill complex, Cloncurry District, Northwest Queensland: a source of fluids for Fe Oxide

Cu-Au mineralization and sodic-calcic alteration: Economic Geology, v. 95, p. 1067-1089.

Phillips, W.J., 1986, Hydraulic fracturing and effects in the formation of mineral deposits: Transactions of the Institution of Mining and Metallurgy, Section B: Applied Earth Sciences, v. 95, p. p. B17–B24.

Philpotts, A.R., 1982., Compositions of immiscible liquids in volcanic rocks: Contributions to Mineral Petrology, 80, 201–218.

Rocco, T., Freda, C., Gaeta, M., Mollo, S., and Dallai, L., 2012, Magma chambers emplaced in carbonate substrate: Petrogenesis of skarn and cumulate rocks and implications for CO2 degassing in volcanic areas: Journal of Petrology, v. 53, p. 2307-2332.

Roedder, E., 1992: Fluid inclusion evidence for immiscibility in magmatic differentiation: Geochimica et Cosmochimica Acta, v. 56, p. 5–20.

Rottier, B., Kouzmanov, K., Bouvier, A.-S., Baumgartner, L.P., W.lle, M., Rezeau, H., Bendez.d, R., and Fontbot., L., 2016, Heterogeneous melt and hypersaline liquid inclusions in shallow porphyry type mineralization as markers of the magmatic-hydrothermal transition (Cerro de Pasco district, Peru): Chemical Geology, v. 447, p. 93–116.

Rowley, P.D., and Barker, D.S., 1978, Geology of the Iron Springs mining district, Utah: Guidebook to Mineral Deposits of Southwestern Utah: Utah Geological Association Publication. v. 7, p. 1-7.

Rudnick, R.L. and Gao, S., 2014, Composition of the continental crust: in Treatise on Geochemistry 2nd Edition, v. 3, p. 1-64.

Runyon, S.E., Seedorff, E., Barton, M.D., Steele-MacInnis, M., Lecumberri-Sanchez, P., and Mazdab, F.K., 2019, Coarse muscovite veins and alteration in porphyry systems: Ore Geology Reviews, v. 113, p. 1-32

Runyon, S.E., Steele-MacInnis, M., Seedorff, E., Lecumberri-Sanchez, P., and Mazdab, F.K., 2017, Coarse muscovite veins and alteration deep in the Yerington batholith, Nevada: insights into fluid exsolution in the roots of porphyry copper systems: Mineralium Deposita, v. 52, p. 463-470.

Rusk, B.G., Reed, M.H., and Dilles, J.H., 2008, Fluid inclusion evidence for magmatic-hydrothermal fluid evolution in the porphyry copper-molybdenum deposit at Butte, Montana: Economic Geology, v. 103, p. 307–334.

Sabet-Mobarhan-Tala, A., Alinia, F., Ghannadpour, S., and Hezarkhani, A., 2015, Geology, geochemistry, and some genetic discussion of the Chador-Malu iron oxide-apatite deposit, Bafq District, Central Iran: Arabian Journal of Geosciences v. 8, p. 8399-8418.

Seedorff, E., and Einaudi, M.T., 2004, Henderson porphyry molybdenum system, Colorado: I. Sequence and abundance of hydrothermal mineral assemblages, flow paths of evolving fluids, and evolutionary style: Economic Geology, v. 99, p. 3-37.

Shan, Q. et al., 2012, Zircon U–Pb ages and geochemistry of the potassic and sodicrhyolites of the Kangbutiebao Formation in the southern margin of Altay, Xinjiang: Acta Petrologica Sinica, v. 28, p. 2132–2144.

Sillitoe, R.H., 2010, Porphyry copper systems: Economic Geology, v. 105, p. 3–41

Sillitoe, R.H., and Burrows, D.R., 2002, New field evidence bearing on the origin of the El Laco magnetite deposit, northern Chile: Economic Geology and the Bulletin of the Society of Economic Geologists, v. 97, p. 1101–1109.

Simon, A. et al., 2018, Kiruna-type iron oxide-apatite (IOA) and iron oxide copper-gold (IOCG) deposits form be a combination of igneous and magmatic-hydrothermal processes: evidence from the Chilean iron belt: Society of Economic Geologist special publications, v. 21, p. 89-114.

Simon, A.C., Pettke, T., Candela, P.A., Piccoli, P.M., and Heinrich, A.H., 2004, Magnetite solubility and iron transport in magmatic-hydrothermal environments: Geochimica et Cosmochimica Acta, v. 68, p. 4905–4914.

Speed, R.C., 1976, Geologic map of the Humboldt lopolith and surrounding terrane, Nevada: Geologic society of America. Map and Chart Series MC-14.

Steele-MacInnis, M., Lecumberri-Sanchez, P., and Bodnar, R. J., 2012, HokieFlincs_H2O-NaCl: A Microsoft Excel spreadsheet for interpreting microthermometric data from fluid inclusions based on the PVTX properties of H2O-NaCl: Computers and Geosciences, v. 49, p. 334–337.

Steele-MacInnis, M., Ridley, J., Lecumberri-Sanchez, P., Schlegel, T. U., and Heinrich, C. A., 2016, Application of low-temperature microthermometric data for interpreting multicomponent fluid inclusion compositions: Earth Science Reviews, v. 159, p. 14–35.

Stefanova, E., Driesner, T., Zajacz, Z., Heinrich, C.A., Petrov, P., and Vasilev, Z., 2014, Melt and Fluid Inclusions in Hydrothermal Veins: The Magmatic to Hydrothermal Evolution of the Elatsite Porphyry Cu-Au Deposit, Bulgaria: Economic Geology, v. 109, p. 1359-1381

Tait, S., 1992, Selective preservation of melt inclusions in igneous phenocrysts: American Mineralogist, v. 77, p. 146-155.

Thomas, J.B., Watson, E.B., Spear, F.S., Shemella, P.T., Nayak, S.K., and Lanzirotti, A., 2010, TitaniQ under pressure: the effect of pressure and temperature on the solubility of Ti in quartz: Contributions to Mineralogy and Petrology, v. 160, p. 743−759.

Torab, F.M., 2008, Geochemistry and metallogeny of magnetite apatite deposits of the Bafq Mining District, Central Iran: Unpub Thesis.

Tornos, F., Velasco, F., and Hanchar, J. M., 2017, The magmatic to magmatic hydrothermal evolution of the El Laco deposit (Chile) and its implications for the genesis of magnetite-apatite deposits: Economic Geology, v. 112, p. 1595–1628.

Tornos, F., Velasco, F., and Hanchar, J., 2016, Iron-rich melts, magmatic, magnetite, and superheated magmatic-hydrothermal systems: The El Laco deposit, Chile: Geology, v. 44, p. 427–430.

Tornos, F., Velasco, F., and Hanchar, J.M. 2017, The magmatic-hydrothermal evolution of the El Laco deposit (Chile) and its implications for the genesis of magnetite-apatite deposits: Econominc Geology. v. 112, p. 1595-1628.

Tornos, F., Velasco, F., Morata, D., Barra, F., and Rojo, M., 2011, The magmatic hydrothermal evolution of the El Laco deposit as tracked by melt inclusions and isotope data: in Barra, F., Reich, M., Campos, E., Tornos, F. (Eds.), Let's Talk Ore deposits, p. 345–3.

Trumbull, R.B., Wittenbrink, R., Hahne, K., Emmermann, R., Busch, W., Gerstenberger, H., and Siebel, W., 1999, Evidence for late Miocene to Recent contamination of arc andesites by crustal melts in the Chilean Andes (25–26°S) and its geodynamic implications: Journal of South American Earth Sciences, v. 12, p. 135–155.

Tuttle, O. F., and N. L. Bowen, 1958, Origin of granite in the light of experimental studies in the system NaA1Si3O8-KA1Si308-SiO2-H2O: Geologic Society of America, v. 74, p. 153.

Veksler, I.V., 2004, Liquid immiscibility and its role at the magmatic–hydrothermal transition: a summary of experimental studies: Chemical Geology, v. 210, p. 7–31.

Veksler, I.V., 2007, et al. Liquid immiscibility and the evolution of basaltic magma: Journal of Petrology, v. 48, p. 2187-2210.

Veksler, I.V., 2009, Extreme iron enrichment and liquid immiscibility in mafic intrusions: Experimental evidence revisited: Lithos, v. 111, p. 72-82.

Velasco, F., Tornos, F. and Hanchar, J.M., 2016, Immiscible iron- and silica-rich melts and magnetite geochemistry at the El Laco volcano (northern Chile): Evidence for a magmatic origin for the magnetite deposits: Ore geology reviews. v. 79, p. 346-366.

Walter, B.F., Steele-MacInnis, M., and Markl, G., 2017, Sulfate brines in fluid inclusions of hydrothermal veins: Compositional determinations in the system H2O-Na-Ca-Cl-SO4: Geochimica et Cosmochimica Acta, v. 209, p. 184-203.

Wark, D.A., and Watson, E.B., 2006, TitaniQ: A titanium-in-quartz geothermometer: Contributions to Mineralogy and Petrology, v. 152, p. 743–754.

Watson, E.B., Wark, D.A., and Thomas, J.B., 2006, Crystallization thermometers for zircon and rutile: Contribution to Mineral Petrology v. 151, p. 413–433.

Webster, J. D., 2004, The exsolution of magmatic hydrosaline chloride liquids: Chemical Geology, v. 210, p. 33–48.

Weis, P., Driesner, T., and Heinrich, C.A., 2012, Porphyry-Copper Ore Shells Form at Stable Pressure-Temperature Fronts Within Dynamic Fluid Plumes: Science, v. 338, p. 1613-1616.

Wen, G., Bi, S. and Li, J., 2017, Role of evaporitic sulfates in iron skarn mineralization: a fluid inclusion and sulfur isotope study from the Xishimen deposit, Handan-Xingtai district, North China Craton: Mineralium Deposita, v. 52, p. 495-514.

Wenzel, T., Baumgartner, L. P., Brügmann, G. E., Konnikov, E. G., and Kislov, E. V., 2002, Partial melting and assimilation of dolomitic xenoliths by mafic magma: The Ioko-Dovyren intrusion (North Baikal region, Russia): Journal of Petrology, v. 43, p. 2049-2074.

Westhues, A., Hanchar, J.M., LeMessurier, M.J., and Whitehouse, M.J., 2017, Evidence for hydrothermal alteration and source regions the Kiruna iron oxide-apatite ore (northern Sweden) from zircon Hf and O isotopes: Geology. v. 45, p. 571-574.

Whiting, D.L., Grover, J.D. Jr., and Benson, W.R., 1992, Geology and mine reclamation studies, iron mines near Cedar City, Utah: in Engineering and environmental geology of southwestern Utah: Utah Geological Association Publication, v. 21, p. 287-313.

Wilson, A.J., Cooke, D.R., and Harper, B.L., 2003, The Ridgeway gold-copper deposit: A high-grade alkalic porphyry deposit in the Lachlan fold belt, New South Wales, Australia: Economic Geology, 98, 1637–1666.

Wyllie, P. J., and Tuttle, O. F., 1960, The system CaO-CO2-H2O and the origin of carbonatites: Journal of Petrology. v. 1, p. 1-46.

Yardley, B.W.D., 2005, Metal concentrations in crustal fluids and their relationship to ore formation: Economic Geology, v. 100, p. 613-632.

Yu, J., Che, L., and Wang, T., 2015, Alteration, oxygen isotope, and fluid inclusion study of the Meishan iron oxide–apatite deposit, SE China: Mineralium Deposita, v. 50, p. 847-869.

Yu, J., Lu, B., Wang, T., and Che, L., 2015, Cretaceous Cu–Au, pyrite, and Fe-oxide–apatite deposits in the Ningwu basin, Lower Yangtze Area, Eastern China: Journal of Asian Earth Sciences, v. 103, p. 150-168.

Yu, J.J., Chen, Y.C., Mao, J.W., Pirajno, F., and Duan, C., 2011, Review of geology, alteration and origin of iron oxide–apatite deposits in the Cretaceous Ningwu volcanic basin, Lower Yangtze River Valley, eastern China: implications for ore genesis and geodynamic setting: Ore Geology Reviews, v. 43, 1p. 70–181.

Zajacz, Z., Halter, W.E., Pettke, T., and Guillong, M., 2008, Determination of fluid/melt partition coefficients by LA-ICPMS analysis of co-existing fluid and silicate melt inclusions: Controls on element partitioning: Geochimica et Cosmochimica Acta, v. 72, p. 2169-2197.

Zandt, G., Velasco, A.A., and Beck, S.L., 1994, Composition and thickness of the southern Altiplano crust, Bolivia: Geology, v. 22, p. 1003–1006.

Zen, E., 1988, Phase relations in peraluminous granitic rocks and their petrographic implications: Annual Review of Earth and Planetary Sciences, v. 16, p. 21-52